Finite element modelling for component-level additive manufacturing applied to residual stress-deformation mitigation and fatigue crack initiation in welded connections

Jinbiao Zhou M.E. (2019)

Supervisors: Prof. Seán Leen and Dr. Richard Barrett

OLLSCOIL NA GAILLIMHE
UNIVERSITY OF GALWAY

A thesis submitted to the University of Galway as fulfilment of the requirements for the Degree of Doctor of Philosophy

Mechanical Engineering, University of Galway

May 2023

Abstract

Additive manufacturing (AM) has attracted significant attention in many applications due to its capability of fabricating complex and customized metal parts. However, the potential for high inherent residual stresses that produce distortion in AM components and have detrimental effects on fatigue life, prevents more widespread application of the AM technique. Efficient and accurate prediction of residual stress and distortion at component-level (macro-scale) is a complex task. Nowadays, the petrochemical and energy industries are evolving towards higher temperature and pressure operating conditions to improve efficiency and thereby reduce emissions, and thus help to reduce the "greenhouse effect", as well as increased operational load cycling, to facilitate increased renewable uptake. Such increased temperature-pressure and load cycling conditions inevitably poses significant new challenges for safe design and life analysis of key high temperature components, requiring materials and structures, such as welded connections, which are resistant to thermal fatigue, creep-fatigue and thermo-mechanical fatigue. The heat-affected zone (HAZ) of welded connections is particularly susceptible to fatigue crack initiation (FCI) due to the increased thermo-mechanical fatigue. This thesis presents the development of computational methods for addressing two specific challenges in relation to additive manufacturing and welding of metals, respectively.

As a first step towards an efficient three-dimensional finite element (FE) methodology for thermo-mechanical simulation of additive manufacturing processes for realistic full-scale engineering components, the directed energy deposition (DED) manufacture of a realistic Ti-6Al-4V component is investigated using a recently developed AM capability of the nonlinear FE code, Abaqus. The method essentially combines the 'element birth' method with a layer-scaling approach for highly efficient simulation of AM processes. It is shown that the method can be implemented to achieve highly-efficient and highly accurate simulation of DED of the complex, large-scale Ti-6Al-4V component with respect to (i) thermal histories for selected sample locations, to facilitate microstructure prediction, for example, and hence, mechanical properties, and (ii) residual stresses, as required for

accurate assessment and design for structural integrity, such as fatigue. The predicted results are successfully validated against published experimental and numerical data. The effects of different scanning strategies on temperature histories and residual stresses are investigated as a basis for identification of optimal manufacturing protocols. Finally, fatigue life predictions of the Ti-6Al-4V component have been considered based on the Basquin-Goodman equation with the effect of residual stress taken into account.

The new Abaqus-based method is implemented for simulation method with detailed validation for powder bed fusion (PBF) manufacture of a complex 3D Inconel 625 benchmark bridge component (macro-scale) to predict residual stress and distortion at component-level (macro-scale) efficiently and accurately. It is shown that the new Abaqus-based method can achieve very good agreement with the published benchmark experimental measurements from neutron diffraction, X-ray diffraction (XRD), contour method and coordinate measurement machine (CMM) by the National Institute of Standards and Technology (NIST) laboratory. The key advantages of this method are the significant improvement in computational efficiency, on the one hand, and the ease of implementation, on the other hand. Both of these will facilitate industrial application of this technique, which will, in turn, foster more widespread use of AM itself. The new modelling method has been applied to identify optimal preheating conditions for mitigation of residual stresses and distortions and, thus, inevitable increase in fatigue life.

A methodology is presented for physically-based prediction of high temperature fatigue crack initiation in 9Cr steels, with specific application to welding-induced material inhomogeneity due to thermally-induced metallurgical transformations. A modified form of the Tanaka-Mura model for slip band formation under cyclically-softening conditions is implemented in conjunction with a physically-based unified cyclic viscoplasticity constitutive model. The physically-based constitutive model accounts for the key strengthening mechanisms, including precipitate hardening and hierarchical grain boundary strengthening, successfully predicting cyclic softening in 9Cr steels. A five-material, finite element model of a P91 cross-weld test specimen, calibrated using the physically-based yield strength and constitutive models, successfully predicts the

measured detrimental effect of welding on high temperature low-cycle fatigue crack initiation for P91 cross weld tests, via the modified Tanaka-Mura model. A key finding here is the requirement to adopt an energy-based Tanaka-Mura method to account for cyclic softening in 9Cr steels, with packet size as the critical length-scale for slip band formation.

The developed AM process (DED and PBF) simulation models and mechanisms-based FCI model are key building blocks towards a pragmatic process-structure-property-performance (PSPP) design tool for industry, which not only can guide the selection of optimal manufacturing protocols, but also facilitate integration of computational modelling for industrial application to complex geometries. The ultimate aim of the work presented here is to directly contribute to this PSPP tool for fatigue of complex geometry AM components including residual stress effects, e.g. conformally-cooled injection moulding dies.

List of Publications

Journal Papers

The work presented in this thesis comprises the following journal publications:

- J. Zhou, R.A. Barrett, S.B. Leen, Three-dimensional finite element modelling for additive manufacturing of Ti-6Al-4V components: Effect of scanning strategies on temperature history and residual stress, Journal of Advanced Joining Processes 5 (2022) 100106. (https://doi.org/10.1016/j.jajp.2022.100106) (**Chapter 3**)

- J. Zhou, R.A. Barrett, S.B. Leen, Finite element modelling for mitigation of residual stress and distortion in macro-scale powder bed fusion components, Proceedings of the Institution of Mechanical Engineers, Part L: Journal of Materials: Design and Applications (2022). (https://doi.org/10.1177/14644207221146288) (**Chapter 4**)

- J. Zhou, Y. Chen, C. O'Hara, D. Tormey, R.A. Barrett, X. Wang, S.B. Leen, Effect of Build Orientation and Surface Roughness on Fatigue Behaviour of Additively Manufactured 316L Stainless Steel. (In preparation) (**Chapter 5**)

- J. Zhou, R.A. Barrett, S.B. Leen, A physically-based method for predicting high temperature fatigue crack initiation in P91 welded steel, International Journal of Fatigue 153 (2021) 106480. (https://doi.org/10.1016/j.ijfatigue.2021.106480) (**Chapter 6**)

Note: Jinbiao Zhou is the primary author and is directly responsible for the theoretical and computational work for each publication.

Conference Proceedings

- J. Zhou, R.A. Barrett, S.B. Leen, "Finite element simulation of additive manufacturing for injection moulding dies", The 2nd International Conference on Advanced Joining Processes 2021, 21-22 October, Sintra, Portugal. (**Chapter 3**)

- J. Zhou, R.A. Barrett, S.B. Leen, "Fatigue performance of additively manufactured 316L stainless steel: Effect of build orientation and surface roughness", 11th European Solid Mechanics Conference 2022, 4-8 July, Galway, Ireland. (**Chapter 5**)

- J. Zhou, R.A. Barrett, S.B. Leen, "Physically-based Fatigue Crack Initiation Model for P91 Welded Steel", The 3rd International Conference on Materials Design and Applications 2020, 5-6 November, Porto, Portugal. (**Chapter 6**)

- J. Zhou, R.A. Barrett, S.B. Leen, "Physically-based process-structure-property-performance modelling of the effects of manufacturing process on fatigue", 25th Annual Sir Bernard Crossland Symposium 2022, 1-2 September, Galway, Ireland. (**Chapter 6**)

Acknowledgements

Firstly, I wish to thank my supervisors Prof. Seán Leen and Dr. Richard Barrett, for their immense knowledge, guidance, and patience throughout my doctoral study. Without their support, I would not be able to finish my doctoral project.

I would like to acknowledge Science Foundation Ireland (SFI) for funding this research as part of the MECHANNICS project under grant number SFI/14/IA/2604 and I-Form project, the SFI research centre for advanced manufacturing, under grant number 16/RC/3872. I am grateful to Dr. Noel Harrison, Prof. Padraic O'Donoghue and Dr. Mingming Tong for their encouragements and significant contributions as members of my GRC committee. I would also like to acknowledge the numerous project members and collaborators, in particular: Dr David Tormey and Christopher O'Hara of Atlantic Technological University, Carlos Souto of AbbVie. I would like to acknowledge the helpful discussions with Dr. Wenyou Zhang of Trinity College Dublin and Prof. Xiaowei Wang of Nanjing Tech University.

I would like to thank the research and technical staff at NUI Galway for their assistance throughout this work, in particular: William Kelly, Patrick Kelly, Dermot McDermott and Dave Finn.

I would also like to sincerely thank all my friends and colleagues, both in China and Ireland, for their support and encouragements in this journey.

Lastly, I would like to express my deepest gratitude to all members of my beloved family.

Table of Contents

Acronyms

AM	Additive manufacturing
DED	Directed energy deposition
DIC	Digital Image Correlation
EBM	Electron beam melting
FE	Finite element
LAGBs	Low angle grain boundaries
LB	Laser beam
PBF	Powder bed fusion
PSPP	Process-structure-property-performance
PWHT	Post-weld heat treatment
SEM	Scanning electron microscope
SS316L	Stainless steel 316L
UTS	Ultimate tensile stress
XRD	X-ray diffraction
YS	Yield strength
2D	Two-dimensional
3D	Three-dimensional

Nomenclature

A	Powder absorptivity coefficient
b	Fatigue strength exponent
B	Rate of decay leading to saturation
c	Concentration of solutes
$\boldsymbol{C}$	Elastic stiffness tensor
C_{p}	Specific heat
d_{m}	Melt pool depth
d_{s}	Heat source spot diameter
d_{b}	Martensitic block width
d_{g}	Grain size
d_{p}	Packet size
E	Young's modulus
f	Yield function
f_{w}	Volume fractions of the LABs
f_{g}	Volume fractions of the HAGBs
ΔF	Helmholtz free energy
$\mathbf{F}$	Deformation gradient
$\mathbf{F}^{\boldsymbol{e}}$	Elastic deformation gradient

$\mathbf{F}^{\boldsymbol{p}}$	Plastic deformation gradient
h	Heat transfer coefficient
L_{h}	Layer height
$\mathbf{L}^{\boldsymbol{p}}$	Plastic velocity gradient tensor
$\mathbf{I}$	Identity tensor
k	Thermal conductivity
k_{B}	Boltzmann's constant
k_{f}	Frictional shear stress
$k_{\mathrm{HP},0}$	Hall-Petch constant at 0 K
$\mathbf{K}_{\mathrm{v}}$	Elastic tensor of elastic-viscous network
$\mathbf{K}_{\mathrm{p}}$	Elastic tensor of elastic-plastic network
M	Taylor factor
M_{s}	Martensite start temperature
$\boldsymbol{m}^{\boldsymbol{\alpha}}$	Normal to slip plane
$\bar{m}$	Equivalent LAB size
n_{g}	Number of dislocations in the pileups
n_{HP}	Hall-Petch exponent
N_{f}	Number of cycles to failure
N_k	Dislocation number

U	Stored strain energy
P	Laser beam power
R	Heat source spot radium
H_{s}	Hatch spacing
v_{s}	Laser beam scanning speed
Q	Saturation value of the isotropic hardening (or softening) stress
q	Heat flux
q_{cond}	Conduction heat flux
q_{conv}	Conduction heat flux
q_{rad}	Radiation heat flux
α	Thermal expansion coefficient
$\dot{\boldsymbol{\gamma}}^{\boldsymbol{\alpha}}$	Slip rate
$\mathbf{s}^{\boldsymbol{\alpha}}$	Slip direction
t	Time
T	Temperature
T_{a}	Ambient temperature
T_{p}	Predefined temperature
w	Martensitic lath width
w_0	Initial martensitic lath width

w_s	Specific fracture energy per unit area
ΔV	Activation volume
ε	Strain
$\boldsymbol{\varepsilon}$	Strain tensor
$\Delta\varepsilon$	Total strain range
$\dot{\varepsilon}_c$	Creep strain rate
ε_e	Elastic strain
$\Delta\varepsilon^{el}$	Elastic strain range
$\Delta\varepsilon^{pl}$	Plastic strain range
ε_f'	Fatigue ductility coefficient
ε_p	Plastic strain
ε_{Total}	Total strain
ε_{xx}	Strain along x direction
ε_{yy}	Strain along y direction
ε_{zz}	Strain along z direction
ε_{rad}	Emissivity coefficient
μ	Shear modulus
ρ_m	Mass density
ρ	Dislocation density

ρ_{i}	Initial dislocation density
$\rho_{\mathrm{w,0}}$	LAB dislocation density
σ_{rad}	Stephan-Boltzmann's constant
σ	Stress
σ_{b}	Kinematic back-stress
σ_{e}	Equivalent (von Mises) stress
$\boldsymbol{\sigma}'$	Deviatoric stress
σ_{ph}	Back-stress contributions due to particles
$\sigma_{\mathrm{ph,INT}}$	Precipitate yield strength in the martensitic lath interiors
$\sigma_{\mathrm{ph,BND}}$	Precipitate yield strength at the GBs
σ_{g}	Back-stress contributions due to dislocation pileups at HAGBs
σ_{w}	Back-stress contributions due to dislocation substructure
σ_{xx}	Stress along x direction (S11)
σ_{yy}	Stress along y direction (S22)
σ_{zz}	Stress along z direction (S33)
$\boldsymbol{\sigma}$	Stress tensor
σ_{a}	Alternating stress
σ_{m}	Mean stress
σ_{r}	Residual stress

σ_{TS}	Ultimate tensile strength
σ_{y}	Yield strength
$\sigma_{\mathrm{y}}^{\mathrm{cyc}}$	Cyclic yield stress
$\boldsymbol{\sigma}_{\mathrm{p}}$	Stress tensor of elastic-plastic network
$\boldsymbol{\sigma}_{\mathrm{v}}$	Stress tensor of elastic-viscous network
$\boldsymbol{\Sigma}'$	Deviatoric stress tensor
τ_{A}	Contributions from dislocations to yield strength
τ_{B}	Contributions from obstacles to yield strength
τ_1^D	Dislocation stress (back stress)
τ_{PN}	Peierls-Nabarro stress
τ_{bd}	Contribution of grain boundaries to yield strength
τ_{SS}	Solid solution strengthening term
τ_{ph}	Precipitates term
τ_{in}	Interstitial solid solution strengthening term
τ_{HP}	Contribution of HAGB to strength
τ_{LAB}	Strengthening due to the LAB dislocation substructure
λ	Precipitate spacing
θ	Angle of misorientation between LABs
ν	Poisson's ratio

1 Introduction

1.1 Background and motivation

1.1.1 The development of next generation power plants

Energy is recognized as the driving force of a country's economic growth, an essential commodity for comprehensive development [1-3]. In addition to its positive role, it is also one of the main sources of greenhouse gas (GHG) emissions [4-6]. Most of the GHG emitted are generated through energy production, such as burning fossil fuels to generate electricity and heat. According to the report given by National Oceanic and Atmospheric Administration, June 2022 was the Earth's 6th warmest on record [7]. Carbon dioxide (CO2) levels and other GHGs in the atmosphere rose to new records in 2022 [8]. GHG emissions need to be reduced at least 50% by 2030 (compared with 1990) and reach net-zero by mid-century to avoid the worst impacts of climate change [9]. As shown in Figure 1.1, both Ireland (see Figure 1.1 (a)) and the European Union (see Figure 1.1 (b)) have increased their share of renewable energy (predominantly from wind and solar) since 2005 to achieve this goal. However, the amount of renewable energy from wind that can be collected at a given time is unpredictable due to the inconsistency of the wind source [10]. Thus, conventional power plant must became capable of starting up and shutting down much more frequently (high flexibility) to adapt to unpredictable availability of renewable sources such as wind [11].

Conventional coal power plants need to adapt to operate with increased efficiency to reduce emissions, in order to tackle climate change [12]. As illustrated in Figure 1.2, the efficiency of the coal power plant is a strong function of the steam turbine inlet pressure (see Figure 1.2 (a)) and temperature (see Figure 1.2 (b)). Operating power plant at higher pressure and temperature ensures more complete combustion of fossil fuels, thereby reducing CO_2 emissions [13]. The increased efficiency of the coal power plant can lead to significant decrease of CO_2 emissions, as shown in Figure 1.3.

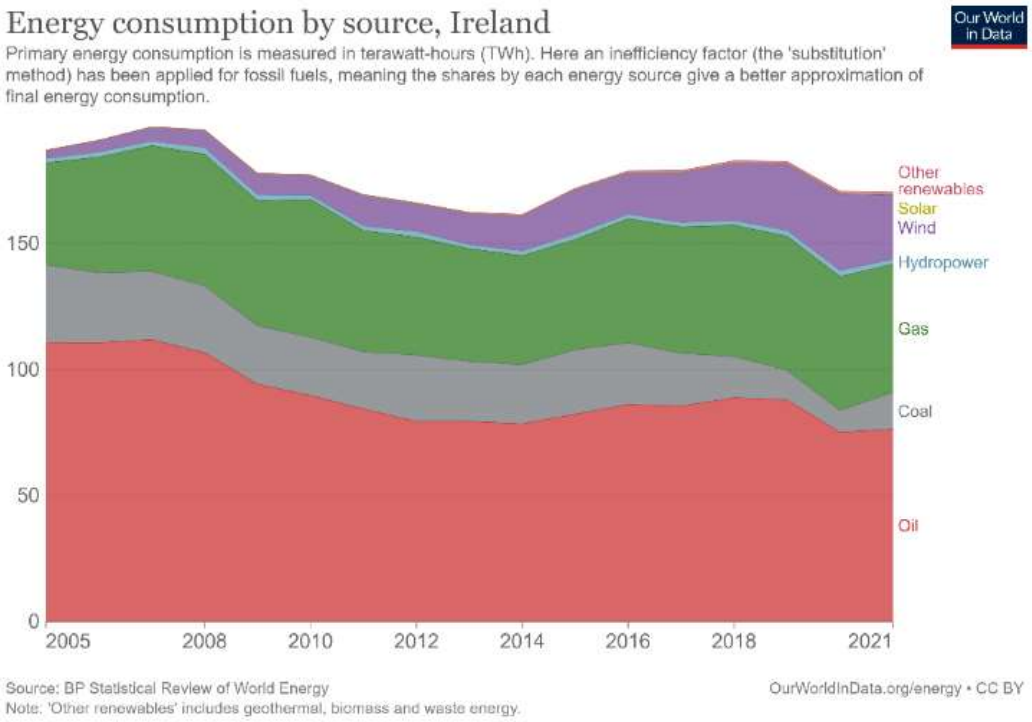

(a)

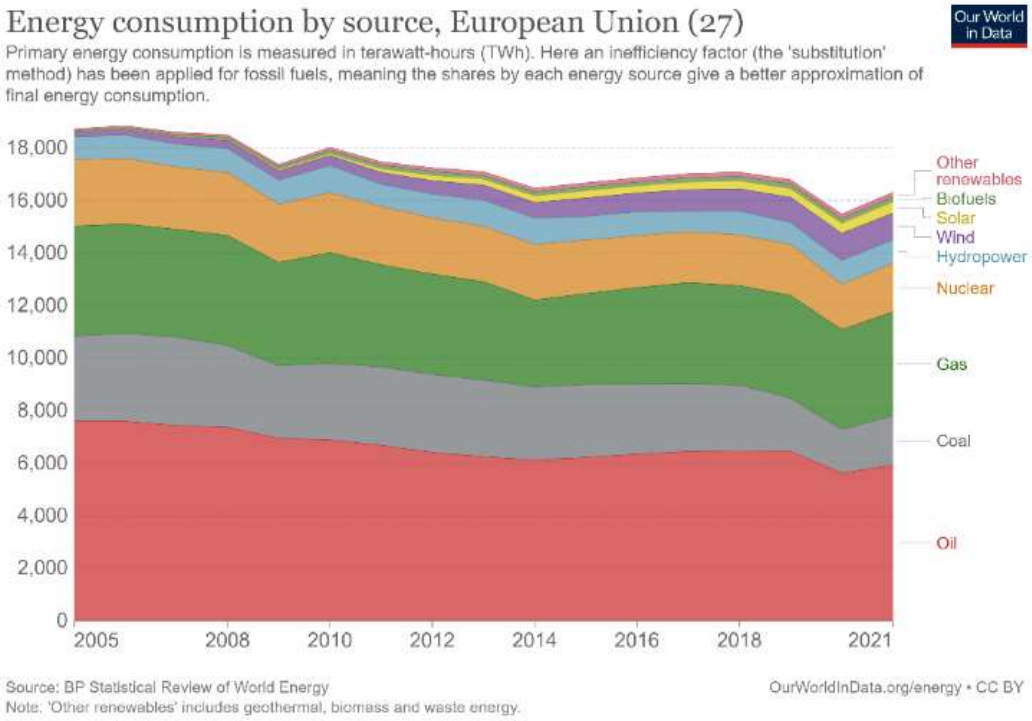

(b)

Figure 1.1. Primary energy consumption by source: (a) Ireland, (b) European Union [14].

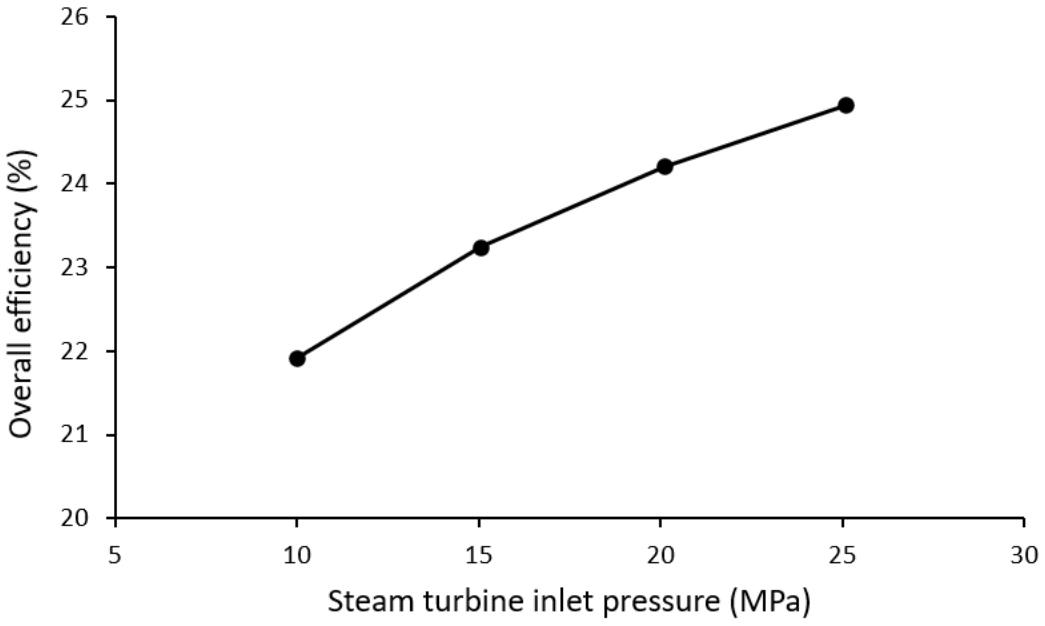

(a)

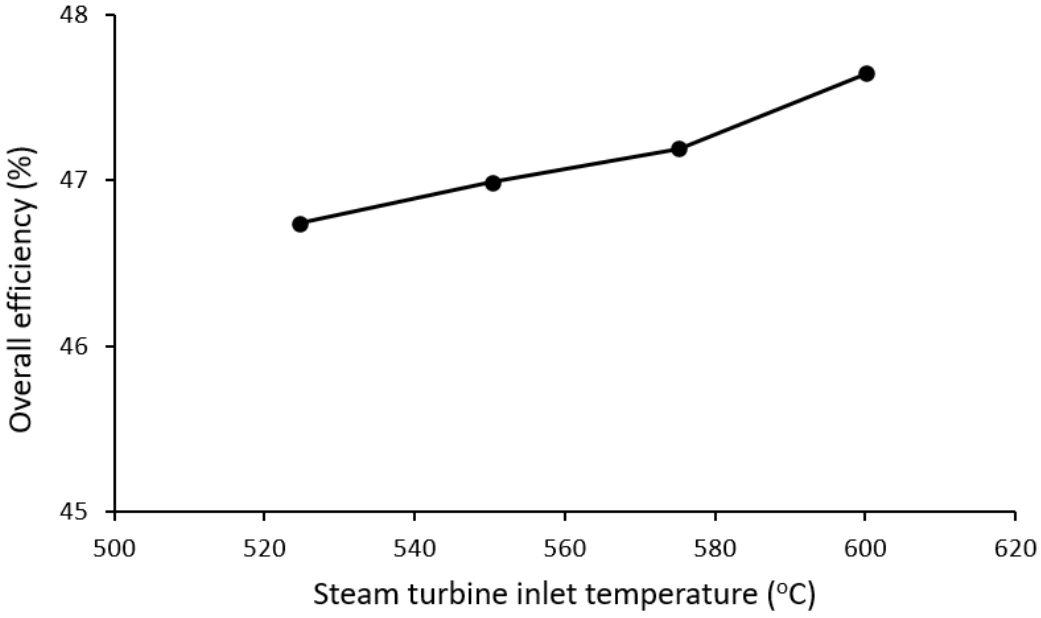

(b)

Figure 1.2. Energy efficiency of the coal power plants: (a) steam turbine inlet pressure, (b) steam turbine inlet temperature, adapted from [15].

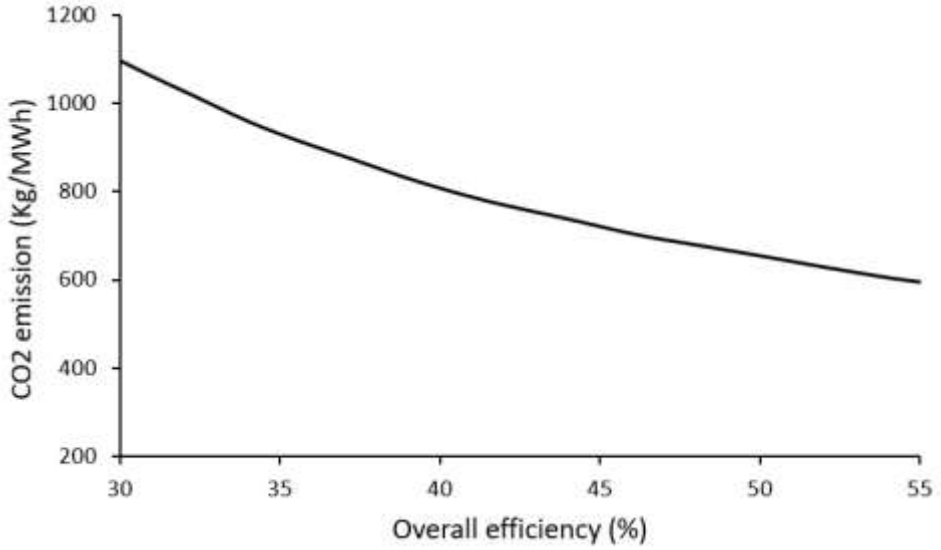

Figure 1.3. Decreasing CO_2 emissions with increasing plant efficiency, adapted from Baczoni et al. [16].

The rise of steam operation parameters leads to a considerable increase in the requirement for the performance of components [17]. Figure 1.4 shows an example of a branched steam header with many complex welded connections in ESB power plant. P91 steel is a 9Cr1Mo nano-strengthened, tempered martensitic alloy for high temperature applications, specially developed for the power generation industry, to give improved efficiency performance due to its high thermal conductivity and low thermal diffusion coefficient [18]. Welding is a key and complex manufacturing technology, which is used to build steam pipelines and header systems in power plants [19]. Due to the severe thermal cycle caused by the welding process, the original microstructure is changed by melting to a liquid pool, which is called weld material (WM) region after solidification. Next to the WM is the heat affected zone (HAZ). The material which is not affected by the welding process is the parent metal (PM) [20, 21]. In the context of increased thermo-mechanical fatigue, e,g, for improved flexibility and efficiency the coal power plant, the heat affected zone (HAZ) of welded connections is particularly susceptible to fatigue crack initiation (FCI) [22, 23]. The HAZ sub-regions can be further divided into inter-critical (ICHAZ), fine-grained (FGHAZ) and coarse-grained (CGHAZ) according to their characteristic micro-structures [24]. Under complex operational loading conditions, failure commonly

initiates within the ICHAZ, which is known as Type-IV cracking [25, 26], as shown in Figure 1.5.

Figure 1.4. Installation of a branched header in ESB power plant (Stephen Scully, ESB Energy International [27]).

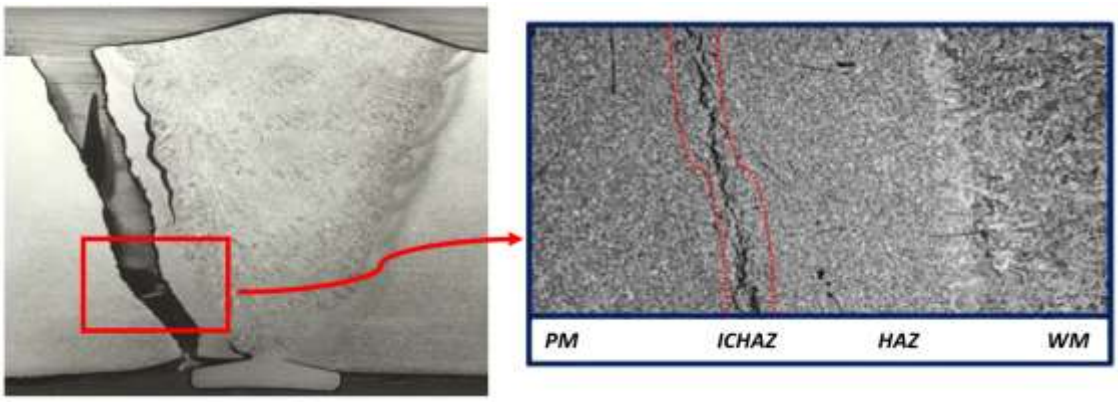

Figure 1.5. Image of cracking in the ICHAZ of P91 welded connection (R Barrett [28]).

The development of petrochemical and energy power industries towards higher pressure and temperature (i.e. plant operating pressures up to 30 MPa and temperatures in excess of 600 °C for P91 steel [28]) will inevitably pose many new challenges to the safe design and life analysis of high temperature key components, requiring materials and structures, such as welded connections, which are resistant to thermal fatigue, creep-fatigue and thermo-mechanical fatigue. A key obstacle to safe design of such plant, to protect

personnel, assets and the environment, is the need for appropriate structural integrity assessment methods. In the face of frequent start-up, shut-down and large-scale load variations, increased occurrence of repeated thermal and mechanical stresses will lead to increased low cycle fatigue damage. An understanding of the effect of welding on fatigue behaviour of P91 welded connections under high temperature low cycle fatigue conditions is thus of the upmost importance.

1.1.2 The application of metal additive manufacturing

Additive manufacturing (AM) or, 3D printing, is one of the critical pillars of Industry 4.0 [29] and the next construction revolution [30]. As shown in Figure 1.6, the global metal additive manufacturing market is valued about EUR 2 billion in 2020, including sales of systems, materials and services. Although the growth slowed down in 2020 due to the COVID-19 pandemic, suppliers have a positive outlook and an expectation that the AM market will be about EUR 7 billion in 2025, which means the compound annual growth rate will be 29.2 %.

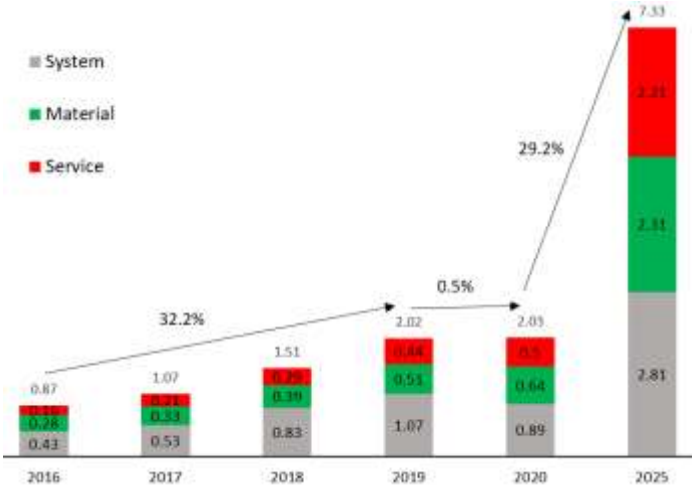

Figure 1.6. Metal additive manufacturing market [31].

The manufacturing industry is responsible for one third of world energy consumption and produces approximately 36 % of global CO_2 emissions [32]. According to a survey of the World Commission on Environment and Development, manufacturing sectors such as aerospace, automotive, and power generation are required to develop sustainable

production and utilization techniques, which requires a shift towards efficient manufacturing to minimize material waste, GHG emissions and disruption to ecosystems [33]. Conventional manufacturing technologies, such as milling, moulding and casting, have some disadvantages, including material waste, low level of complexity, low customization and increased carbon emissions [34, 35]. AM significantly eliminates these problems, enabling rapid prototyping and digital adaptability [36]. AM provides a promising method for preparing complex 9Cr steel components, which are widely used in pressure vessel parts in thermal power plants and nuclear power plants. Compared to conventionally-manufactured 9Cr steel, 9Cr steel produced using AM has a significantly higher maximum tensile strength of 1058 MPa compared to 650 MPa for standard cast 9Cr steel [37]. It is estimated that adoption of AM instead of conventional manufacturing can reduce energy consumption and GHG emissions due to manufacturing industries by 5% by 2025 [38]. Furthermore, during the global COVID-19 pandemic, the supply chain of basic and emergency commodities, including medical care equipment, personal protective equipment (PPE) and raw materials, was disrupted, resulting in insufficient supply of medical and health equipment. Traditional manufacturing industry was affected by lockdowns and transportation restrictions, but AM emerged as an alternative for rapid distribution of PPE and medical devices [39, 40]. For example, AM was recently adopted to develop a lightweight and ergonomic face shield which no accessories needed, as illustrated in Figure 1.8.

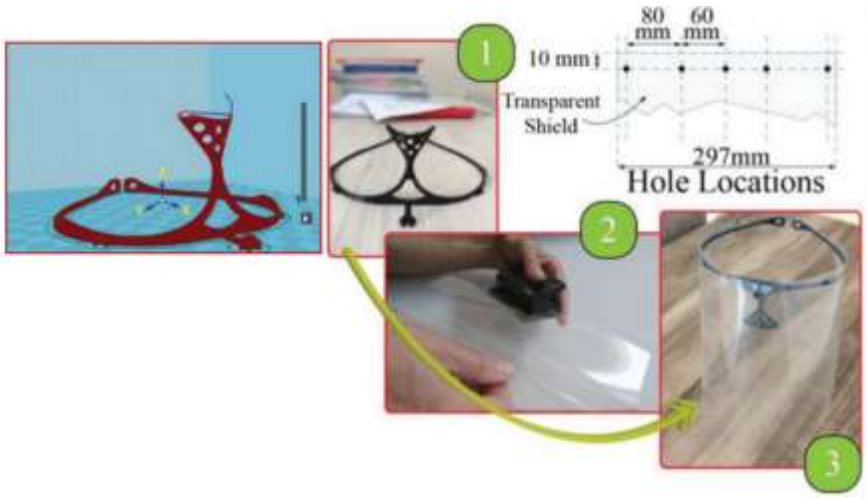

Figure 1.7. 3D printed light weight and single frame designed medical face shield [41].

With the development of technology and raw materials, AM is being adopted in various sectors of manufacturing [42, 43]. In the past, AM was mainly applied to polymer material processing and rapid prototyping [44, 45]. Nowadays, there is significant growth of applications for AM in metal manufacturing and for fabricating critical components in net or near-net shape forms with good tolerance and properties [46, 47]. Since AM allows manufacturing of very complex structures typically not possible or feasible using conventional manufacturing processes in terms of time and money, new areas of AM applications can be found. Two specific examples are as follows:

(i) Medical applications: AM has a wide range of application in the medical field, particularly for those with complex structures or perhaps customised (personalized) geometries [48]. Figure 1.7 shows a Ti-6Al-4V tibial stem containing a solid core and porous structure, with which the weight of the metallic structure can be lower and the stiffness can also be selected to better match the modulus of different bone types [49]. Furthermore, the growing application or need for AM in the medical sector is motivated by the increasing requirement for customized medical parts [50].

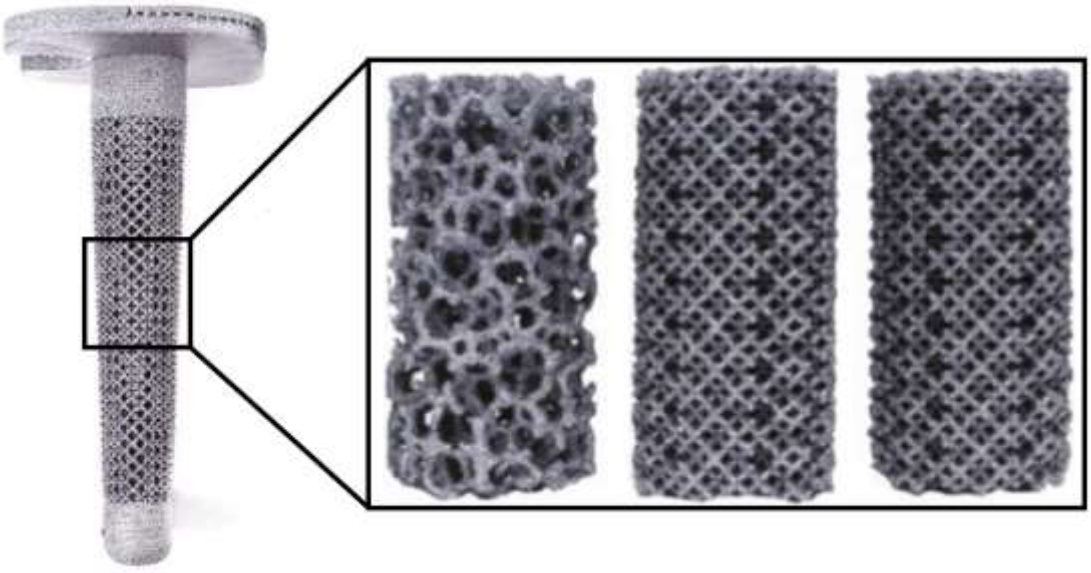

Figure 1.8. Ti-6Al-4V tibial stem with different porous structure [51].

(ii) Aerospace sector: Another prominent application of AM can be seen in the aerospace sector [52]. Significant cost and lead-time reductions, novel complex design solutions and integration of multiple components to improve performance or risk management are the fundamental opportunities in this sector. NASA has demonstrated complex turbomachinery in various applications, as illustrated in Figure 1.9.

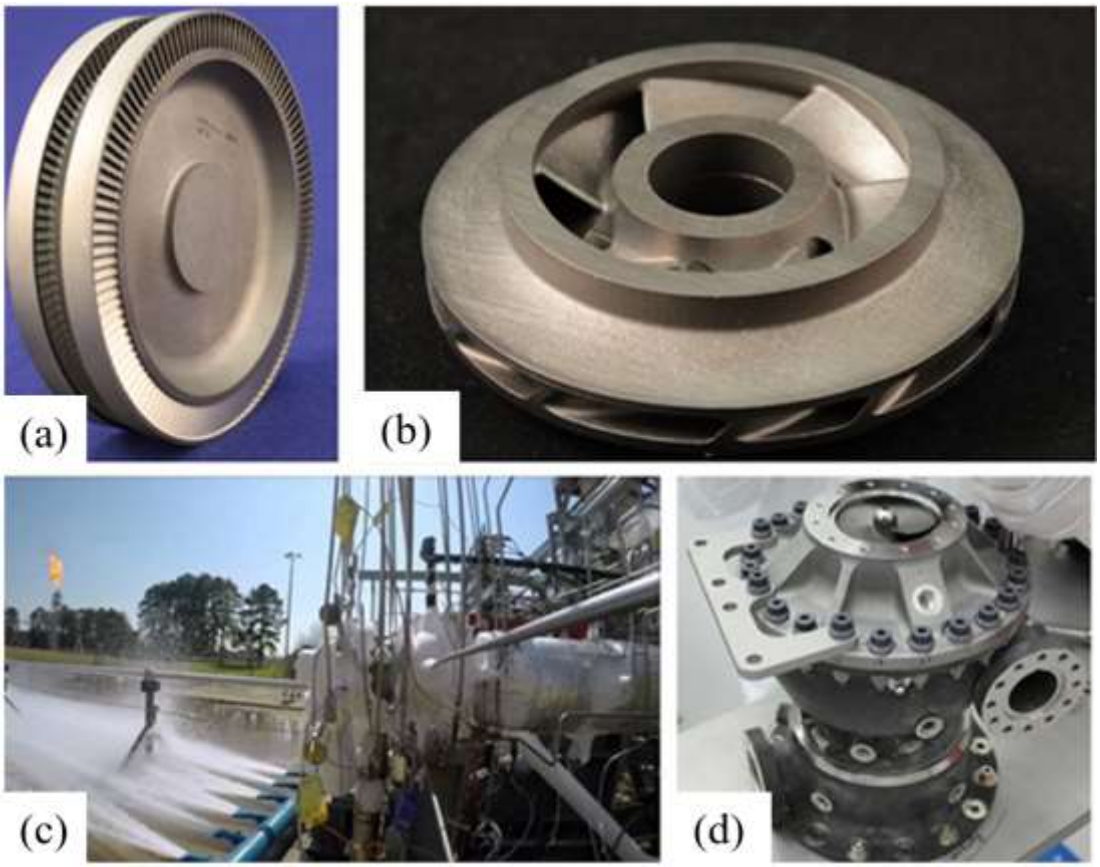

Figure 1.9. Application of AM in liquid hydrogen and liquid oxygen turbopumps at NASA MSFC, (a) turbopump stator, (b) turbopump impeller, (c) turbomachinery, (d) turbopump [53].

With the establishment of new fields of AM and related research, there is a greater emphasis on control of properties and solving underlying problems in the past. Residual stress (RS) is one of the most common causes of build failures in metal AM, which has a detrimental effect on mechanical strength and geometrical accuracy, particularly fatigue resistance [54-56], and the management of RS is one of the important problems. As demonstrated in Figure 1.10, the printed components can partly detach from the substrate,

due to significant RS within the components. Additionally, RS causes failure for in-service components since tensile RS causes increase of mean stress and, hence, reduced fatigue life of components in service [57]. RS is formed during the AM process and cannot be completely removed although it can be potentially managed and controlled through the use of a support structure and appropriate process parameter selection during printing, as investigated in this thesis. Support structures can bear the weight of the part as well as compensate for distortion along the horizontal direction [58]. Various process parameters, such as the laser power, scanning speed and scanning strategy, can affect the final part in terms of RS and residual distortion. Thus, it is important to investigate the effect of process parameters on RS. Coupled with this is the requirement for the mitigation of RS and distortion, particularly for large-scale components.

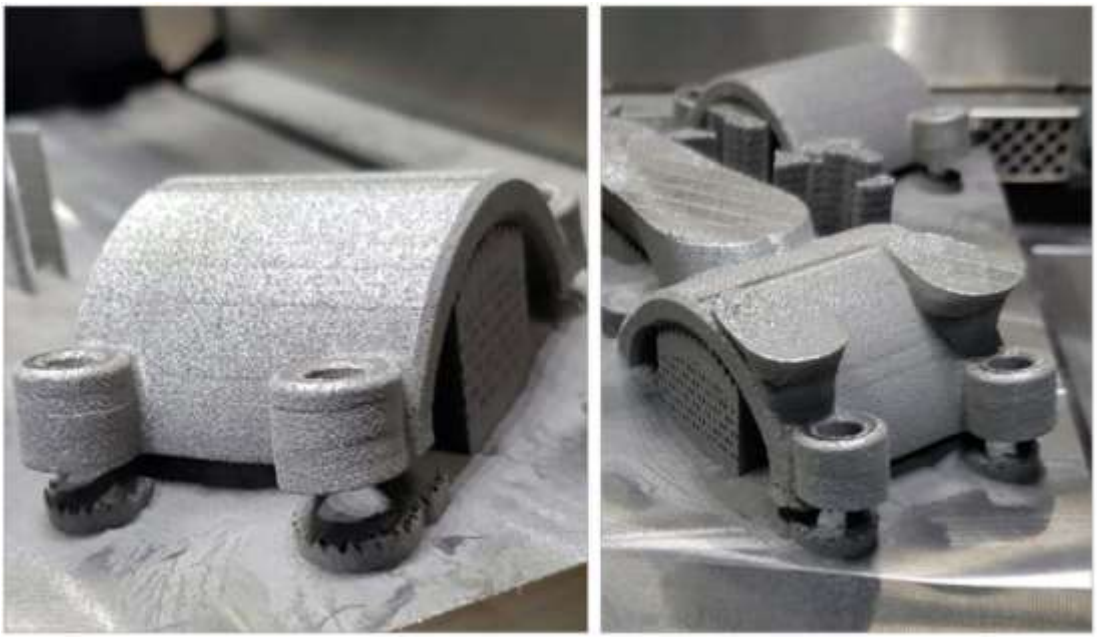

Figure 1.10. Additive manufactured components partly detached from the build due to residual stress (Courtesy of Alexander Liu).

1.2 Aims and Objectives

The overall aim of this thesis is to develop computational methods for addressing two specific challenges in relation to additive manufacturing and welding of metals, to provide pragmatic solutions to significant challenges, with a focus on fatigue of welds and RS in

AM. This work will guide the selection of optimal manufacturing protocols and integration of computational modelling for industrial application of complex geometries. Specifically, the primary objectives of this work are as follows:

1) Develop computationally efficient and accurate thermo-mechanical FE models for prediction of temperature-time histories, residual stress distributions and distortions of realistic (macro-scale) Ti-6Al-4V components manufactured by DED, using the recently-developed built-in AM module in the Abaqus general purpose, nonlinear FE code.
2) Development of optimized scanning strategies for identification of optimal manufacturing protocols and exploring approaches to mitigate the residual stress and optimize distortion of large-scale DED Ti-6Al-4V parts.
3) Application of FE-based AM modelling method to PBF process for Inconel 625 part, including validation against published benchmark experimental measurements by the National Institute of Standards and Technology (NIST) laboratory.
4) Experimental measurement of RS in PBF 316L stainless steel specimens, including investigating effects of build orientation and surface roughness on fatigue behaviour.
5) Develop a physically based FE method for prediction of fatigue crack initiation in P91 welded joints under high temperature low cycle fatigue conditions.

1.3 Overview of thesis

This thesis mainly focuses on the physically based computational modelling of effects of manufacturing. Chapters 1 and 2 are Introduction and Literature Review, respectively. Chapters 3 to 6 are research papers corresponding to the different objectives in this thesis.

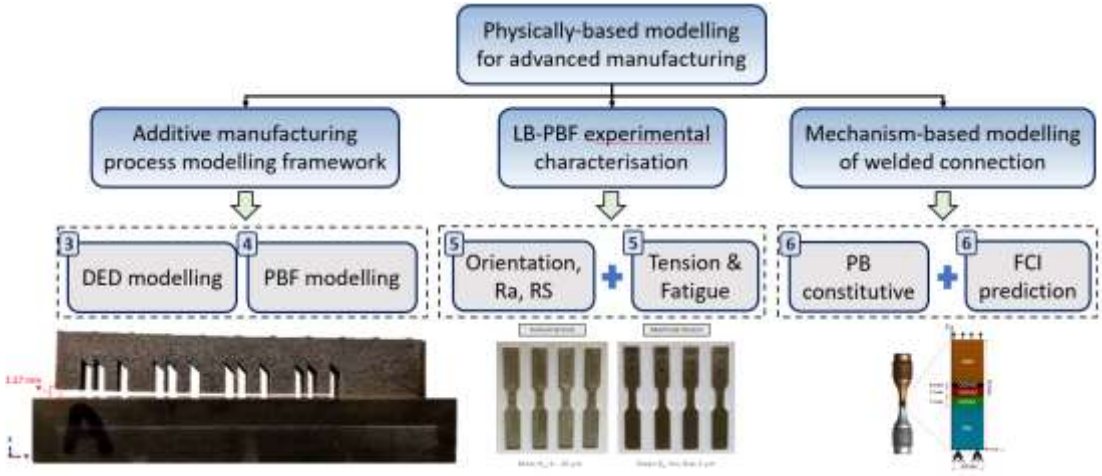

Figure 1.11. Breakdown of chapter content in thesis showing interaction and integration leading to achievement of overall thesis objective.

Chapter 2 presents a review of literature most relevant to this research work, including an overview on the studied materials, welding and additive manufacturing techniques, the numerical modelling of the additive manufacturing and welding process (including RS prediction in metal AM components and FCI prediction in welded connections) and material behavior modelling. Chapter 2 also incorporates the descriptions of fatigue, in terms of fatigue testing, microstructural behavior due to cyclic loading and fatigue life prediction model.

Chapter 3 presents three-dimensional, finite element modelling for simulation of a realistic Ti-6Al-4V component using directed energy deposition. The predicted results are successfully validated against published experimental and numerical data. The effects of different scanning strategies on temperature histories and residual stresses are investigated as a basis for identification of optimal manufacturing protocols. Finally, fatigue life predictions of the Ti-6Al-4V component have been considered based on the Basquin-Goodman equation with the effect of residual stress taken into account. This chapter validates the FE-based AM process modelling method, which is adopted to facilitate modelling of the PBF process with complex engineering parts in Chapter 4.

Chapter 4 presents a finite element simulation method for PBF manufacture of a complex 3D benchmark bridge component made from Inconel 625. The simulation results are successfully validated against the published benchmark experimental measurements from neutron diffraction, X-ray diffraction (XRD), contour method and coordinate measurement machine (CMM) by the National Institute of Standards and Technology (NIST) laboratory. The effects of substrate removal and preheating on mitigation of both residual stresses and distortions are investigated. Ultimately, the results in this chapter will guide the selection of optimal manufacturing protocols and integration of the FE-based AM modelling for industrial application with complex geometries.

Chapter 5 presents the results of a test programme for mechanical and microstructural characterisation of LB-PBF 316L stainless steel, including measurement of density, surface roughness, residual stress, as well as mechanical, i.e. tensile and fatigue testing, at Nanjing Tech University. The LB-PBF 316L stainless steel specimens were manufactured by an industry partner AbbVie in collaboration with Atlantic Technological University (Sligo), as part of the I-Form Centre for Advanced Manufacturing in Ireland collaboration with University of Galway.

Chapter 6 presents a methodology for physically-based prediction of high temperature fatigue crack initiation in 9Cr steels, with a focus on material inhomogeneity due to welding-induced metallurgical transformations. A modified form of the Tanaka-Mura model for slip band formation under cyclically-softening conditions is implemented in conjunction with a physically-based unified cyclic viscoplasticity constitutive model. The physically-based constitutive model accounts for the key strengthening mechanisms, including precipitate hardening and hierarchical grain boundary strengthening, successfully predicting cyclic softening in 9Cr steels. A five-material, finite element model of a P91 cross-weld test specimen, calibrated using the physically-based yield strength and constitutive models, successfully predicts the measured detrimental effect of welding on high temperature low-cycle fatigue crack initiation for P91 cross weld tests, via the modified Tanaka-Mura model. A key finding of this chapter is the requirement to adopt an energy-based Tanaka-Mura method to account for cyclic softening in 9Cr steels,

with packet size as the critical length-scale for slip band formation. This chapter provides fundamental understanding of the significant effect of highly flexible operation on the service life of welded connections and physically-based Tanaka-Mura model for fatigue crack initiation prediction. This is the first time that such an approach has been developed for fatigue of welded connections.

Chapter 7 presents the main conclusions of this thesis and outlines a set of recommendations for future work.

1.4 References

[1] U. Okyay, E. Aricioglu, F. Yucel, Energy consumption and economic growth nexus: Evidence from developed countries in Europe, International Journal of Energy Economics and Policy 4(3) (2014) 411-419.
[2] A. Belke, F. Dobnik, C. Dreger, Energy consumption and economic growth: New insights into the cointegration relationship, Energy Economics 33(5) (2011) 782-789.
[3] A. Komarnicka, A. Murawska, Comparison of Consumption and Renewable Sources of Energy in European Union Countries—Sectoral Indicators, Economic Conditions and Environmental Impacts, Energies 14(12) (2021) 3714.
[4] G.A. Marrero, Greenhouse gases emissions, growth and the energy mix in Europe, Energy Economics 32(6) (2010) 1356-1363.
[5] M. Sterpu, G. Soava, A. Mehedintu, Impact of economic growth and energy consumption on greenhouse gas emissions: Testing environmental curves hypotheses on EU countries, Sustainability 10(9) (2018) 3327.
[6] S. Akdag, H. Yıldırım, Toward a sustainable mitigation approach of energy efficiency to greenhouse gas emissions in the European countries, Heliyon 6(3) (2020) e03396.
[7] K.C. Nadeau, I. Agache, M. Jutel, I. Annesi Maesano, M. Akdis, V. Sampath, G. d'Amato, L. Cecchi, C. Traidl‐Hoffmann, C.A. Akdis, Climate change: A call to action for the united nations, Allergy 77(4) (2022) 1087-1090.
[8] S.C. Neubauer, Comment on “Extreme Level of CO2 Accumulation Into the Atmosphere due to the Unequal Global Carbon Emission and Sequestration” by MF Hossain, Water Air Soil Pollut 233(9) (2022) 1-7.
[9] I. Tsiropoulos, W. Nijs, D. Tarvydas, P. Ruiz, Towards net-zero emissions in the EU energy system by 2050, Publications Office of the European Union (2020) 118592.
[10] B.K. Sovacool, P.L. Ratan, Conceptualizing the acceptance of wind and solar electricity, Renewable and Sustainable Energy Reviews 16(7) (2012) 5268-5279.
[11] A.S. Brouwer, M. Van Den Broek, A. Seebregts, A. Faaij, Impacts of large-scale intermittent renewable energy sources on electricity systems, and how these can be modeled, Renewable and Sustainable Energy Reviews 33 (2014) 443-466.
[12] W. Nwankwo, K.E. Ukhurebor, U.O. Aigbe, Climate change and innovation technology: A review, Renewable Energy 20 (2020) 23.

[13] M.R. Abu-Zahra, L.H. Schneiders, J.P. Niederer, P.H. Feron, G.F. Versteeg, CO2 capture from power plants: Part I. A parametric study of the technical performance based on monoethanolamine, International Journal of Greenhouse Gas Control 1(1) (2007) 37-46.
[14] H. Ritchie, M. Roser, Energy, Our World In Data, 2020.
[15] A. Darmawan, M. Aziz, M.W. Ajiwibowo, M.K. Biddinika, K. Tokimatsu, B. Lokahita, Integrated ammonia production from the empty fruit bunch, Innovative Energy Conversion from Biomass Waste 3 (2021) 149.
[16] A. Baczoni, C. da Silva Santos, G. Peabody, Are the environmental sustainability projects really cutting power station profitability?, Power & Electricity World Africa, 2011.
[17] T.K. Ray, A. Datta, A. Gupta, R. Ganguly, Exergy-based performance analysis for proper O&M decisions in a steam power plant, Energy Conversion Management 51(6) (2010) 1333-1344.
[18] R. Viswanathan, J. Henry, J. Tanzosh, G. Stanko, J. Shingledecker, B. Vitalis, R. Purgert, US program on materials technology for ultra-supercritical coal power plants, Journal of Materials Engineering and Performance 14(3) (2005) 281-292.
[19] S.A. David, J.A. Siefert, Z. Feng, Welding and weldability of candidate ferritic alloys for future advanced ultrasupercritical fossil power plants, Science and Technology of Welding and Joining 18(8) (2013) 631-651.
[20] M. Li, R.A. Barrett, S. Scully, N.M. Harrison, S.B. Leen, P.E. O'Donoghue, Cyclic plasticity of welded P91 material for simple and complex power plant connections, International Journal of Fatigue 87 (2016) 391-404.
[21] T.P. Farragher, S. Scully, N. O'Dowd, C.J. Hyde, S. Leen, High temperature, low cycle fatigue characterization of P91 weld and heat affected zone material, Journal of Pressure Vessel Technology 136(2) (2014) 021403.
[22] F. Abe, M. Tabuchi, M. Kondo, S. Tsukamoto, Suppression of Type IV fracture and improvement of creep strength of 9Cr steel welded joints by boron addition, International Journal of Pressure Vessels and Piping 84(1-2) (2007) 44-52.
[23] V. Shankar, K. Mariappan, R. Sandhya, M. Mathew, Evaluation of low cycle fatigue damage in grade 91 steel weld joints for high temperature applications, Procedia Engineering 55 (2013) 128-135.
[24] C. Pandey, M.M. Mahapatra, P. Kumar, N. Saini, Effect of weld consumable conditioning on the diffusible hydrogen and subsequent residual stress and flexural strength of multipass welded P91 steels, Metallurgical and Materials Transactions B 49(5) (2018) 2881-2895.
[25] C. Pandey, M.M. Mahapatra, P. Kumar, Effect of post weld heat treatments on fracture frontier and type IV cracking nature of the crept P91 welded sample, Materials Science and Engineering: A 731 (2018) 249-265.
[26] M. Li, F.W. Sun, R.A. Barrett, E. Meade, D.F. Li, P.E. O'Donoghue, S.B. Leen, N. O'Dowd, Influence of material inhomogeneity on the mechanical response of a tempered martensite steel, Proceedings of the Institution of Mechanical Engineers, Part L: Journal of Materials: Design and Applications 231(1-2) (2017) 14-22.
[27] S. Scully, Personal Communication to Sean Leen, ESB Energy International (2014).
[28] R.A. Barrett, Experimental characterisation and computational constitutive modelling of high temperature degradation in 9Cr steels including microstructural effects,

National University of Ireland, Galway, 2016.
[29] C. Salkin, M. Oner, A. Ustundag, E. Cevikcan, A conceptual framework for Industry 4.0, Industry 4.0: Managing the Digital Transformation, Springer, Cham 2018.
[30] S.M. Sepasgozar, A. Shi, L. Yang, S. Shirowzhan, D.J. Edwards, Additive manufacturing applications for industry 4.0: A systematic critical review, Buildings 10(12) (2020) 231.
[31] AMPOWER, Metal additive manufacturing market 2021, 2021.
[32] IEA, Tracking industrial energy efficiency and CO2 emissions, International Energy Agency 34(2) (2007) 1-12.
[33] WCED, World commission on environment and development, Our Common Future 17(1) (1987) 1-91.
[34] M. Merklein, D. Junker, A. Schaub, F. Neubauer, Hybrid additive manufacturing technologies–an analysis regarding potentials and applications, Physics Procedia 83 (2016) 549-559.
[35] T. Pereira, J.V. Kennedy, J. Potgieter, A comparison of traditional manufacturing vs additive manufacturing, the best method for the job, Procedia Manufacturing 30 (2019) 11-18.
[36] C. Van Sice, J. Faludi, Comparing environmental impacts of metal additive manufacturing to conventional manufacturing, Proceedings of the Design Society 1 (2021) 671-680.
[37] J. Feng, P. Zhang, Z. Jia, Z. Yu, C. Fang, H. Yan, H. Shi, Y. Tian, F. Xie, Laser additive manufacturing and post-heat treatment on microstructure and mechanical properties of 9Cr steel, International Journal of Pressure Vessels and Piping 198 (2022) 104681.
[38] M. Gebler, A.J.S. Uiterkamp, C. Visser, A global sustainability perspective on 3D printing technologies, Energy Policy 74 (2014) 158-167.
[39] R.C. Advincula, J.R.C. Dizon, Q. Chen, I. Niu, J. Chung, L. Kilpatrick, R. Newman, Additive manufacturing for COVID-19: devices, materials, prospects, and challenges, Mrs Communications 10(3) (2020) 413-427.
[40] P.K. Arora, R. Arora, A. Haleem, H. Kumar, Application of additive manufacturing in challenges posed by COVID-19, Materials Today: Proceedings 38 (2021) 466-468.
[41] Y. Wang, A. Ahmed, A. Azam, D. Bing, Z. Shan, Z. Zhang, M.K. Tariq, J. Sultana, R.T. Mushtaq, A. Mehboob, Applications of additive manufacturing (AM) in sustainable energy generation and battle against COVID-19 pandemic: The knowledge evolution of 3D printing, Journal of Manufacturing Systems 60 (2021) 709-733.
[42] S.H. Huang, P. Liu, A. Mokasdar, L. Hou, Additive manufacturing and its societal impact: a literature review, The International Journal of Advanced Manufacturing Technology 67(5) (2013) 1191-1203.
[43] S.A. Tofail, E.P. Koumoulos, A. Bandyopadhyay, S. Bose, L. O'Donoghue, C. Charitidis, Additive manufacturing: Scientific and Technological Challenges, Market Uptake and Opportunities, Materials Today 21(1) (2018) 22-37.
[44] L.J. Love, C.E. Duty, B.K. Post, R.F. Lind, P.D. Lloyd, V. Kunc, W.H. Peter, C.A. Blue, Breaking barriers in polymer additive manufacturing, Oak Ridge National Lab.(ORNL), Oak Ridge, TN (United States). Manufacturing Demonstration Facility (MDF), United States, 2015.
[45] L.J. Tan, W. Zhu, K. Zhou, Recent progress on polymer materials for additive manufacturing, Advanced Functional Materials 30(43) (2020) 2003062.

[46] W.E. Frazier, Metal additive manufacturing: a review, Journal of Materials Engineering and Performance 23(6) (2014) 1917-1928.
[47] A. Gisario, M. Kazarian, F. Martina, M. Mehrpouya, Metal additive manufacturing in the commercial aviation industry: A review, Journal of Manufacturing Systems 53 (2019) 124-149.
[48] C. Li, D. Pisignano, Y. Zhao, J. Xue, Advances in medical applications of additive manufacturing, Engineering 6(11) (2020) 1222-1231.
[49] A. Du Plessis, I. Yadroitsava, I. Yadroitsev, S. Le Roux, D. Blaine, Numerical comparison of lattice unit cell designs for medical implants by additive manufacturing, Virtual and Physical Prototyping 13(4) (2018) 266-281.
[50] R. Kumar, M. Kumar, J.S. Chohan, The role of additive manufacturing for biomedical applications: A critical review, Journal of Manufacturing Processes 64 (2021) 828-850.
[51] L.E. Murr, S.M. Gaytan, E. Martinez, F. Medina, R.B. Wicker, Next generation orthopaedic implants by additive manufacturing using electron beam melting, International Journal of Biomaterials 2012 (2012) 245727.
[52] S.C. Altıparmak, B. Xiao, A market assessment of additive manufacturing potential for the aerospace industry, Journal of Manufacturing Processes 68 (2021) 728-738.
[53] B. Blakey-Milner, P. Gradl, G. Snedden, M. Brooks, J. Pitot, E. Lopez, M. Leary, F. Berto, A. du Plessis, Metal additive manufacturing in aerospace: A review, Materials & Design 209 (2021) 110008.
[54] P.J. Withers, H. Bhadeshia, Residual stress. Part 1–measurement techniques, Materials science and Technology 17(4) (2001) 355-365.
[55] P. Edwards, M. Ramulu, Fatigue performance evaluation of selective laser melted Ti–6Al–4V, Materials Science and Engineering: A 598 (2014) 327-337.
[56] P. Edwards, A. O'conner, M. Ramulu, Electron beam additive manufacturing of titanium components: properties and performance, Journal of Manufacturing Science and Engineering 135(6) (2013) 061016.
[57] W. Jiang, X. Xie, T. Wang, X. Zhang, S.-T. Tu, J. Wang, X. Zhao, Fatigue life prediction of 316L stainless steel weld joint including the role of residual stress and its evolution: Experimental and modelling, International Journal of Fatigue 143 (2021) 105997.
[58] T. Mishurova, S. Cabeza, T. Thiede, N. Nadammal, A. Kromm, M. Klaus, C. Genzel, C. Haberland, G. Bruno, The influence of the support structure on residual stress and distortion in SLM Inconel 718 parts, Metallurgical and materials transactions A 49 (2018) 3038-3046.

2 Literature review

2.1 Introduction

As addressed in Chapter 1, this thesis aims to develop computational methods for predicting the development and effects of manufacturing for additive manufacturing technologies, which includes: (i) welding and (ii) 3D printing (i.e. directed energy deposition and powder bed fusion). In order to develop an efficient and accurate computational model, it is necessary to understand the additive manufacturing process, corresponding process modelling and material behavior modelling methods. The main sections of this literature review chapter are broken down into five key considerations:

a) Section 2.2 provides a review of welding and additive manufacturing processes, including process description, failure in welded connections and residual stress in additive manufacturing processes.
b) Section 2.3 presents a review of the state-of-the-art of numerical modelling methods for metal additive manufacturing, including governing equations, process-level modelling and component-level modelling techniques.
c) Section 2.4 presents a review of the state-of-the-art of numerical modelling of welding, including the welding process modelling approach and representative welded specimen modelling approach.
d) Section 2.5 provides a review of material behavior modeling, including phenomenological modelling, crystal plasticity finite element modelling and physically-based modelling.
e) Section 2.6 presents a review of relevant failure phenomena aspects, including fatigue testing, microstructural behavior due to cyclic loading and life prediction model.
f) Section 2.7 details the studied materials for high temperature applications and for additive manufacturing applications, such as P91 steel, Ti-6Al-4V, Inconel 625.

2.2 Welding and Additive Manufacturing

2.2.1 Manufacturing process description

The American Welding Society (AWS) defines the welding process as "a materials joining process which produces coalescence of materials by heating them to suitable temperatures with or without the application of pressure or by the application of pressure alone and with or without the use of filler material" [1]. The welding technique has been widely used for various industrial applications (e.g. building, aerospace application and automobile manufacturing), without which many commonly used items cannot be produced, such as bridges, pipelines, offshore sustainable energy platforms and electronic devices [2].

Figure 2.1 shows the list of welding processes according to the AWS. Welding of 9Cr-1Mo steel is typically performed using the arc welding process such as gas tungsten arc welding (GTAW), submerged arc welding (SAW) or shielded metal arc welding (SMAW) [3, 4]. A power source is used to create an electrical arc between the electrode and the workpiece during the arc welding processes, in order to connect two metal pieces by fusion.

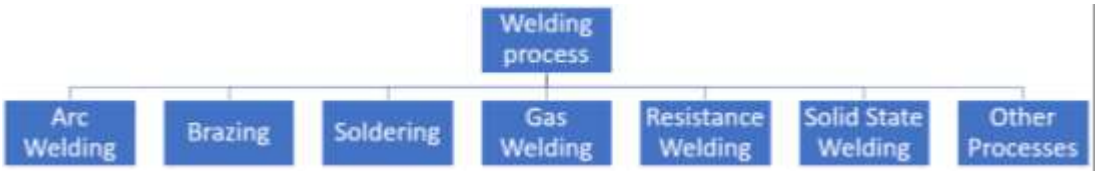

Figure 2.1. AWS categorization of Welding processes.

Directed Energy Deposition (DED) is a 3D printing method in which the metal powder is fed coaxially into the focused energy source (laser or electron beam) and fuses with a previously deposited layer, as illustrated in Figure 2.2. Either powder or wire can be utilized as the feedstock material in the DED process. An enclosed chamber is not necessarily required in the DED system. Similar to the conventional welding process, the feedstock material is fed onto the molten pool by means of a shielded gas flow during the DED process.

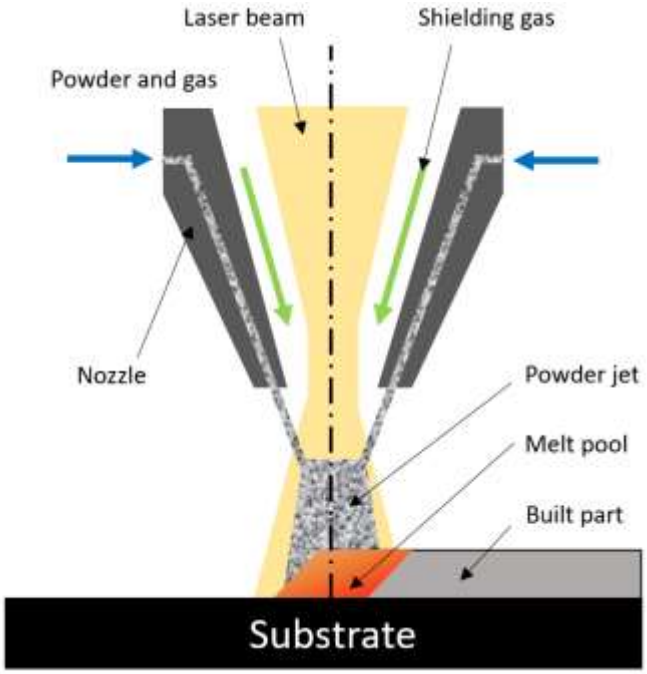

Figure 2.2. Schematic illustration of directed energy deposition process.

The DED process can be divided into categories based on the feedstock material. The powder-based DED technique includes the laser engineered net shaping (LENS) [5, 6], direct metal deposition (DMD) [7], and 3D laser cladding (LC) [8]. Wire and arc additive manufacturing (WAAM) is an example of wire-based DED technique, which is very similar to the welding process [9]. DED techniques are commonly used to repair and maintain the functional or structural parts, especially in heavy industry, which are very expensive to replace. Table 2.1 provides a brief summary of the advantages and disadvantages of DED technology.

Table 2.1. Advantages and disadvantages of DED technology [10].

Advantages	**Disadvantages**
High build rates	Inconsistent finish
Large build area	Low process resolution
Multiple materials	Difficult achieving high dimensional and geometrical accuracy

In powder bed fusion (PBF) based AM process, a thin layer of metal powder is laid first and then the metal powder is melted by a laser beam or electron beam according to a controlled trajectory, as shown in Figure 2.3. The PBF process is typically performed in an enclosed chamber with a protective gas environment (such as argon or nitrogen) or under vacuum conditions, to slow down or preclude the oxidation process [11].

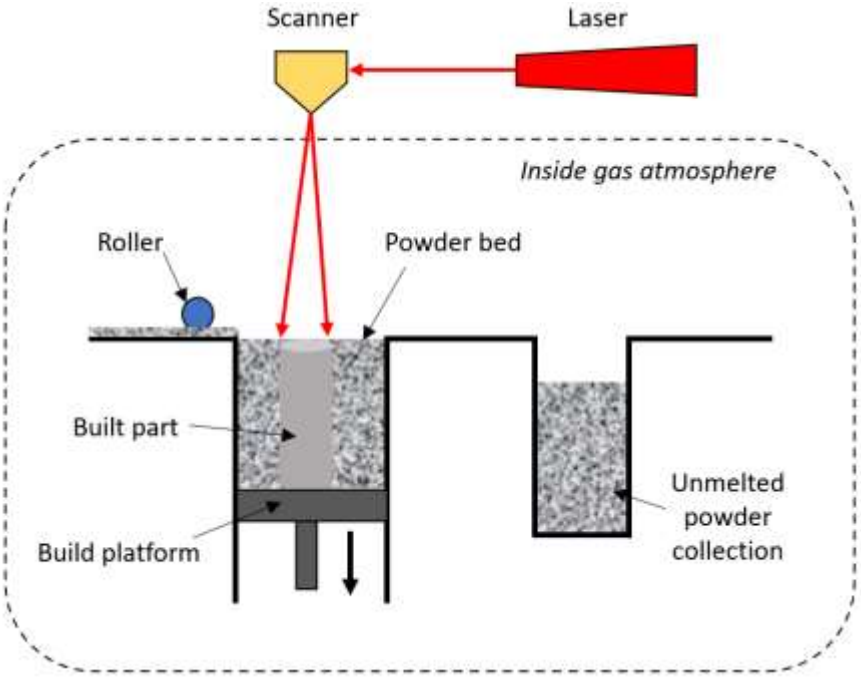

Figure 2.3. Schematic illustration of powder bed fusion process.

The PBF process can be classified into two dominant groups based on the heat source: laser beam or electron beam. Examples are as follows: selective laser sintering (SLS) [12], selective laser melting (SLM) [13], direct metal laser sintering (DMLS) [14], and electron beam melting (EBM) [15]. The PBF process has been widely used in various industrial applications, such as the medical sector for manufacturing custom implants. The advantages and disadvantages of PBF technology are briefly summarized in Table 2.2. Table 2.3 compares the main features of DED and PBF process, showing that both methods have their own advantages, and the appropriate method should be selected according to manufacturing requirements.

Table 2.2. Advantages and disadvantages of PBF technology [16].

Advantages	Disadvantages
High geometric fidelity	Relatively slow speed
Wide material choice	Size limitations
Powder recycling	Restrictions on material compatibility

Table 2.3. General comparison between DED and PBF processes [16, 17].

Feature	DED	PBF
Part complexity	Relatively simple geometry with less resolution	Complex geometry with high resolution
Part size	Unlimited	Limited
Repair or add features	Able to add material onto 3D surfaces	Limited, horizontal build plane required
Multi-material	Programmatically grade	Limited

2.2.2 Failure in welded connections

Unexpected failures commonly occur within welded joints in power plant. The welded joints can be divided into different regions including parent material (PM), heat affected zone (HAZ) and weld material (WM), as shown in Figure 1.1. Moreover, the HAZ can be divided into three distinct sub-regions: intercritical heat affected zone (ICHAZ) at the interface with the PM, fine grain heat affected zone (FGHAZ), coarse grain heat affected zone (CGHAZ) at the interface with the WM. Figure 1.1 shows the typical locations of four types of cracking [18], as follows:

- Type I cracking: usually in the WM region.
- Type II cracking: usually in the WM and HAZ region, crossing the fusion line.
- Type III cracking: usually occurs in the CGHAZ region.
- Type IV cracking: usually originates and propagates from FGHAZ or ICHAZ regions.

Type IV cracking is the most common failure mode for P91 welded joints. Figure 2.4 presents a detailed image of type IV cracking in the ICHAZ of a P91 welded joint. The

location of type IV cracking in ICHAZ region is mainly related to the accumulation of creep deformation coupled with extensive creep cavitation in the ICHAZ [19].

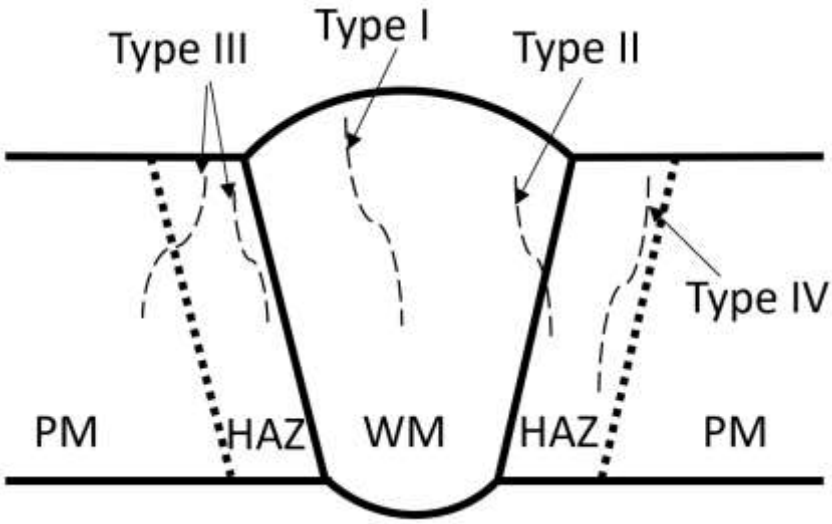

Figure 2.4. Schematic diagram of the welded joint, showing different types of cracking.

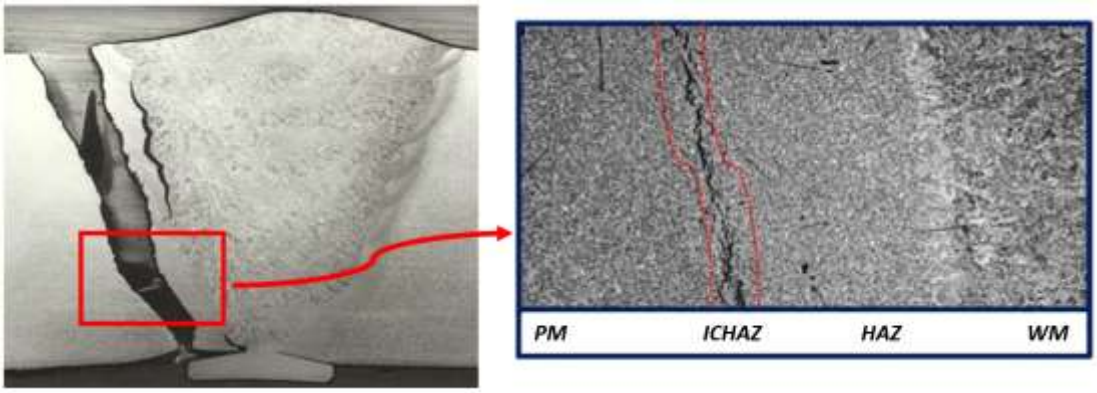

Figure 2.5. Type IV cracking in the ICHAZ region of P91 welded joint (R Barrett [20]).

2.2.3 Residual stress in welded and AM components

2.2.3.1 Overview of residual stress

Residual stress (RS) is the stress that remains in a solid material after the original cause of the stresses has been removed [21]. Mechanisms for generating residual stresses include (i) non-uniform plastic deformation (e.g. bending, forging, rolling manufacturing processes), (ii) surface modification (e.g. grinding and peening machining processes) and

(iii) presence of large thermal gradients (e.g. welding and additive manufacturing process) [22].

Residual stresses are classified into three types according to the length scale over which they exists, i.e. Type I, Type II and Type III [23]. Type I RS is a macroscopic stress across the part, which can result in large deformation to the part. Type II RS is a microscale stress within a small domain such as grains or phases. Type III RS is at the atomic scale (e.g. around dislocations). Both Type II and III RS are commonly called micro-stresses, which are not considered in the present work. The main focus of this study is on Type I macroscopic RS in AM parts.

AM processes are extremely susceptible to generation of RS due to large temperature gradients, rapid cooling rates and repeated heating- melting-solidification-remelting-solidification steps [24]. The temperature gradient mechanism (TGM) inducing residual stresses for a single laser track is shown in Figure 2.6(a) and the cool-down mechanism inducing residual stresses of an entire layer is shown in Figure 2.6(b) indicating the mechanisms of RS and deformation formation in AM parts, which are based on the material expansion or contraction behaviour during heating or cooling processes. The material expands when the laser beam starts melting the metal powder, which will be limited as the surrounding material is colder. Compressive RS will be developed in the heat affected zone while tensile RS will be developed in the solidified material during the heating process of a single laser track (see Figure 2.6 (a)), which will result in plastic deformation if the stress exceeds the yield strength. The thermally expanded area starts cooling down and contracts during the cooling process, similarly, and contraction will be constrained by the surrounding material. Tensile and compressive RS will be developed in the heat affected zone and the solidified material, respectively, leading to bending in the opposite direction (see Figure 2.6(b)). The temperature of the new melted top layer is always higher than the underlying layer during the heating process (see Figure 2.7(a)). During the cooling process, the contraction in the warmer upper layer is greater than the colder underlying layer. However, the contraction is inhibited due to the connection of both layers, causing tensile and compressive RS in the upper and underlying layer,

respectively (see Figure 2.7(b)). The final AM part will be in a complex non-uniform stress state due to the iterative heating and cooling processes.

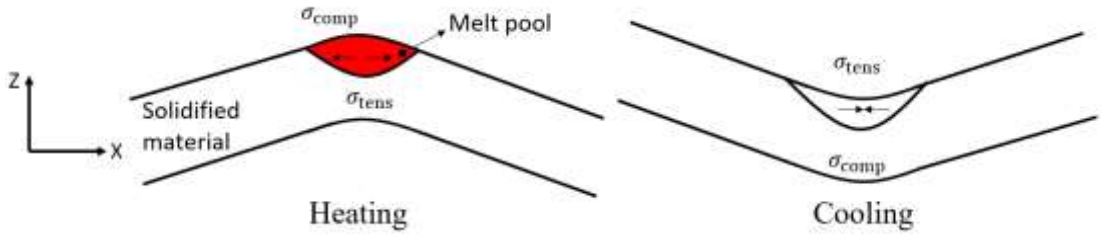

(a) (b)

Figure 2.6. TGM inducing residual stresses of a single laser track: (a) Heating, (b) Cooling (σ_{tens}: tensile residual stress, σ_{comp}: compressive residual stress), adapted from [25].

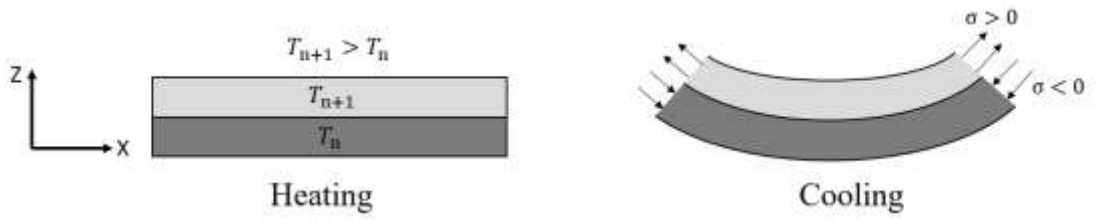

(a) (b)

Figure 2.7. Cool-down inducing residual stresses of an entire layer: (a) Heating, (b) Cooling, adapted from [26].

2.2.3.2 Residual stress and cracking problems

The non-uniform residual stresses in additively manufactured components have detrimental consequences for causing failure (e.g. cracking and rupture) during and after manufacturing [27]. Figure 2.8(a) illustrates high residual stresses causing failure during manufacturing, as the deformed component hinders the movement of the powder re-coating system, causing the printing process to stop. This not only causes waste of powder and energy, but also increases the entire production time. Figure 2.8(b) shows another challenge after the AM process, in which large deformation caused by the high inherent RS is found in the AM part after separation from the substrate. The distortion would decrease the dimensional accuracy, which may result in the built part being rejected for critical applications, such as aerospace and biomedical [28, 29].

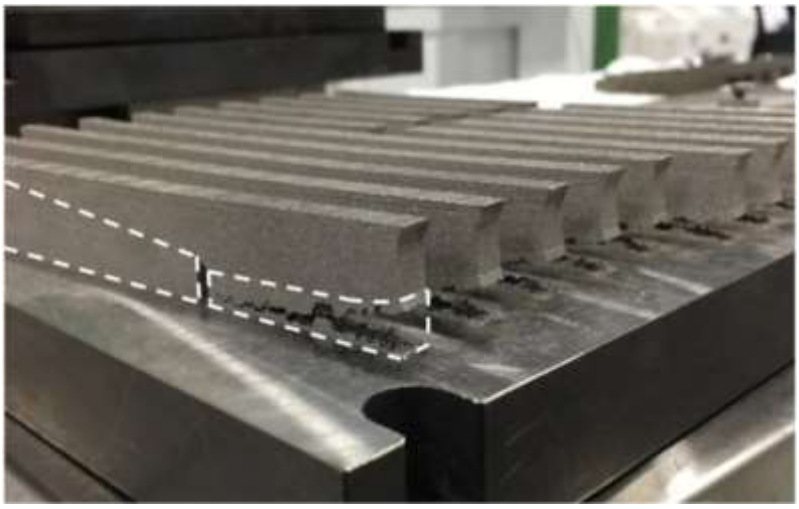

(a)

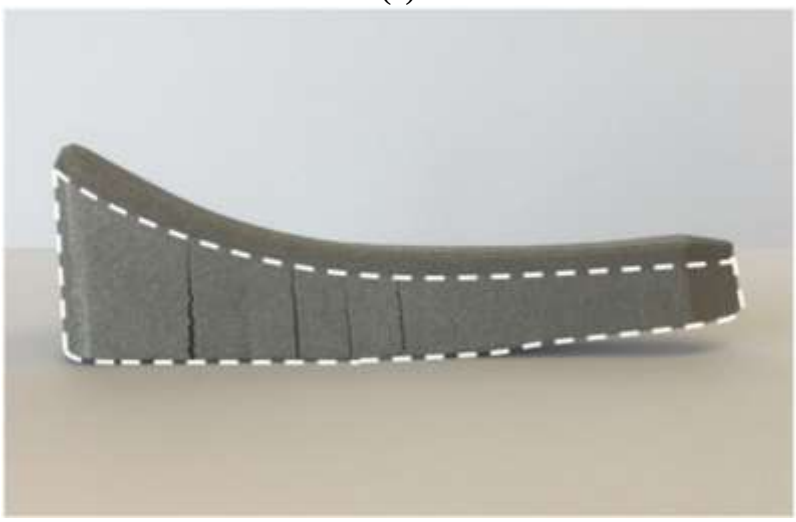

(b)

Figure 2.8. Large deformation due to residual stress in the AM component: (a) failure during manufacturing, (b) failure after manufacturing [27].

The residual stress in the welded connections are caused by thermal expansion and contraction of the weld material and parent material [30]. Generally, in order to improve the toughness and eliminate the welding residual stress, the welded connections should be subjected to post-weld heat treatment (PWHT) [31]. It should be noted that a PWHT process has been carried out in the welded P91 joints investigated here [32], in which the residual stress are negligible.

2.3 Numerical modelling of additive manufacturing

2.3.1 Governing equations

2.3.1.1 Thermal analysis

The governing equation of the thermal analysis is the heat conduction equation [33]:

$$\rho C_{\mathrm{p}} \frac{dT}{dt} + \boldsymbol{\nabla} \cdot \mathbf{q} = Q + \dot{D}_{\mathrm{mech}} \tag{2.1}$$

where ρ is density ($\mathrm{kg/m^3}$), C_{p} is the temperature dependent specific heat ($\mathrm{J/(kgK)}$), T denotes temperature (K), t is time (s), $\mathbf{q}$ is heat flux vector, and Q is heat source (e.g. laser beam, electron beam, welding torch, etc.), $\dot{D}_{\mathrm{mech}}$ is thermo-mechanical dissipation. The heat flux vector $\mathbf{q}$ due to conduction is given as follows:

$$\mathbf{q} = -k\boldsymbol{\nabla}T \tag{2.2}$$

where k is the temperature dependent thermal conductivity ($\mathrm{W/(mK)}$), $\boldsymbol{\nabla} = \frac{\boldsymbol{\partial}}{\boldsymbol{\partial x}}\vec{\boldsymbol{\imath}} + \frac{\boldsymbol{\partial}}{\boldsymbol{\partial y}}\vec{\boldsymbol{\jmath}} + \frac{\boldsymbol{\partial}}{\boldsymbol{\partial z}}\vec{\boldsymbol{k}}$. The heat loss due to heat convection can be formulated as:

$$q_{\mathrm{conv}} = h_{\mathrm{conv}}(T_{\mathrm{sur}} - T_{\mathrm{a}}) \tag{2.3}$$

where h_{conv} is heat transfer convection coefficient ($\mathrm{W/(m^2K)}$), T_{sur} is surface temperature of the specimen (K), T_{a} is ambient temperature (K). The heat loss due to radiation can be formulated as:

$$q_{\mathrm{rad}} = \varepsilon_{\mathrm{rad}}\sigma_{\mathrm{rad}}(T_{\mathrm{sur}}^4 - T_{\mathrm{a}}^4) \tag{2.4}$$

where $\varepsilon_{\mathrm{rad}}$ is the emissivity coefficient, and σ_{rad} is the Stefan–Boltzmann constant.

2.3.1.2 Heat source equations

The Goldak double ellipsoidal model, which has been widely adopted to describe the laser heat source Q during DED process modelling [6, 34-37], is defined by:

$$\begin{aligned} Q &= q_f \quad when\ x_{\mathrm{l}} \geq 0 \\ Q &= q_r \quad when\ x_{\mathrm{l}} < 0 \end{aligned} \tag{2.5}$$

$$q_{f/r} = \frac{6\sqrt{3} f_{f/r} AP}{abc\pi\sqrt{\pi}} e^{\left(-\frac{3x_l^2}{c_{f/r}^2} - \frac{3y_l^2}{a^2} - \frac{3z_l^2}{b^2}\right)}$$

where f_f and f_r are 'box size' factors, A is the heat source absorption coefficient, P is laser power (W) and x_l, y_l, z_l are local coordinates with origin centered on the moving heat source when the scanning speed v reaches the maximum value, a, b are the dimensions along the y_l and z_l axis of the ellipsoid and c_f and c_r are the front length and rear length along the x_l axis of the ellipsoid, as shown in Figure 2.9**.** Generally, a, c_f and c_r are taken as the laser spot radius and b is taken as the melt pool depth [5, 36]**.**

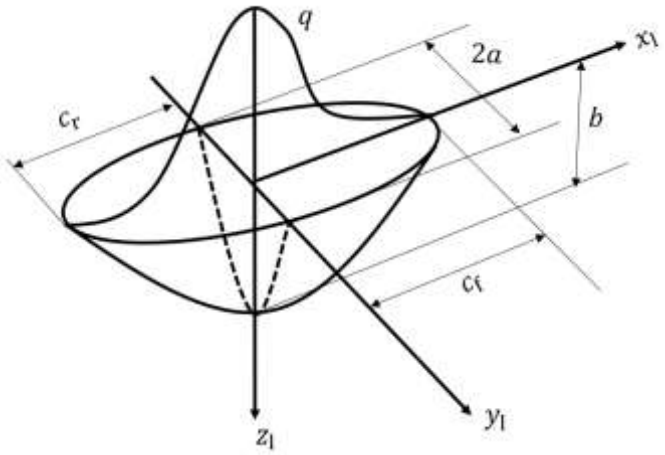

Figure 2.9. The Goldak double ellipsoid heat source model for DED process.

A concentrated point heat source is widely used to model the laser heat source Q during the PBF process modelling [36, 38], expressed as:

$$Q = \frac{2AP}{abc\pi\sqrt{\pi}} \exp\left(-\frac{(x_l + vt)^2}{a} + \frac{y_l^2}{b} + \frac{z_l^2}{c}\right) \quad (2.6)$$

where v is the velocity of moving laser heat source, and a, b and c are in Figure 2.9.

An important and widely-used parameter for process design in AM is the volumetric energy density, E_v, defined for comparing processing conditions [39, 40], as:

$$E_v = \frac{P}{vHL} \quad (2.7)$$

where H is hatch spacing and L is layer thickness. Low volumetric energy density values lead to a lack of fusion (LOF) porosity, indicating that the energy is not sufficient to completely melt the powder [41]. Conversely, high volumetric energy density values result in over-melting, commonly known as keyhole porosity [42].

According to the basic Okerblom's formulae [43], the thermal impulse due to welding can be calculated as:

$$Q = \eta_0 \frac{UI_w}{v_w} \tag{2.8}$$

where η_0 is the thermal efficiency, U is voltage, I_w is current and v_w is speed of welding.

2.3.1.3 Mechanical analysis

The governing equation of the mechanical analysis is the stress equilibrium equation [44], given as:

$$\boldsymbol{\nabla \cdot \sigma} = 0 \tag{2.9}$$

where $\boldsymbol{\sigma}$ is the stress tensor. The mechanical constitutive law for elastic problem is defined as:

$$\boldsymbol{\sigma = C : \varepsilon_e = C : (\varepsilon_{Total} - \varepsilon_p - \varepsilon_T)} \tag{2.10}$$

where $\boldsymbol{C}$ is the stiffness tensor, $\boldsymbol{\varepsilon_{Total}}$, $\boldsymbol{\varepsilon_e}$, $\boldsymbol{\varepsilon_p}$, $\boldsymbol{\varepsilon_T}$ are total, elastic, plastic and thermal strain tensors, respectively. The thermal strain tensor driving the residual stress is calculated according to:

$$\boldsymbol{\varepsilon_T} = \alpha \Delta T \boldsymbol{I} \tag{2.11}$$

where α is temperature dependent thermal expansion coefficient (1/K), ΔT is change in temperature (K) and $\boldsymbol{I}$ is identity tensor.

2.3.2 Process-level modelling

Finite element (FE) modelling of the AM process is a potentially powerful technique for full-field quantification of temporal-spatial distributions of key thermo-mechanical

variables (e.g. temperature, deformation, strain, stress) directly or indirectly controlling the mechanical behaviour of fabricated components. In general, existing AM process modelling methods can be categorized into process-level (high fidelity) and component-level (low fidelity) models [45]. Detailed process-level modelling has been performed using a small step increment and a fine mesh with at least one element per layer. The number of elements in each layer should be selected to achieve a balance between accuracy and computational efficiency. A common approach for simulating AM processes, including welding and 3D printing, is the computationally-intensive 'element birth and death' method, also commonly referred to as the 'Model Change' method [46]. Hussein et al. [47] proposed a three-dimensional (3D) transient finite element (FE) model to predict the temperature and stress fields within a single 316L stainless steel layer built on the powder bed using the PBF process, revealing difference in the temperature and stress in different locations of the layer (see Figure 2.10), but without explicit comparisons against experimental measurements. Hodge et al. [48] presented a continuum thermo-mechanical modelling method for calculation of the thermal and mechanical history of a PBF manufactured 316L stainless steel cube (12 layers in total) and highlighted the limitations of the Bathe algorithm [49] for phase change modelling due to the significant computational resources required. Yang et al. [5] recently presented a 3D thermo-elastic-plastic model using this approach to follow precisely the physical deposition path for a 5-layer DED of Ti-6Al-4V. However, the high computational cost of these methods makes AM modelling of full scale and complex 3D components almost impossible. Hence, this method is typically limited to small-scale geometries, e.g. small numbers of layers or tracks. Yang et al. [50] developed a FE model with a moving heat flux implemented via a user subroutine to predict the thermal history and spatial distributions of temperature for the PBF process using the 'Model Change' technique in Abaqus [51] and a process-structure model which can be used as a process design tool. In this case, the focus was on validation of temperature history against experimental measurement from the single-track PBF of Ti-6Al-4V, for prediction of phase transformations using a Kolmogorov-Johnson-Mehl-Avrami (KJMA) model. The process-structure method successfully predicted alpha and beta phase fractions. However, the conventional 'Model Change' technique (e.g. in Abaqus) is too computationally-expensive for larger scale engineering components.

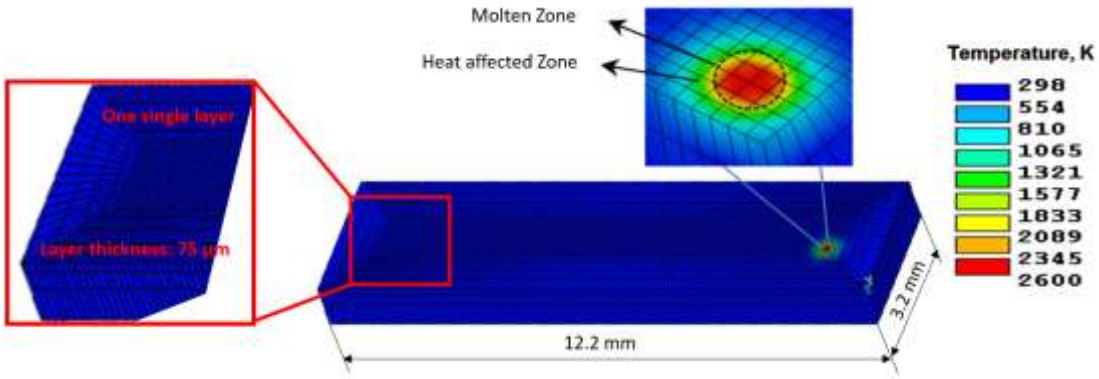

Figure 2.10. FE model representing the single layers built on the powder bed, adapted from [47].

2.3.3 Component-level modelling

Although modelling in the process-level can capture the rapidly evolving temperature and details of melt pool process physics, the computational domain is prohibitively small (typically only a few layers thick) due to the high computational cost [52, 53]. Hence, component-level modelling methods are required for investigating residual stress or the macro-scale, e.g. for real components. Zaeh et al. [54] presented a layer-by-layer modelling method (see Figure 2.11) to evaluate and quantify residual stress and deformation in relatively simple macro-scale components manufactured using the PBF process and highlighted the limitations of the layer-by-layer approach for predicting residual deformations. Barrett et al. [55] proposed a 2D layer-by-layer FE model to predict residual stress in a PBF manufactured Ti-6Al-4V hip stem component (using a simplified 2D geometrical representation), highlighting the importance of post-build heat treatment, but without explicit comparisons against experimental test data. Recently, an automated Python-based method for sectioning of 2D FE models of macro-scale components for efficient model generation in the layer-by-layer method was developed [56], providing a framework for layer scaling in FE modelling of PBF. However, this method was not compared with test data for temperature histories or residual stresses. The layer-by-layer FE-based method was investigated for residual stress prediction of 3D PBF parts by Chen et al. [57], with a particular focus on geometrical shape (e.g. tri-prism, cylinder, block),

solid and hollow. A key limitation of the layer-by-layer method is the inability to represent the laser beam moving path and, hence, to investigate the effects of different scanning strategies, for example.

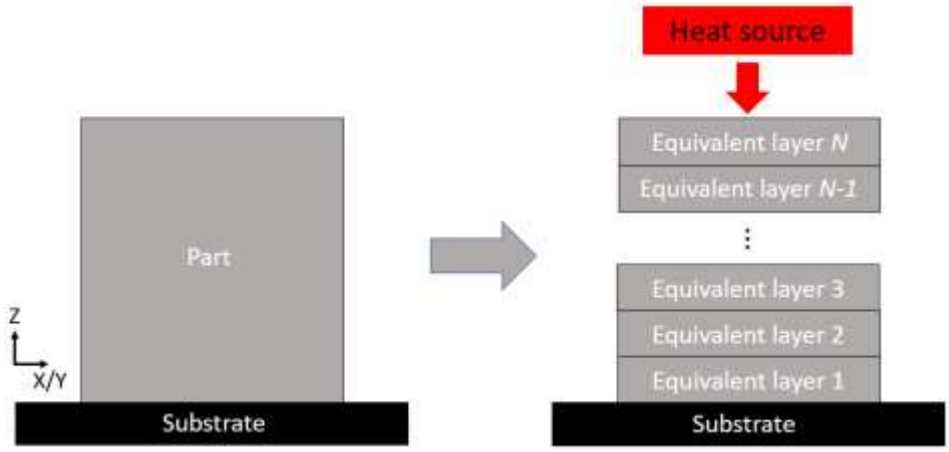

Figure 2.11. The schematic diagram of the layer-by-layer method.

Promoppatum et al. [58] investigated the inherent strain based approach for prediction of residual stress development in PBF Inconel 718 parts, with comparison against neutron diffraction measured results for validation of the developed FE framework. A key limitation of the inherent strain approach is the challenge in determining accurate inherent strain fields since they strongly depend on the AM process parameters. Bayat et al. [59] presented a component-level FE-based thermo-mechanical model for predicting residual stresses and distortions for PBF Ti-6Al-4V. The flash heating (FH) method, where an equivalent heat source was applied uniformly to the recently activated meta-layer instead of resolving the meso-scale laser-material interaction, was used as the initial multi-scaling approach to improve computational efficiency. However, the FH method is insensitive to scanning strategy, which leads to unrealistic prediction of residual deformation. Williams et al. [60] introduced a pragmatic FE-based component-level model for residual stress and distortion prediction in PBF process. Several layers are combined into a thicker computational section or block in their model, which is thus referred to a 'block dump' approach. For example, 16 layers were amalgamated to a height of 0.8 mm section in the model; the difference between the predicted distortion and the experimental measurement

using digital image correlation (DIC) was within 5% for a bridge component (of major dimension: 40 mm × 10 mm × 10 mm) made from 316L stainless steel. The 'block dump' approach can capture the thermo-mechanical conditions with reasonable accuracy, but high-performance computing (e.g. 12 CPUs is their study) is often required. Recently, a new highly-efficient AM module has been developed within the general-purpose FE-based software Abaqus, which, on the one hand, replicates the actual 3D printing process very realistically and with high fidelity, e.g. using actual 3D printing stereolithography (STL) files, whilst, on the other hand, providing a much more efficient process for modelling complex geometries, including a graphical user interface (GUI) [51]. This approach, which is the main method investigated here, is hereafter referred to simply as 'Abaqus AM', and has recently been evaluated by Song et al. [36] for AM (laser DED and PBF) of complex, three-dimensional Inconel 718 components; the results were compared to experimental measurements of residual stresses and distortions, the latter obtained using (i) a combined focused ion beam (FIB) slitting, and digital image correlation (DIC) method and (ii) X-ray diffraction (XRD), at different length-scales, and the maximum difference between FE predictions and FIB-DIC measurements is about 38.6% (viz. 610 MPa, as compared to 440 MPa). It was concluded that (i) further work is required on the effects of measured plastic anisotropy on as-built properties [61] and (ii) future research needs to focus on more accurate measurements of these critical material properties at elevated temperature to improve process simulation accuracy. The ability of the 'Abaqus AM' method to model the PBF process with complex engineering parts will be investigated in this thesis, including the effects of scanning strategy and preheating strategy on residual stress and distortion.

2.4 Numerical modelling of welding

2.4.1 Governing equations

Modelling of the welding process is a thermo-mechanical problem by neglecting fluid flow, plasma physics etc. and hence the governing equations left are the heat balance and force equilibrium for the thermal and mechanical analysis, respectively, which are the same as those presented above in Section 2.3.1.

2.4.2 Welding process modelling

Numerical modelling approaches for welded structures may generally be classified into two categories. The first category is process modelling of the welding process with the objective to predict residual stresses, deformations and sometimes microstructure and mechanical properties and behaviour, requires through-process simulation to enable prediction of the thermal (e.g. temperature distribution) and mechanical performance (e.g. residual stress) of welded components. Finite element modelling has been widely used to predict thermomechanical behaviour and/or material microstructural evolution during welding processes [62-65]. Commercial FE packages capable of simulating welding process include Abaqus [66], Sysweld [67] and ANSYS [68]. Yaghi et al. [69] presented a FE method for welding of P91 pipes with 4- or 36-pass welds in a pipe, using the 'Model Change' technique. The distributed heat flux, DFLUX, which has been primarily applied in the welding process modelling, is given by:

$$\mathrm{DFLUX} = \frac{U \cdot I \cdot \eta}{V} \tag{2.12}$$

where U is the voltage, I the current, η the arc efficiency and V is the weld pass volume. Figure 2.12 shows the thermal contour plots at different numbers of completed passes for an axisymmetric 36-pass model, as simulated by Mac Ardghail et al. [70]. The letter developed a modelling framework to predict the effects of welding on thermo-mechanical performance of 9Cr martensitic steel, the predicted evolution of welding-induced heat-affected zone was shown to be qualitatively consistent with experimentally-observed trends in prior-austenite grain size, hardness, lath width and regions in which austenite transformation occurred at high temperature. Vemanaboina et al. [71] presented a welding process simulation model for temperature and residual stress analysis, indicating that residual stress is higher at fusion zone compared to HAZ and parent metal. However, full process modelling of power plant pipes and components can be computationally expensive, which may be impractical for industrial design application, particularly for large structures.

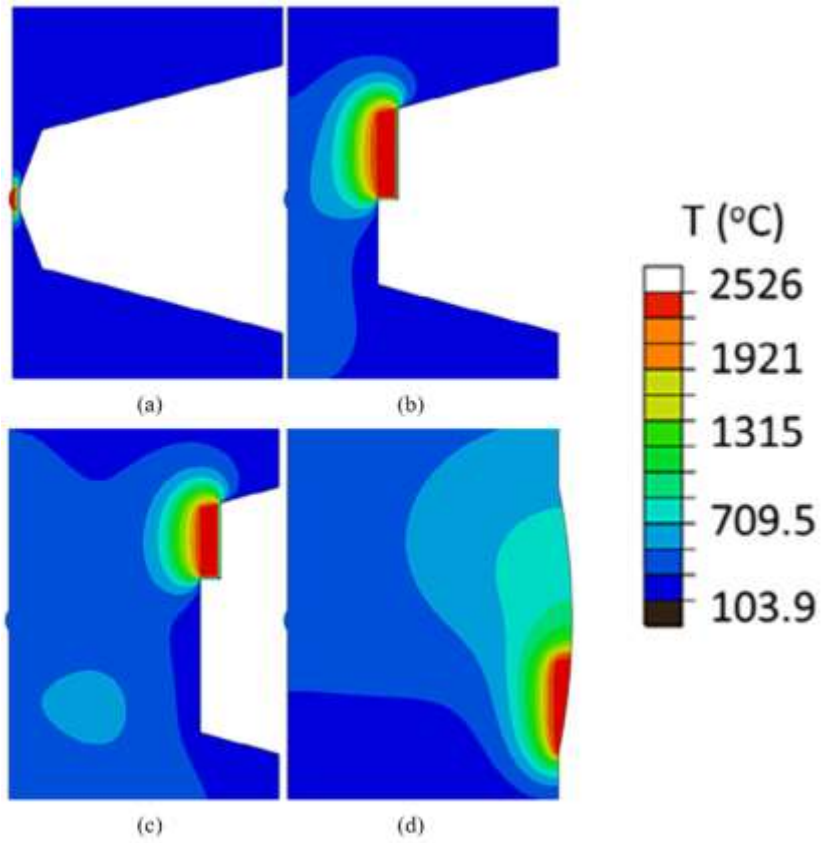

Figure 2.12. Thermal contour plots at different numbers of completed passes for a 36-pass welding process modelling: (a) 1st pass, (b) 9th pass, (c) 22nd pass and (d) 36th pass, adapted from [70].

2.4.3 Representative welded specimen modelling

The second category of modelling for welding is focused on mechanical behaviour prediction for the welding induced inhomogeneity of material, e.g. heat affected regions. Experimental testing is used to characterize the material properties of different zones of welded joints to provide input for mechanical analysis of welded joints based on identification of the welded connection into different sub-zone, such as HAZ, WM and PM. For example, as three-material model was developed by Li et al. [72] to simulate the mismatch of high temperature cyclic plasticity in the three different welded regions (PM, HAZ and weld material (WM)) based on the work of Farragher et al [73]. The HAZ was treated as a homogeneous material in their work, thereby omitting key aspects, such as HAZ sub-regions and heterogeneous microstructure and material properties. During

welding, the temperature is high enough to cause transformation to a different microstructure [74]. It has been confirmed that significant variation in yield strength [75] and hardness [76, 77] can be found in the various heat-affected microstructural zones, which is critical for predicting fatigue life of HAZ. Therefore, incorporation of each subregion of welded joints is necessary for the development of more accurate computational models for effect of welding process on fatigue life prediction. Some experimental methods have been proposed to study the heterogeneity of material properties of welded joints. For example, through the creep tests of Hyde et al. [78], the creep material data for HAZs can be obtained, and via digital image correlation (DIC) tests, Touboul et al. [79] have characterised the plasticity response (including high temperature) of each zone (ICHAZ, CGHAZ, FGHAZ, WM and PM) of P91 welded joint at room temperature and 625 ^{o}C. However, additional experimental work is required for different temperatures and test strain-ranges. The five-material cross-weld HTLCF model (see Figure 2.13) to capture the material property inhomogeneity in P91 cross-weld specimens will be developed in this thesis.

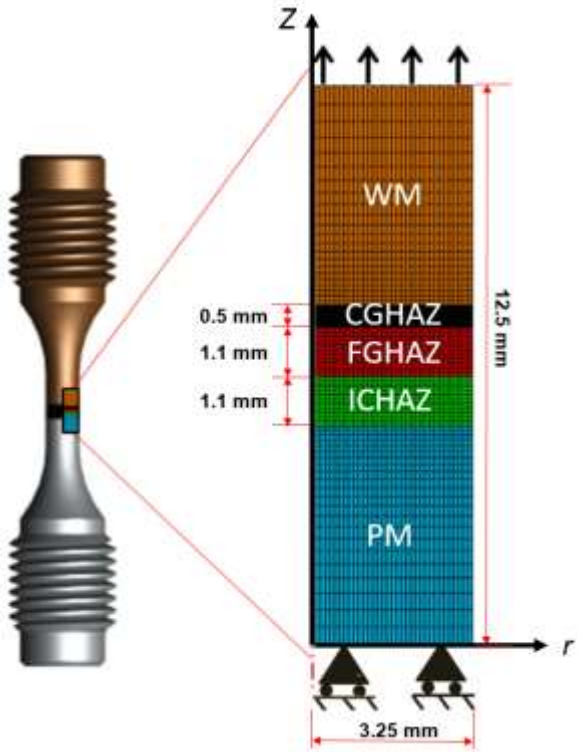

Figure 2.13. Schematic of P91 cross-weld specimen.

2.5 Material behaviour modeling

2.5.1 Phenomenological modelling

The stress-strain response of the elastic-perfectly plastic (EPP) model is shown in Figure 2.14 with a two-dimensional (2D) yield surface. The yield function for the EPP model is written as follows [80]:

$$f = \sigma_{\mathrm{e}} - k \tag{2.13}$$

where f is the yield function, k is the yield stress, and σ_{e} is the equivalent (von Mises) stress, given as:

$$\sigma_{\mathrm{e}} = (\frac{3}{2}\boldsymbol{\sigma}' : \boldsymbol{\sigma}')^{1/2} \tag{2.14}$$

where $\boldsymbol{\sigma}'$ is the deviatoric stress, given by:

$$\boldsymbol{\sigma}' = \boldsymbol{\sigma} - \frac{1}{3}\mathrm{Tr}(\boldsymbol{\sigma})\boldsymbol{I} \tag{2.15}$$

The yield function is used to determine whether the material has yielded or not. The yield criterion is given by:

$$\begin{aligned} f < 0&: \text{elastic deformation} \\ f = 0&: \text{plastic deformation} \end{aligned} \tag{2.16}$$

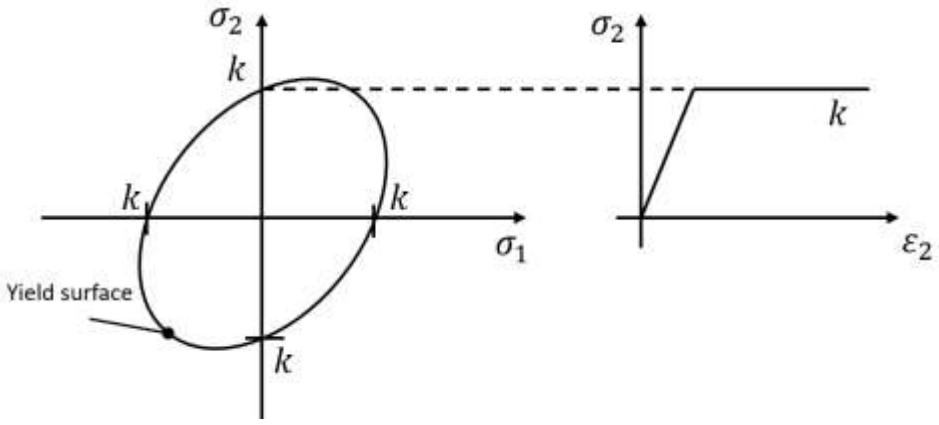

Figure 2.14. The 2D yield surface and stress-strain response for uniaxial loading with elastic-perfectly plastic (EPP) material model.

Figure 2.15 depicts the non-linear kinematic hardening (NLKH) of a material under uniaxial loading, where the yield surface translates while the size and shape remain unchanged during plastic loading. The kinematic back-stress term $\boldsymbol{\chi}$ is included to describe the position of the yield surface. Within the Ziegler non-linear kinematic hardening model [81], two uniaxial kinematic back-stress terms are defined to describe the initial and later strain hardening regions, as following:

$$\dot{\boldsymbol{\chi}}_i = \frac{C_i}{(k+R)}(\boldsymbol{\sigma} - \boldsymbol{\chi})\dot{p} - \gamma_i \boldsymbol{\chi}_i \dot{p} \tag{2.17}$$

$$\dot{\boldsymbol{\chi}} = \dot{\boldsymbol{\chi}}_1 + \dot{\boldsymbol{\chi}}_2 \tag{2.18}$$

where C_i is the kinematic hardening modulus, R is the isotropic stress, p is the effective plastic strain-rate and γ_i is the rate of decay.

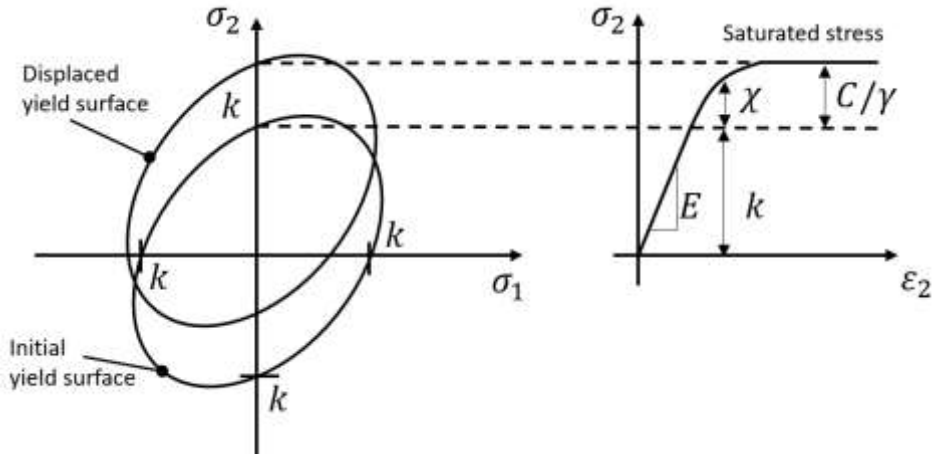

Figure 2.15. The 2D yield surface and stress-strain response for uniaxial loading with non-linear kinematic hardening (NLKH) material model.

Figure 2.16 shows the non-linear isotropic hardening (NLIH) of a material subjected to a uniaxial load. The yield surface expands without changing position during plastic loading. The isotropic stress R is incorporated in the yield function to model the isotropic hardening (or softening), of which the evolution is given by Chaboche [82, 83], as following:

$$\dot{R} = B(Q - R)\dot{p} \tag{2.19}$$

where B controls the rate of decay leading to saturation and Q is the saturation value of the isotropic hardening (or softening) stress. A negative value of Q allows the cyclic softening of materials (e.g. P91 [84]) to be simulated at the continuum level.

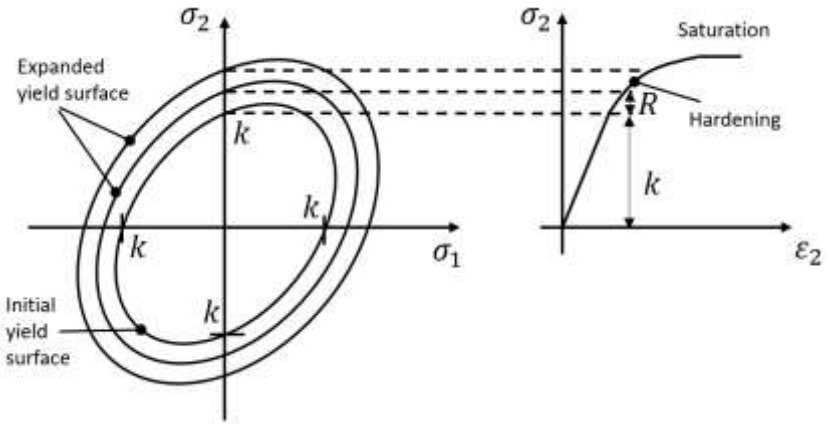

Figure 2.16. The 2D yield surface and stress-strain response for uniaxial loading with non-linear isotropic hardening (NLIH) material model.

Observations from experimental testing indicate that the stress-strain response is typically a combination of kinematic and isotropic hardening. It is necessary to combine both hardening rules to accurately predict the constitutive response. Figure 2.17 illustrates the stress-strain behavior of the combined non-linear kinematic isotropic hardening (NLKIH) incorporating the Bauschinger effect with an expanded yield surface. The yield function of NLKIH plasticity is given as:

$$f = \left(\frac{3}{2}(\boldsymbol{\sigma}' - \boldsymbol{\chi}') : (\boldsymbol{\sigma}' - \boldsymbol{\chi}')\right)^{1/2} - R - k \tag{2.20}$$

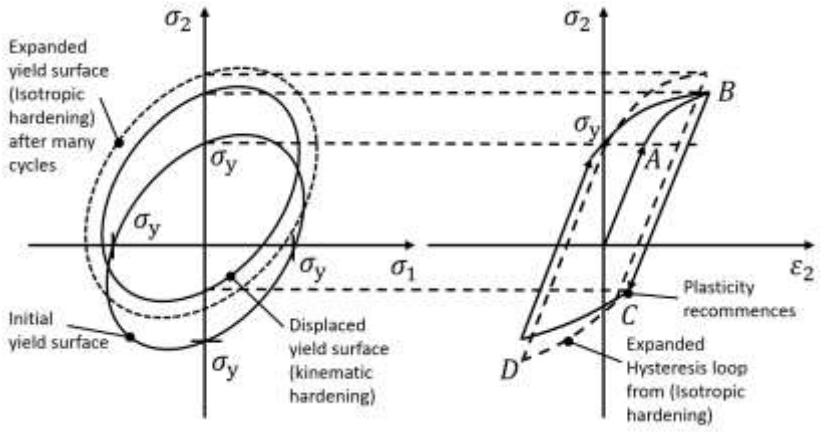

Figure 2.17. The evolution in 2D yield surface and cyclic stress-strain response for uniaxial loading with combined non-linear kinematic and isotropic hardening (NLKIH) material model.

The two-layer viscoplasticity model developed by Kichenin et al. [85] and implemented in Abaqus [51] can be implemented to define the constitutive behavior of materials, in which significant time-dependent as well as time-independent plasticity is observed, as shown in Figure 2.18. This material model has also been successfully applied to nickel-chromium alloys for high temperature forming tools [86] and for welded P91 joints [73].

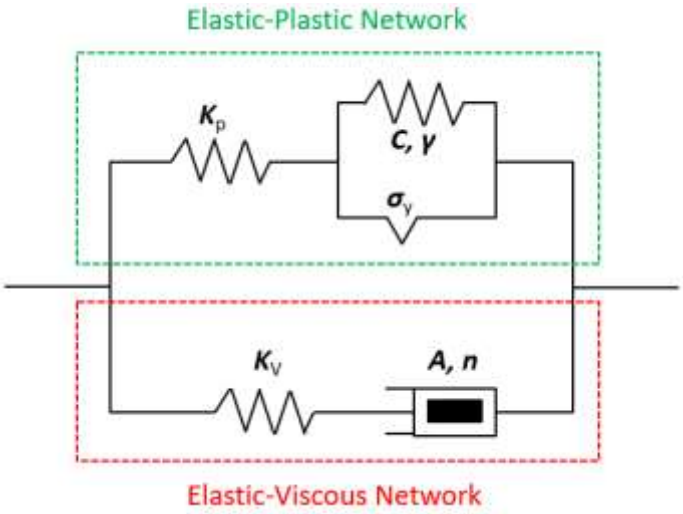

Figure 2.18. Idealization of two-layer viscoplasticity model, adapted from [86].

The temperature-dependent two-layer viscoplasticity model is adopted with combined non-linear kinematic and isotropic hardening model to capture the cyclic plasticity behavior and Norton power law for the secondary creep, of which the general equations are given as below:

$$\varepsilon_{\mathrm{p}}^{el} = \frac{1+\upsilon}{K_{\mathrm{p}}}\boldsymbol{\sigma}_{\mathrm{p}} - \frac{\nu}{K_{\mathrm{p}}}\mathrm{tr}(\boldsymbol{\sigma}_{\mathrm{p}})\mathbf{I} \tag{2.21}$$

$$\varepsilon_{\mathrm{v}}^{el} = \frac{1+\upsilon}{K_{\mathrm{v}}}\boldsymbol{\sigma}_{\mathrm{v}} - \frac{\nu}{K_{\mathrm{v}}}\mathrm{tr}(\boldsymbol{\sigma}_{\mathrm{v}})\mathbf{I} \tag{2.22}$$

where υ is Poisson's ratio, $\mathbf{I}$ is unit tensor of second-rank, tr expresses the trace of a tensor, and $\boldsymbol{\sigma}_{\mathrm{p}}$, $\boldsymbol{\sigma}_{\mathrm{v}}$ are the stress tensors for the elastic-plastic and elastic-viscous networks respectively, defined as:

$$\boldsymbol{\sigma}_{\mathrm{v}} = \mathbf{K}_{\mathrm{v}} : (\boldsymbol{\varepsilon} - \boldsymbol{\varepsilon}_{\mathrm{v}}) \tag{2.23}$$

$$\boldsymbol{\sigma}_{\mathrm{p}} = \mathbf{K}_{\mathrm{p}} : (\boldsymbol{\varepsilon} - \boldsymbol{\varepsilon}_{\mathrm{p}}) \tag{2.24}$$

$$\boldsymbol{\sigma} = \boldsymbol{\sigma}_{\mathrm{p}} + \boldsymbol{\sigma}_{\mathrm{v}} \tag{2.25}$$

where $\mathbf{K}_{\mathrm{v}}$ and $\mathbf{K}_{\mathrm{p}}$ are the elastic tensors of the elastic-viscous and elastic-plastic networks respectively. The creep strain is obtained from the multiaxial version of the following Norton power law [87]:

$$\dot{\varepsilon}_{\mathrm{c}} = A\sigma^{n} \tag{2.26}$$

where A and n are temperature-dependent material constants, $\dot{\varepsilon}_{\mathrm{c}}$ is the creep strain rate. The combined contributions of elastic-plastic and elastic-viscous networks of the material can be defined by introducing the parameter F, as follows:

$$F = \frac{K_{\mathrm{v}}}{K_{\mathrm{p}} + K_{\mathrm{v}}} \tag{2.27}$$

2.5.2 Crystal plasticity finite element modelling

In recent decades, microstructure-based modelling methods have been developed to understand and quantify the stress-strain response at the microscale (e.g. grain level) [88-90]. In these models, the microscale intrinsic response typically relies on the theory of crystal plasticity, which is typically implemented in FE tools [91, 92]. Length-scale dependence has been successfully incorporated into crystal plasticity FE (CPFE) models to account for strain gradient effects, allowing accurate modelling and prediction of local deformation at the grain level [93-95].

Basic theory of crystal plasticity is simply reviewed here. The deformation gradient **F** can be represented by a multiplicative decomposition, as:

$$\mathbf{F} = \mathbf{F}^{\boldsymbol{e}} \cdot \mathbf{F}^{\boldsymbol{p}} \tag{2.28}$$

where $\mathbf{F}^{\boldsymbol{e}}$ denotes the elastic deformation gradient due to lattice stretching and rotation of the crystal lattice, and $\mathbf{F}^{\boldsymbol{p}}$ captures the plastic deformation gradient due to dislocations, as shown in Figure 2.19. The hardening and yield of a material is only related to plastic deformation.

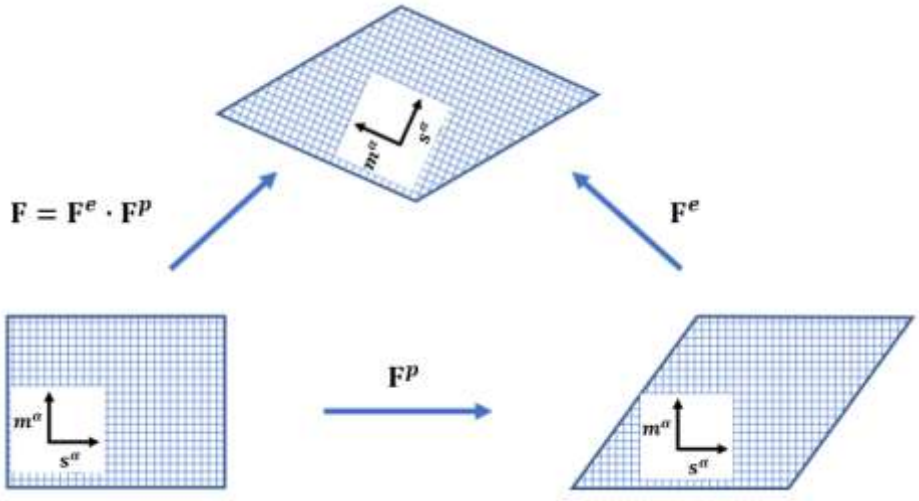

Figure 2.19. Schematic of the decomposition of the deformation gradient **F**.

Following the work of Hill et al. [96], Asaro et al. [97] and Peirce et al. [98], the plastic velocity gradient tensor due to dislocation slip, $\mathbf{L}^{\boldsymbol{p}}$, can be expressed as:

$$\mathbf{L}^{\boldsymbol{p}} = \dot{\mathbf{F}}^{\boldsymbol{p}}(\mathbf{F}^{\boldsymbol{p}})^{-\mathbf{1}} \tag{2.29}$$

The plastic velocity gradient $\mathbf{L}^{\boldsymbol{p}}$ can be calculated as the sum of shear rates on all active slip systems based on the kinematics of slip motion, as:

$$\mathbf{L}^{\boldsymbol{p}} = \sum_{\boldsymbol{\alpha}=\mathbf{1}}^{\boldsymbol{N}} \dot{\boldsymbol{\gamma}}^{\boldsymbol{\alpha}}(\mathbf{s}^{\boldsymbol{\alpha}} \otimes \boldsymbol{m}^{\boldsymbol{\alpha}}) \tag{2.30}$$

where $\boldsymbol{N}$ is the total number of active slip systems (e.g. FCC material has 12 slip systems (four planes, three directions per plane)), α represents the current slip system. $\dot{\boldsymbol{\gamma}}^{\boldsymbol{\alpha}}$, $\mathbf{s}^{\boldsymbol{\alpha}}$ and $\boldsymbol{m}^{\boldsymbol{\alpha}}$ define the slip rate, slip direction and normal to slip plane, respectively. $\otimes$ indicates a dyadic product.

With the microscopic aspects of CPFE modelling, it is possible to capture the material response in regions of steep microstructural gradients, which is highly attractive in predicting component lifetime. However, the disadvantage of CPFE is that the computational domain of CPFE modelling is typically too small (e.g. $50\ \mu m \times 50\ \mu m \times 50\ \mu m$ [99]) to combine effects such as heat input from remote (e.g. several millimetres away) or stress redistribution from material locations remote to the area of interest. Furthermore, it is computationally expensive to use CPFE modelling as it involves solving

boundary-valued problems containing many degrees of freedom, which limits the size of the microstructure that can be investigated [100].

2.5.3 Physically-based modelling

2.5.3.1 Physically-based yield strength model

Barrett et al. [101] recently presented a temperature-independent, physically-based (PB) yield strength (YS) model for P91 steel. The model assumes that the yield strength is composed of contributions from dislocations, τ_A, and obstacles such as particles and boundaries, τ_{B}, following the model of Kocks et al. [102], as follows:

$$\sigma_{\mathrm{y}} = M(\tau_A^2 + \tau_B^2)^{1/2} \tag{2.31}$$

where M is the Taylor factor. τ_A is defined by the Taylor hardening expression:

$$\tau_A = \alpha_1 \mu b \sqrt{\rho_{\mathrm{i}}} \tag{2.32}$$

where α_1 is a material constant between 0.2 and 0.5, μ is temperature dependent shear modulus, b is magnitude of Burgers vector and ρ_{i} is dislocation density, whilst τ_{B} is defined as the sum of various obstacle contributions:

$$\tau_{\mathrm{B}} = \tau_{\mathrm{PN}} + \tau_{\mathrm{bd}} + \tau_{\mathrm{SS}} + \tau_{\mathrm{ph}} + \tau_{\mathrm{in}} \tag{2.33}$$

where τ_{PN} is the Peierls-Nabarro stress, τ_{bd} is the contribution of GBs, τ_{SS} is the substitutional solid solution strengthening term, τ_{ph} is the precipitates term and τ_{in} is interstitial solid solution strengthening term.

The Peierls model underestimates the dislocation width so it overestimates the intrinsic strength of the material compared with the real crystal. Therefore, the Nabarro model [103] was used by Barrett et al. [101]:

$$\tau_{\mathrm{PN}} = \frac{2\mu}{1-\nu} \exp\left(\frac{-2\pi}{1-\nu}\right) \tag{2.34}$$

HAGBs cause dislocation pinning, which delays dislocations and resists inelastic deformation. The well-known Hall-Petch relation was used to simulate the strengthening of HAGBs. The contribution of GBs to yield strength was also considered for the

strengthening due to the LAB dislocation substructure, τ_{LAB}. As a result, the yield stress caused by GBs increases was given by:

$$\tau_{\mathrm{bd}} = \tau_{\mathrm{HP}} + \tau_{\mathrm{LAB}} \tag{2.35}$$

Based on the test data of Sakui et al. [104, 105] for pure Fe, an exponential relationship between the Hall-Petch constant k_{HP} and temperature is observed. So, the contribution of HAGB to strength was:

$$\tau_{\mathrm{HP}} = \frac{k_{\mathrm{HP}}(T)}{d_{\mathrm{g}}^{n_{\mathrm{HP}}}} = k_{\mathrm{HP},0}\exp\left(\frac{-T}{T^*}\right)\frac{1}{d_{\mathrm{g}}^{n_{\mathrm{HP}}}} \tag{2.36}$$

where $k_{\mathrm{HP},0}$ is the Hall-Petch constant at 0 K, T^* is a constant (326K), d_{g} is grain size and n_{HP} is the Hall-Petch exponent with a value of approximately ½. In the materials with hierarchical microstructure, d_{g} is assumed to be the minimum HAGB size (the mean block width, d_{b}). As discussed by Maruyama et al. [106], τ_{LAB} is inversely proportional to the LAB size, $\bar{m}$. Therefore, the contribution of LAB dislocation substructure to yield strength is as follows:

$$\tau_{\mathrm{LAB}} = \frac{\alpha_2 \mu b}{\bar{m}} \tag{2.37}$$

where α_2 is a material parameter with a value (between 2 and 3). The equivalent LAB size is defined using the mean slip length model of Naylor [107]:

$$\bar{m} = \frac{2}{\pi}\left[w\mathrm{In}\left(\tan\left(\arccos\left(\frac{w}{l}\right)\right) + \frac{l}{w}\right) + l\frac{\pi}{2} - l\arccos\left(\frac{w}{l}\right)\right] \tag{2.38}$$

where w is the LAB width. The right-hand side of Eq. (2.38) reduces to w for an equal-axed subgrain microstructure (i.e. for $l = w$).

Solute atoms (e.g. Mn and Ni) produce a local stress field in the matrix material, thus increasing the shear stress required to move dislocations near the solute atoms. The effect of the substitutional solutes with the contribution of m multicomponent on the overall yield strength is [108]:

$$\tau_{\mathrm{ss}}^{P} = \sum_{i=1}^{m} \tau_{\mathrm{ss,i}}^{P} \tag{2.39}$$

where the constant p is the inverse of the concentration exponent and $\tau_{\mathrm{ss,i}}$ is the increase in shear stress due to solute i.

The existence of C and N atoms in the interstitial lattice is explained by a simplified hypothesis, that is, the increase in strength is proportional to the composition in $wt.\%$ to the power of 1/2 [109]:

$$\tau_{\text{in}} = \frac{1}{M}\left\{k_C[\text{C}(wt.\%)]^{1/2} + k_N[\text{N}(wt.\%)]^{1/2}\right\} \tag{2.40}$$

where k_C is the hardening constant for C interstitial while the k_N is the hardening constants for N interstitials.

The contribution of precipitates to yield strength was defined by Barrett et al. [101] via the Ashby-Orowan equation [110]:

$$\tau_{\text{ph}} = 0.045\frac{\mu b}{\lambda}\text{In}\frac{r}{b} \tag{2.41}$$

where λ is precipitate spacing and r is particle radius. In order to explain the inhomogeneous distribution of carbides in the microstructure of 9Cr steels, the effect of precipitates on the yield strength was defined by:

$$\tau_{\text{ph}} = \left(1 - f_{\text{w}} - f_{\text{g}}\right)\tau_{\text{ph,INT}} + (f_{\text{w}} + f_{\text{g}})\tau_{\text{ph,BND}} \tag{2.42}$$

where $\tau_{\text{ph,INT}}$ is the proportion of the precipitate yield strength in the martensitic lath interiors, $\tau_{\text{ph,BND}}$ is the precipitate yield strength at the GBs and f_{w} and f_{g} are the volume fractions of the low angle and high-angle boundaries, respectively.

2.5.3.2 Physically-based cyclic viscoplasticity model

It is well known that the high-temperature 9Cr martensitic–ferritic steels undergo softening during high temperature cyclic deformation [111]. This is attributable to thermomechanical deformation induced microstructure evolution, including specifically reduced dislocation density due to dislocation annihilation and martensitic lath widening [101]. The physically-based cyclic viscoplasticity model of Barrett et al. [112] based on a dislocation-mechanics framework was specifically developed to represent this complex nano-, micro-scale behavior for macro-scale simulations. The inelastic strain-rate is defined as a function of a set of key microstructural variables:

$$\dot{\varepsilon}_{\text{in}} = f(d_{\text{b}}, w, \lambda, c, \rho) \tag{2.43}$$

where d_b is martensitic block width, w is martensitic lath width, λ is precipitate spacing, c is concentration of solutes and ρ is dislocation density. More specifically:

$$\dot{\varepsilon}_{in} = A\exp\left(\frac{-\Delta F}{k_B T}\right)\sinh\left(\frac{\boldsymbol{\sigma}_v \Delta V}{M k_B T}\right)\mathrm{sgn}\,(\sigma - \sigma_b) \tag{2.44}$$

where A is the pre-exponential viscous constant, ΔF is Helmholtz free energy, k_B is Boltzmann's constant, T is absolute temperature, ΔV is activation volume, $\boldsymbol{\sigma}_v$ is viscous stress, σ is stress, σ_b is the kinematic back-stress. The viscous (thermal) stress under uniaxial loading is defined as:

$$\sigma_v = |\sigma - \sigma_b| - \sigma_y^{cyc} \tag{2.45}$$

where σ_y^{cyc} is cyclic yield stress.

The kinematic back-stress is shown as below:

$$\sigma_b = \sigma_{ph} + \sigma_g + \sigma_w \tag{2.46}$$

where σ_{ph}, σ_g and σ_w are the back-stress contributions due to particles, dislocation pileups at HAGBs, and dislocation substructure, respectively. In the initial microstructure of 9Cr steels, the arrangement of precipitates is the MX particles inside the martensitic lath and the $M_{23}C_6$ carbides distributed along the HAGBs and LABs. Therefore, using the volume fraction approach, the rate change of precipitate strengthening can be defined as:

$$\sigma_{ph} = \left(1 - f_w - f_g\right)\sigma_{ph,INT} + (f_w + f_g)\sigma_{ph,BND} \tag{2.47}$$

where f_w and f_g are the volume fractions of the LABs and HAGBs, respectively, and $\sigma_{ph,INT}$ and $\sigma_{ph,BND}$ are the precipitate yield strength in the martensitic lath interiors and at the GBs. The back-stress, σ_g, at the HAGBs is:

$$\sigma_g = \frac{Mb\mu}{\alpha_g d_g} n_g \tag{2.48}$$

where α_g is a material constant with a value of 0.5, n_g is the number of dislocations in the pileups and d_g represents the mean distance between HAGBs. The back-stress, σ_w, due to the dislocation substructure is:

$$\sigma_w = \frac{M\mu}{1 - v}\sqrt{\frac{0.45\theta b}{2\pi w}} \tag{2.49}$$

where θ is the angle of misorientation between LABs.

The total dislocations density, ρ, includes the mobile dislocation density, $\vec{\rho}$, and immobile dislocation densities along LABs, HAGBs and within martensitic lath interiors, ρ_{w}, ρ_{g}, and ρ_{i}, respectively; therefore, the total dislocation density is:

$$\rho = \vec{\rho} + f_{\mathrm{w}}\rho_{\mathrm{w}} + f_{\mathrm{g}}\rho_{\mathrm{g}} + \left(1 - f_{\mathrm{w}} - f_{\mathrm{g}}\right)\rho_{\mathrm{i}} \tag{2.50}$$

The martensitic lath substructure plays an essential role in the strength and toughness of P91 steel [113, 114]. The widening of laths during cyclic loading is defined by Barrett et al. [112] and Giroux et al. [111] as:

$$w = \frac{w_0 \rho_{\mathrm{w},0}}{\rho_{\mathrm{w}}} \tag{2.51}$$

where w_0 and $\rho_{\mathrm{w},0}$ are the initial lath width and LAB dislocation density, respectively. Further details of the original implementation of this model are given in Barrett et al. [112]. The model has never been applied to weld-induced microstructure inhomogeneity.

2.6 Failure

2.6.1 Fatigue testing

Fatigue failure has been the concern of engineers for centuries. Fatigue testing is required to evaluate the influence of manufacturing processes and in-service environments on fatigue performance. Wöhler first performed the fatigue testing of railway axles and introduced the concept of S-N curves, which relate applied stress to fatigue life [115]. Figure 2.20 illustrates the three categories of fatigue: (i) low cycle fatigue (LCF), (ii) high cycle fatigue (HCF), (iii) ultra-high cycle fatigue (UHCF). LCF is the type of fatigue which is caused by cyclic plastic strain under a low number of load cycles before failure ($N_f < 10^5$ cycles). HCF is the type of fatigue caused by cyclic elastic strain under a large number of load cycles before failure ($10^5 < N_f < 10^6$ cycles). UHCF is the type of fatigue with very long service life as well as high loading frequency ($N_f > 10^7$ cycles). An important difference between LCF and HCF is that most of the life is spent on crack propagation in LCF, while most of the fatigue life is devoted to crack initiation in HCF. Figure 2.21 shows the four stages of fatigue, including cyclic hardening or softening, crack

initiation, crack propagation and final fracture. There are two main types of fatigue testing: (i) load- or stress-controlled testing, where the load amplitude is constant and (ii) displacement- or strain- controlled testing, where the displacement amplitude is unchanged.

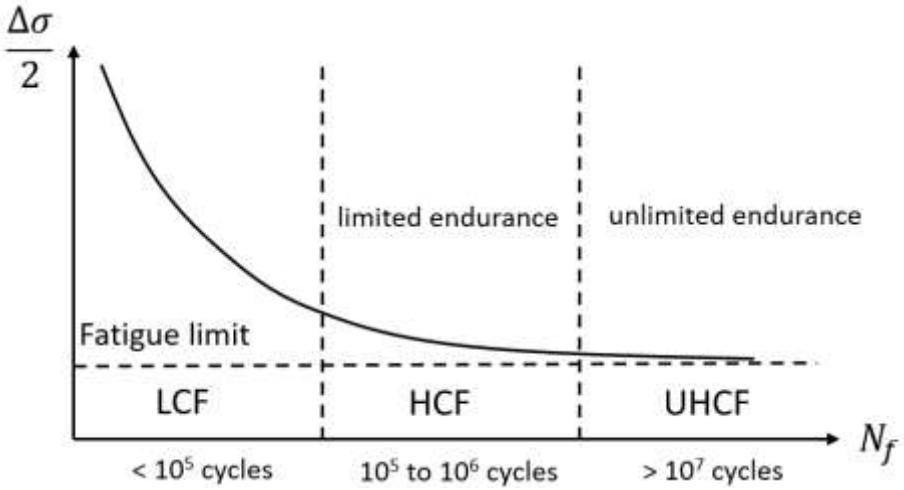

Figure 2.20. Diagram of the different fatigue domains.

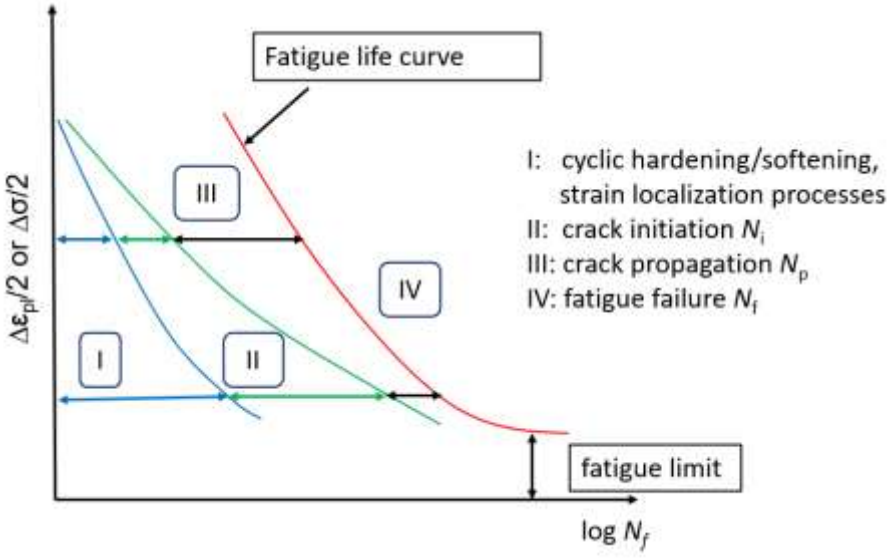

Figure 2.21. Diagram of the four stages of fatigue.

2.6.2 Microstructural behaviour due to cyclic loading

Hardening/softening phenomenon under cyclic loading is attributed to the microstructure changes during cyclic loading [112, 116, 117]. Shankar et al. [118] reported that 9Cr-1Mo ferritic steels show cyclic softening, as illustrated in Figure 2.22. The microstructural evolution was summarized as: (i) reduction of dislocation density due to martensitic transformation and (ii) degradation of strength due to coarsening of precipitates, causes the softening. Yu et al. [119] performed LCF tests on additively manufactured 316L. It is seen that AM 316L also shows a continuous softening (see Figure 2.23), which is attributed to suppressed martensitic transformation and dislocation unpinning from cell boundaries. The cyclic response during fatigue of SS316L is related to the evolution of dislocation structure, such as the formation of persistent slip bands (PSB), deformation twinning and strain-induced martensitic phase transformation [120-122].

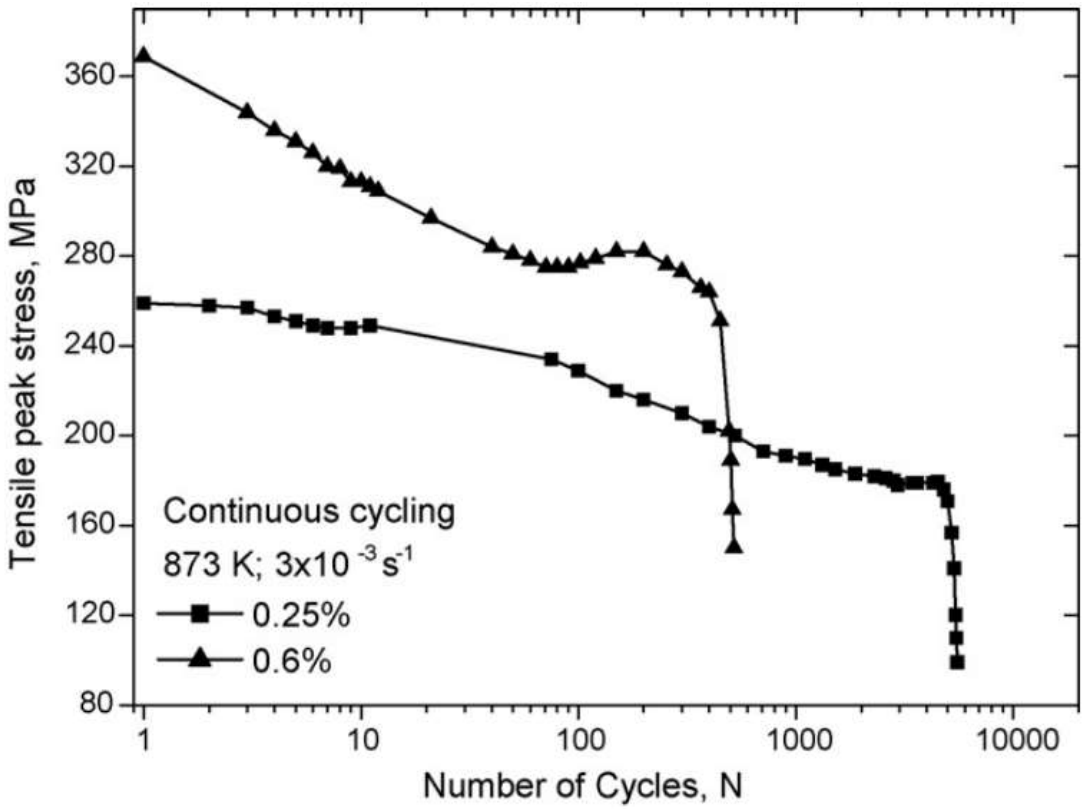

Figure 2.22. Cyclic softening curves of 9Cr-1Mo steel under different strain amplitudes [118].

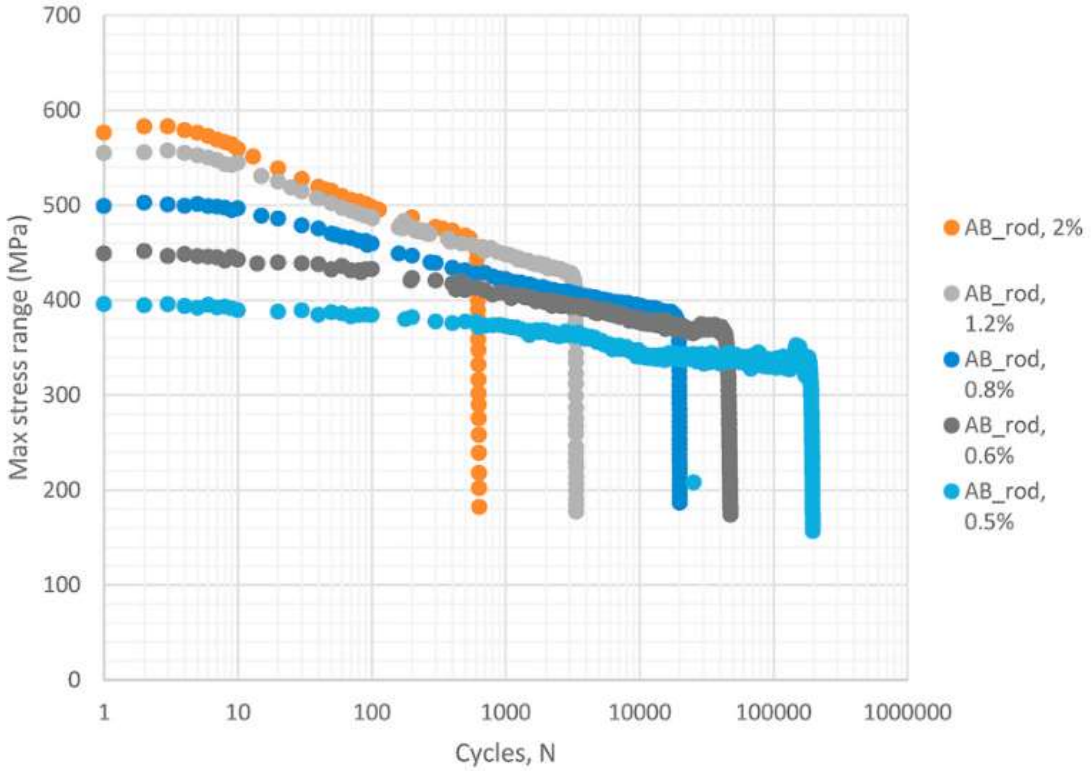

Figure 2.23. Cyclic softening curves of additively manufactured 316L samples under different loading levels [119].

2.6.3 Life prediction models

2.6.3.1 Traditional model

Fatigue failure is typically categorized as being within either the LCF or HCF regime. Figure 2.24 illustrates the schematic of the Coffin-Manson equation for LCF and the Basquin equation for HCF [123].

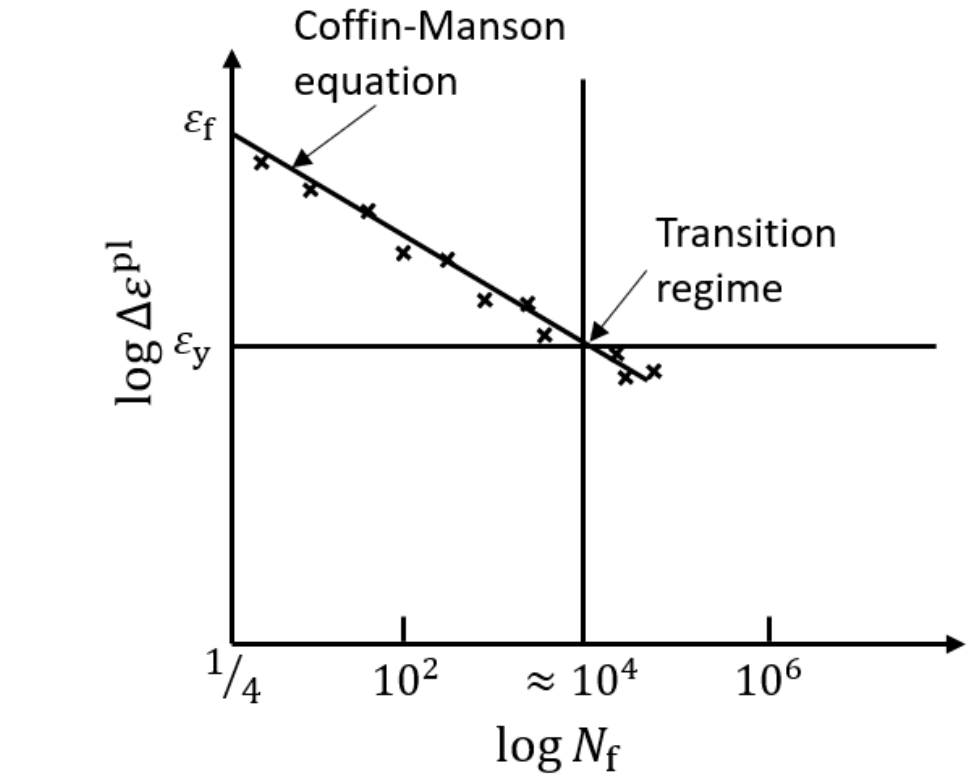

(a)

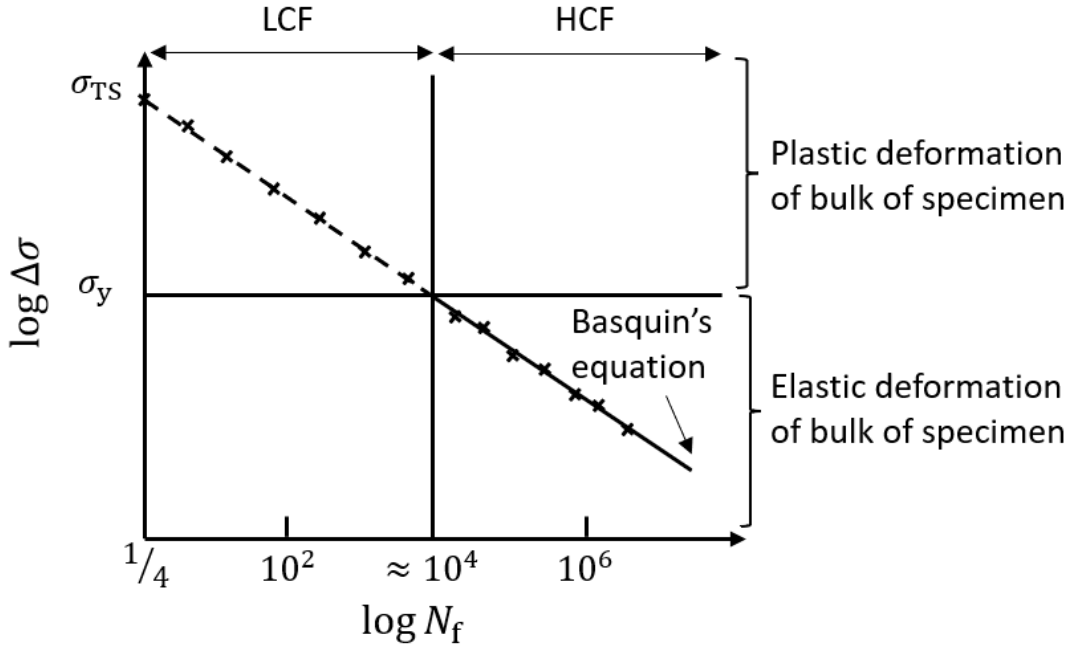

(b)

Figure 2.24. Schematic of (a) Coffin-Manson equation for LCF loading and (b) Basquin equation for HCF loading.

The Coffin-Manson equation [124, 125] (see Figure 2.24(a)) is based on the relationship obtained by plotting log of plastic strain amplitude versus log of number of reversals ($2N_f$) to failure, as follows:

$$\frac{\Delta\varepsilon^{pl}}{2} = \varepsilon_f'(2N_f)^c \tag{2.52}$$

where $\Delta\varepsilon^{pl}$ is plastic strain amplitude, ε_f' is the fatigue ductility coefficient, c is the fatigue ductility exponent and N_f is the number of cycles to failure. For fully reversed loading in the HCF regime, fatigue life typically follows a log-log relationship with stress amplitude, which is most often described using the Basquin equation [126] (see Figure 2.24(b)), as follows:

$$\frac{\Delta\sigma}{2} = \sigma_f'(2N_f)^b \tag{2.53}$$

where $\Delta\sigma$ is stress range, σ_f' is the fatigue strength coefficient, b is the fatigue strength exponent. Combining the Coffin-Manson and Basquin relationships, the total strain-life relationship [127] for predicting failure in the mixed LCF-HCF regime is given as:

$$\frac{\Delta\varepsilon}{2} = \frac{\Delta\varepsilon^{el}}{2} + \frac{\Delta\varepsilon^{pl}}{2} = \frac{\sigma_f'}{E}(2N_f)^b + \varepsilon_f'(2N_f)^c \tag{2.54}$$

where $\Delta\varepsilon$ is total strain range and $\Delta\varepsilon^{el}$ is elastic strain range. One equation for relating fatigue life to stress range, mean stress and residual stress is given by combining the well-known Goodman equation for effect of mean stress [128, 129] with Basquin's equation, as follows:

$$\frac{\sigma_a}{\sigma_f'(1 - \frac{\sigma_m + \sigma_r}{\sigma_{TS}})} = (N_f)^b \tag{2.55}$$

where σ_a is alternating stress, σ_m is mean stress, σ_r is residual stress and σ_{TS} is ultimate tensile strength.

2.6.3.2 Tanaka-Mura model

Tanaka and Mura [130] presented a micromechanical fatigue nucleation model in which dislocations accumulate irreversibly on the slip band of grains, leading to an energy-based crack initiation criterion. The energy-based formulation of Tanaka-Mura is specifically appropriate and suitable for such cyclically-induced microstructure and dislocation

evolution, as compared to more commonly-used stress-based approaches. Figure 2.25(a) shows the dislocation motion in a favourably oriented grain, of size 2a. Figure 2.25(b) shows the assumed mechanistic basis for fatigue persistent slip bands (PSBs) corresponding to packet size in the P91 microstructure.

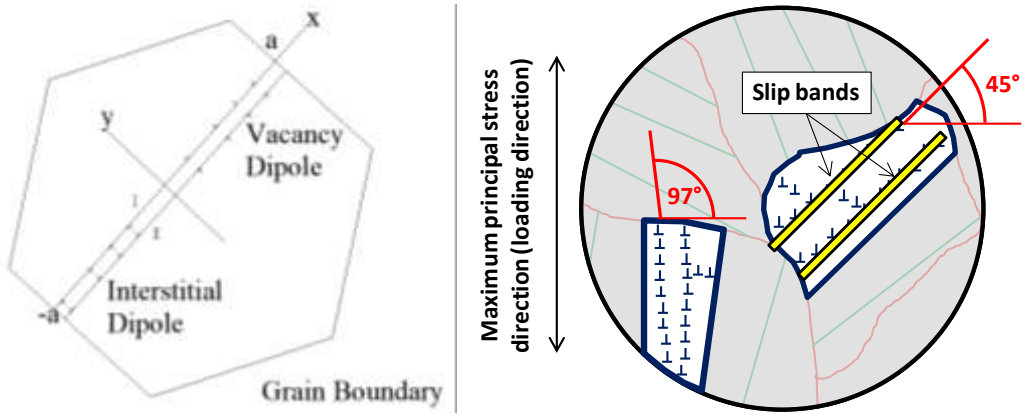

(a) (b)

Figure 2.25. (a) Dislocation motion in a grain, adapted from [130], (b) illustration of fatigue persistent slip bands assumed to correspond to packet size in hierarchical microstructure of P91 steels.

Under the first loading of stress τ_1 greater than the frictional stress k_{f}, the dislocation distribution with density $D_1(x)$ is produced on layer I. By assuming k_{f} to be constant, the equilibrium condition of dislocations inside layer I is expressed as:

$$\tau_1^D + \tau_1 - k_{\mathrm{f}} = 0 \tag{2.56}$$

where τ_1^D is the dislocation stress (back stress) given by

$$\tau_1^D = \frac{A\int_{-a}^{a} D_1(x')dx'}{(x-x')} \tag{2.57}$$

The domain of the dislocation distribution is -a < x < a and

$$A = \frac{\mu b}{2\pi(1-\upsilon)} \tag{2.58}$$

where b is the Burgers vector, μ the shear modulus. The domain of the dislocation distribution is $-\mathrm{a} < \mathrm{x} < \mathrm{a}$, where a is half of the grain size. The dislocation density $D_1(x)$

can be got by solved with the use of the inversion formula of Muskhelishvili under the condition of the unbounded density at two tips of the pileup x = ±a, as following:

$$\begin{aligned} D_1(x) &= \frac{1}{\pi^2 A}\frac{1}{(a^2-x^2)^{\frac{1}{2}}}\int_{-a}^{a}(a^2-x^2)^{\frac{1}{2}}\frac{\tau_1-k_{\mathrm{f}}}{x-x'}dx' \\ &= \frac{x}{\pi A}\frac{\tau_1-k_{\mathrm{f}}}{(a^2-x^2)^{\frac{1}{2}}} \end{aligned} \tag{2.59}$$

The total number of dislocations between x = 0 and a is

$$N_1 = \int_0^a D_1(x)dx = \frac{(\tau_1-k_{\mathrm{f}})a}{\pi A} \tag{2.60}$$

The total plastic displacement γ_1 in $-\mathrm{a} \le \mathrm{x} \le \mathrm{a}$ is:

$$\gamma_1 = \int_{-a}^{a}\emptyset(\mathrm{x})dx = \int_{-a}^{a} bD_1(x)xdx = \frac{\pi(1-\upsilon)(\tau_1-k_{\mathrm{f}})a^2}{\mu} \tag{2.61}$$

The stored energy of dislocations per unit thickness of the specimen is:

$$U_1 = -\frac{1}{2}\int_{-a}^{a}\tau_1^D\emptyset(\mathrm{x})dx = \frac{\gamma_1(\tau_1-k_{\mathrm{f}})}{2} \tag{2.62}$$

The increment of dislocation $D_k(x)$, the dislocation number N_k, the plastic strain increment γ_k, the back stress increment τ_k^D, and the stored energy U_k at the kth step of the forward and reverse loading processes are obtained in a similar manner.

$$\begin{cases} D_k(x) = (-1)^{k+1}\Delta D(x) \\ N_k = (-1)^{k+1}\Delta N \\ \gamma_k = (-1)^{k+1}\Delta\gamma \\ \tau_k^D = (-1)^{k+1}(2k_{\mathrm{f}}-\Delta\tau) \end{cases} \tag{2.63}$$

The Tanaka-Mura model assumes that if the stored strain energy due to dislocation accumulation becomes equal to a critical value of surface energy after *N* cycles, the layers of dislocation dipoles transform into a free surface, i.e. a micro-crack. The life to crack initiation N_{i} is thereby defined as the number of cycles when the following energy condition is satisfied:

$$\begin{cases} U \geq 2d_{\mathrm{p}}w_{\mathrm{s}} \\ \Delta U = \dfrac{\Delta\gamma(\Delta\tau - 2k_{\mathrm{f}})}{2} \\ \Delta\tau = \dfrac{\Delta\sigma}{M} \\ \Delta\gamma = \dfrac{\Delta\varepsilon^{\mathrm{pl}}}{M} \end{cases} \tag{2.64}$$

where $\Delta\tau$ is the shear stress range, $\Delta\sigma$ is the stress range ($\Delta\sigma = \sigma_{\max} - \sigma_{\min}$), $\Delta\gamma$ is the shear plastic strain range, $\Delta\varepsilon^{\mathrm{pl}}$ is the plastic strain range ($\Delta\varepsilon^{\mathrm{pl}} = \varepsilon^{\mathrm{pl}}_{\max} - \varepsilon^{\mathrm{pl}}_{\min}$), M is the Taylor factor (taken here as 2.9, based on bcc ferritic-martenstic P91 material), U is the stored strain energy, d_{p} is the packet size, k_{f} is frictional shear stress and w_{s} is the specific fracture energy per unit area.

Wu [131] presented a modified Tanaka–Mura model based on the following plastic strain expression:

$$\gamma_1 = \frac{1}{a}\int_0^a bD_1(x)dx = \frac{2(1-\nu)(\tau_1 - k)}{\mu} \tag{2.65}$$

and a new fatigue crack nucleation life expression in terms of plastic strain as:

$$n_{\mathrm{c}} = \frac{8(1-\nu)w_{\mathrm{s}}}{\mu b}\frac{1}{\Delta\gamma^2} \tag{2.66}$$

which is different with the original version of Tanaka-Mura model. However, Wu [131] only validated model against limited data on a small number of materials. In this thesis, the original Tanaka-Mura energy-based model, which has been correlated with experimental results [132-135], was adopted and also the first time applied to account for cyclic softening in 9Cr steels, with packet size as the critical length-scale for slip band formation.

2.7 Studied materials

2.7.1 Materials for high temperature applications

P91 steel, which is a 9Cr1Mo nano-strengthened, tempered martensitic alloy, has been widely used for high temperature applications, such as the power generation industry,

owing to its high creep strength and corrosion resistance [136, 137]. The typical chemical composition ranges of P91 are shown in Table 2.4, where the balance is Fe [138, 139]. The main alloying elements of P91 are Cr, Mo, and Ni. Cr provides corrosion resistance, while Mo increases resistance to pitting corrosion in chloride environments [140]. Ni improves the strength and hardness without sacrificing ductility and toughness.

Table 2.4. Typical chemical composition ranges of P91 steel (wt. %).

Cr	**Mo**	**Ni**	**C**	**Mn**	**P**
8.00-9.50	0.85-1.05	0.4 max	0.08-0.12	0.30-0.60	0.02 max
S	**Si**	**V**	**Nb**	**N**	**Al**
0.01 max	0.20-0.50	0.18-0.25	0.03-0.10	0.03-0.07	0.04 max

The microstructure of P91 is complex and hierarchical in nature, contributing to the high creep strength, consisting of prior austenite grains (PAG), packets, blocks and laths [101, 112], demarcated by high angle grain boundaries (HAGBs), as illustrated in Figure 1.1. Blocks are the regions demarcated by a misorientation angle of about 45° between adjacent blocks, with a typical size of about 4 μm in width [116]. Martensitic laths are the lowest substructure with high dislocation-density in P91 steel, with a typical width of about 0.7 μm [116]. Martensitic laths evolve into sub-grains when exposed to high temperature in long-term, with reduced dislocation-density [101]. Barrett et al. [101] proposed a physically-based high temperature yield strength model for P91 steels which includes the interdependent effects of dislocations, solutes, precipitates and grain boundaries based on the work of Panait [141, 142], Sauzay [117] and others [143, 144].

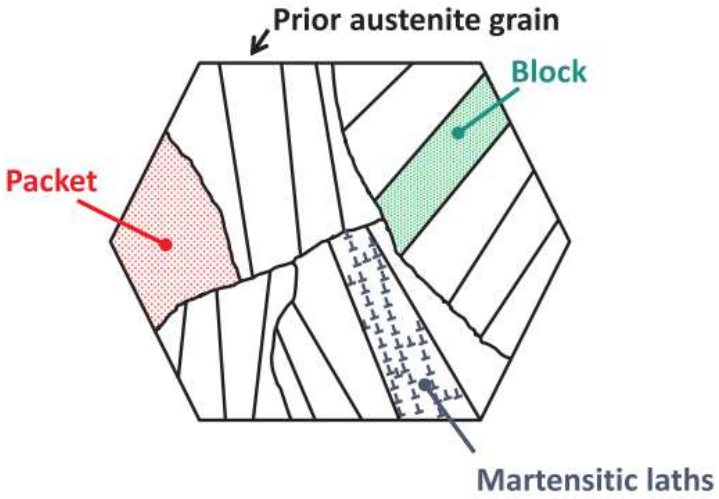

Figure 2.26. Hierarchical microstructure of P91 steel (R Barrett [101]).

P91 requires carefully-controlled heat treatment to achieve the desired microstructure and mechanical properties, specifically the required martensitic structure (full martensitic transformation occurs and the level of δ-ferrite is minimised to less than 8 %) which confers high temperature creep resistance [138, 139]. The heat treatment process for martensitic steel typically involves normalizing and tempering, as shown in Figure 2.27. Generally, the temperature for normalizing and tempering are 1000 to 1200 °C and around 730 to 780 °C, respectively.

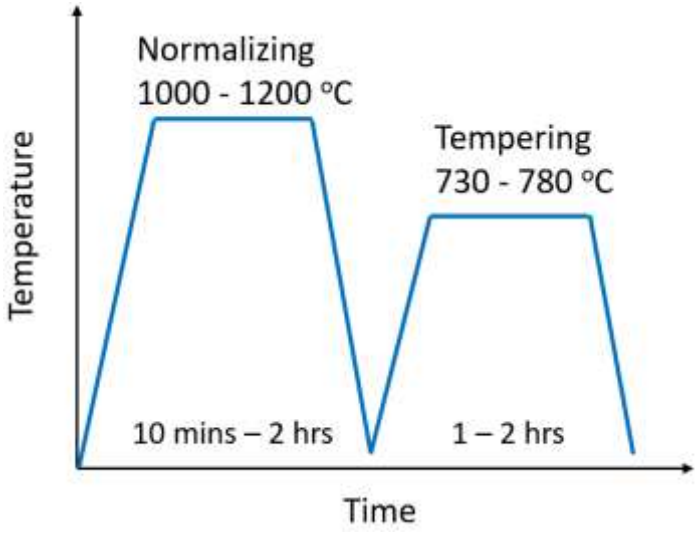

Figure 2.27. Heat treatment process in P91 steels.

Normalising heat-treatment involves heating the material to an elevated temperature and then allowing it to cool back to room temperature. Large austenite grains of approximately equal size throughout the steel are produced during the heating process, while martensite transformation happens during the cooling process, where the hierarchical microstructure with high dislocation density is formed, following by the tempering heat-treatment process. The $M_{23}C_6$ (M = Cr, Fe, Mo, W) carbides are dispersed along grain and lath boundaries and MX (M = Nb, V; X = C, N) carbonitrides within the martensitic lath interiors during tempering. They prevent dislocation motion, and further improve creep strength.

2.7.2 Materials for additive manufacturing

Ti-6Al-4V titanium alloy has been widely used for different applications (e.g. biomedical devices or aerospace) due to its high strength with low density, including fatigue strength, corrosion resistance and biocompatibility [35, 145]. Furthermore, it is one of the most popular metals utilised in additive manufacturing (AM) [146]. Table 2.5 shows the chemical composition of typical Ti-6Al-4V powder for AM [147]. The main alloying elements are Al and V, which contribute to hardening and provide phase stability. The alloying element Al stabilizes the hexagonal close packed (HCP) α phase, while V stabilizes the body centred cubic (BCC) β phase. Ti-6Al-4V is a dual phase (α + β) titanium alloy; various mixture of α + β microstructure can be obtained depending on the processing and heat treatment. Better mechanical properties can be obtained by different combinations of thermomechanical processing and heat treatment cycles which refine the alpha and beta phases [148].

Table 2.5. Chemical composition of typical Ti-6Al-4V powder used for AM (wt. %). The balance is Ti.

Al	V	O	N	C	H	Fe	Y
5.5-6.5	3.5-4.5	0.13	0.05	0.08	0.012	0.25	0.005

Figure 2.28 shows the scanning electron microscope (SEM) morphology of the typical Ti-6Al-4V powders for AM, which exhibit a spherical morphology. Ti-6Al-4V metal powders are classified into different grades based on the size and purity. The powder size of Ti-6Al-4V for the powder bed fusion (PBF) process is typically 20 to 40 μm, while that for the directed energy deposition (DED) process is 45 to 150 μm [149]. The densification of final AM samples is dependent on the particle size [150]. Moreover, high-purity metal powders are required for producing AM parts with desirable mechanical properties [151].

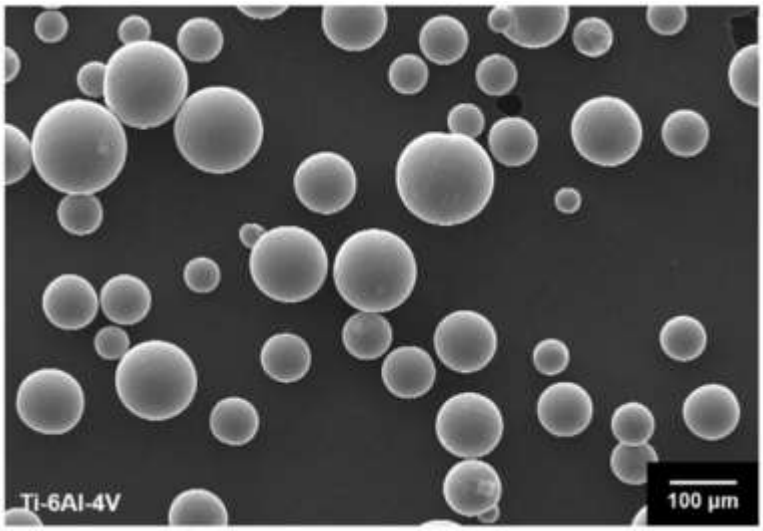

Figure 2.28. SEM morphology of the Ti-6Al-4V powder [145].

The phase diagram of titanium with 6wt% aluminium is shown in Figure 2.29. The microstructure of AM Ti-6Al-4V components usually consists of columnar prior β-grains containing colony and/or basket-weave α + β with martensite [152]. The β transition temperature of Ti-6Al-4V depends on the content of V (see Figure 2.29). The volume fraction of β phase is about 100% when the temperature is higher than 994°C (i.e. β transus point) [153]. Solid-state phase transformation from prior β to α happens during the cooling process. Furthermore, the transformation from β phase to α' phase (hcp martensite) is observed when Ti-6Al-4V alloy passes through M_s (martensite start temperature) upon quenching from all β region. Figure 2.30 presents the optical micrograph of an as-built PBF Ti-6Al-4V sample, which is dominated by the fine needle-shaped α' martensite phase. Rafi et al. [154] investigated the effect of cooling rate on microstructural evolution of Ti-

6Al-4V using two different metal additive manufacturing processes, SLM and electron beam melting (EBM). Their results show that the microstructure of SLM parts are composed of an α' martensitic phase, while the EBM parts contain primarily α and a small amount of β phase.

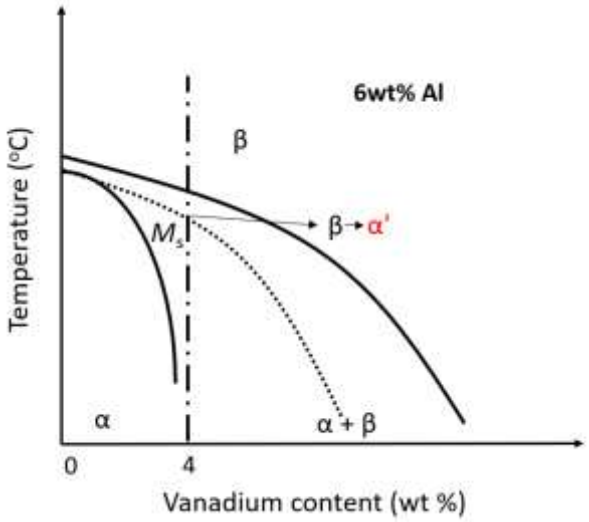

Figure 2.29. Phase diagram of titanium with 6wt% Al.

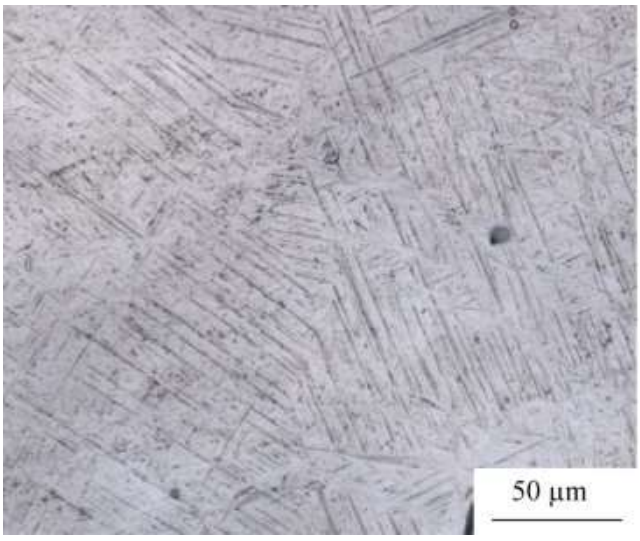

Figure 2.30. Optical micrograph of as-built PBF Ti-6Al-4V revealing α' martensite phase [155].

Nickle-based superalloy Inconel 625 is another commonly used metal for AM. It is mainly used in the aerospace and marine industry, particularly for gas turbine components, due to its high strength and excellent corrosion resistance in harsh environments [156, 157]. Moreover, it can maintain structural integrity and mechanical performance even at high temperature conditions (from cryogenic to approximately 1000 °C) [158, 159]. The entire chemical composition of typical Inconel 625 powder for AM is provided in Table 2.6, and the balance is Ni [160]. High level of Cr and Mo content contributes to the excellent corrosion resistance. The addition of Ti and Al content is mainly used for refining purposes to improve the weldability of the material [161].

Table 2.6. Chemical composition of typical Inconel 625 powder (wt. %). The balance is Ni.

Cr	**Mo**	**Fe**	**Nb**	**Co**	**Cu**	**Mn**
20.0-23.0	8.0-10.0	5.0 max	3.15-4.15	1.0 max	0.5 max	0.5 max
Si	**Al**	**Ti**	**C**	**Ta**	**P**	**Al**
0.5 max	0.4 max	0.4 max	0.1 max	0.05 max	0.015 max	0.015 max

The SEM morphology of the typical Inconel 625 powder for AM is shown in Figure 2.31, displaying a spherical morphology with the presence of minor satellites. The Inconel 625 powder size for PBF process is typically 15 to 45 μm, while that for DED process is 45 to 150 μm [162].

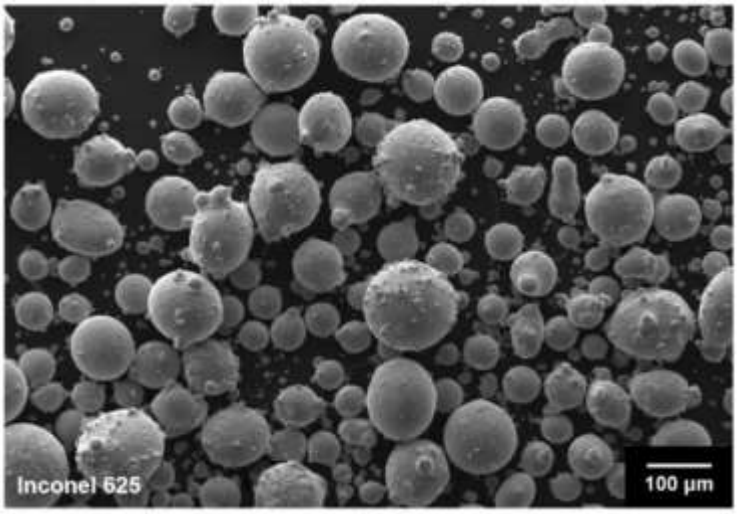

Figure 2.31. SEM morphology of the Inconel 625 powder [145].

The microstructure of AM Inconel 625 samples consist of columnar grains (CG) along the building direction, as illustrated in Figure 2.32. The size distribution of these CGs is large, with a maximum of about 350-400 µm and a minimum of about 5-10 µm [163]. The formation of non-equilibrium phases and exhibition of dendritic structures oriented in the build direction are commonly observed in as-built Inconel 625 due to the high temperature gradient and cooling rate during the AM process [164, 165]. The cellular structure is considered to be the primary dendritic structure altered by extremely high cooling rates. Dinda et al. [166] investigated the microstructure and material properties of DED Inconel 625 samples using optical microscopy, SEM, X-ray diffraction and microhardness tests, demonstrating that Inconel 625 could be a suitable material for AM as all samples produced were defect-free.

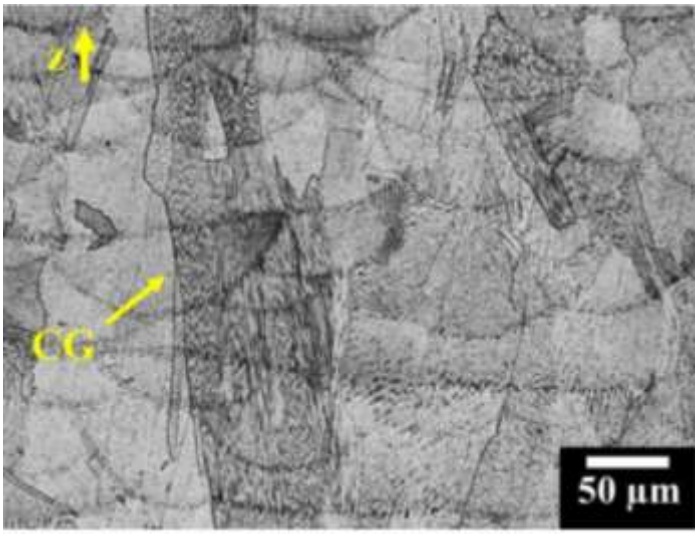

Figure 2.32. Optical micrograph of as-built PBF Inconel 625 showing columnar grains [163].

Stainless steel 316L is the other one of the most widely used material for AM given its characteristics of good mechanical properties and excellent corrosion resistance [167, 168]. This alloy is suitable for various applications (e.g. petrochemical, nuclear and medical implants) [169, 170]. The chemical composition of typical SS316L powder for AM is shown in Table 2.7, and the balance is made up of Fe [171]. High amount of Cr and Ni are contained in this alloy. Cr is important for maintaining excellent corrosion resistance while Ni stabilizes the austenite phase by balancing the effect of chromium. The low C content in this alloy makes it more difficult for carbides to precipitate, which could reduce its corrosion resistance and mechanical properties.

Table 2.7. Chemical composition of typical SS316L powder (wt. %). The balance is Fe.

Cr	Ni	Mo	Mn	Si
18	14	3	2 max	1 max
N	**O**	**P**	**C**	**S**
0.1 max	0.1 max	0.045 max	0.03 max	0.03 max

Figure 2.33 shows the SEM morphology of the typical SS316L powder for AM. Most particles are perfectly spherical except that some contain occasional satellites. The

SS316L powder in the diameter range of 5-45 μm and 50-150 μm are commonly used for PBF and DED processes, respectively [172].

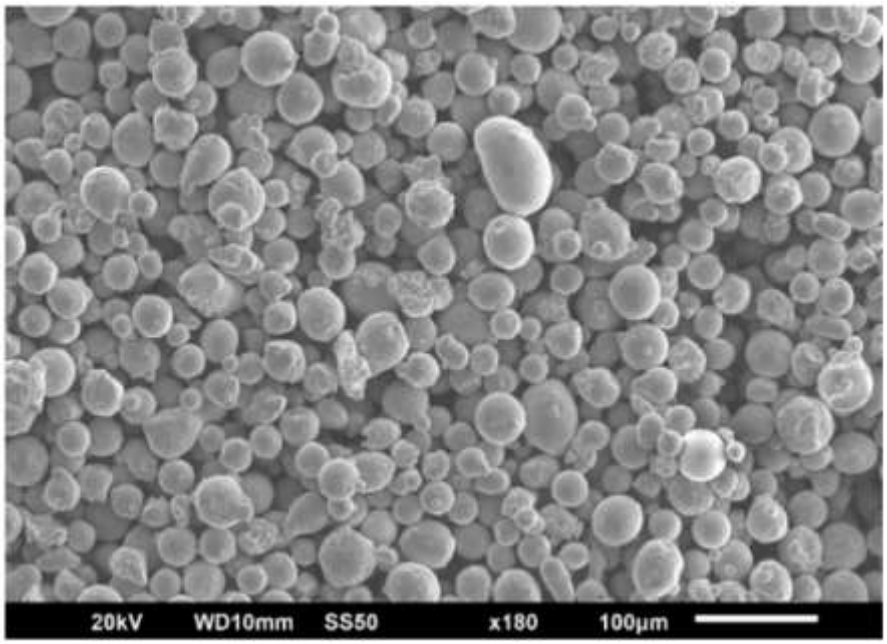

Figure 2.33. SEM morphology of SS316L powder [171].

SS316L is a variant of austenitic stainless steel consisting of a γ-austenitic FCC lattice structure. The optical micrograph of as-built PBF SS316L is provided in Figure 2.34, which showing complex solidification microstructure commonly observed in AM fabricated SS316L parts [173, 174]. Typical melt pool feature can be observed. The grains are elongated along the building direction and epitaxially grown on the melt pool boundaries. The average grain size determined from PBF SS316L is relatively smaller than the typical grain size observed in conventionally produced SS316L (viz. 17 μm compared to 30-60 μm) [175]. Wang et al. investigated the development of grain structure of PBF SS316L parts, highlighting that different crystallization types can be found in different regions of melt pool due to impact of various temperature gradients, and higher thermal input will result in coarser cell structure [176].

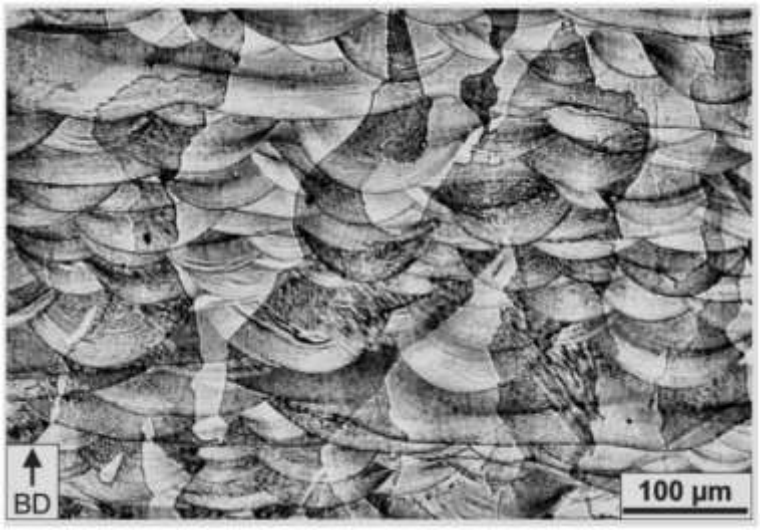

Figure 2.34. Optical micrograph of as-built PBF SS316L [177].

2.8 Conclusions

The literature review chapter summarises the studied materials, welding and additive manufacturing process and corresponding problems, and numerical methodologies relevant to modelling the welding and additive manufacturing process. A review of material behaviour modelling and failure has been carried out to provide a background for the research presented in this thesis. The work in the literature can be summarised as:

- Numerical models for simulating additive manufacturing process at process-level and component-level.
- Numerical analysis of welding, including process modelling and representative specimen development.
- Development of modelling methods for characterizing material behaviours.
- Development of life prediction models for fatigue failure.

However, clear gaps in the literature exist relating to the following aspects:

- Development and validation of a computationally-efficient method for three-dimensional FE simulation of AM (e.g. DED, PBF) of realistic components (e.g. with complex geometrical features, such as in conformally-cooled injection moulding dies) for accurate and reliable prediction of temperature histories (e.g.

for microstructure prediction), and residual stresses and deformations, e.g. for fatigue life prediction.

- Development of efficient FE-based methods for investigation of methods for mitigation of residual stresses and distortion (e.g. scanning strategies, preheating) for realistic, complex-geometry components. .
- Development of physically-based method for effects of welding (e.g. microstructure inhomogeneity) on fatigue crack initiation in welded connections, such as those used in high temperature 9Cr steels for next generation high flexibility, high efficiency power plant.

In summary, there are two visible aspects of this thesis: (i) metal additive manufacturing, i.e. DED and PBF; (ii) welding. The metal additive manufacturing aspect is from the I-Form project, of which one of the objectives is to develop a computational platform for multi-scale, multi-physics AM modelling; however, the work so far in I-Form is focussed mainly on single track or single or few layers and thus is not directly applicable to real component manufacture. Thus, a clear gap was identified in relation to FE modelling for AM of real complex components, but still with physically-based accuracy with respect to thermal histories (for microstructure evolution prediction) and residual stress and distortion prediction (Chapter 3 and 4). The welding aspect is from the MECHANNICS project, of which one of the objectives is to develop an integrated multi-scale process modelling and life prediction methodology for next generation welded connections. It is essential to state that process modelling of the welding had already been completed by Spyridon A. Alexandratos [178] and Padraig Mac Ardghail [70] in MECHANNICS. A key gap, however, existed is completing the PB modelling method developed by Richard Barrett [101, 112], to investigate the effects of manufacturing on FCI for welded power plant connections (Chapter 5). This is critical for design of reliable next generation power plant.

2.9 References

[1] AWS, Code for Arc and Gas Welding in Building Construction, American Welding Society1990.

[2] D. Varshney, K. Kumar, Structured review of papers on the use of different activating flux and welding techniques, Ain Shams Engineering Journal 12(3) (2021) 3339-3351.
[3] B. Raj, S. Saroja, K. Laha, T. Karthikeyan, M. Vijayalakshmi, K. Bhanu Sankara Rao, Methods to overcome embrittlement problem in 9Cr–1Mo ferritic steel and its weldment, Journal of Materials Science 44(9) (2009) 2239-2246.
[4] B. Arivazhagan, M. Kamaraj, Metal-cored arc welding process for joining of modified 9Cr-1Mo (P91) steel, Journal of Manufacturing Processes 15(4) (2013) 542-548.
[5] Q. Yang, P. Zhang, L. Cheng, Z. Min, M. Chyu, A.C. To, Finite element modeling and validation of thermomechanical behavior of Ti-6Al-4V in directed energy deposition additive manufacturing, Additive Manufacturing 12 (2016) 169-177.
[6] C. Baykasoglu, O. Akyildiz, D. Candemir, Q. Yang, A.C. To, Predicting Microstructure Evolution During Directed Energy Deposition Additive Manufacturing of Ti-6Al-4V, Journal of Manufacturing Science and Engineering 140(5) (2018) 051003.
[7] J. Mazumder, Laser-aided direct metal deposition of metals and alloys, Elsevier2017.
[8] D. Kotoban, S. Grigoriev, I. Shishkovsky, Study of 3D laser cladding for Ni85Al15 superalloy, Physics Procedia 56 (2014) 262-268.
[9] M. Dinovitzer, X. Chen, J. Laliberte, X. Huang, H. Frei, Effect of wire and arc additive manufacturing (WAAM) process parameters on bead geometry and microstructure, Additive Manufacturing 26 (2019) 138-146.
[10] D. Svetlizky, M. Das, B. Zheng, A.L. Vyatskikh, S. Bose, A. Bandyopadhyay, J.M. Schoenung, E.J. Lavernia, N. Eliaz, Directed energy deposition (DED) additive manufacturing: Physical characteristics, defects, challenges and applications, Materials Today 49 (2021) 271-295.
[11] P.V. Cobbinah, R.A. Nzeukou, O.T. Onawale, W.R. Matizamhuka, Laser powder bed fusion of potential superalloys: a review, Metals 11(1) (2020) 58.
[12] A. Mazzoli, Selective laser sintering in biomedical engineering, Medical & Biological Engineering & Computing 51(3) (2013) 245-256.
[13] C.Y. Yap, C.K. Chua, Z.L. Dong, Z.H. Liu, D.Q. Zhang, L.E. Loh, S.L. Sing, Review of selective laser melting: Materials and applications, Applied Physics Reviews 2(4) (2015) 041101.
[14] K.V. Venkatesh, V.V. Nandini, Direct metal laser sintering: a digitised metal casting technology, The Journal of Indian Prosthodontic Society 13(4) (2013) 389-392.
[15] C. Körner, Additive manufacturing of metallic components by selective electron beam melting—a review, International Materials Reviews 61(5) (2016) 361-377.
[16] V. Bhavar, P. Kattire, V. Patil, S. Khot, K. Gujar, R. Singh, A review on powder bed fusion technology of metal additive manufacturing, Additive Manufacturing Handbook (2017) 251-253.
[17] D.-G. Ahn, Directed energy deposition (DED) process: state of the art, International Journal of Precision Engineering and Manufacturing-Green Technology 8(2) (2021) 703-742.
[18] D. Abson, J. Rothwell, Review of type IV cracking of weldments in 9–12% Cr creep strength enhanced ferritic steels, International Materials Reviews 58(8) (2013) 437-473.
[19] K. Laha, K. Chandravathi, P. Parameswaran, K. Rao, S. Mannan, Characterization of microstructures across the heat-affected zone of the modified 9Cr-1Mo weld joint to understand its role in promoting type IV cracking, Metallurgical and Materials Transactions A 38(1) (2007) 58-68.

[20] R.A. Barrett, Experimental characterisation and computational constitutive modelling of high temperature degradation in 9Cr steels including microstructural effects, National University of Ireland, Galway, 2016.
[21] P.J. Withers, H. Bhadeshia, Residual stress. Part 2–Nature and origins, Materials Science and Technology 17(4) (2001) 366-375.
[22] G.S. Schajer, C.O. Ruud, Overview of residual stresses and their measurement, Practical Residual Stress Measurement Methods (2013) 1-27.
[23] J. Everaerts, X. Song, B. Nagarajan, A.M. Korsunsky, Evaluation of macro-and microscopic residual stresses in laser shock-peened titanium alloy by FIB-DIC ring-core milling with different core diameters, Surface and Coatings Technology 349 (2018) 719-724.
[24] N. Levkulich, S. Semiatin, J. Gockel, J. Middendorf, A. DeWald, N. Klingbeil, The effect of process parameters on residual stress evolution and distortion in the laser powder bed fusion of Ti-6Al-4V, Additive Manufacturing 28 (2019) 475-484.
[25] P. Mercelis, J.P. Kruth, Residual stresses in selective laser sintering and selective laser melting, Rapid Prototyping Journal 12 (2006) 254-265.
[26] T. Simson, A. Emmel, A. Dwars, J. Böhm, Residual stress measurements on AISI 316L samples manufactured by selective laser melting, Additive Manufacturing 17 (2017) 183-189.
[27] L. Cheng, A. To, Part-scale build orientation optimization for minimizing residual stress and support volume for metal additive manufacturing: Theory and experimental validation, Computer-Aided Design 113 (2019) 1-23.
[28] S. Mohd Yusuf, S. Cutler, N. Gao, The impact of metal additive manufacturing on the aerospace industry, Metals 9(12) (2019) 1286.
[29] E. Alabort, D. Barba, R.C. Reed, Design of metallic bone by additive manufacturing, Scripta Materialia 164 (2019) 110-114.
[30] S. Maddox, Fatigue design rules for welded structures, Fracture and fatigue of welded joints and structures, Elsevier2011.
[31] D. Deng, H. Murakawa, Prediction of welding residual stress in multi-pass butt-welded modified 9Cr–1Mo steel pipe considering phase transformation effects, Computational Materials Science 37(3) (2006) 209-219.
[32] T.P. Farragher, Thermomechanical analysis of P91 power plant components, Materials Science and Engineering: A 437 (2014) 183-196.
[33] W. Zhang, M. Tong, N.M. Harrison, Multipart Build Effects on Temperature and Residual Stress by Laser Beam Powder Bed Fusion Additive Manufacturing, 3D Printing and Additive Manufacturing (2021).
[34] J. Goldak, A. Chakravarti, M. Bibby, A new finite element model for welding heat sources, Metallurgical transactions B 15(2) (1984) 299-305.
[35] C. Baykasoğlu, O. Akyildiz, M. Tunay, A.C. To, A process-microstructure finite element simulation framework for predicting phase transformations and microhardness for directed energy deposition of Ti6Al4V, Additive Manufacturing 35 (2020) 101252.
[36] X. Song, S. Feih, W. Zhai, C.-N. Sun, F. Li, R. Maiti, J. Wei, Y. Yang, V. Oancea, L. Romano Brandt, A.M. Korsunsky, Advances in additive manufacturing process simulation: Residual stresses and distortion predictions in complex metallic components, Materials & Design 193 (2020) 108779.
[37] P. Michaleris, Modeling metal deposition in heat transfer analyses of additive

manufacturing processes, Finite Elements in Analysis and Design 86 (2014) 51-60.
[38] A. Nycz, Y. Lee, M. Noakes, D. Ankit, C. Masuo, S. Simunovic, J. Bunn, L. Love, V. Oancea, A. Payzant, C.M. Fancher, Effective residual stress prediction validated with neutron diffraction method for metal large-scale additive manufacturing, Materials & Design 205 (2021) 109751.
[39] E.O. Olakanmi, K.W. Dalgarno, R.F. Cochrane, Laser sintering of blended Al ‐ Si powders, Rapid Prototyping Journal 18(2) (2012) 109-119.
[40] P. Ferro, R. Meneghello, G. Savio, F. Berto, A modified volumetric energy density–based approach for porosity assessment in additive manufacturing process design, The International Journal of Advanced Manufacturing Technology 110 (2020) 1911-1921.
[41] Z. Sun, X. Tan, S.B. Tor, W.Y. Yeong, Selective laser melting of stainless steel 316L with low porosity and high build rates, Materials & Design 104 (2016) 197-204.
[42] S. Clijsters, T. Craeghs, S. Buls, K. Kempen, J.-P. Kruth, In situ quality control of the selective laser melting process using a high-speed, real-time melt pool monitoring system, The International Journal of Advanced Manufacturing Technology 75 (2014) 1089-1101.
[43] J. Farkas, K. Jármai, Special cases of the calculation of residual welding distortions, Welding in the World 51 (2007) 69-73.
[44] C. Li, J.F. Liu, X.Y. Fang, Y.B. Guo, Efficient predictive model of part distortion and residual stress in selective laser melting, Additive Manufacturing 17 (2017) 157-168.
[45] M. Narvan, A. Ghasemi, E. Fereiduni, S. Kendrish, M. Elbestawi, Part deflection and residual stresses in laser powder bed fusion of H13 tool steel, Materials & Design 204 (2021) 109659.
[46] S.-H. Kim, J.-B. Kim, W.-J. Lee, Numerical prediction and neutron diffraction measurement of the residual stresses for a modified 9Cr–1Mo steel weld, Journal of Materials Processing Technology 209(8) (2009) 3905-3913.
[47] A. Hussein, L. Hao, C. Yan, R. Everson, Finite element simulation of the temperature and stress fields in single layers built without-support in selective laser melting, Materials & Design (1980-2015) 52 (2013) 638-647.
[48] N. Hodge, R. Ferencz, J. Solberg, Implementation of a thermomechanical model in diablo for the simulation of selective laser melting, Lawrence Livermore National Laboratory, Livermore, CA (United States), 2013.
[49] W.D. Rolph III, K.J. Bathe, An efficient algorithm for analysis of nonlinear heat transfer with phase changes, International Journal for Numerical Methods in Engineering 18(1) (1982) 119-134.
[50] X. Yang, R.A. Barrett, M. Tong, N.M. Harrison, S.B. Leen, Towards a process-structure model for Ti-6Al-4V during additive manufacturing, Journal of Manufacturing Processes 61 (2021) 428-439.
[51] Abaqus Analysis User's Guide, Dassault Systemes (2018).
[52] B. Cheng, S. Shrestha, K. Chou, Stress and deformation evaluations of scanning strategy effect in selective laser melting, Additive Manufacturing 12 (2016) 240-251.
[53] Y. Li, K. Zhou, P. Tan, S.B. Tor, C.K. Chua, K.F. Leong, Modeling temperature and residual stress fields in selective laser melting, International Journal of Mechanical Sciences 136 (2018) 24-35.
[54] M.F. Zaeh, G. Branner, Investigations on residual stresses and deformations in selective laser melting, Production Engineering 4(1) (2010) 35-45.
[55] R.A. Barrett, T. Etienne, C. Duddy, N.M. Harrison, Residual stress prediction in a

powder bed fusion manufactured Ti6Al4V hip stem, AIP Conference Proceedings 1896 (2017) 040018.
[56] W. Zhang, M. Tong, N.M. Harrison, Resolution, energy and time dependency on layer scaling in finite element modelling of laser beam powder bed fusion additive manufacturing, Additive Manufacturing 28 (2019) 610-620.
[57] C. Chen, S. Chang, J. Zhu, Z. Xiao, H. Zhu, X. Zeng, Residual stress of typical parts in laser powder bed fusion, Journal of Manufacturing Processes 59 (2020) 621-628.
[58] P. Promoppatum, V. Uthaisangsuk, Part scale estimation of residual stress development in laser powder bed fusion additive manufacturing of Inconel 718, Finite Elements in Analysis and Design 189 (2021) 103528.
[59] M. Bayat, C.G. Klingaa, S. Mohanty, D. De Baere, J. Thorborg, N.S. Tiedje, J.H. Hattel, Part-scale thermo-mechanical modelling of distortions in Laser Powder Bed Fusion – Analysis of the sequential flash heating method with experimental validation, Additive Manufacturing 36 (2020) 101508.
[60] R.J. Williams, C.M. Davies, P.A. Hooper, A pragmatic part scale model for residual stress and distortion prediction in powder bed fusion, Additive Manufacturing 22 (2018) 416-425.
[61] J.P. Pragana, I.M. Bragança, L. Reis, C.M. Silva, P.A. Martins, Formability of wire-arc deposited AISI 316L sheets for hybrid additive manufacturing applications, Proceedings of the Institution of Mechanical Engineers, Part L: Journal of Materials: Design and Applications 235(12) (2021) 2839-2850.
[62] S. Wen, P. Hilton, D. Farrugia, Finite element modelling of a submerged arc welding process, Journal of Materials Processing Technology 119(1-3) (2001) 203-209.
[63] A. Sullivan, J.D. Robson, H.R. Shercliff, G. McShane, Process modelling of friction stir welding for aerospace aluminium alloys, Advanced Materials Research 15 (2007) 351-356.
[64] E. Ceretti, L. Fratini, C. Giardini, D. La Spisa, Numerical modelling of the linear friction welding process, International Journal of Material Forming 3(1) (2010) 1015-1018.
[65] C. Bühr, P.A. Colegrove, A.R. McAndrew, A computationally efficient thermal modelling approach of the linear friction welding process, Journal of Materials Processing Technology 252 (2018) 849-858.
[66] W. Li, F. Wang, S. Shi, T. Ma, Performance, Numerical simulation of linear friction welding based on ABAQUS environment: Challenges and perspectives, Journal of Materials Engineering and Performance 23(2) (2014) 384-390.
[67] T.R. Lima, S.M. Tavares, P.M. De Castro, Residual stress field and distortions resulting from welding processes: numerical modelling using Sysweld, Ciência & Tecnologia dos Materiais 29(1) (2017) 56-61.
[68] A. Capriccioli, P. Frosi, Multipurpose ANSYS FE procedure for welding processes simulation, Fusion Engineering and Design 84(2-6) (2009) 546-553.
[69] A.H. Yaghi, T.H. Hyde, A.A. Becker, J.A. Williams, W. Sun, Residual stress simulation in welded sections of P91 pipes, Journal of Materials Processing Technology 167(2-3) (2005) 480-487.
[70] P. Mac Ardghail, N. Harrison, S.B. Leen, A through-process, thermomechanical model for predicting welding-induced microstructure evolution and post-weld high-temperature fatigue response, International Journal of Fatigue 112 (2018) 216-232.

[71] H. Vemanaboina, S. Akella, R.K. Buddu, Welding Process Simulation Model for Temperature and Residual Stress Analysis, Procedia Materials Science 6 (2014) 1539-1546.
[72] M. Li, R.A. Barrett, S. Scully, N.M. Harrison, S.B. Leen, P.E. O'Donoghue, Cyclic plasticity of welded P91 material for simple and complex power plant connections, International Journal of Fatigue 87 (2016) 391-404.
[73] T.P. Farragher, S. Scully, N. O'Dowd, C.J. Hyde, S. Leen, High temperature, low cycle fatigue characterization of P91 weld and heat affected zone material, Journal of Pressure Vessel Technology 136(2) (2014) 021403.
[74] H. Bhadeshia, Models for the elementary mechanical properties of steel welds, Institute of materials, London 650 (1997) 229-284.
[75] V. Shankar, B. AK, Comparative evaluation of tensile properties of simulated heat affected zones of P91 steel weld joint, Materials at High Temperatures 37(2) (2020) 114-128.
[76] C. Pandey, M. Mahapatra, P. Kumar, N. Saini, A. Srivastava, Microstructure and mechanical property relationship for different heat treatment and hydrogen level in multi-pass welded P91 steel joint, Journal of Manufacturing Processes 28 (2017) 220-234.
[77] C. Pandey, The Characterization of Soft Fine‐Grained Heat‐Affected Zones in P91 Weldments under Creep Exposure Conditions, Steel Research International 91(1) (2019) 1900342.
[78] T.H. Hyde, W. Sun, Determining high temperature properties of weld materials, JSME International Journal Series A Solid Mechanics and Material Engineering 43(4) (2000) 408-414.
[79] M. Touboul, J. Crepin, G. Rousselier, F. Latourte, S. Leclercq, Identification of Local Viscoplastic Properties in P91 Welds from Full Field Measurements at Room Temperature and 625 °C, Experimental Mechanics 53(3) (2012) 455-468.
[80] F. Dunne, N. Petrinic, Introduction to computational plasticity, OUP Oxford2005.
[81] A.S. Khan, S. Huang, Continuum theory of plasticity, John Wiley & Sons1995.
[82] J. Chaboche, G. Rousselier, On the plastic and viscoplastic constitutive equations—Part I: Rules developed with internal variable concept, Journal of Pressure Vessel Technology 105 (1983) 153–158.
[83] J.-L. Chaboche, G. Rousselier, On the plastic and viscoplastic constitutive equations—Part II: application of internal variable concepts to the 316 stainless steel, Journal of Pressure Vessel Technology 105 (1983) 159-164.
[84] A. Saad, C.J. Hyde, W. Sun, T. Hyde, Thermal-mechanical fatigue simulation of a P91 steel in a temperature range of 400–600 C, Materials at High Temperatures 28(3) (2011) 212-218.
[85] J. Kichenin, K. Van Dang, K. Boytard, Finite-element simulation of a new two-dissipative mechanisms model for bulk medium-density polyethylene, Journal of Materials Science 31(6) (1996) 1653-1661.
[86] S.B. Leen, A. Deshpande, T.H. Hyde, Experimental and numerical characterization of the cyclic thermomechanical behavior of a high temperature forming tool alloy, Journal of Manufacturing Science and Engineering 132(5) (2010) 051013.
[87] F.H. Norton, The creep of steel at high temperatures, McGraw-Hill Book Company1929.
[88] D.-F. Li, N.P. O'Dowd, Investigating ductile failure at the microscale in engineering

steels: A micromechanical finite element model, Pressure Vessels and Piping Conference 55058 (2012) 137-143.
[89] T. Kazerani, J. Zhao, A microstructure-based model to characterize micromechanical parameters controlling compressive and tensile failure in crystallized rock, Rock Mechanics and Rock Engineering 47(2) (2014) 435-452.
[90] S. Gao, S. Geng, P. Jiang, G. Mi, C. Han, L. Ren, Numerical analysis of the deformation behavior of 2205 duplex stainless steel TIG weld joint based on the microstructure and micro-mechanical properties, Materials Science Engineering: A 815 (2021) 141303.
[91] T. Hochrainer, S. Sandfeld, M. Zaiser, P. Gumbsch, Continuum dislocation dynamics: towards a physical theory of crystal plasticity, Journal of the Mechanics Physics of Solids 63 (2014) 167-178.
[92] C.-S. Han, H. Gao, Y. Huang, W.D. Nix, Mechanism-based strain gradient crystal plasticity—I. Theory, Journal of the Mechanics Physics of Solids 53(5) (2005) 1188-1203.
[93] F. Dunne, R. Kiwanuka, A. Wilkinson, Crystal plasticity analysis of micro-deformation, lattice rotation and geometrically necessary dislocation density, Proceedings of the Royal Society A: Mathematical, Physical Engineering Sciences 468(2145) (2012) 2509-2531.
[94] D.-F. Li, R.A. Barrett, P.E. O'Donoghue, N.P. O'Dowd, S.B. Leen, A multi-scale crystal plasticity model for cyclic plasticity and low-cycle fatigue in a precipitate-strengthened steel at elevated temperature, Journal of the Mechanics and Physics of Solids 101 (2017) 44-62.
[95] N.G. Prastiti, Y. Xu, D.S. Balint, F.P. Dunne, Discrete dislocation, crystal plasticity and experimental studies of fatigue crack nucleation in single-crystal nickel, International Journal of Plasticity 126 (2020) 102615.
[96] R. Hill, J. Rice, Constitutive analysis of elastic-plastic crystals at arbitrary strain, Journal of the Mechanics Physics of Solids 20(6) (1972) 401-413.
[97] R.J. Asaro, J. Rice, Strain localization in ductile single crystals, Journal of the Mechanics Physics of Solids 25(5) (1977) 309-338.
[98] D. Peirce, R.J. Asaro, A. Needleman, Material rate dependence and localized deformation in crystalline solids, Acta metallurgica 31(12) (1983) 1951-1976.
[99] C. Liu, P. Shanthraj, M. Diehl, F. Roters, S. Dong, J. Dong, W. Ding, D. Raabe, An integrated crystal plasticity–phase field model for spatially resolved twin nucleation, propagation, and growth in hexagonal materials, International Journal of Plasticity 106 (2018) 203-227.
[100] J. Segurado, R.A. Lebensohn, J. LLorca, Computational homogenization of polycrystals, Advances in Applied Mechanics 51 (2018) 1-114.
[101] R.A. Barrett, P.E. O'Donoghue, S.B. Leen, A physically-based high temperature yield strength model for 9Cr steels, Materials Science and Engineering: A 730 (2018) 410-424.
[102] U.F. Kocks, A.S. Argon, M.F. Ashby, Thermodynamics and kinetics of slip, Pergamon Press1975.
[103] F. Nabarro, Dislocations in a simple cubic lattice, Proceedings of the Physical Society 59(2) (1947) 256.
[104] S. Sakui, T. Sakai, The effect of strain rate, temperature and grain size on the lower yield stress and flow stress of polycrystalline pure iron, Tetsu-to-Hagané 58(10) (1972)

1438-1455.
[105] S. Spigarelli, M. El Mehtedi, D. Ciccarelli, M. Regev, Effect of grain size on high temperature deformation of AZ31 alloy, Materials Science and Engineering: A 528(22-23) (2011) 6919-6926.
[106] K. Maruyama, K. Sawada, J.-i. Koike, Strengthening mechanisms of creep resistant tempered martensitic steel, ISIJ International 41(6) (2001) 641-653.
[107] J. Naylor, The influence of the lath morphology on the yield stress and transition temperature of martensitic-bainitic steels, Metallurgical Transactions A 10(7) (1979) 861-873.
[108] Q. Zhao, B. Holmedal, Y. Li, E. Sagvolden, O.M. Løvvik, Multi-component solid solution and cluster hardening of Al–Mn–Si alloys, Materials Science and Engineering: A 625 (2015) 153-157.
[109] G. Krauss, Martensite in steel: strength and structure, Materials Science and Engineering: A 273 (1999) 40-57.
[110] M. Ashby, Proceedings of the Second Bolton Landing Conference on Oxide Dispersion Strengthening, Science Publishers New York, 1968.
[111] P.-F. Giroux, Experimental study and simulation of cyclic softening of tempered martensite ferritic steels, École Nationale Supérieure des Mines de Paris, 2011.
[112] R.A. Barrett, P.E. O'Donoghue, S.B. Leen, A physically-based constitutive model for high temperature microstructural degradation under cyclic deformation, International Journal of Fatigue 100 (2017) 388-406.
[113] Q. Li, Modeling the microstructure–mechanical property relationship for a 12Cr–2W–V–Mo–Ni power plant steel, Materials Science and Engineering: A 361(1-2) (2003) 385-391.
[114] S. Maropoulos, N. Ridley, The dependence of mechanical properties on structure in low alloy steel forgings, Journal of Materials Science 40(18) (2005) 4753-4759.
[115] L. Tóth, S.Y. Yarema, Formation of the science of fatigue of metals. Part 1. 1825–1870, Materials Science 42(5) (2006) 673-680.
[116] M. Sauzay, H. Brillet, I. Monnet, M. Mottot, F. Barcelo, B. Fournier, A. Pineau, Cyclically induced softening due to low-angle boundary annihilation in a martensitic steel, Materials Science and Engineering: A 400 (2005) 241-244.
[117] M. Sauzay, B. Fournier, M. Mottot, A. Pineau, I. Monnet, Cyclic softening of martensitic steels at high temperature—Experiments and physically based modelling, Materials Science and Engineering: A 483 (2008) 410-414.
[118] V. Shankar, M. Valsan, K.B.S. Rao, R. Kannan, S.L. Mannan, S.D. Pathak, Low cycle fatigue behavior and microstructural evolution of modified 9Cr–1Mo ferritic steel, Materials Science and Engineering: A 437(2) (2006) 413-422.
[119] C.-H. Yu, A. Leicht, R.L. Peng, J. Moverare, Low cycle fatigue of additively manufactured thin-walled stainless steel 316L, Materials Science and Engineering: A 821 (2021).
[120] R. Alain, P. Violan, J. Mendez, Low cycle fatigue behavior in vacuum of a 316L type austenitic stainless steel between 20 and 600 C Part I: Fatigue resistance and cyclic behavior, Materials Science and Engineering: A 229(1-2) (1997) 87-94.
[121] M. Gerland, R. Alain, B.A. Saadi, J. Mendez, Low cycle fatigue behaviour in vacuum of a 316L-type austenitic stainless steel between 20 and 600 C—Part II: Dislocation structure evolution and correlation with cyclic behaviour, Materials Science

and Engineering: A 229(1-2) (1997) 68-86.
[122] M. Pham, C. Solenthaler, K. Janssens, S. Holdsworth, Dislocation structure evolution and its effects on cyclic deformation response of AISI 316L stainless steel, Materials Science and Engineering: A 528(7-8) (2011) 3261-3269.
[123] M.F. Ashby, D.R.H. Jones, Engineering Materials 1: An Introduction to Their Properties and Applications, Oxford, 1996.
[124] Coffin, Jr., L. F., A study of the effects of cyclic thermal stresses on a ductile metal, Transactions of the American Society of Mechanical Engineers 76(6) (1954) 931-949.
[125] S.S. Manson, Behavior of materials under conditions of thermal stress, National Advisory Committee for Aeronautics1953.
[126] O. Basquin, The exponential law of endurance tests, American Society for Testing and Materials Proceedings 10 (1910) 625-630.
[127] M.L. Martin, C. Looney, P. Bradley, D. Lauria, R. Amaro, A.J. Slifka, Unification of hydrogen-enhanced damage understanding through strain-life experiments for modeling, Engineering Fracture Mechanics 216 (2019) 106504.
[128] C.A. Sweeney, P.E. McHugh, J.P. McGarry, S.B. Leen, Micromechanical methodology for fatigue in cardiovascular stents, International Journal of Fatigue 44 (2012) 202-216.
[129] R.J. Devaney, P.E. O'Donoghue, S.B. Leen, Maintenance, Global and local fatigue analysis of X100 and X60 steel catenary riser girth welds, Journal of Structural Integrity and Maintenance 2(3) (2017) 181-189.
[130] K. Tanaka, T. Mura, A Dislocation Model for Fatigue Crack Initiation, Journal of Applied Mechanics 48(1) (1981) 97-103.
[131] X. Wu, On Tanaka-Mura's fatigue crack nucleation model and validation, Fatigue & Fracture of Engineering Materials & Structures 41(4) (2018) 894-899.
[132] R. Tryon, T. Cruse, A reliability ‐ based model to predict scatter in fatigue crack nucleation life, Fatigue & Fracture of Engineering Materials & Structures 21(3) (1998) 257-267.
[133] N. Jezernik, J. Kramberger, T. Lassen, S. Glodež, Numerical modelling of fatigue crack initiation and growth of martensitic steels, Fatigue & Fracture of Engineering Materials & Structures 33(11) (2010) 714-723.
[134] J. Kramberger, N. Jezernik, P. Göncz, S. Glodež, Extension of the Tanaka–Mura model for fatigue crack initiation in thermally cut martensitic steels, Engineering Fracture Mechanics 77(11) (2010) 2040-2050.
[135] T. Hoshide, K. Kusuura, Life prediction by simulation of crack growth in notched components with different microstructures and under multiaxial fatigue, Fatigue & Fracture of Engineering Materials & Structures 21(2) (1998) 201-213.
[136] R. Viswanathan, J. Henry, J. Tanzosh, G. Stanko, J. Shingledecker, B. Vitalis, R. Purgert, US program on materials technology for ultra-supercritical coal power plants, Journal of Materials Engineering and Performance 14(3) (2005) 281-292.
[137] A. Shibli, Performance of modern high strength steels (P91, P92) in high temperature plant, ASME Pressure Vessels and Piping Conference 42878 (2007) 161-170.
[138] R. Swindeman, M. Santella, P. Maziasz, B. Roberts, K. Coleman, Issues in replacing Cr–Mo steels and stainless steels with 9Cr–1Mo–V steel, International Journal of Pressure Vessels and Piping 81(6) (2004) 507-512.
[139] F. Abe, Analysis of creep rates of tempered martensitic 9% Cr steel based on

microstructure evolution, Materials Science and Engineering: A 510 (2009) 64-69.
[140] H.-Y. Ha, T.-H. Lee, J.-H. Bae, D.W. Chun, Molybdenum effects on pitting corrosion resistance of FeCrMnMoNC austenitic stainless steels, Metals 8(8) (2018) 653.
[141] C. Panait, W. Bendick, A. Fuchsmann, A.-F. Gourgues-Lorenzon, J. Besson, Study of the microstructure of the Grade 91 steel after more than 100,000 h of creep exposure at 600 C, International Journal of Pressure Vessels and Piping 87(6) (2010) 326-335.
[142] C.G. Panait, A. Zielińska-Lipiec, T. Koziel, A. Czyrska-Filemonowicz, A.-F. Gourgues-Lorenzon, W. Bendick, Evolution of dislocation density, size of subgrains and MX-type precipitates in a P91 steel during creep and during thermal ageing at 600 C for more than 100,000 h, Materials Science and Engineering: A 527(16-17) (2010) 4062-4069.
[143] S. Prasad, V. Rajkumar, H.K. KC, Numerical simulation of precipitate evolution in ferritic–martensitic power plant steels, Calphad 36 (2012) 1-7.
[144] F. Abe, Precipitate design for creep strengthening of 9% Cr tempered martensitic steel for ultra-supercritical power plants, Science and Technology of advanced materials 9(1) (2008) 013002.
[145] F. Lia, J.Z. Park, J.S. Keist, S. Joshi, R.P. Martukanitz, Thermal and microstructural analysis of laser-based directed energy deposition for Ti-6Al-4V and Inconel 625 deposits, Materials Science and Engineering: A 717 (2018) 1-10.
[146] H.D. Nguyen, A. Pramanik, A. Basak, Y. Dong, C. Prakash, S. Debnath, S. Shankar, I. Jawahir, S. Dixit, D. Buddhi, A critical review on additive manufacturing of Ti-6Al-4V alloy: microstructure and mechanical properties, Journal of Materials Research and Technology 18(4641) (2022) 4661.
[147] X. Yang, R.A. Barrett, N.M. Harrison, S.B. Leen, A physically-based structure-property model for additively manufactured Ti-6Al-4V, Materials & Design 205 (2021) 109709.
[148] P.P. Singh, R. Gupta, V. Anil Kumar, R.C. Gundakaram, S.K. Singh, Tailoring the Microstructure and Mechanical Properties of Titanium Alloy Ti6Al4V Forgings with Different Combinations of Thermo-Mechanical Processing and Heat Treatment Cycles, Transactions of the Indian National Academy of Engineering 6(3) (2021) 839-855.
[149] D. Bhaskar, H. Francis, Additive manufacturing of titanium alloys: State of the art, challenges, and opportunities, Oxford: Elsevier Inc, 2016.
[150] J.L. Cabezas-Villa, J. Lemus-Ruiz, D. Bouvard, O. Jiménez, H.J. Vergara-Hernández, L. Olmos, Sintering study of Ti6Al4V powders with different particle sizes and their mechanical properties, International Journal of Minerals, Metallurgy, and Materials 25(12) (2018) 1389-1401.
[151] S.D. Jadhav, J. Vleugels, J.P. Kruth, J. Van Humbeeck, K. Vanmeensel, Mechanical and electrical properties of selective laser‐melted parts produced from surface‐oxidized copper powder, Material Design & Processing Communications 2(2) (2020) 94.
[152] E. Brandl, D. Greitemeier, Microstructure of additive layer manufactured Ti–6Al–4V after exceptional post heat treatments, Materials Letters 81 (2012) 84-87.
[153] W. Xu, M. Brandt, S. Sun, J. Elambasseril, Q. Liu, K. Latham, K. Xia, M. Qian, Additive manufacturing of strong and ductile Ti–6Al–4V by selective laser melting via in situ martensite decomposition, Acta Materialia 85 (2015) 74-84.
[154] H. Rafi, N. Karthik, H. Gong, T.L. Starr, B.E. Stucker, Microstructures and mechanical properties of Ti6Al4V parts fabricated by selective laser melting and electron

beam melting, Journal of Materials Engineering and Performance 22(12) (2013) 3872-3883.
[155] Y.-L. Hao, S.-J. Li, R. Yang, Biomedical titanium alloys and their additive manufacturing, Rare Metals 35(9) (2016) 661-671.
[156] S. Parizia, G. Marchese, M. Rashidi, M. Lorusso, E. Hryha, D. Manfredi, S. Biamino, Effect of heat treatment on microstructure and oxidation properties of Inconel 625 processed by LPBF, Journal of Alloys and Compounds 846 (2020) 156418.
[157] Z. Xu, B. Guan, X. Wei, J. Lu, J. Ding, W. Wang, High-temperature corrosion behavior of Inconel 625 alloy in a ternary molten salt of NaCl-CaCl2-MgCl2 in air and N2, Solar Energy 238 (2022) 216-225.
[158] A. Kreitcberg, V. Brailovski, S. Turenne, Elevated temperature mechanical behavior of IN625 alloy processed by laser powder-bed fusion, Materials Science and Engineering: A 700 (2017) 540-553.
[159] A. Chyrkin, K.O. Gunduz, I. Fedorova, M. Sattari, A. Visibile, M. Halvarsson, J. Froitzheim, K. Stiller, High-temperature oxidation behavior of additively manufactured IN625: effect of microstructure and grain size, Corrosion Science (2022) 110382.
[160] P. Wang, B. Zhang, C.C. Tan, S. Raghavan, Y.-F. Lim, C.-N. Sun, J. Wei, D. Chi, Microstructural characteristics and mechanical properties of carbon nanotube reinforced Inconel 625 parts fabricated by selective laser melting, Materials & Design 112 (2016) 290-299.
[161] S. Floreen, G.E. Fuchs, W.J. Yang, The metallurgy of alloy 625, Superalloys 718(625) (1994) 13-37.
[162] A. Gamon, E. Arrieta, P.R. Gradl, C. Katsarelis, L.E. Murr, R.B. Wicker, F. Medina, Microstructure and hardness comparison of as-built inconel 625 alloy following various additive manufacturing processes, Results in Materials 12 (2021) 100239.
[163] G. Marchese, M. Lorusso, S. Parizia, E. Bassini, J.-W. Lee, F. Calignano, D. Manfredi, M. Terner, H.-U. Hong, D. Ugues, M. Lombardi, S. Biamino, Influence of heat treatments on microstructure evolution and mechanical properties of Inconel 625 processed by laser powder bed fusion, Materials Science and Engineering: A 729 (2018) 64-75.
[164] N.J. Harrison, I. Todd, K. Mumtaz, Reduction of micro-cracking in nickel superalloys processed by Selective Laser Melting: A fundamental alloy design approach, Acta Materialia 94 (2015) 59-68.
[165] G. Marchese, X. Garmendia Colera, F. Calignano, M. Lorusso, S. Biamino, P. Minetola, D. Manfredi, Characterization and comparison of Inconel 625 processed by selective laser melting and laser metal deposition, Advanced Engineering Materials 19(3) (2017) 1600635.
[166] G. Dinda, A. Dasgupta, J. Mazumder, Laser aided direct metal deposition of Inconel 625 superalloy: Microstructural evolution and thermal stability, Materials Science and Engineering: A 509(1-2) (2009) 98-104.
[167] R.J. Williams, F. Vecchiato, J. Kelleher, M.R. Wenman, P.A. Hooper, C.M. Davies, Effects of heat treatment on residual stresses in the laser powder bed fusion of 316L stainless steel: Finite element predictions and neutron diffraction measurements, Journal of Manufacturing Processes 57 (2020) 641-653.
[168] S. Afkhami, M. Dabiri, H. Piili, T. Björk, Effects of manufacturing parameters and mechanical post-processing on stainless steel 316L processed by laser powder bed fusion,

Materials Science and Engineering: A 802 (2021) 140660.
[169] W. Beard, R. Lancaster, J. Adams, D. Buller, Fatigue Performance of Additively Manufactured Stainless Steel 316L for Nuclear Applications, 2019 International Solid Freeform Fabrication Symposium, University of Texas at Austin, 2019.
[170] H.M. Khan, S. Waqar, E. Koç, Evolution of temperature and residual stress behavior in selective laser melting of 316L stainless steel across a cooling channel, Rapid Prototyping Journal 28 (2022) 1272-1283.
[171] J. Hajnys, M. Pagac, J. Mesicek, J. Petru, M. Krol, Influence of Scanning Strategy Parameters on Residual Stress in the SLM Process According to the Bridge Curvature Method for AISI 316L Stainless Steel, Materials (Basel) 13(7) (2020) 1659.
[172] M. Kumaran, V. Senthilkumar, Experimental characterization of stainless steel 316L alloy fabricated with combined powder bed fusion and directed energy deposition, Welding in the World 65(7) (2021) 1373-1388.
[173] N. Diaz Vallejo, C. Lucas, N. Ayers, K. Graydon, H. Hyer, Y. Sohn, Process Optimization and Microstructure Analysis to Understand Laser Powder Bed Fusion of 316L Stainless Steel, Metals 11(5) (2021) 832.
[174] H. Sohrabpoor, V. Salarvand, R. Lupoi, Q. Chu, W. Li, B. Aldwell, W. Stanley, S. O'Halloran, R. Raghavendra, C.-H. Choi, Microstructural and mechanical evaluation of post-processed SS 316L manufactured by laser-based powder bed fusion, Journal of Materials Research and Technology 12 (2021) 210-220.
[175] C.-H. Yu, A. Leicht, R.L. Peng, J. Moverare, Low cycle fatigue of additively manufactured thin-walled stainless steel 316L, Materials Science and Engineering: A 821 (2021) 141598.
[176] D. Wang, C. Song, Y. Yang, Y. Bai, Investigation of crystal growth mechanism during selective laser melting and mechanical property characterization of 316L stainless steel parts, Materials & Design 100 (2016) 291-299.
[177] A. Leicht, Laser powder bed fusion of 316L stainless steel, Chalmers University of Technology Gothenburg, Sweden, 2020.
[178] S.A. Alexandratos, L. Shi, N.P. O'Dowd, Parameter Study of a Thermal Analysis of a Bead-on-Plate Weld, Pressure Vessels and Piping Conference 51685 (2018) V06BT06A083.

3 Three-dimensional finite element modelling for additive manufacturing of Ti-6Al-4V components: effect of scanning strategies on temperature history and residual stress

Jinbiao Zhou[1,2,3], Richard A. Barrett[1,2,3], Sean B. Leen[1,2,3]

[1]Mechanical Engineering, College of Engineering and Informatics, University of Galway.

[2]Ryan Institute for Environmental, Marine and Energy Research, University of Galway.

[3]I-Form Advanced Manufacturing Research Centre, Ireland.

Jinbiao Zhou: Conceptualization, Methodology, Software, Writing - original draft.

Summary

This chapter presents and validates a new FE-based AM process modelling method, using the new AM module in Abaqus, applied to DED manufacture of Ti-6Al-4V, with a key focus on measurement and prediction of thermal histories and residual stresses. It also shows the key effects of residual stresses on fatigue life.

3.1 Abstract

A key challenge for metal additive manufacturing is the requirement to adapt process-structure-property methods currently under development to realistic, complex geometries. Of specific concern in the present work is the requirement for accurate computation in such realistic geometries of (i) thermal histories, to facilitate microstructure prediction, and hence, mechanical properties, and (ii) residual stresses, as required for accurate assessment and design for structural integrity, such as fatigue cracking. This paper presents three-dimensional, finite element modelling for simulation of a realistic Ti-6Al-4V component using directed energy deposition. The predicted results are successfully validated against published experimental and numerical data. The effects of different scanning strategies on temperature histories and residual stresses are investigated as a basis for identification of optimal manufacturing protocols. Finally, fatigue life predictions of the Ti-6Al-4V component have been considered based on the Basquin-Goodman equation with the effect of residual stress taken into account.

3.2 Introduction

Additive manufacturing (AM) provides an unprecedented opportunity to produce complex metal parts through layer-by-layer addition of materials and offers a number of advantages over traditional manufacturing methods, including (i) ability to convert directly from three-dimensional computer aided design (CAD) models to near net-shape manufactured components in a single step, (ii) ability to manufacture features not typically achievable with conventional manufacturing, e.g. re-entrant corners and features, (iii) minimal waste

of raw material (powder), and (iv) possibility for recycling of powder, leading to reduced time to market via accelerated prototyping and component or product customization at low cost [1]. AM processes can be generally classified into two main categories: (i) directed energy deposition (DED) (Figure 3.1 (a)), in which the metal powder is fed coaxially into the beam and fuses with previously deposited thin layer, and (ii) powder bed fusion (PBF) (Figure 3.1 (b)), in which a thin layer of powder is laid and then the metal powder is melted by the laser beam or electron beam according to a controlled trajectory [2, 3]. More details of AM technologies can be found elsewhere [4-6]. In this research work, the focus is mainly on laser directed energy deposition process. DED is able to manufacture and repair metal parts with high-performance and low-cost. Compared with conventional subtractive manufacturing methods, DED has unique advantages, especially in the manufacture of complex-shaped multi-materials or functionally graded components [7].

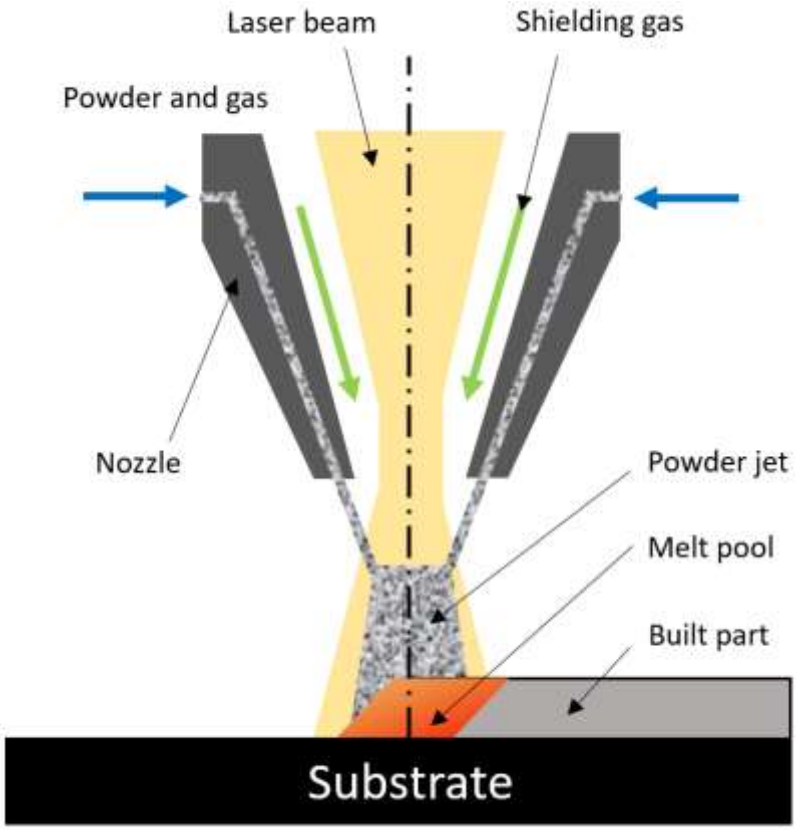

(a)

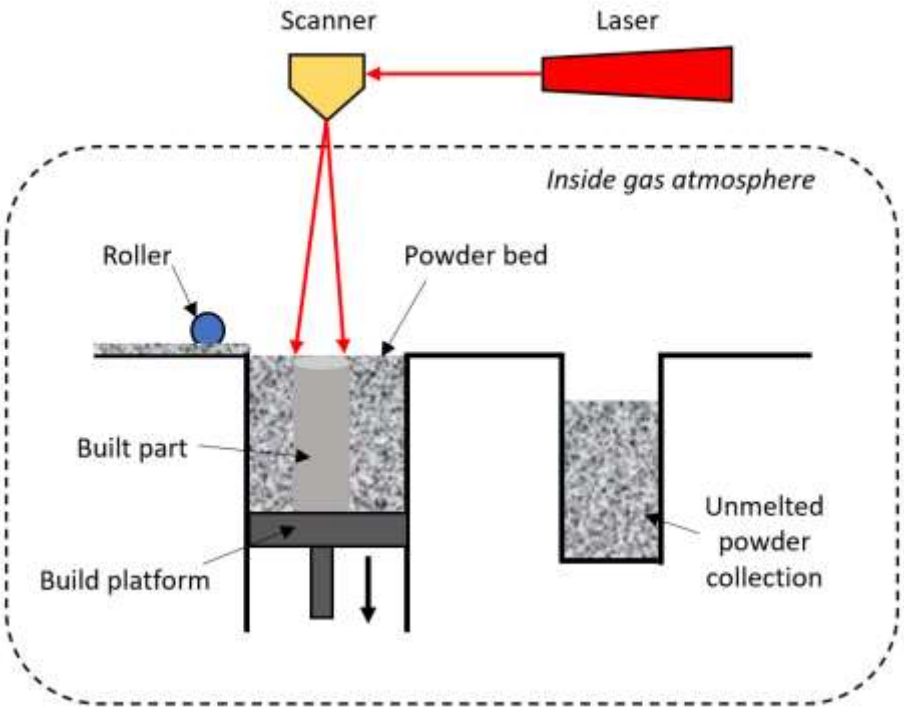

(b)

Figure 3.1. Schematic illustrations of AM processes: (a) Directed Energy Deposition (DED) and (b) Powder Bed Fusion (PBF), adapted from Song et al. [8].

Although the advantages of AM are widely recognized, the residual stresses induced by the high and non-uniform thermal gradients during the laser heating and cooling cycles in the AM process is one of the major issues [9]. Residual stresses have a detrimental effect on mechanical strength and geometrical accuracy, particularly on fatigue resistance [10-12]. Hence, it is important to investigate and quantify the effects of manufacturing process on residual stresses, and resulting properties, e.g. fatigue life, for both the AM process and final AM components.

Finite element (FE) modelling of the AM process is a potentially powerful technique for full-field quantification of temporal-spatial distributions of key thermo-mechanical variables (e.g. temperature, deformation, strain, stress) directly or indirectly controlling the mechanical behavior of fabricated components. Several numerical models have been developed previously to simulate the AM process, with a focus on predicting thermal

history and residual stresses and deformations. Zaeh et al. [13] presented a layer-by-layer modelling method to evaluate and quantify residual stress and deformation in relatively simple macro-scale components manufactured using the PBF process and highlighted the limitations of the layer-by-layer approach for predicting residual deformations. Barrett et al. [14] proposed a 2D layer-by-layer FE model to predict residual stress in a PBF manufactured Ti-6Al-4V hip stem component (using a simplified 2D geometrical representation), highlighting the importance of post-build heat treatment, but without explicit comparisons against experimental test data. Recently, an automated Python-based method for sectioning of 2D FE models of macroscale components for efficient model generation in the layer-by-layer method was developed [15], providing a framework for layer scaling for FE modelling of the PBF process. However, this method was not compared with test data for temperature histories or residual stresses. The layer-by-layer FE-based method was investigated for residual stress prediction of 3D PBF parts by Chen et al. [16], with a particular focus on geometrical shape (e.g. tri-prism, cylinder, block), solid and hollow. However, a key limitation of the layer-by-layer method is the inability to represent laser beam moving path and, hence, to investigate the effects of different scanning strategies, for example. The importance of scanning strategy (linear, zigzag, chessboard and contour) on residual deformation and surface finish in DED was demonstrated experimentally by Ribeiro et al. [17]. The contour strategy showed least distortion and best surface finish. The influence of scanning strategy on porosity, hardness and mechanical properties of Al2319 block structure were investigated by Matthieu et al [18]. The oscillation strategy showed comparable average percentage area porosity, hardness, UTS and YS to those reported in the literature. A common approach for simulating AM processes, including welding and 3D printing, is the computationally-intensive ‘element birth and death’ method, also commonly referred to as the ‘Model Change’ method. Yang et al. [19] recently presented a 3D thermo-elastic-plastic model using this approach to follow precisely the physical deposition path for a 5-layer DED of Ti-6Al-4V. However, the high computational cost of these methods makes AM modelling of full scale and complex 3D components almost impossible. Hence, this method is typically limited to small-scale geometries, e.g. low numbers of layers or tracks.

Chiumenti et al. [20] conducted a systematic assessment of different FE modelling techniques (e.g. layer-by-layer, hatch-by-hatch, element-by-element) for PBF, in terms of computational cost and numerical accuracy, particularly focusing on temperature prediction. Again, it recommended that the 'element birth and death' (high fidelity) method can be used for effects of different scanning strategies. Yang et al. [21] developed a FE model with a moving heat flux implemented via a user subroutine to predict the thermal history and spatial distributions of temperature of the PBF process and a process-structure model which can be used as a process design tool. In this case, the focus was on validation of temperature history against experimental measurement from the single-track PBF of Ti-6Al-4V, for prediction of phase transformations using a Kolmogorov-Johnson-Mehl-Avrami (KJMA) model. The process-structure method successfully predicted alpha and beta phase fractions. A key objective of the present work is to adapt this process-structure method for realistic, large-scale components; however, the conventional 'Model Change' technique, e.g. in Abaqus [19, 21], is too computationally-expensive for such components. Recently, a new highly-efficient AM module has been developed within the general-purpose FE-based software Abaqus, which, on the one hand, replicates the actual 3D printing process very realistically and with high fidelity, e.g. using actual 3D printing stereolithography (STL) files, whilst, on the other hand, providing a much more efficient process for modelling complex geometries, including a graphical user interface (GUI) [22]. This approach, which is the main method investigated in this paper, is hereafter referred to simply as 'Abaqus AM', and has recently been evaluated by Song et al. [8] for AM (laser DED and PBF) of complex, three-dimensional Inconel 718 components; the results were compared to experimental measurements of residual stresses and distortions, the latter obtained using (i) a combined focused ion beam (FIB) slitting, and digital image correlation (DIC) method and (ii) X-ray diffraction (XRD), at different length-scales. The predicted residual distortions were reasonably accurate in general whereas predicted residual stresses compared favorably for some components and not so favorably for others. It was concluded that (i) further work is required on the effects of measured plastic anisotropy on as-built properties [23] and (ii) future research needs to focus on more accurate measurements of these critical material properties at elevated temperature to

improve process simulation accuracy. A similar modelling approach by Yang et al. [24] achieved high accuracy compared to experimental measurements for predicting residual strains in PBF of Inconel 625. Apart from the residual stress prediction, it is also important to investigate the effect of residual stress on fatigue life of components with complex geometry. Jiang et al. [25] evaluated the role of residual stress on fatigue life of 316L stainless steel; the results showed that the tensile residual stress caused increase of mean stress and, hence, decrease of the fatigue life. Devaney et al. [26] applied a Basquin-Goodman methodology relating fatigue life to stress range and mean stress [27] to estimate the fatigue life at different locations in a complex welded X100 steel catenary riser connection; the results showed superior performance of the X100 material compared to more conventional X70 steels for example.

This paper presents three-dimensional, finite element modelling for prediction of temperature-time histories and residual stress distributions of a realistic (macro-scale) Ti-6Al-4V component manufactured using DED. A comparative assessment is presented, initially, between the (highly efficient but less accurate) layer-by-layer FE-based method and the new (efficient and high accuracy) 'Abaqus AM' method, in terms of temperature-time histories against (i) previously-published 'Model Change' results [19, 21] and (ii) measured cooling rates. The latter are key for metallurgical transformations [21], and hence, as-built mechanical property prediction. A more detailed validation of the new Abaqus-based modelling method is then presented by way of comparison against published thermocouple data from a DED process of the three-dimensional component. The accuracy and efficiency of the new Abaqus-based method is verified by comparison to previously-published numerical results for residual stress prediction. A study on the effects of scanning strategy on three-dimensional temperature and residual stress distributions is presented, as a basis for identification of optimal manufacturing protocols and to demonstrate the effectiveness of the proposed modelling method. Finally, some sample fatigue life calculations are presented using a combined Basquin-Goodman approach, to demonstrate typical effects of the predicted AM-induced residual stresses for sample locations in the manufactured component, including the effect of scanning

strategy, followed by some discussions and conclusions. Attention is focused here on uniaxial high cycle fatigue behavior for long life of components; hence the Basquin model is adopted, due to its simplicity and widespread use [28]; the Goodman equation is widely used to incorporate the effects of mean stress on high cycle fatigue [27], and is therefore also adopted here to assess effects of residual stresses on HCF life for the AM Ti-6Al-4V components.

3.3 Methodology

There are several physical phenomena to consider in the DED process, including the thermal transfer, moving heat source, and material deposition. The widely-used sequentially coupled thermal and mechanical FE analysis approach is adopted to describe the DED process accurately and efficiently [8, 24, 29-31]. 3D transient thermal analysis is performed first, and then the thermal loading from the heat transfer analysis are coupled to the same FE model for mechanical analysis.

3.3.1 Thermal mechanisms

3.3.1.1 Heat transfer equations

The main thermal mechanisms in DED are (i) conduction within the part, (ii) conduction between the part and substrate, and (iii) convection and radiation between the active layer and the surrounding air, as shown in Figure 3.2. The governing equation for the heat transfer process is written using the energy equation [32], as follows:

$$\rho \frac{dH(\mathbf{r},t)}{dt} = -\nabla \cdot \mathbf{q} + Q + \dot{D}_{\text{mech}} \tag{3.1}$$

where **r** represents an arbitrary reference material point in a Lagrangian domain Ω, ρ is material density (kg/m^3), H is enthalpy, t is time (s), **q** is heat flux vector, and Q is laser heat source, $\dot{D}_{\text{mech}}$ is thermo-mechanical dissipation. The temporal rate of enthalpy can be expressed as:

$$\frac{dH(\mathbf{r},t)}{dt} = C_{\mathrm{p}}(T)\frac{dT(\mathbf{r},t)}{dt} \tag{3.2}$$

where C_{p} is the temperature dependent specific heat ($\mathrm{J/(kgK)}$), T denotes temperature (K). The heat flux vector $\mathbf{q}$ is given by Fourier's law, as:

$$\mathbf{q} = -k(T)\nabla T \tag{3.3}$$

where k is the temperature dependent thermal conductivity ($\mathrm{W/(mK)}$), which, for simplification purposes, is assumed to be isotropic here [19, 33]. Of course, thermal conductivity may possibly be anisotropic due to the mechanisms of AM metal [34], future work will investigate this further. The thermo-mechanical dissipation $\dot{D}_{\mathrm{mech}}$ is defined as [35]:

$$\dot{D}_{\mathrm{mech}} = \boldsymbol{\sigma} : \dot{\boldsymbol{\varepsilon}}^{\mathrm{vp}} \tag{3.4}$$

where $\boldsymbol{\sigma}$ is the stress tensor and $\dot{\boldsymbol{\varepsilon}}^{\mathrm{vp}}$ is the visco-plastic strain tensor. The heat loss due to heat convection is given by Newton's law of cooling, as:

$$q_{\mathrm{conv}} = h_{\mathrm{conv}}(T_{\mathrm{s}} - T_{\mathrm{env}}) \tag{3.5}$$

where h_{conv} is heat transfer convection coefficient ($\mathrm{W/(m^2K)}$), T_{s} is surface temperature of the specimen (K), T_{env} is environmental temperature (K). Here, a forced convection coefficient $h_{\mathrm{conv-force}} = 55\ \mathrm{W/(m^2K)}$ was used during the printing process, while a free convection coefficient $h_{\mathrm{conv-free}} = 5\ \mathrm{W/(m^2K)}$ was applied as the reference [19, 36, 37] because the argon atmosphere is no longer available after the printing process and convection becomes uniform on all surfaces. The heat loss due to radiation is defined by Stefan-Boltzmann's law:

$$q_{\mathrm{rad}} = \varepsilon_{\mathrm{rad}}\sigma_{\mathrm{rad}}(T_{\mathrm{s}}^4 - T_{\mathrm{env}}^4) \tag{3.6}$$

where $\varepsilon_{\mathrm{rad}}$ is the emissivity coefficient, and σ_{rad} is the Stefan–Boltzmann constant. Here, the emissivity was assumed to be temperature independent as 0.54 [36], and the Stefan-Boltzmann's constant was set as $5.669 \times 10^{-8}\ \mathrm{W/(m^2K^4)}$ [38, 39].

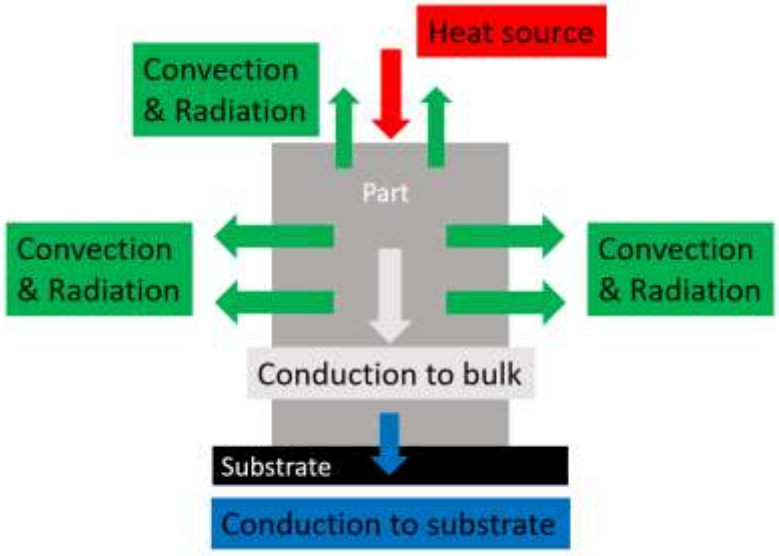

Figure 3.2. Thermal transfer mechanisms during the DED process.

3.3.1.2 Heat source equations

The Goldak double ellipsoidal model, which has been widely adopted to describe the laser heat source Q in Eq. (3.7) during the DED process modelling [8, 33, 40-42], is employed in the present work, defined as:

$$\begin{aligned} Q &= q_f \quad when\ x_l \geq 0 \\ Q &= q_r \quad when\ x_l < 0 \\ q_{f/r} &= \frac{6\sqrt{3} f_{f/r} AP}{abc\pi\sqrt{\pi}} e^{\left(-\frac{3x_l^2}{c_{f/r}^2}-\frac{3y_l^2}{a^2}-\frac{3z_l^2}{b^2}\right)} \end{aligned} \tag{3.7}$$

where f_f and f_r are 'box size' factors with a value of 1, A is the heat source absorption coefficient, P is the laser power (W) and x_l, y_l, z_l are the local coordinates with origin centered on the moving heat source when the scanning speed v reaches the maximum value, a, b are the dimensions along the y_l and z_l axis of the ellipsoid and c_f and c_r are the front length and rear length along the x_l axis of the ellipsoid, as shown in Figure 3.3**.** Generally, a, c_f and c_r are taken as the laser spot radius, b is taken as the melt pool depth [8, 19]**.** The inputs for the Goldak heat source model are based on the DED manufacturing

parameters of the experimental conditions investigated here [19], as summarized in Table 3.1.

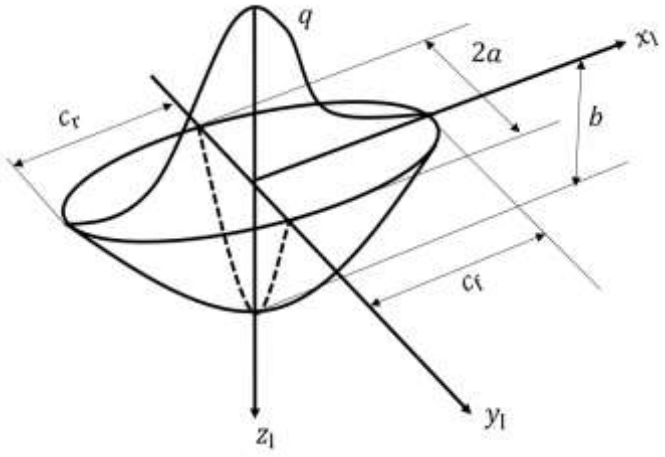

Figure 3.3. The Goldak double ellipsoid heat source model for DED process.

Table 3.1. Printing process parameters applied.

Symbol	Parameters	Value
P	Laser power (W)	300
A	Heat source absorption coefficient	0.45
v	Laser scanning speed (mm/s)	2
R	Laser spot radius (mm)	1.36
d_{m}	Melt pool depth (mm)	0.816

3.3.2 Mechanical mechanisms

The balance of momentum equation used for the mechanical analysis is given by [39, 43]:

$$\nabla \cdot \boldsymbol{\sigma} + \mathbf{b} = 0 \tag{3.8}$$

where $\boldsymbol{\sigma}$ is the Cauchy stress tensor and $\mathbf{b}$ is the body force tensor. The mechanical constitutive law of the elastic problem is defined as:

$$\boldsymbol{\sigma} = \boldsymbol{C} : \boldsymbol{\varepsilon}_{\mathbf{e}} \tag{3.9}$$

where $\boldsymbol{C}$ is the fourth order elastic tensor and $\boldsymbol{\varepsilon_e}$ is the elastic strain tensor, which is calculated by:

$$\boldsymbol{\varepsilon_e} = \boldsymbol{\varepsilon_{Total}} - \boldsymbol{\varepsilon_p} - \boldsymbol{\varepsilon_T} \tag{3.10}$$

where $\boldsymbol{\varepsilon_{Total}}$, $\boldsymbol{\varepsilon_p}$, $\boldsymbol{\varepsilon_T}$ are the total, the plastic and the thermal strain tensors, respectively. The thermal strain tensor is defined as:

$$\boldsymbol{\varepsilon_T} = \alpha \Delta T \boldsymbol{I} \tag{3.11}$$

where α is the thermal expansion coefficient (1/K), ΔT is the change in temperature (K) and $\boldsymbol{I}$ is identity tensor. The tensile testing on the AM Ti-6Al-4V, which is used in the experiment investigated here [19], shows extensive plastic deformation with limited work hardening [44]. Hence, the widely employed elastic perfectly plastic model is adopted to define the constitutive behaviour of material in this study [45, 46].

3.3.3 Additive manufacturing simulation techniques

3.3.3.1 Layer-by-layer method

The macroscale part is sectioned into microscale equivalent layers along the building direction for the layer-by-layer model (see Figure 3.4), in which the whole layer is heated by an equivalent heat resource simultaneously, to save computational cost in AM modelling [14, 15, 47]. The equivalent heat source Q_{e} is defined based on the printing process parameters (see Table 3.1):

$$Q_{\mathrm{e}} = \frac{AP}{d_{\mathrm{s}} d_{\mathrm{m}} H} \tag{3.12}$$

where d_{s} is the laser spot radius (mm), d_{m} is the melt pool depth (mm) and H is the hatch spacing (mm), taken as laser spot diameter here. The heating time t_{heat} of each equivalent layer is calculated by:

$$t_{heat} = \frac{d_s}{v} \tag{3.13}$$

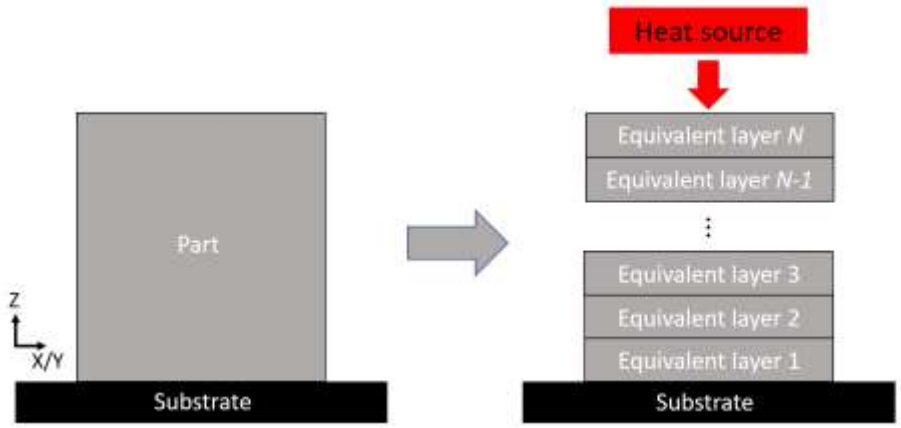

Figure 3.4. The schematic diagram of the layer-by-layer method.

3.3.3.2 Present FE-based AM method (Abaqus AM module)

Historically, the 'Model Change' technique has been used to simulate the addition of new material with time. This is computationally inefficient for progressive material addition, and is limited to simple geometries [33]. FE analysis software companies have developed specialist simulation tools for simulating the complete AM process, such as Atlas 3D [48], Simufact [49], ANSYS [50]. A recent review article by Peter et al. [51], which discusses in detail the relative merits of a number of prominent simulation software tools for AM, highlights the non-availability of temperature distributions as a key limitation of such offerings. The Abaqus software [52], which is a typical commercial code with a state-of-the-art AM plug-in, is investigated here for simulation of the complete AM process for complex components. This Abaqus AM plug-in does not have the limitation identified by Peters et al. [51], which is specifically important for understanding residual stress distributions and predicting microstructure evolution [21]. This implementation is significantly more efficient for (i) progressive element activation for modelling the deposition of materials and (ii) moving heat fluxes for modelling the laser heating process. The Event Series module is utilized to prescribe the combination of toolpath and process conditions which needs to be interpreted numerically both in time and space according to the element activation and related heat input. The newly introduced toolpath-mesh intersection module, which makes the model set-up simpler and less time-consuming, can

then be used to calculate the relevant information required for the thermal and structural FE analysis automatically after defining the event series in input files [8]. This is used to determine which elements have intersected with a path that is defined in time and space, for example the path of a tool. Previous methods were limited to adding elements at the start of a step, and required explicit definition of the elements to be included [13, 19-21]. The toolpath-mesh intersection module allows for a much looser coupling between the toolpath and the rest of the model, giving simpler and faster model set-up. The overall approach is illustrated in Figure 3.5.

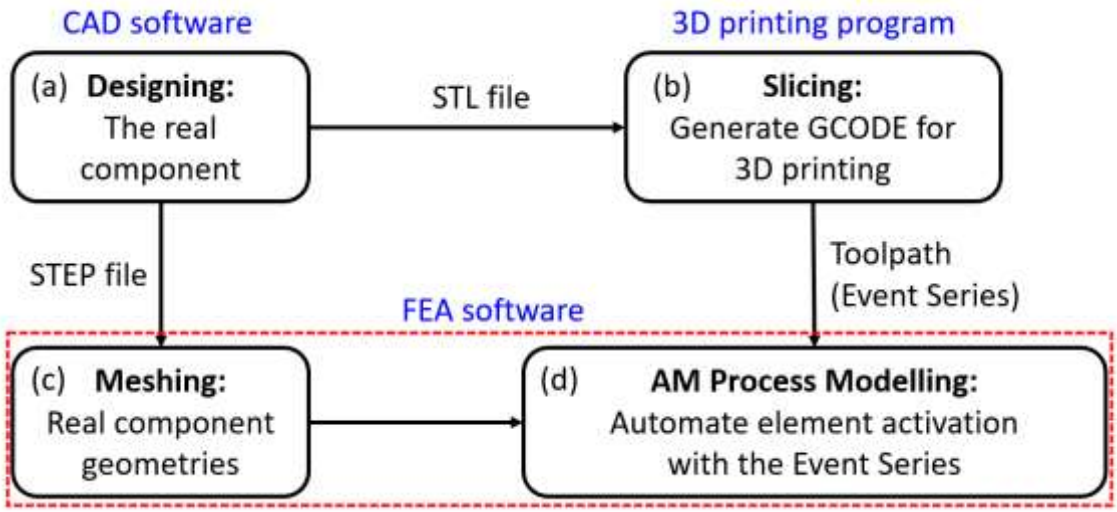

Figure 3.5. Overall AM modelling flowchart: (a) step 1: Designing, (b) step 2: Slicing, (c) step 3: Meshing, (d) step 4: AM process modelling.

3.3.4 Rectangular model and material properties

A five-layer hollow rectangular-shaped specimen (long length 41.86 mm, short length 22.37 mm, height 4.43 mm, and width 2.72 mm) on a square substrate (width 101.6 mm and thickness 3.18 mm) is modelled corresponding to the experimental arrangement [19] using the 'Abaqus AM' method to simulate the DED process (Figure 3.6 (a)). The layer height L_h is 0.886 mm. A detailed mesh convergence study is conducted to establish a suitable refined element size for the built part, with the final mesh (Figure 3.6 (b)) using

an element size (0.68 mm in x direction, four elements in width) based on the suggestions proposed in Refs [19, 33, 36], and converged to within 5% with respect to stress. The converged FE model contains 8562 elements and 13152 nodes. Eight-node linear heat transfer elements (DC3D8) and eight-node linear elements with full integration (C3D8) are chosen for the thermal and mechanical analysis, respectively [8]. For both thermal and mechanical analysis, the full element activation [24] is utilized to simulate the addition of material during the AM process.

The build direction for the hollow rectangular-shaped specimen is defined in the global z-direction (Figure 3.6 (b)). Temperature-dependent material properties of Ti-6Al-4V are employed in this study as taken from [36], presented in Table 3.2. The material density and Poisson's ratio are assumed to be a constant of 4430 kg/m^3 and 0.34 respectively [19]. Porosity is one of the key manufacturing defects that tend to negatively affect properties of AM components, e.g. density [53]. Nonetheless, through careful control, it has been shown that it is possible to achieve low porosity; for example, Skvortsova et al. [54] measured a density of 4420 kg/m^3 for AM Ti-6Al-4V, which is almost identical to that conventional Ti-6Al-4V (4440 kg/m^3). The initial temperature of the whole model is set to be an ambient temperature of 27 ^{o}C. The substrate, which is also made of Ti-6Al-4V, is clamped at the left side to match the experimental settings, as shown in Figure 3.6 (b).

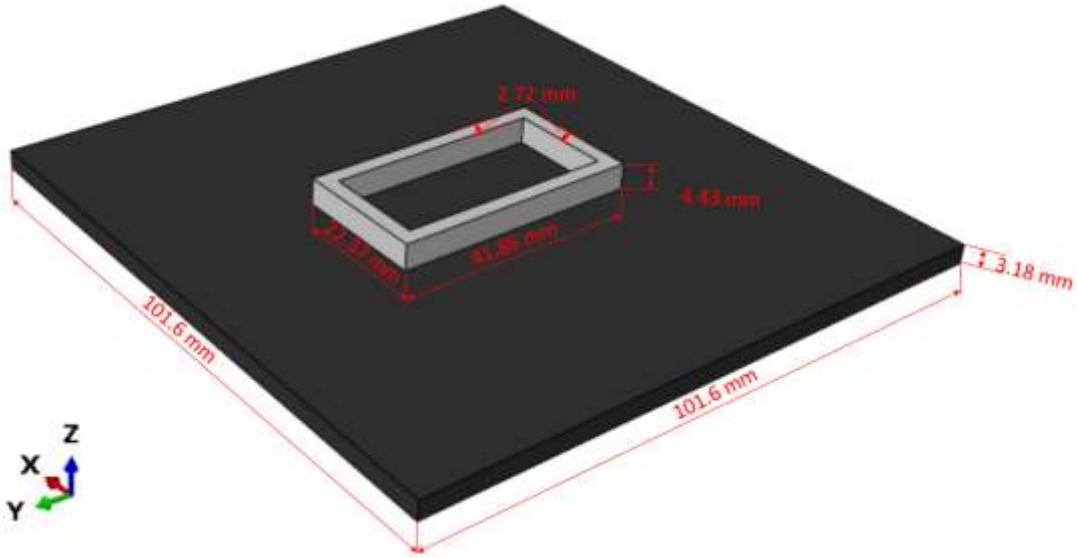

(a)

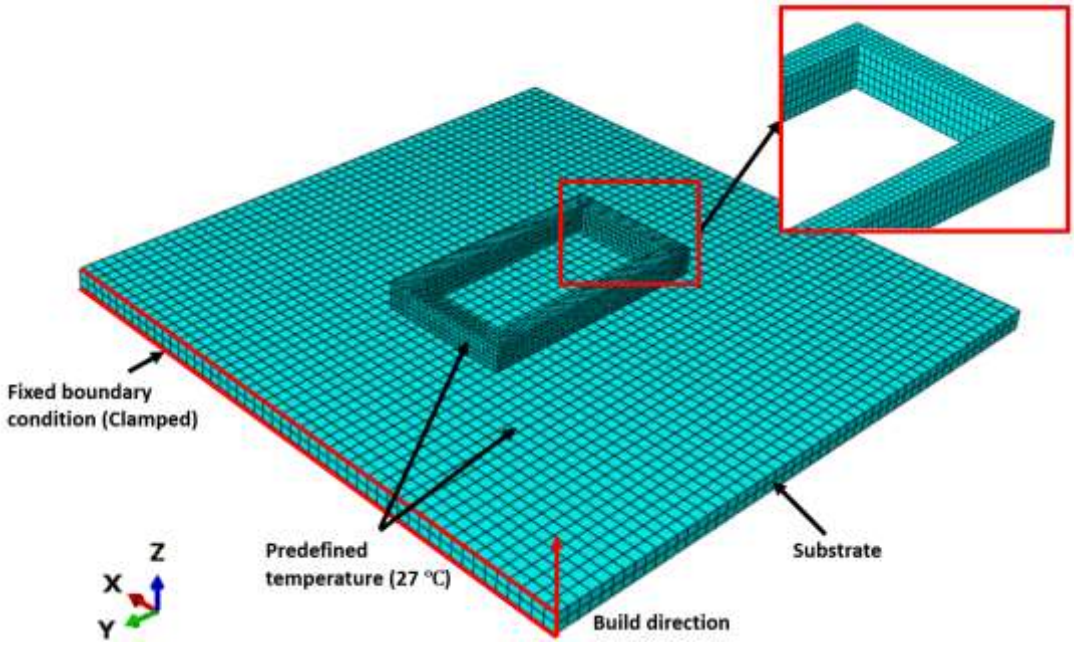

(b)

Figure 3.6. Finite element model of substrate and part geometry for DED simulation (a) Model configurations, (b) Finite element mesh and boundary conditions.

Table 3.2. Temperature dependent material properties of Ti-6Al-4V [36].

Temperature T (°C)	**Specific heat C_p (J/kg/°C)**	**Conductivity k (W/m/°C)**	**Thermal expansion coefficient α (μ m/m/°C)**	**Elastic Modulus E (MPa)**	**Yield strength σ_y (MPa)**
20	565	6.6	8.64	103950	768.15
93	565	7.3	8.82	100100	735.3
205	574	9.1	9.09	94190	684.9
250	586	9.7	9.2	91810	664.65
315	603	10.6	9.33	88380	635.4
425	649	12.6	9.55	82580	585.9
500	682	13.9	9.7	78630	552.15
540	699	14.6	9.7	76520	534.15
650	770	17.5	9.7	70720	484.65

3.3.5 Scanning strategies

Three different scanning strategies are employed in the DED process modelling to investigate the effect on thermal distribution and resulted residual stress. These are denoted as strategies A [19], B [55], C, respectively, as shown in Figure 3.7. ‘1’, ‘2’, ‘3’, ‘4’ are marked to represent the deposition sequence of the hollow rectangular-shaped specimen: green points and bold arrow lines represent the start and direction of each deposition layer. The maximum times that the deposited material has to cool before the new layer to be deposited for strategy A, B and C are 58.8 s, 78 s and 117.6 s, respectively. Different material deposition and moving heat event series are programmed to define the motion of powder and the laser moving path according to the respective scanning strategies.

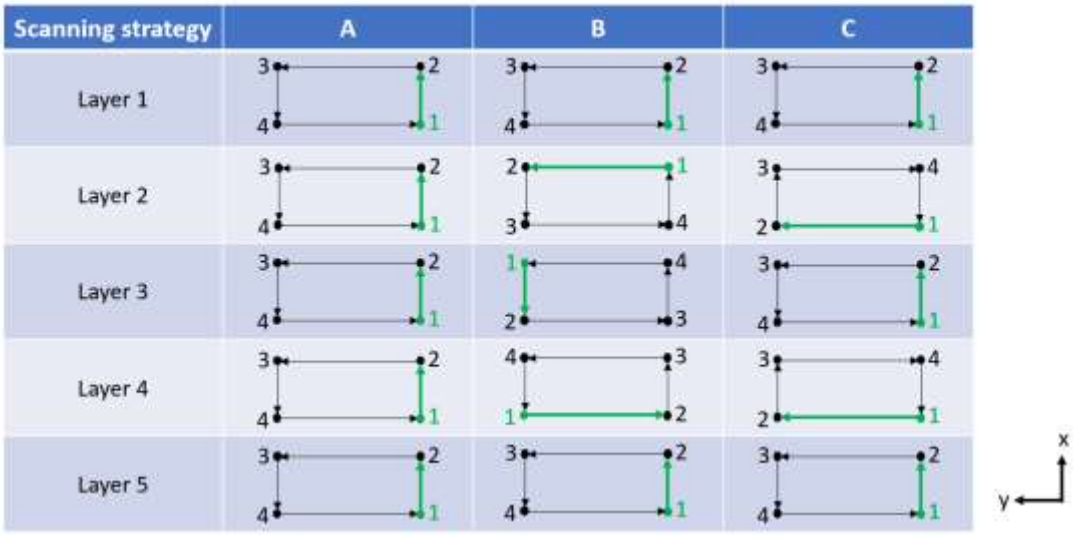

Figure 3.7. Schematic diagram of different scanning strategies.

3.4 Results

3.4.1 Verification and validation of AM simulation techniques

3.4.1.1 Verification of AM simulation techniques

In this present study, the DED process for Ti-6Al-4V specimens is investigated using both the layer-by-layer method and the 'Abaqus AM' method to verify the accuracy of the proposed AM modelling techniques via comparison to published results. Figure 3.8 shows the position of a selected point (at the center of the first layer), which is 38.8 mm away from the laser start point (left corner of first layer). The comparison of the FE-predicted thermal history for the selected point by layer-by-layer modelling against the numerical results using the 'Model Change' technique reported by Baykasoglu et al. [33] for the same point is shown in Figure 3.9. A similar temperature profile is predicted by the layer-by-layer method; however, a time difference is clearly shown between the time of peak temperature of the layer-by-layer method and that in Ref [33]. For example, the time of the first peak predicted by the layer-by-layer method is 1.36 s, while the first peak in the published result arrives at 19.4 s: the cause of the difference is that the whole layer is heated simultaneously using the layer-by-layer method, since the real laser travelling time has not been modelled. The first temperature peak (first layer deposition) in both methods

is almost identical, approximately 1800 ^{o}C. However, subsequent peaks are significantly different in magnitude; e.g. the layer-by-layer method underpredicts the second peak by about 500 ^{o}C (viz. 1200 ^{o}C compared to 1700 ^{o}C). These differences after the first layer are primarily attributed to longer cooling times in the layer-by-layer method. Figure 3.10 presents the FE-predicted thermal history at the same selected point using the 'Abaqus AM' method, corresponding to the deposition of five layers. This clearly shows five primary peaks in temperature; both the trend and peak temperature are in good agreement with the published numerical results [33]. The comparison of predicted and measured cooling rates is summarised in Table 3.3, including the measured result from the DED Ti-6Al-4V experiment by Lia et al. [56]. The FE-predicted cooling rate using the 'Abaqus AM' method is seen to be significantly closer to the test measurement than the prediction by Baykasoglu et al. [33]. It is important to note that for the case here using 8 CPUs, the total runtime for this model is around 4 hours for the thermal analysis, using the 'Abaqus AM' method, compared to approximately 6 times larger using the 'Model Change' technique.

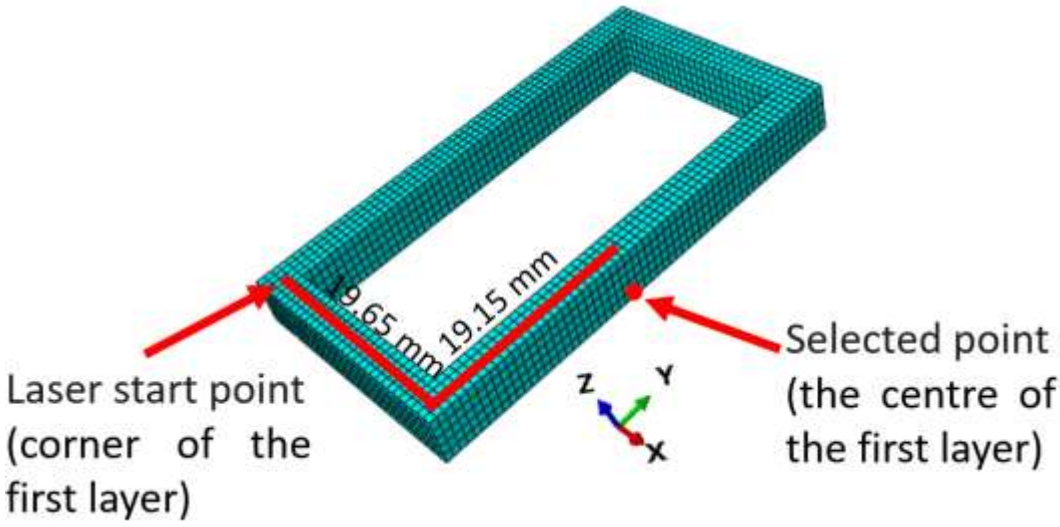

Figure 3.8. Illustration of position of selected point (at the centre of the first layer).

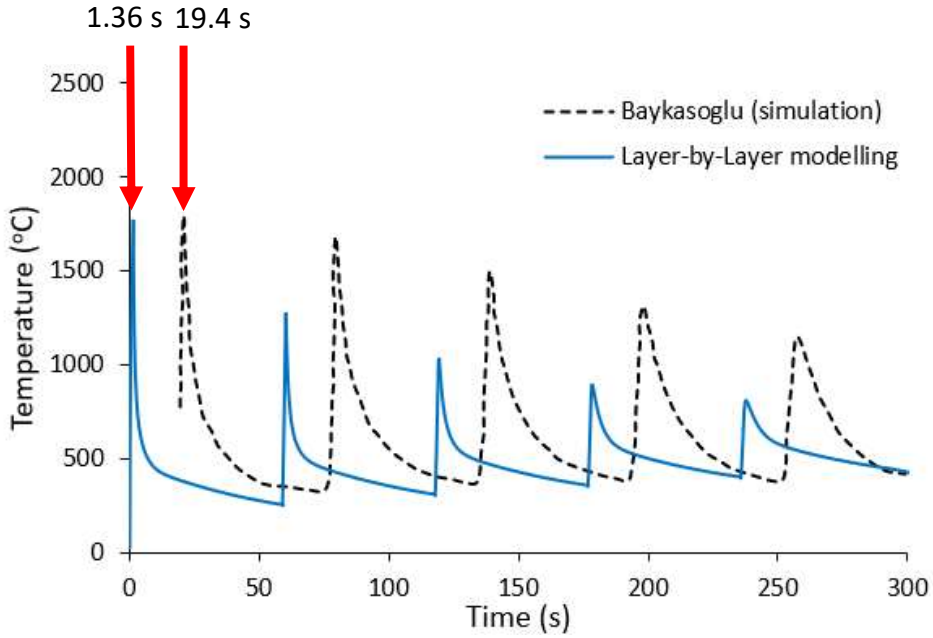

Figure 3.9. Comparison of FE-predicted thermal history for selected point using the layer-by-layer method against independent numerical results from Baykasoglu et al. [33] using the more computationally-expensive 'Model Change' technique.

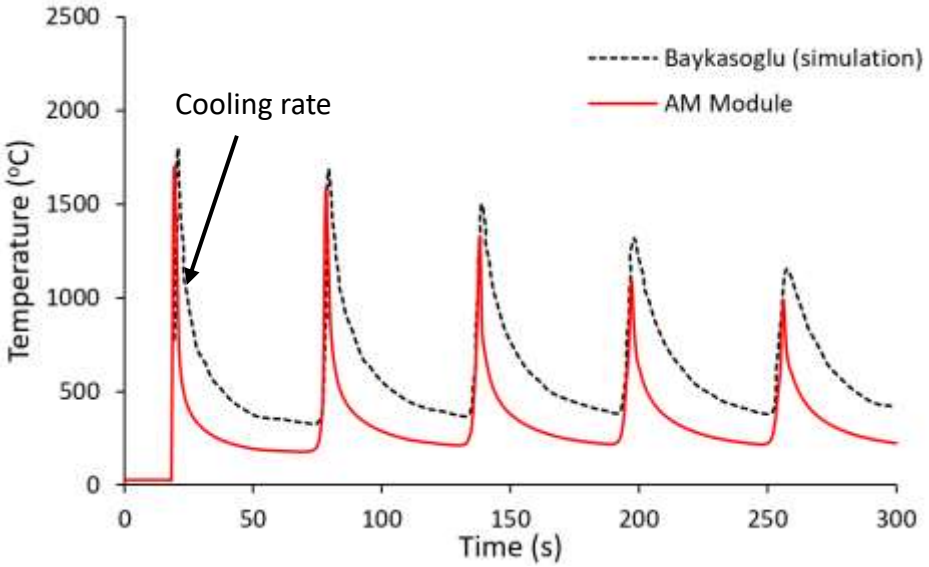

Figure 3.10. Comparison of FE-predicted thermal history for selected point against independent numerical results from Baykasoglu et al. [33] using the more computationally-expensive 'Model Change' technique.

Table 3.3. Comparison of predicted and measured cooling rates of DED Ti-6Al-4V.

Source	Cooling rate (^{o}C/s)
Simulation [33]	~ 30
Present work with 'Abaqus AM'	~ 173
Test [56]	219 ± 6.1

3.4.1.2 Validation of AM simulations

The FE thermal analysis results are validated by comparison to the experimental measurement results reported by Yang et al. [19], where the rectangular shaped Ti-6Al-4V specimen was produced using the Optomec LENS system [57], and two Omega SA1XL-K-72 thermocouples (TC) were attached on the top and bottom surfaces of the substrate to collect the temperature data during the heating (printing) and cooling processes. Time and temperature were recorded with 100 Hz sampling rate. The locations of the two TCs are shown in Figure 3.11, where the solid black circle represents TC1 on the top surface of the substrate and the empty black circle represents TC2 on the bottom surface of the substrate.

The predicted temperature histories are obtained at the same TC locations as in the experimental measurements. Figure 3.12 shows the temperature comparison between the predicted (using the layer-by-layer method and the AM Module method) and experimental measurements. It is clear from Figure 3.12 that during the heating process (from 0 s to 293.9 s), the experimental results and the numerical results using the AM Module method follow a very similar trend, and similarly during the cooling process (from 294 s to 1600 s), while the predictions using the layer-by-layer method are much higher than the experimental measurements. The comparison also validates the developed FE model through the thickness direction (z direction) (Figure 3.11) as TC1 and TC2 are on the top and bottom surfaces of the substrate, respectively. Compared to TC1, the measured

temperature at TC2 is higher, especially during the heating process, which is due to TC2 being 5 mm closer to the deposition part in the x direction (Figure 3.11) than TC1.

The predicted temperature field distribution at the end of printing (before the start of the cooling process) is shown in Figure 3.13: both the contour plot and maximum temperature (viz. 2432 ^{o}C, as compared to 2447 ^{o}C) are found to be comparable to the numerical results reported by Yang et al. [19]. The predicted contours of residual stress σ_x and σ_y along the x and y direction are shown in Figure 3.14. Figure 3.15 presents the comparison of predicted maximum of spatial residual stress. Regardless of maximum stress location or value, both σ_x and σ_y are in close agreement with the predictions from Yang et al. [19], using the more computationally-expensive 'Model Change' technique.

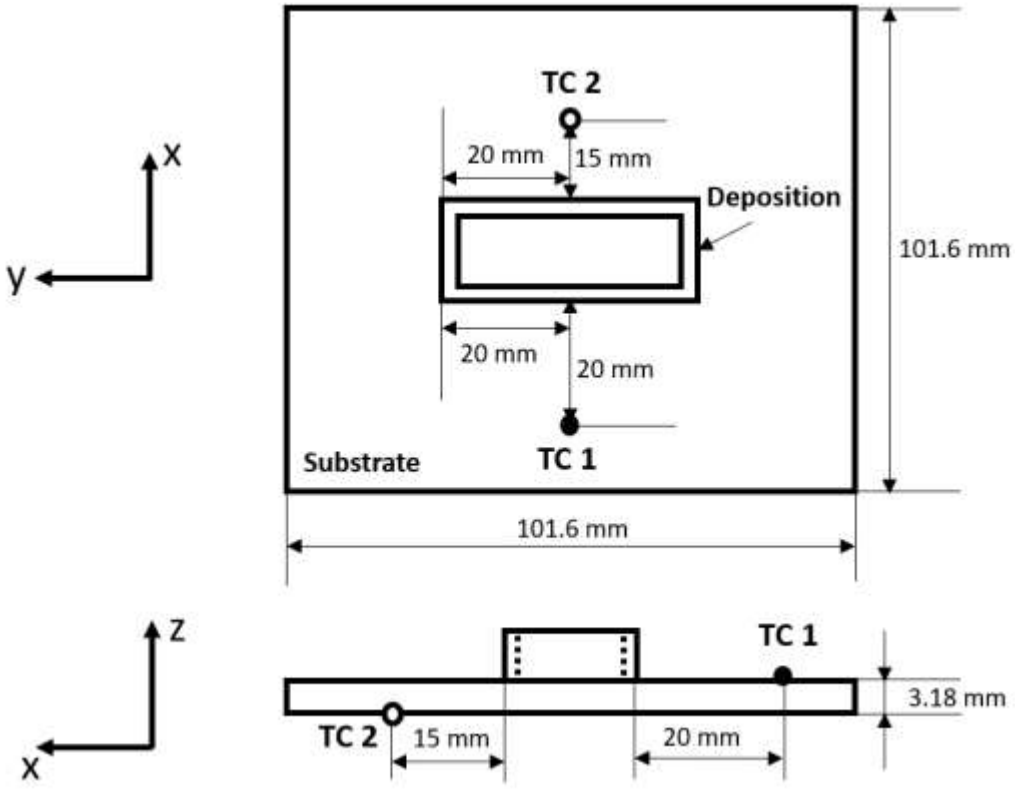

Figure 3.11. Locations of the two thermocouples measurement points: TC1 (solid circle) on top surface and TC2 (empty circle) on bottom surface of the substrate.

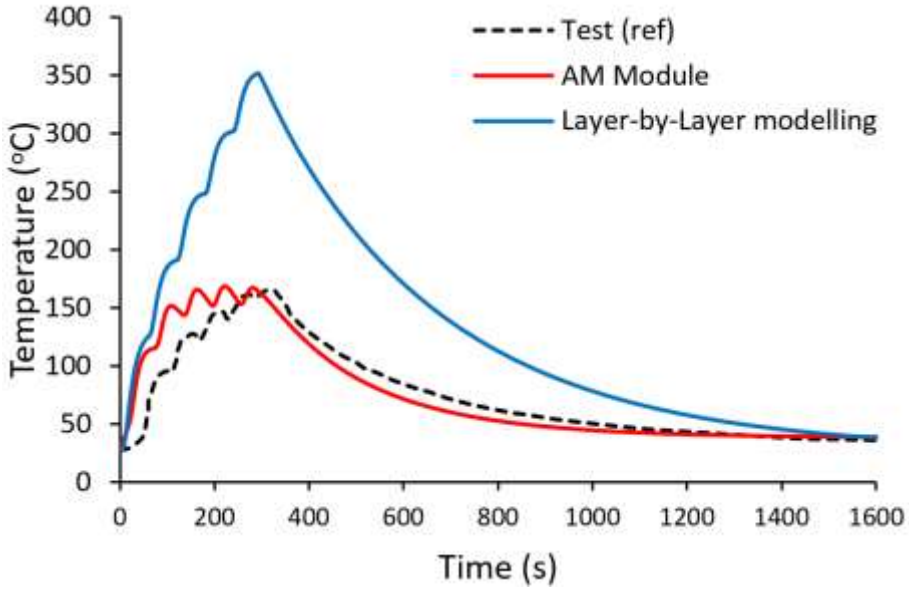

(a)

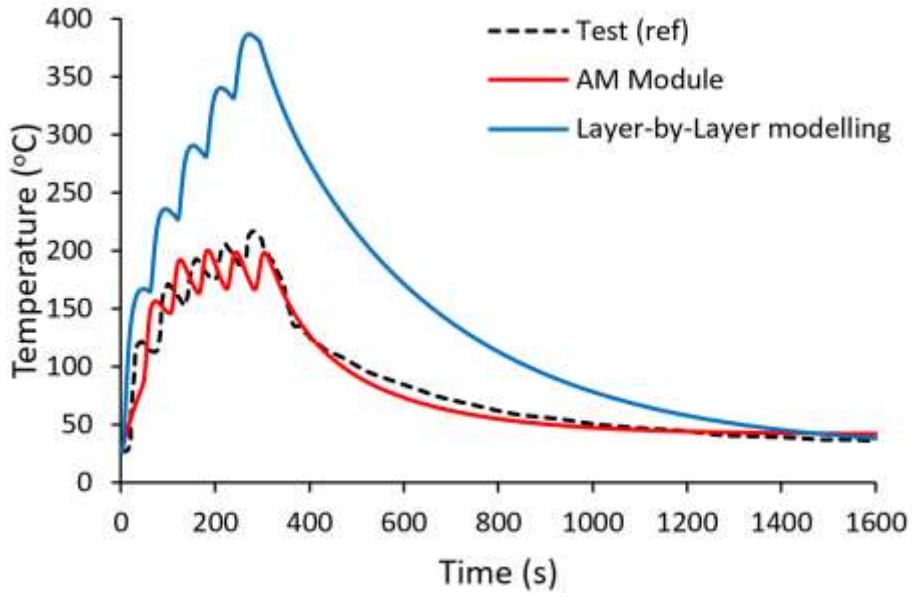

(b)

Figure 3.12. Temperature history comparison between the predicted using the layer-by-layer method and the AM Module method and experimental measurements (Ref [19]) at (a) TC1 and (b) TC2.

Figure 3.13. The predicted temperature distribution with scanning strategy A (Figure 3.7) at the end of the printing before cooling starts.

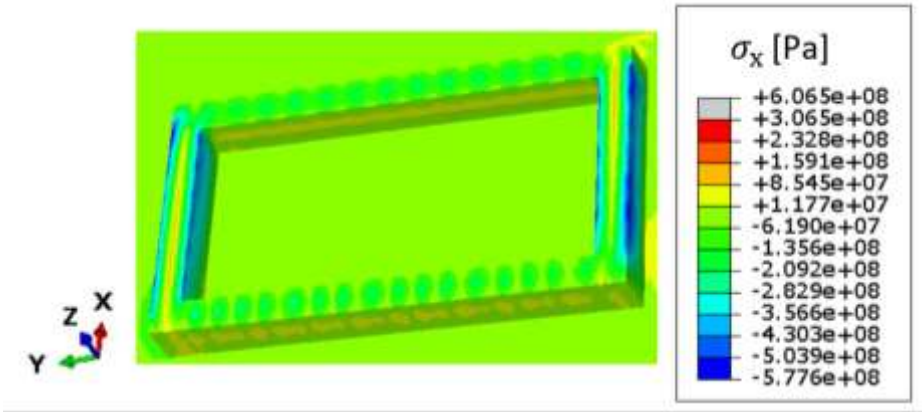

(a)

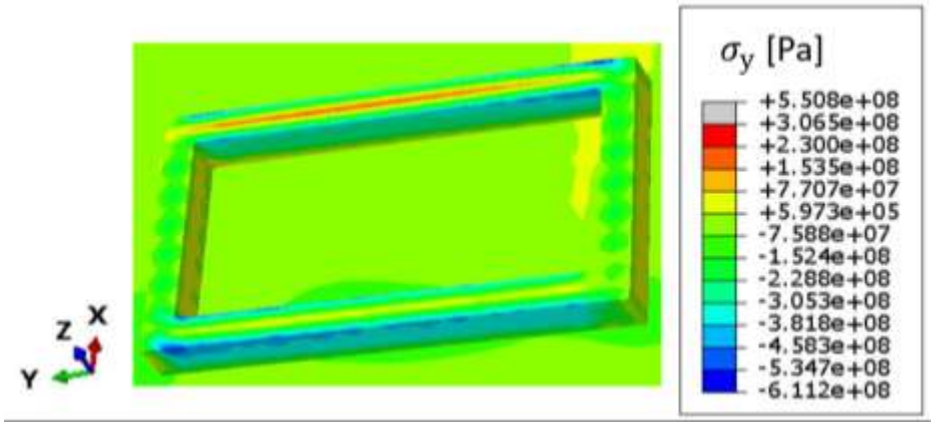

(b)

Figure 3.14. The predicted stress distribution with scanning strategy A (Figure 3.7): (a) σ_x: residual stress along the x direction and (b) σ_y: residual stress along the y direction.

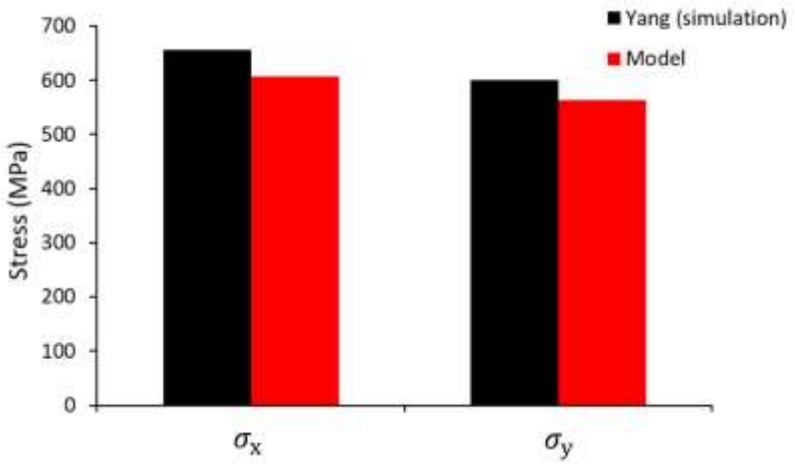

Figure 3.15. The comparison of predicted maximum (spatial) residual stress.

3.4.2 Thermal profile of different scanning strategies

To understand the influence of scanning strategy on the thermal profile, the temperature distributions at certain layers with the different scanning strategies are extracted. The laser scanning sequence is varied while the same laser heat source is employed for all scanning strategies. As a result, the thermal distributions are different based on the scanning strategy. The FE modelling results for the temperature contours with the same legend of the additively manufactured rectangular shaped Ti-6Al-4V specimen at the end of layer 4 with using various scanning strategies are demonstrated in Figure 3.16. The maximum temperature at layer 4 of the rectangular specimen in relation to the respective scanning strategies is indicated by the text and arrow on each image in Figure 3.16. It is clearly shown that both the value and location of maximum temperatures with each scanning strategy are different. Comparing all the scanning strategies, Strategy A (Figure 3.7) exhibits the highest maximum temperature at the bottom of the long side of the specimen (2214 ^{o}C, Figure 3.16 (a)), while Strategy C (Figure 3.7) exhibits the lowest maximum temperature at the right short side of the specimen (2145 ^{o}C, Figure 3.16 (c)). This may be due to the changing direction between each layer providing longer cooling time for the specimen, which may be further improved by including dwell times between individual layers to allow for additional cooling [58]. Strategy B has a predicted maximum

temperature on the left short side of the specimen (2148 ^{o}C, Figure 3.16 (b)), where the start point is changed for each layer (Figure 3.7).

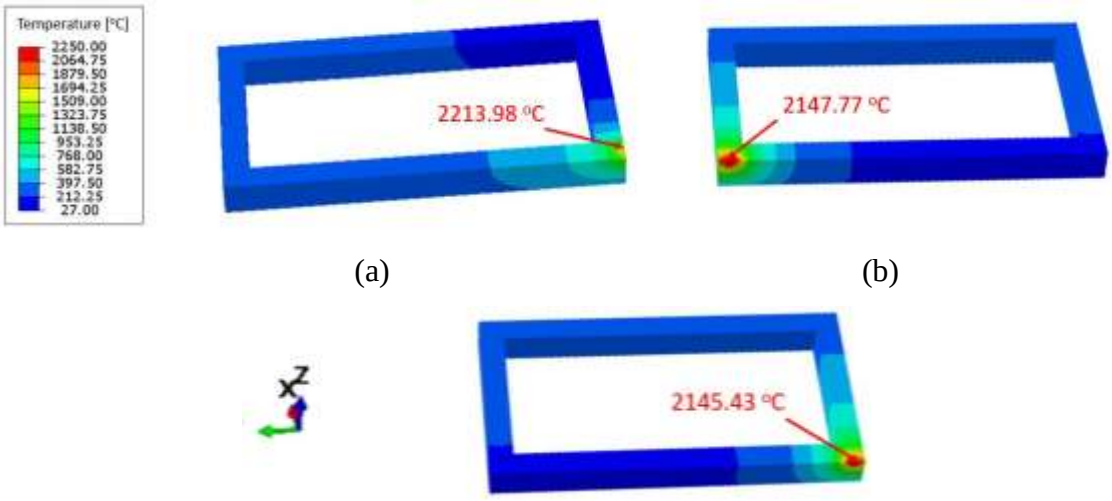

Figure 3.16. The temperature contours at the end of layer 4 with different scanning strategies (see Figure 3.7): (a) Strategy A, (b) Strategy B, (c) Strategy C.

3.4.3 Residual stress of different scanning strategies

Figure 3.17 shows the FE results of the final maximum principal stress distributions for the rectangular shaped Ti-6Al-4V specimens using the different scanning strategies. The scanning strategy (both laser scanning start point and direction) is seen to have an influence on the maximum principal stress distributions. Strategy B gives the highest maximum principal stress (818.6 MPa, Figure 3.17 (b)) but a more uniform distribution when compared to the Strategy A, which gives the second highest maximum principal stress (780.5 MPa, Figure 3.17 (a)), demonstrating the effect of changing the start point between each layer. Strategy C gives the lowest maximum principal stress (733.8 MPa, Figure 3.17 (c)) indicating the beneficial effect of changing the laser direction between each layer, in terms of mitigating residual stress. Specifically, the model predicts about 12 % decrease of maximum principal stress in scanning strategy C compared to that of scanning strategy B.

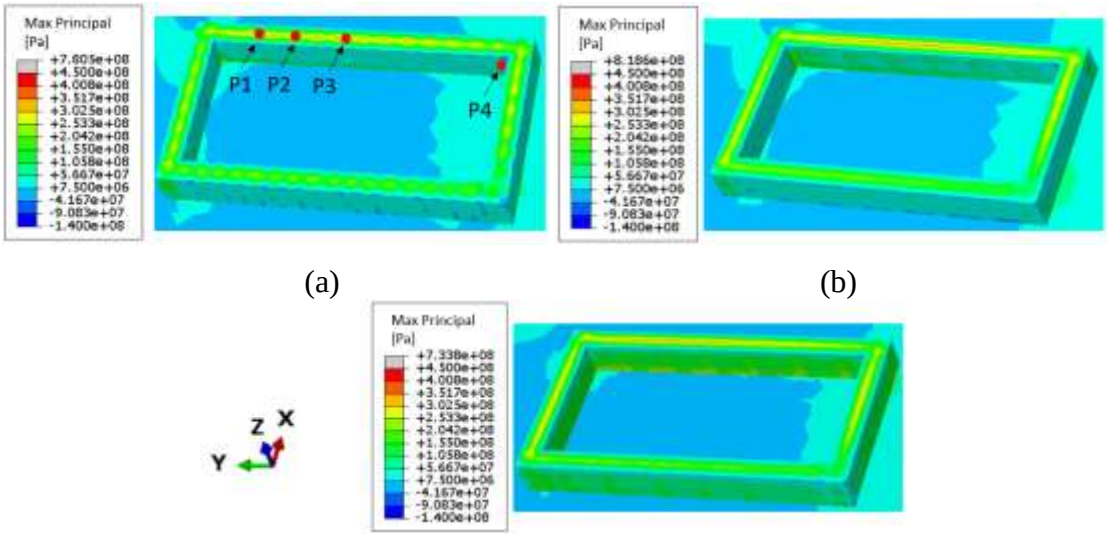

Figure 3.17. The final maximum principal stress for different scanning strategies before releasing substrate constraints: (a) Strategy A, (b) Strategy B, (c) Strategy C.

Figure 3.18 presents the predicted final σ_x residual stresses for the rectangular shaped Ti-6Al-4V specimens before releasing the substrate constraint, which shows that the σ_x stress on the short side of the rectangular shaped specimen is always higher than on the long side. Figure 3.18 (a) shows that the highest σ_x stress (606.5 MPa) occurs with Strategy A (Figure 3.7), which is 7 % larger than Strategy B (562.8 MPa, Figure 3.18 (b)). Strategy C gives the lowest σ_x stress (528.5 MPa), as shown in Figure 3.18 (c), which is 13 % lower than Strategy A. Strategies B and C have similar σ_x stress distributions and more uniform σ_x stress distributions on the longer side of the specimen than Strategy A.

Figure 3.19 shows the σ_y residual stress distributions. Strategy B produces a significantly higher σ_y residual stresses (693 MPa, Figure 3.19 (b)) than the other two scanning strategies (Strategy A: 550.8 MPa, see Figure 3.19 (a) and Strategy C: 595.3 MPa, see Figure 3.19 (c)), which are different with the σ_x residual stresses (Figure 3.18). Strategy A is predicted have the lowest σ_y stress (550.8 MPa) but highest σ_x stress (606.5 MPa), which may be caused by the higher temperature (Figure 3.16). Except for Strategy A, the

other two scanning strategies have similar and more uniform σ_y stress distributions on the shorter side.

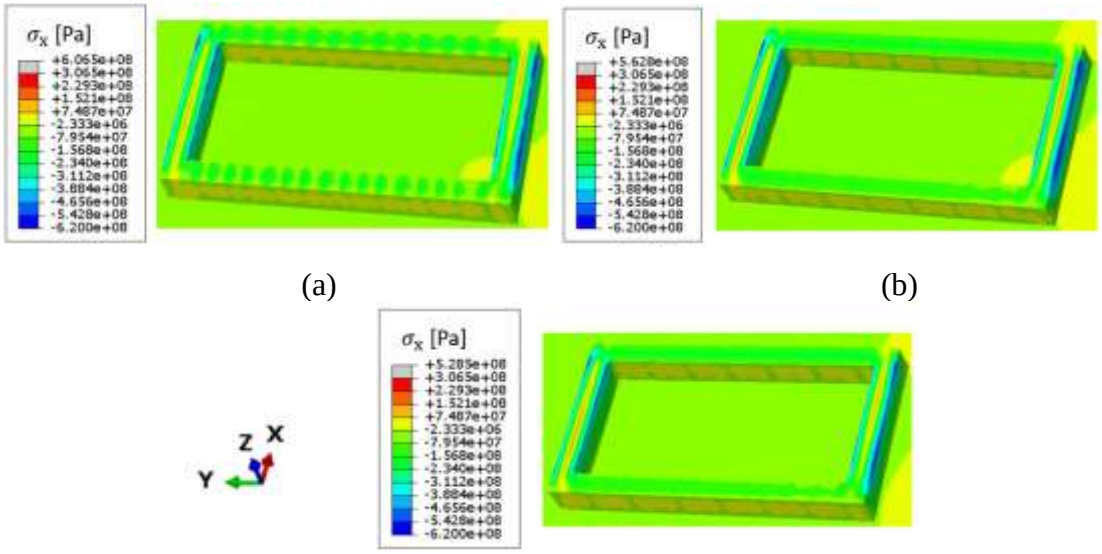

Figure 3.18. The final σ_x residual stress distributions for different scanning strategies: (a) Strategy A, (b) Strategy B, (c) Strategy C.

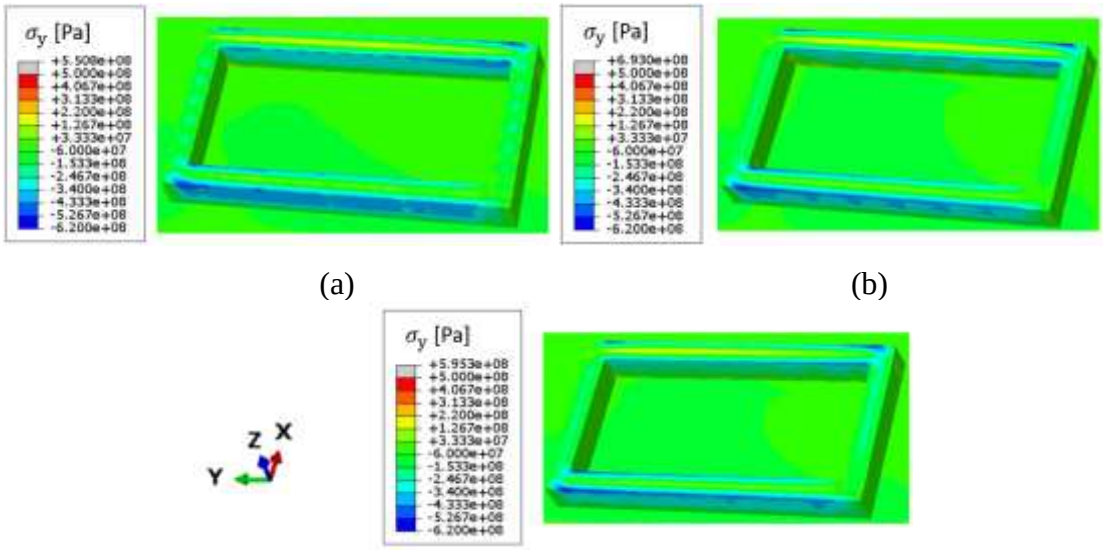

Figure 3.19. The final σ_y residual stress distributions for different scanning strategies: (a) Strategy A, (b) Strategy B, (c) Strategy C.

Figure 3.20 shows the maximum principal stress distributions for the short side (along Line 1) on the top of the substrate. It can be seen that the highest maximum principal stress is generated for Strategy B along Line 1. Figure 3.21 shows the comparison of predicted highest residual stress (σ_x, σ_y and maximum principal stress) for all three scanning strategies (Figure 3.7). Figure 3.22 shows the comparison of predicted maximum distortion for all different scanning strategies. The results of maximum principal stress and directional residual stress show that Strategy B gives the highest maximum principal and σ_y stresses, while Strategy C gives the lowest maximum principal and σ_x stresses. Changing the laser direction between layers (Strategy C, Figure 3.7) caused a 46.7 MPa lower maximum principal stress and 0.32 mm lower maximum distortion compared to keeping the same laser sequence for each layer (Strategy A, Figure 3.7), which indicates that changing the laser direction between layers is beneficial for reducing residual stress and distortion.

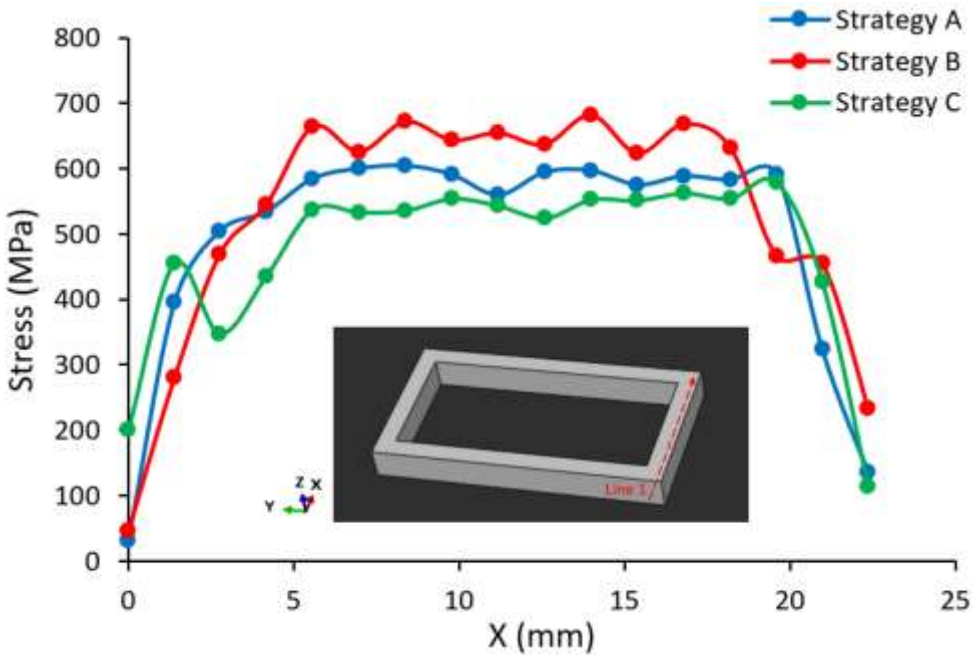

Figure 3.20. Comparison of maximum principal stress distributions for different scanning strategies along Line 1.

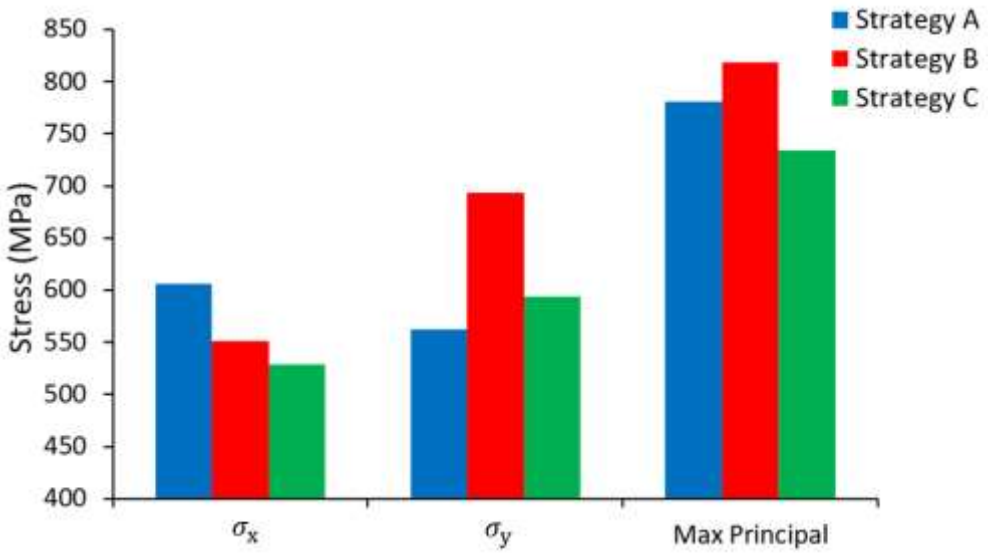

Figure 3.21. Comparison of predicted maximum final residual stresses for different scanning strategies.

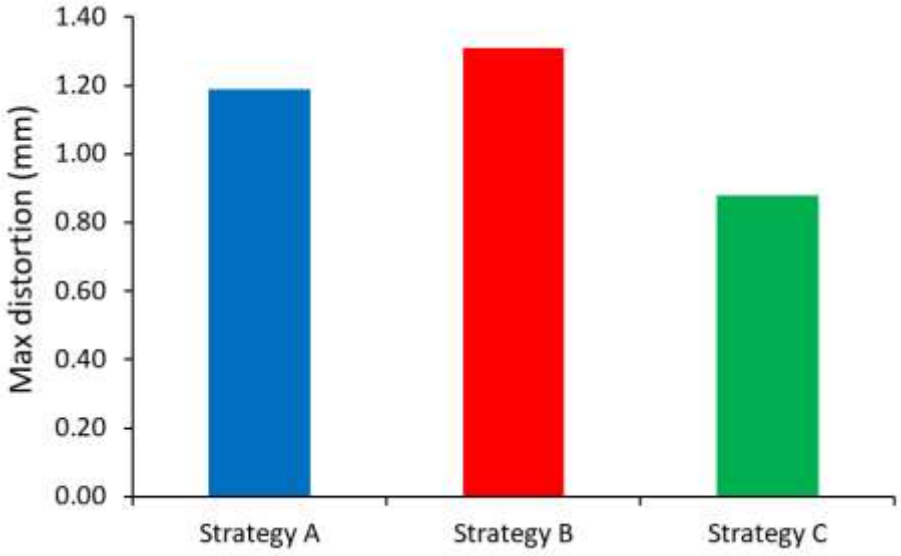

Figure 3.22. Comparison of predicted maximum distortions for different scanning strategies.

3.4.4 Fatigue life prediction

The equation relating fatigue life N_f to stress range, mean stress and residual stress is given by combining the well-known Goodman equation for effect of mean stress with Basquin's equation [26, 27]:

$$N_f = \left[\frac{\sigma_a}{\sigma_f'\left(1 - \frac{\sigma_m + \sigma_r}{\sigma_{TS}}\right)}\right]^{\frac{1}{b}} \tag{3.14}$$

where σ_f' and b are high-cycle fatigue material constants, known as fatigue strength coefficient (MPa) and exponent, respectively, σ_a is alternating stress range (MPa), σ_m is mean stress (MPa), σ_r is residual stress (MPa) and σ_{TS} is ultimate tensile strength (MPa). Typical identified material constants and mechanical properties of as-built AM Ti-6Al-4V used in Eq. (3.14) are provided in Table 3.4 [59-61]. The alternating stress range and the mean stress are assumed to be 200 MPa and 100 MPa, respectively. Life predictions for four different sample locations, P1, P2, P3 and P4 (see Figure 3.17 (a)) within the as-built AM Ti-6Al-4V component under Strategy A are given in Table 3.5. Table 3.6 shows the life predictions of as-built AM Ti-6Al-4V component at the location of maximum principal stress for each scanning strategy (Figure 3.17). It is important to note that different AM process parameters can lead to different mechanical properties as well as fatigue behavior [61]. Specifically, for example, the fatigue strength coefficient for DED Ti-6Al-4V is almost double that for PBF, and the predicted N_f for DED is significantly lower than that for PBF.

Table 3.4. Identified material constants and mechanical properties of as-built AM Ti-6Al-4V.

AM process	Fatigue strength coefficient σ_f' (MPa)	Fatigue strength exponent b	Ultimate tensile strength σ_{TS} (MPa)
PBF [59, 60]	1163	-0.046	1182
DED [61]	2310	-0.136	1038

Table 3.5. Life predictions of as-built AM Ti-6Al-4V component at different positions under Strategy A (positions as labelled in Figure 3.17 (a)).

	Position 1	Position 2	Position 3	Position 4
Residual stress σ_r (MPa)	650	700	750	-100
$\sigma_m + \sigma_r$ (MPa)	750	800	850	0
Basquin-Goodman N_f (PBF)	1.31×10^7	9.05×10^5	4.29×10^4	$> 10^8$
Basquin-Goodman N_f (DED)	5.24×10^3	1.29×10^3	227	6.50×10^7

	Position 1	Position 2	Position 3	Position 4
Residual stress σ_r (MPa)	650	700	750	-100
$\sigma_m + \sigma_r$ (MPa)	750	800	850	0
Basquin-Goodman N_f (DED)	5.24×10^3	1.29×10^3	227	6.50×10^7

Table 3.6. Life predictions of as-built AM Ti-6Al-4V component at the maximum principal stress position under different strategies.

	Strategy A	Strategy B	Strategy C
Residual stress σ_r (MPa)	780.5	818.6	733.8
$\sigma_m + \sigma_r$ (MPa)	880.5	918.5	833.8
Basquin-Goodman N_f (PBF)	5.27×10^3	280	1.21×10^5
Basquin-Goodman N_f (DED)	61	8	418

3.5 Discussion

The present computational model offers an efficient and accurate method for simulation of the DED process of macro-scale metal components, which includes prediction of thermal histories during AM process and AM-induced residual stresses with effects of

different scanning strategies. To the authors' knowledge, this is the first time the 'Abaqus AM' method has been presented for comparison against the layer-by-layer method (see Figure 3.4) and investigation of effects of scanning strategies in DED process. Existing research usually focuses on one or two aspects with specific AM modelling techniques and AM process parameters, such as predicting residual stress with the layer-by-layer method [14, 16], thermal analysis of DED process with different scanning strategies [62], thermal and mechanical behaviour prediction in the DED process using the 'Model Change' technique [19, 33].

In the thermal process simulation presented here, the layer-by-layer method is adopted to predict the thermal history of the rectangular shaped Ti-6Al-4V specimen (Figure 3.6) during the DED process for simulation simplification and computational cost saving; however, the effect of scanning strategy cannot be investigated due to the simplification with respect to material deposition [63] ((e.g. see Figure 3.9). The new 'Abaqus AM' is employed to simulate the complete AM process (Figure 3.5), and the generally-accepted double ellipsoidal volumetric Goldak heat source model (Figure 3.3) is implemented via the built-in subroutine function to describe the heat flux during the DED process [40], in which the layer thickness is usually greater than that of the PBF process [64], where the Gaussian surface heat flux is often used due to the minuscule layer thickness [21]. The predicted thermal history, including peak temperatures and cooling rate, is validated by comparison with published numerical and experimental results (see Figure 3.10, Figure 3.12) [19, 56]. It is clear that the model captures the peak temperatures accurately well, and predicts a larger cooling rate compared to previous published 'Model Change' prediction (viz. ~ 200 ^{o}C/s, as compared to ~ 100 ^{o}C) (Table 3.3) [33]. However, the prediction by the present model is within the typical cooling rate range (< 10^{3} ^{o}C/s) [65], given significant improvement compared to the experimental measurement (219 ± 6.1 ^{o}C/s) from a five-layer Ti-6Al-4V DED process [56]. The accuracy of the present model could potentially be further improved by including other physical phenomena, such as laser-powder interaction, phase transition (melting, vaporization and solidification), molten pool hydrodynamics [66, 67].

In the current process simulation, a sequentially coupled thermal and mechanical FE analysis strategy is employed due to the weak nature of mechanical to thermal field coupling in the DED process [24, 63]. It is worth pointing out that a fully coupled thermal-mechanical analysis, with much higher computational cost, has been compared to the sequentially coupled thermal-mechanical, with significant difference observed [19]. When the laser heating source starts along the x direction for depositing the shorter side of the first layer of the rectangular shaped Ti-6Al-4V specimen (Figure 3.7), compressive stress is generated in front of the heating source due to thermal expansion; tensile stress is generated due to thermal contraction when the cooling starts after the heating source passes [29, 68]. The predicted maximum temperature in Figure 3.13 is within 1% of the results reported by Yang et al [19]. The tensile (positive) σ_{x} residual stress causes a bending shape deformation along the shorter side of the specimen when the part reaches room temperature after the cooling period (see Figure 3.14 (a)). The same analysis can be used for the tensile σ_{y} residual stress along the y direction when the longer side of the specimen is being deposited (see Figure 3.14 (b)). The predictions obtained from the present model are in reasonable agreement with the published numerical and experimental results [19, 33], providing confidence in the modelling approach.

Finally, the effect of scanning strategy on thermal profile and residual stress is investigated by defining different event series for simulating the laser beam movement path in Figure 3.7. The present work managed to reveal and capture the impact of scanning strategy, which shows that the scanning strategy can determine both the temperature (Figure 3.16) and stress distributions (Figure 3.17, Figure 3.18, Figure 3.19) of the rectangular shaped Ti-6Al-4V specimen. Significant influence of scanning strategy on final part residual stress is also predicted by Zhang et.al. [39] and Lu et al. [55]. Woo et al. [69] experimentally measured residual stress of DED manufactured specimens with different strategies (bidirectional, orthogonal and island scan) using four different methods (the contour method, neutron diffraction, and deep/incremental center hole drilling), demonstrating benefits of optimized residual stress distributions, as the range of stress

values (from tension to compression) was significantly alleviated from 950 MPa, for the bidirectional scan, to 430 MPa, for the island scan. The results obtained by different measurement methods are consistent. Table 3.5 shows that the increase of the tensile residual stress significantly decreased the fatigue life for both PBF and DED process (see life predictions at positions from Position 1 to Position 3), and there will be a beneficial effect with compressive residual stress (see life predictions at Position 4). Based on the results shown in Figure 3.20, Figure 3.21 and

	Position 1	Position 2	Position 3	Position 4
Residual stress σ_r (MPa)	650	700	750	-100
$\sigma_m + \sigma_r$ (MPa)	750	800	850	0
Basquin-Goodman N_f (DED)	5.24×10^3	1.29×10^3	227	6.50×10^7

Table 3.6, an appropriate scanning strategy should be selected for optimizing residual stress, particularly for mitigating tensile residual stresses, which are detrimental to fatigue performance of AM parts [70]. It can be seen that the predicted lives, using the Basquin fatigue parameters identified for DED Ti-6Al-4V, are significantly shorter than those for PBF. For example, Table 3.5 shows a minimum life of about 227 cycles using the DED properties for Strategy A at the different selected locations;

	Position 1	Position 2	Position 3	Position 4
Residual stress σ_r (MPa)	650	700	750	-100
$\sigma_m + \sigma_r$ (MPa)	750	800	850	0
Basquin-Goodman N_f (DED)	5.24×10^3	1.29×10^3	227	6.50×10^7

Table 3.6 shows an even more detrimental predicted effect of scanning strategy, with respect to DED or PBF, showing a minimum life of 8 cycles for Strategy B with DED properties, compared to 280 cycles using the PBF properties.

A key next step for the present work, is the extension to include the effect of substrate constraints. Recently, Zhang et al. [39] have investigated the influence of substrate constraints on the residual stress, a decrease of around 200 MPa in maximum principal stress was found when comparing the predicted residual stress before and after releasing the substrate constraints.

The development of a process-structure-property (PSP) tool could make a significant contribution to the AM process optimization, such as saving time and cost compared to existing trial-and-error methods. Recently, Yang et al. [71] have presented a physically-based structure-property model for assessing the mechanical properties (yield stress, ultimate tensile strength, uniform elongation and flow stress) of PBF manufactured Ti-6Al-4V, including the effects of solutes, grain size, phase volume fraction and dislocation density, the predicted tensile stress-strain responses are validated against measured tensile test data from 25 ^{o}C to 1000 ^{o}C. The effects of temperature-dependence on tensile stress-strain response is captured more accurately by including solid-state phase transformation (SSPT) effects, while stress is significantly over-predicted for temperatures above 400 ^{o}C when excluding the SSPT effects. In future work, it is planned to combine the current model with the process-structure model [21] for microstructure prediction based on the FE predicted thermal histories, and with the structure-property model [71] for resultant mechanical properties prediction of realistic, large-scale AM components, for capturing the effects of key AM manufacturing parameters for AM process optimization. Fatigue life prediction is particularly important for AM processed metals [72]. It is also intended to integrate the achieved PSP tool with our previously developed physically-based fatigue crack initiation (FCI) model [73] to predict effects of AM manufacturing process on the fatigue response of complex AM geometries, such as the conformal cooling injection moulding tools.

3.6 Conclusions

This paper presents a finite element modelling framework for the full process simulation of complex Ti-6Al-4V components in directed energy deposition additive manufacturing process. The method is based on the combined use of (i) application of the present FE-based AM method to define the additive manufacturing process parameters (moving heat source, toolpath, laser power, etc) as event series for input and (ii) the sequentially coupled thermo-mechanical analysis for the prediction of thermal profile and residual stress. The key conclusions are:

- The thermal and mechanical analysis are successfully validated against published numerical and experimental measurements, giving close agreement for temperature histories at different measurement locations. In particular, the new model shows significantly improved agreement of cooling rate, a key parameter for predicting phase transformations, with the measured result, compared to previously published simulations.
- Comparison with the more simplified, but commonly-used layer-by-layer method, with measured thermal histories and the proposed Abaqus AM method, has demonstrated that the layer-by-layer method is significantly less accurate for capturing peak temperatures and specific temporal variation (e.g. cooling rate), particularly in relation to layer-based phenomena, as expected. The computational cost of the layer-by-layer method could be further improved by using the ‘Layer scaling’ technique.
- The scanning strategy is shown to have a significant effect on temperature profile and residual stress of the rectangular shaped Ti-6Al-4V specimen during directed energy deposition. Changing laser direction between layers was shown to be beneficial for mitigating detrimental residual stress.
- Basquin-Goodman high cycle fatigue life calculations, for sample locations (residual stresses) within the as-built AM Ti-6Al-4V component, have demonstrated (i) the detrimental effects of AM-induced tensile residual stress, (ii) the beneficial effect of AM-induced compressive residual stress, (iii) the capability

for mitigating detrimental residual stress effects via design of scanning strategy, and (iv) the significantly lower fatigue lives for DED than PBF, based on previously-measured DED and PBF HCF fatigue constants.

- The modelling results demonstrate the capability of the present FE-based AM method, which greatly reduces input-output data and computational time and makes the additive manufacturing process simulation of complex engineering components more feasible. Although this study focussed on the laser directed energy deposition process, the method is equally applicable to other AM processes, such as laser powder bed fusion process. Future work will focus on such processes.
- Further research work will require more accurate experimental measurements, such as the material constitutive behaviour and properties at elevated temperatures, to improve the accuracy of additive manufacturing process simulation.

3.7 References

[1] M. Attaran, The rise of 3-D printing: The advantages of additive manufacturing over traditional manufacturing, Business Horizons 60(5) (2017) 677-688.
[2] T. Gatsos, K.A. Elsayed, Y. Zhai, D.A. Lados, Review on Computational Modeling of Process–Microstructure–Property Relationships in Metal Additive Manufacturing, JOM 72(1) (2020) 403-419.
[3] S.M. Thompson, L. Bian, N. Shamsaei, A. Yadollahi, An overview of Direct Laser Deposition for additive manufacturing; Part I: Transport phenomena, modeling and diagnostics, Additive Manufacturing 8 (2015) 36-62.
[4] W.E. Frazier, Metal additive manufacturing: a review, Journal of Materials Engineering and Performance 23(6) (2014) 1917-1928.
[5] A. Vafadar, F. Guzzomi, A. Rassau, K. Hayward, Advances in metal additive manufacturing: a review of common processes, industrial applications, and current challenges, Applied Sciences 11(3) (2021) 1213.
[6] B. Blakey-Milner, P. Gradl, G. Snedden, M. Brooks, J. Pitot, E. Lopez, M. Leary, F. Berto, A. du Plessis, Metal additive manufacturing in aerospace: A review, Materials & Design (2021) 110008.
[7] D. Feenstra, R. Banerjee, H. Fraser, A. Huang, A. Molotnikov, N. Birbilis, Critical review of the state of the art in multi-material fabrication via directed energy deposition, Current Opinion in Solid State and Materials Science 25(4) (2021) 100924.
[8] X. Song, S. Feih, W. Zhai, C.-N. Sun, F. Li, R. Maiti, J. Wei, Y. Yang, V. Oancea, L. Romano Brandt, A.M. Korsunsky, Advances in additive manufacturing process

simulation: Residual stresses and distortion predictions in complex metallic components, Materials & Design 193 (2020) 108779.
[9] E.R. Denlinger, J.C. Heigel, P. Michaleris, Residual stress and distortion modeling of electron beam direct manufacturing Ti-6Al-4V, Proceedings of the Institution of Mechanical Engineers, Part B: Journal of Engineering Manufacture 229(10) (2015) 1803-1813.
[10] P.J. Withers, H. Bhadeshia, Residual stress. Part 1–measurement techniques, Materials science and Technology 17(4) (2001) 355-365.
[11] P. Edwards, M. Ramulu, Fatigue performance evaluation of selective laser melted Ti–6Al–4V, Materials Science and Engineering: A 598 (2014) 327-337.
[12] P. Edwards, A. O'conner, M. Ramulu, Electron beam additive manufacturing of titanium components: properties and performance, Journal of Manufacturing Science and Engineering 135(6) (2013) 061016.
[13] M.F. Zaeh, G. Branner, Investigations on residual stresses and deformations in selective laser melting, Production Engineering 4(1) (2010) 35-45.
[14] R.A. Barrett, T. Etienne, C. Duddy, N.M. Harrison, Residual stress prediction in a powder bed fusion manufactured Ti6Al4V hip stem, AIP Conference Proceedings 1896 (2017) 040018.
[15] W. Zhang, M. Tong, N.M. Harrison, Resolution, energy and time dependency on layer scaling in finite element modelling of laser beam powder bed fusion additive manufacturing, Additive Manufacturing 28 (2019) 610-620.
[16] C. Chen, S. Chang, J. Zhu, Z. Xiao, H. Zhu, X. Zeng, Residual stress of typical parts in laser powder bed fusion, Journal of Manufacturing Processes 59 (2020) 621-628.
[17] K.S. Ribeiro, F.E. Mariani, R.T. Coelho, A study of different deposition strategies in direct energy deposition (DED) processes, Procedia Manufacturing 48 (2020) 663-670.
[18] M. Rauch, U.V. Nwankpa, J.-Y. Hascoet, Investigation of deposition strategy on wire and arc additive manufacturing of aluminium components, Journal of Advanced Joining Processes 4 (2021) 100074.
[19] Q. Yang, P. Zhang, L. Cheng, Z. Min, M. Chyu, A.C. To, Finite element modeling and validation of thermomechanical behavior of Ti-6Al-4V in directed energy deposition additive manufacturing, Additive Manufacturing 12 (2016) 169-177.
[20] M. Chiumenti, E. Neiva, E. Salsi, M. Cervera, S. Badia, J. Moya, Z. Chen, C. Lee, C. Davies, Numerical modelling and experimental validation in Selective Laser Melting, Additive Manufacturing 18 (2017) 171-185.
[21] X. Yang, R.A. Barrett, M. Tong, N.M. Harrison, S.B. Leen, Towards a process-structure model for Ti-6Al-4V during additive manufacturing, Journal of Manufacturing Processes 61 (2021) 428-439.
[22] Abaqus Analysis User's Guide, Dassault Systemes (2018).
[23] J.P. Pragana, I.M. Bragança, L. Reis, C.M. Silva, P.A. Martins, Formability of wire-arc deposited AISI 316L sheets for hybrid additive manufacturing applications, Proceedings of the Institution of Mechanical Engineers, Part L: Journal of Materials: Design and Applications 235(12) (2021) 2839-2850.
[24] Y. Yang, M. Allen, T. London, V. Oancea, Residual Strain Predictions for a Powder Bed Fusion Inconel 625 Single Cantilever Part, Integrating Materials and Manufacturing

Innovation 8(3) (2019) 294-304.
[25] W. Jiang, X. Xie, T. Wang, X. Zhang, S.-T. Tu, J. Wang, X. Zhao, Fatigue life prediction of 316L stainless steel weld joint including the role of residual stress and its evolution: Experimental and modelling, International Journal of Fatigue 143 (2021) 105997.
[26] R.J. Devaney, P.E. O'Donoghue, S.B. Leen, Global and local fatigue analysis of X100 and X60 steel catenary riser girth welds, Journal of Structural Integrity and Maintenance 2(3) (2017) 181-189.
[27] C.A. Sweeney, P.E. McHugh, J.P. McGarry, S.B. Leen, Micromechanical methodology for fatigue in cardiovascular stents, International Journal of Fatigue 44 (2012) 202-216.
[28] R.I. Stephens, A. Fatemi, R.R. Stephens, H.O. Fuchs, Metal fatigue in engineering, John Wiley & Sons2000.
[29] J. Ding, P. Colegrove, J. Mehnen, S. Ganguly, P.S. Almeida, F. Wang, S. Williams, Thermo-mechanical analysis of Wire and Arc Additive Layer Manufacturing process on large multi-layer parts, Computational Materials Science 50(12) (2011) 3315-3322.
[30] F.E. Bock, J. Herrnring, M. Froend, J. Enz, N. Kashaev, B. Klusemann, Experimental and numerical thermo-mechanical analysis of wire-based laser metal deposition of Al-Mg alloys, Journal of Manufacturing Processes 64 (2021) 982-995.
[31] L. Li, F. Liou, Numerical Investigation of Thermo-Mechanical Field during Selective Laser Melting Process with Experimental Validation, Metals 11(7) (2021) 1003.
[32] M. Chiumenti, M. Cervera, N. Dialami, B. Wu, L. Jinwei, C.A. de Saracibar, Numerical modeling of the electron beam welding and its experimental validation, Finite Elements in Analysis and Design 121 (2016) 118-133.
[33] C. Baykasoglu, O. Akyildiz, D. Candemir, Q. Yang, A.C. To, Predicting Microstructure Evolution During Directed Energy Deposition Additive Manufacturing of Ti-6Al-4V, Journal of Manufacturing Science and Engineering 140(5) (2018) 051003.
[34] M. Li, J.S. Kang, Y. Hu, Anisotropic thermal conductivity measurement using a new Asymmetric-Beam Time-Domain Thermoreflectance (AB-TDTR) method, Review of Scientific Instruments 89(8) (2018) 084901.
[35] M. Chiumenti, M. Cervera, C.A. de Saracibar, N. Dialami, Numerical modeling of friction stir welding processes, Computer Methods in Applied Mechanics and Engineering 254 (2013) 353-369.
[36] J. Heigel, P. Michaleris, E.W. Reutzel, Thermo-mechanical model development and validation of directed energy deposition additive manufacturing of Ti–6Al–4V, Additive Manufacturing 5 (2015) 9-19.
[37] M.F. Gouge, J.C. Heigel, P. Michaleris, T.A. Palmer, Modeling forced convection in the thermal simulation of laser cladding processes, The International Journal of Advanced Manufacturing Technology 79(1-4) (2015) 307-320.
[38] S.A. Khairallah, A.T. Anderson, A. Rubenchik, W.E. King, Laser powder-bed fusion additive manufacturing: Physics of complex melt flow and formation mechanisms of pores, spatter, and denudation zones, Acta Materialia 108 (2016) 36-45.
[39] W. Zhang, M. Tong, N.M. Harrison, Scanning strategies effect on temperature, residual stress and deformation by multi-laser beam powder bed fusion manufacturing,

Additive Manufacturing 36 (2020) 101507.
[40] J. Goldak, A. Chakravarti, M. Bibby, A new finite element model for welding heat sources, Metallurgical transactions B 15(2) (1984) 299-305.
[41] C. Baykasoğlu, O. Akyildiz, M. Tunay, A.C. To, A process-microstructure finite element simulation framework for predicting phase transformations and microhardness for directed energy deposition of Ti6Al4V, Additive Manufacturing 35 (2020) 101252.
[42] P. Michaleris, Modeling metal deposition in heat transfer analyses of additive manufacturing processes, Finite Elements in Analysis and Design 86 (2014) 51-60.
[43] M. Chiumenti, M. Cervera, A. Salmi, C.A. De Saracibar, N. Dialami, K. Matsui, Finite element modeling of multi-pass welding and shaped metal deposition processes, Computer Methods in Applied Mechanics and Engineering 199(37-40) (2010) 2343-2359.
[44] B. Baufeld, O. van der Biest, Mechanical properties of Ti-6Al-4V specimens produced by shaped metal deposition, Science and Technology of Advanced Materials 10(1) (2009) 015008.
[45] A. Anca, V.D. Fachinotti, G. Escobar‐Palafox, A. Cardona, Computational modelling of shaped metal deposition, International Journal for Numerical Methods in Engineering 85(1) (2011) 84-106.
[46] E.R. Denlinger, J. Irwin, P. Michaleris, Thermomechanical modeling of additive manufacturing large parts, Journal of Manufacturing Science and Engineering 136(6) (2014) 061007.
[47] M.F. Zaeh, G. Branner, Investigations on residual stresses and deformations in selective laser melting, Production Engineering 4(1) (2009) 35-45.
[48] P. Mehta, C.G. Berdanier, M. Malviya, C. Miller, G. Manogharan, An Empirical Study Linking Additive Manufacturing Design Process to Success in Manufacturability, 2019 International Solid Freeform Fabrication Symposium, University of Texas at Austin, 2019.
[49] Q. Chen, X. Liang, D. Hayduke, J. Liu, L. Cheng, J. Oskin, R. Whitmore, A.C. To, An inherent strain based multiscale modeling framework for simulating part-scale residual deformation for direct metal laser sintering, Additive Manufacturing 28 (2019) 406-418.
[50] M. Li, J. Li, D. Yang, B. He, Dimensional Deviation Management for Selective Laser Melted Ti6Al4V Alloy Blade, Frontiers in Materials 7 (2020) 42.
[51] N. Peter, Z. Pitts, S. Thompson, A. Saharan, Benchmarking build simulation software for laser powder bed fusion of metals, Additive Manufacturing 36 (2020) 101531.
[52] Abaqus Analysis User's Guide, Dassault Systems (2020).
[53] T. de Terris, O. Andreau, P. Peyre, F. Adamski, I. Koutiri, C. Gorny, C. Dupuy, Optimization and comparison of porosity rate measurement methods of Selective Laser Melted metallic parts, Additive Manufacturing 28 (2019) 802-813.
[54] S.V. Skvortsova, M.A. German, V.S. Spektor, Structure and Properties of Alloy Ti–6Al–4V Samples Fabricated by 3D Printing, Russian Metallurgy (Metally) 2019(9) (2019) 863-872.
[55] X. Lu, M. Cervera, M. Chiumenti, J. Li, X. Ji, G. Zhang, X. Lin, Modeling of the Effect of the Building Strategy on the Thermomechanical Response of Ti-6Al-4V Rectangular Parts Manufactured by Laser Directed Energy Deposition, Metals 10(12) (2020).

[56] F. Lia, J.Z. Park, J.S. Keist, S. Joshi, R.P. Martukanitz, Thermal and microstructural analysis of laser-based directed energy deposition for Ti-6Al-4V and Inconel 625 deposits, Materials Science and Engineering: A 717 (2018) 1-10.
[57] S. Riza, S. Masood, C. Wen, Laser-assisted additive manufacturing for metallic biomedical scaffolds, Elsevier2014.
[58] C. Guevenoux, S. Hallais, A. Charles, E. Charkaluk, A. Constantinescu, Influence of interlayer dwell time on the microstructure of Inconel 718 Laser Cladded components, Optics & Laser Technology 128 (2020) 106218.
[59] D. Agius, K.I. Kourousis, C. Wallbrink, T. Song, Cyclic plasticity and microstructure of as-built SLM Ti-6Al-4V: The effect of build orientation, Materials Science and Engineering: A 701 (2017) 85-100.
[60] R. Biswal, A.K. Syed, X. Zhang, Assessment of the effect of isolated porosity defects on the fatigue performance of additive manufactured titanium alloy, Additive Manufacturing 23 (2018) 433-442.
[61] A. Sterling, N. Shamsaei, B. Torries, S.M. Thompson, Fatigue Behaviour of Additively Manufactured Ti-6Al-4V, Procedia Engineering 133 (2015) 576-589.
[62] Y. Zhang, H. Jing, L. Xu, Y. Han, L. Zhao, Effects of different scanning patterns on nickel alloy-directed energy deposition based on thermal analysis, Virtual and Physical Prototyping 16 (2021) 98-115.
[63] R.J. Williams, C.M. Davies, P.A. Hooper, A pragmatic part scale model for residual stress and distortion prediction in powder bed fusion, Additive Manufacturing 22 (2018) 416-425.
[64] Y. Zhang, L. Wu, X. Guo, S. Kane, Y. Deng, Y.-G. Jung, J.-H. Lee, J. Zhang, Additive manufacturing of metallic materials: a review, Journal of Materials Engineering and Performance 27(1) (2018) 1-13.
[65] D. Herzog, V. Seyda, E. Wycisk, C. Emmelmann, Additive manufacturing of metals, Acta Materialia 117 (2016) 371-392.
[66] J.I. Arrizubieta, A. Lamikiz, F. Klocke, S. Martínez, K. Arntz, E. Ukar, Evaluation of the relevance of melt pool dynamics in Laser Material Deposition process modeling, International Journal of Heat and Mass Transfer 115 (2017) 80-91.
[67] A. Aggarwal, A. Chouhan, S. Patel, D. Yadav, A. Kumar, A. Vinod, K. Prashanth, N. Gurao, Role of impinging powder particles on melt pool hydrodynamics, thermal behaviour and microstructure in laser-assisted DED process: A particle-scale DEM–CFD–CA approach, International Journal of Heat and Mass Transfer 158 (2020) 119989.
[68] J. Ding, Thermo-mechanical analysis of wire and arc additive manufacturing process, Cranfield University, 2012.
[69] W. Woo, D.-K. Kim, E.J. Kingston, V. Luzin, F. Salvemini, M.R. Hill, Effect of interlayers and scanning strategies on through-thickness residual stress distributions in additive manufactured ferritic-austenitic steel structure, Materials Science and Engineering: A 744 (2019) 618-629.
[70] N. Shamsaei, J. Simsiriwong, Fatigue behaviour of additively-manufactured metallic parts, Procedia Structural Integrity 7 (2017) 3-10.
[71] X. Yang, R.A. Barrett, N.M. Harrison, S.B. Leen, A physically-based structure-property model for additively manufactured Ti-6Al-4V, Materials & Design 205 (2021)

109709.
[72] Z. Zhan, H. Li, K.Y. Lam, Development of a novel fatigue damage model with AM effects for life prediction of commonly-used alloys in aerospace, International Journal of Mechanical Sciences 155 (2019) 110-124.
[73] J. Zhou, R.A. Barrett, S.B. Leen, A physically-based method for predicting high temperature fatigue crack initiation in P91 welded steel, International Journal of Fatigue 153 (2021) 106480.

4 Finite element modelling for mitigation of residual stress and distortion in macro-scale powder bed fusion components

Jinbiao Zhou[1,2,3], Richard A. Barrett[1,2,3], Sean B. Leen[1,2,3]

[1]Mechanical Engineering, College of Engineering and Informatics, University of Galway.

[2]Ryan Institute for Environmental, Marine and Energy Research, University of Galway.

[3]I-Form Advanced Manufacturing Research Centre, Ireland.

Jinbiao Zhou: Conceptualization, Methodology, Software, Writing - original draft.

Summary:

This chapter adopts the AM simulation technique presented in the previous chapter and applies it to the prediction of residual strains, stresses and deformations in the NIST published benchmark for PBF of Inconel 625. Ultimately, the results in this chapter will guide the selection of optimal manufacturing protocols and integration of the FE-based AM modelling for industrial application with complex geometries.

4.1 Abstract

Powder bed fusion (PBF) has attracted significant attention in many applications due to its capability of fabricating complex and customized metal parts. However, the potential for high inherent residual stresses that produce distortion in additive manufacturing (AM) components, prevents more widespread application of the AM technique. Efficient and accurate prediction of residual stress and distortion at component-level (macro-scale) is a complex task. Although process-level (meso-scale) thermo-mechanical simulations have resulted in accurate predictions for small-scale parts, the computational times (typically weeks) and memory requirements for application of such methods to component-level are prohibitive. The main goal of the current study therefore is to present an efficient and accurate finite element (FE) simulation method with detailed validation for PBF manufacture of a complex 3D Inconel 625 benchmark bridge component (macro-scale). The simulation results are successfully validated against the published benchmark experimental measurements from neutron diffraction, X-ray diffraction (XRD), contour method and coordinate measurement machine (CMM) by the National Institute of Standards and Technology (NIST) laboratory. A key additional novelty of the present work is the investigation of the effects of substrate removal and preheating on mitigation of residual stresses and distortions using the validated model. Ultimately, these results will guide the selection of optimal manufacturing protocols and integration of the FE-based AM modelling for industrial application with complex geometries. The ultimate aim of the present work is to facilitate fatigue life prediction of complex geometry AM components including residual stress effects, e.g. conformally-cooled injection moulding dies (for different material than Inconel 625).

4.2 Introduction

Powder bed fusion (PBF) is one of several additive manufacturing (AM) technologies for fabricating complex shape, custom-designed components in which a thin layer of metal powder is first laid and then a moving laser (or electron) beam is applied as the heat source to fully melt the metal powder according to the controlled trajectory [1, 2]. However, high inherent tensile residual stress caused by large thermal gradients and cooling rates, which leads to distortions and cracks in the AM part, is a major concern for PBF [3-5]. Tensile residual stress is detrimental to the fatigue performance of manufactured parts [6, 7]. Hence, it is important to understand the effects of component-level geometry on how residual stresses develop during PBF, i.e. not just at the material or process level, and how to mitigate residual stress and distortion induced in components manufactured by PBF.

Previous work on the analysis of residual stresses in PBF has been conducted using experimental and numerical methods [8, 9]. Several experimental measurements have been made to systematically investigate the magnitude of residual stress and distortion during PBF. Simson et al. [10] investigated residual stress in PBF samples made from 316L austenitic stainless steel at different depths and on two outer surfaces using X-ray diffraction (XRD), showing that the orientation of the main stress components is dependent on the examined layer. For example, the residual stresses at the top surface are higher in the laser scanning direction than those in the perpendicular direction. Phan et al. [11] conducted high-fidelity residual strain and residual stress benchmark measurements in PBF built Inconel 625 bridge-shaped component using neutron diffraction, XRD and contour method. The distortion of the component was measured using the coordinate measurement machine (CMM). The results using different techniques are in reasonable agreement with each other. These results are used here to validate the proposed new FE-based AM process model for residual stresses, strains and distortions in complex geometries. Barros et al. [12] measured residual stress of PBF Inconel 718 cuboid specimens in the as-built state and after standard solution annealing and ageing heat treatment conditions using the hole-drilling strain-gage method and highlighted that

residual stress decreased markedly after the heat treatment. Teixeira et al. [13] have recently presented a detailed review of residual stress development in PBF for Inconel 718 and concluded that although optimized heat treatment can successfully reduce residual stresses for Inconel 718, there are still significant process-structure-property challenges, including investigation of different heat treatment strategies, as investigated in this work for Inconel 625. Mishurova et al. [14] evaluated the effect of the support structure and substrate removal on residual stress and distortion in PBF Inconel 718 parts by means of XRD and highlighted that (i) the removal from the substrate leads to residual stress redistribution and relaxation on the sample and (ii) the supporting structures between the AM built sample and the substrate are useful for compensating the distortion. However, it is not possible to provide supporting structures in all the areas of printed components, and post-print removal is typically difficult. The effects of preheating on residual stress reduction and mechanical properties enhancement of PBF Ti-6Al-4V were demonstrated experimentally by Ali et al. [15]. The generated residual stresses were 88.3% lower at the component preheated at 470 °C compared to that preheated at 100 °C and the yield strength and elongation of components with 570 °C preheating temperature improved by 3.2% and 66.2%, respectively. In general, experimental methods are time-consuming and cost-intensive for routine assessment of residual stress or design studies to mitigate residual stresses [16]. Accordingly, numerical modelling methods, validated against relevant experimental data, are potentially efficient alternatives to predict residual stress and distortion in AM processes, and to facilitate quick and cost-effective AM design and optimization [17].

In general, existing AM process modelling methods can be categorized into process-level [18-20] and component-level [21-23] models. Detailed process-level modelling has been performed using a small step increment and a fine mesh with at least one element per layer. Hussein et al. [18] proposed a three-dimensional (3D) transient finite element (FE) model to predict the temperature and stress fields within a single 316L stainless steel layer built on the powder bed using the PBF process, revealing differences in temperature and stresses at different locations of the layer, but without explicit comparisons against

experimental measurements. Hodge et al. [19] presented a continuum thermo-mechanical modelling method for calculation of the thermal and mechanical history of a PBF manufactured 316L stainless steel cube (12 layers in total) and highlighted the limitations of the Bathe algorithm [24] for phase change modelling due to significant computational resources required. Recently, Yang et al. [20] developed a 3D FE model for predicting the thermal history and spatial distributions of temperature in the PBF process using the 'element birth and death' technique in Abaqus (commonly referred as the 'Model Change' technique [25]), and extended to solid-state phase transformation for Ti-6Al-4V. In this case, the predictions of thermal history and molten pool dimensions were successfully validated against measured data [26]. Although modelling at the process-level can capture the rapidly evolving temperature and details of melt pool process physics, the computational domain is typically small (e.g. only a few layers of thickness) due to high computational cost [27, 28]. Promoppatum et al. [21] investigated the inherent strain based approach for prediction of residual stresses in PBF Inconel 718 parts, with comparison against neutron diffraction measured results for validation of the developed FE framework. A key limitation of the inherent strain approach is the challenge in determining accurate inherent strain fields since they strongly depend on the AM process parameters. Bayat et al. [22] developed a component-level FE-based thermo-mechanical model for predicting residual stresses and distortions for PBF Ti-6Al-4V, using the flash heating (FH) method as a multi-scaling approach to improve computational efficiency. However, the FH method is insensitive to the scanning strategy, which leads to unrealistic prediction of residual deformation. Williams et al. [23] introduced a pragmatic FE-based component-level model for residual stress and distortion prediction in PBF process. Several layers were combined into a thicker computational section or block in their model, which is based on the 'block dump' approach. For example, 16 layers were amalgamated to a height of 0.8 mm section in the model; the differences between predicted and measured (using digital image correlation (DIC)) distortion were within 5% for the bridge component made from 316L stainless steel. The 'block dump' approach can capture the thermo-mechanical conditions with reasonable accuracy, but high-performance computing is often required. The recently developed AM built-in module of the general-

purpose FE software Abaqus [29] (hereafter referred as 'Abaqus AM') was evaluated by Song et al. [9] for both PBF and (Directed Energy Deposition) DED process of Inconel 718; the residual stress predictions from FE simulation captures the trend from the Focused Ion Beam (FIB) slitting + DIC measured results, and the maximum difference between FE predictions and FIB-DIC measurements is about 38.6% (viz. 610 MPa, as compared to 440 MPa). In our previous work [30], a 3D FE model using Abaqus AM was developed to predict thermal histories and residual stresses in a realistic DED Ti-6Al-4V component.

The objectives of the present study are (i) to develop and validate an efficient and accurate process simulation model for component-level PBF, based on benchmark experimental test data, and (ii) to investigate the application of this model to development and mitigation of residual stresses and distortions in complex PBF components. Firstly, a 3D FE-based method is developed to predict the thermo-mechanical behaviour of the NIST benchmark PBF manufactured Inconel 625 bridge structure [11]. A detailed validation of the FE-based model is presented by comparison against the published benchmark measurements. Residual stress and distortion predictions using the FE-based method are shown to agree closely with the measured data. The validated model is employed to investigate the influence of substrate removal, and preheating and cooling rates on mitigating both residual stresses and distortions, as a guideline for selection of optimal manufacturing protocols and to demonstrate the effectiveness of the developed FE-based method.

4.3 Methodology

To improve computational efficiency, the widely-adopted sequentially coupled thermo-mechanical analysis of PBF process is used in this study [23, 31]. The transient heat transfer analysis is conducted first, for which the thermal loads are induced by the input laser during the printing process, as shown in Figure 4.1, followed by a static mechanical analysis, where the calculated temperature field is imported to determine the residual stress caused by thermal expansion. The governing equations of both the thermal and

mechanical analysis are briefly summarized in this section. More details of the thermal transfer and mechanical mechanisms can be found in [32].

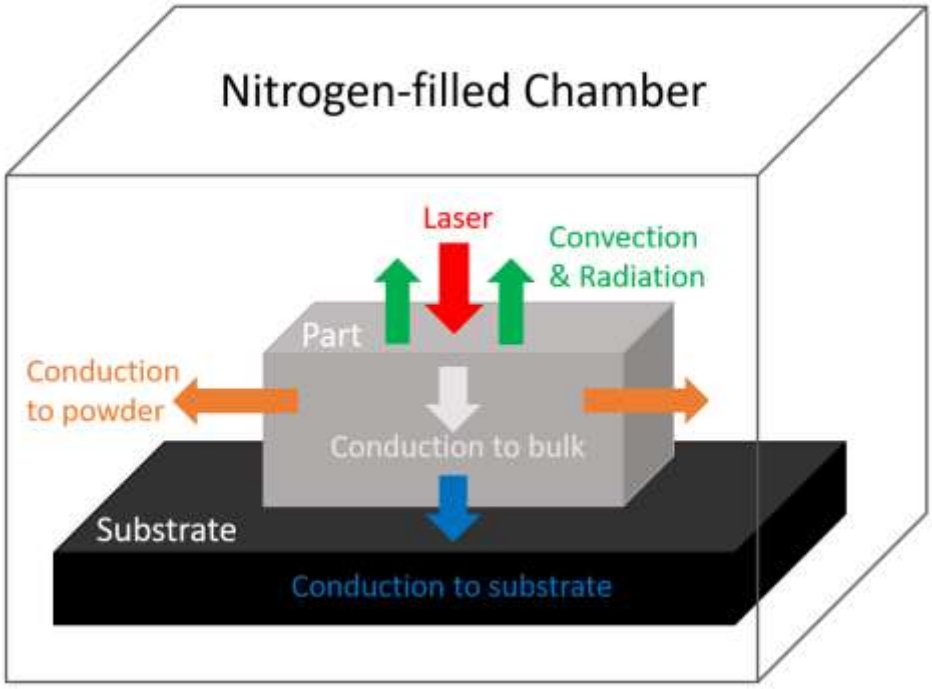

Figure 4.1. Heat transfer mechanisms in the PBF process.

4.3.1 Governing equations

4.3.1.1 Thermal analysis

The governing equation of the thermal analysis is the heat conduction equation [33]:

$$\rho C_{\mathrm{p}} \frac{dT}{dt} + \nabla \cdot \mathbf{q} = Q + \dot{D}_{\mathrm{mech}} \tag{4.1}$$

where ρ is density ($\mathrm{kg/m^3}$), C_{p} is the temperature dependent specific heat ($\mathrm{J/(kgK)}$), T denotes temperature (K), t is time (s), $\mathbf{q}$ is heat flux vector, and Q is laser heat source, $\dot{D}_{\mathrm{mech}}$ is thermo-mechanical dissipation. The heat flux vector $\mathbf{q}$ due to conduction is given as follows:

$$\mathbf{q} = -k\nabla T \tag{4.2}$$

where *k* is the temperature dependent thermal conductivity ($\mathrm{W/(mK)}$). The heat loss due to heat convection can be formulated as:

$$q_{\mathrm{conv}} = h_{\mathrm{conv}}(T_{\mathrm{sur}} - T_{\mathrm{a}}) \tag{4.3}$$

where h_{conv} is heat transfer convection coefficient ($\mathrm{W/(m^2K)}$), taken as $18\ \mathrm{W/(m^2K)}$ during the printing process in this study [3], T_{sur} is surface temperature of the specimen (K), T_{a} is ambient temperature in build chamber (K). The heat loss due to radiation can be formulated as:

$$q_{\mathrm{rad}} = \varepsilon_{\mathrm{rad}}\sigma_{\mathrm{rad}}(T_{\mathrm{sur}}^4 - T_{\mathrm{a}}^4) \tag{4.4}$$

where $\varepsilon_{\mathrm{rad}}$ is the emissivity coefficient, and σ_{rad} is the Stefan–Boltzmann constant. Here the emissivity $\varepsilon_{\mathrm{rad}}$ and the Stefan-Boltzmann's constant σ_{rad} were set as 0.45 [34] and $5.669 \times 10^{-8}\ \mathrm{W/(m^2K^4)}$ [35], respectively. The laser heat source *Q* is modelled as a concentrated point heat source during the PBF process modelling [9, 36], which is expressed as:

$$Q = \frac{2\eta P}{abc\pi\sqrt{\pi}}\exp(-\frac{(x+vt)^2}{a} + \frac{y^2}{b} + \frac{z^2}{c}) \tag{4.5}$$

where P is the laser power, η is the absorptance, v is the velocity of moving laser heat source, a, b and c are the dimensions of the heat source along the x, y, and z axes, respectively.

4.3.1.2 Mechanical analysis

The governing equation of the mechanical analysis is the stress equilibrium equation [37], given as:

$$\nabla \cdot \boldsymbol{\sigma} = 0 \tag{4.6}$$

where $\boldsymbol{\sigma}$ is the stress tensor. The mechanical constitutive law for the elastic problem is defined as:

$$\boldsymbol{\sigma} = \boldsymbol{C} : \boldsymbol{\varepsilon_e} = \boldsymbol{C} : (\boldsymbol{\varepsilon_{Total}} - \boldsymbol{\varepsilon_p} - \boldsymbol{\varepsilon_T}) \tag{4.7}$$

where $\boldsymbol{C}$ is the stiffness tensor, $\boldsymbol{\varepsilon_{Total}}$, $\boldsymbol{\varepsilon_e}$, $\boldsymbol{\varepsilon_p}$, $\boldsymbol{\varepsilon_T}$ are the total, the elastic, the plastic and the thermal strain tensors, respectively. The thermal strain tensor driving the residual stress is calculated according to:

$$\boldsymbol{\varepsilon_T} = \alpha \Delta T \boldsymbol{I} \tag{4.8}$$

where α is the temperature dependent thermal expansion coefficient (1/K), ΔT is the change in temperature (K) and $\boldsymbol{I}$ is identity tensor.

4.3.2 Finite element modelling of PBF process

Since the macro-scale residual stress and distortion cannot be predicted using the process-level modelling approach due to the prohibitively high computational cost, the component-level modelling approach is implemented here [23]. An overview of the PBF process modelling is illustrated in Figure 4.2.

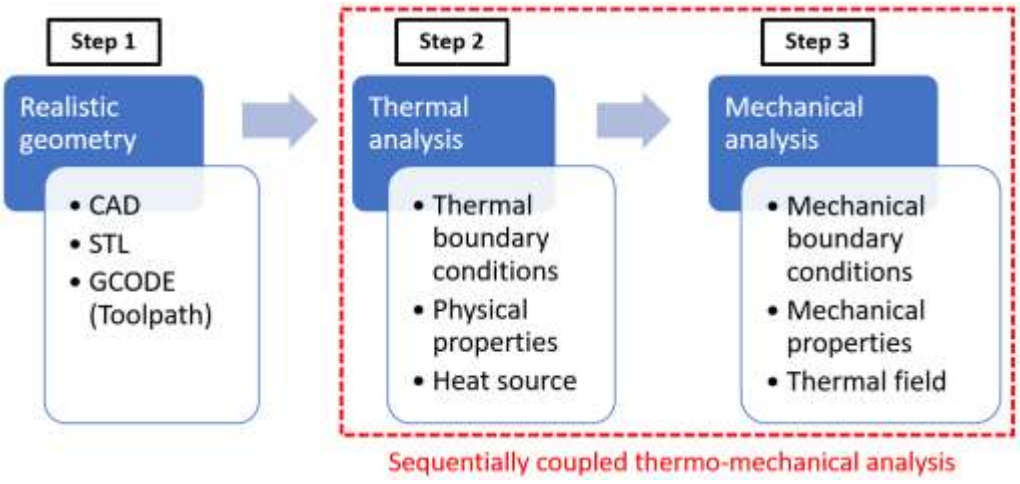

Figure 4.2. Overview of the PBF process modelling: Step 1: Realistic geometry, Step 2: Thermal analysis, Step 3: Mechanical analysis.

The FE analysis is performed using Abaqus/CAE 2020 [38]. The built bridge-shaped geometry on a cuboid substrate modelled here using the 'Abaqus AM' method, of which more details can be found in our previous paper [30], is based on that experimentally examined by Phan et al. [11], as shown in Figure 4.3. The dimensions of the printed

component are 75 mm (L) × 5 mm (W) × 12.5 mm (H). The dimensions of the substrate are 81 mm (L) × 11 mm (W) × 12.7 mm (H). Figure 4.3 (b) presents the FE model and mesh design. A detailed mesh convergence study was performed to achieve a judicious balance between required computational resource and results accuracy (within 5% with respect to the maximum principal stress), as shown in Figure 4.4. The element size of meshes P, Q and R (essentially uniform mesh distribution used in the bridge model) are 400 μm, 200 μm and 100 μm, respectively. The converged FE mesh Q consists of 486472 elements and 530988 nodes. The average element size in the bridge structure is 214 μm (L) × 200 μm (W) × 200 μm (H), i.e. layer scale-up factor of 10 (10 layers merged within one element layer). Similar mesh densities have been presented in Song et al. [9]. The ratio of element size to the characteristic length of component (12 mm) is 0.016. It should be noted that the mesh of the substrate is coarser (500 μm (L) × 500 μm (W) × 500 μm (H)), thus reducing computational cost whilst maintaining accuracy. The step increment is set as one time increment per build layer [9]. Eight-node linear heat transfer elements (DC3D8) are used for the heat transfer analysis, and eight-node linear elements with full integration (C3D8) are then applied for the mechanical analysis [9, 36].

Build direction is defined as the Z-direction for the PBF modelling, and the recoating is performed from right to left (along the opposite direction of the X-axis, see Figure 4.5). The bottom surface of the substrate is fixed as shown in Figure 4.5. The ambient temperature (T_a) in the build chamber and the predefined temperature (T_p) of the substrate are set the same as in the experiment, i.e. 313 K and 353 K, respectively [11]. In this study, the "cut" element set (see Figure 4.5) between the bridge structure and the substrate is created to simulate the electric discharge machining (EDM) removal process, achieved by deactivating the "cut" element set after the whole bridge was built. The distortion of the bridge structure can be predicted and compared with the benchmark measurement.

(a)

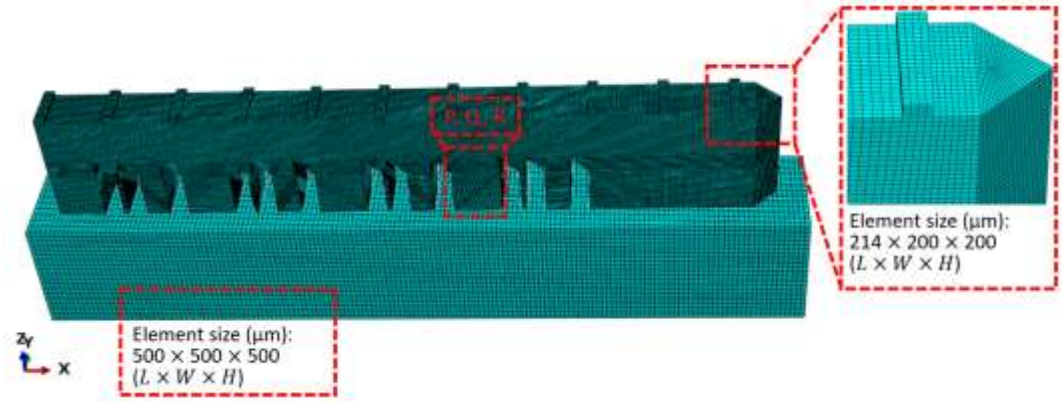

(b)

Figure 4.3. Configurations of the PBF modelling: (a) Dimensions of bridge structure printed by Phan et al. [11], (b) FE model and mesh design.

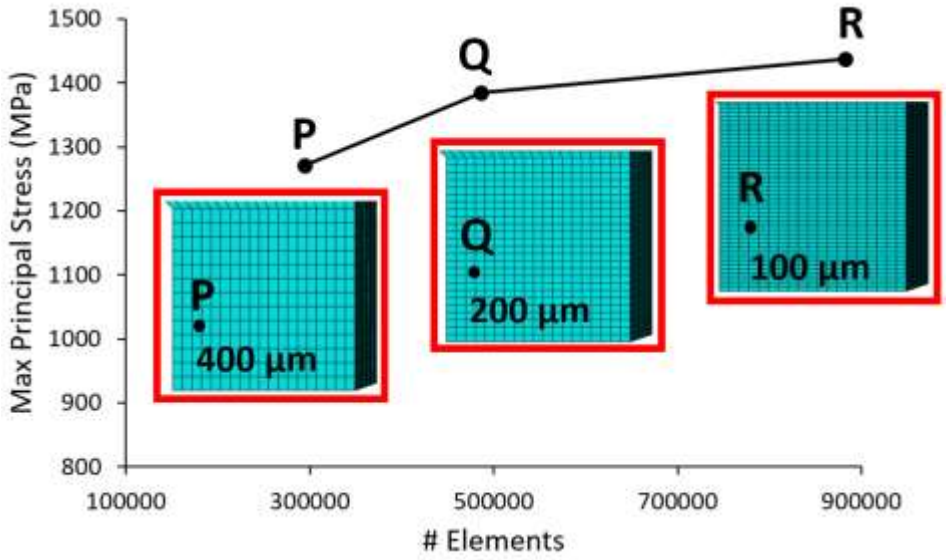

Figure 4.4. Mesh convergency study (locations of P, Q and R see Figure 4.3).

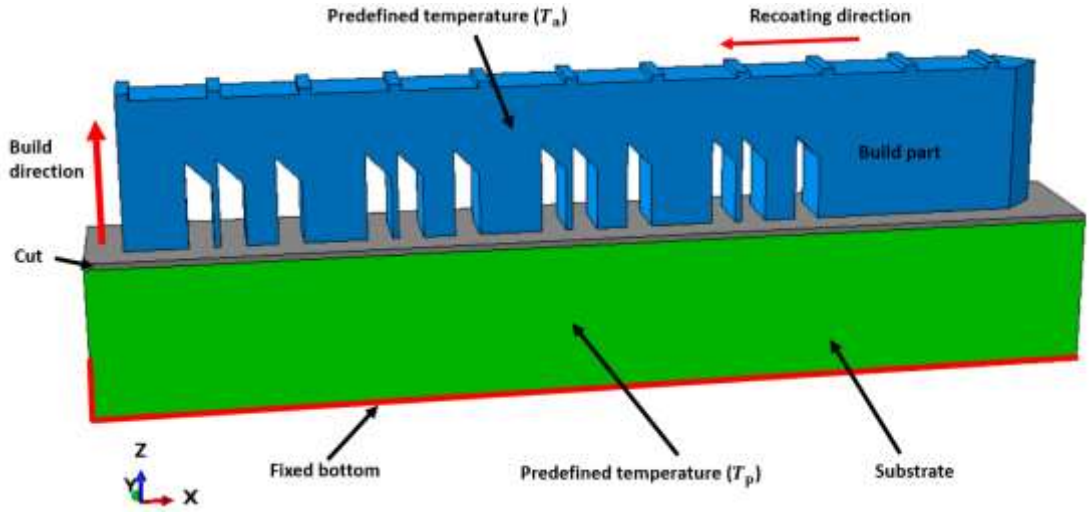

Figure 4.5. Boundary conditions of the FE model.

4.3.3 Material properties and process parameters

The temperature-dependent material properties of Inconel 625 employed in this study are shown in Figure 4.6, including thermal conductivity, specific heat, thermal expansion, Poisson's ratio, Young's modulus and yield stress [39, 40]. The material density is taken as a constant value of 8440 kg/m^3. The widely used elastic perfectly plastic (EPP) model is adopted to define the plasticity of Inconel 625 [41, 42]. The process parameters for the computational PBF modelling are summarized in Table 4.1, which are the same as the experiment conditions investigated here [11, 43]. The laser path employed in the PBF modelling is converted from G-code (i.e. combination of motion and action commands for the 3D printer) according to the scanning strategy (see Figure 4.7, adapted from the NIST AM-Bench website [43]), including horizontal infill scans (parallel to the X-axis) and vertical scans (parallel to the Y-axis) for odd and even layers, respectively. The average layer time is 52 s during the printing of bridge legs.

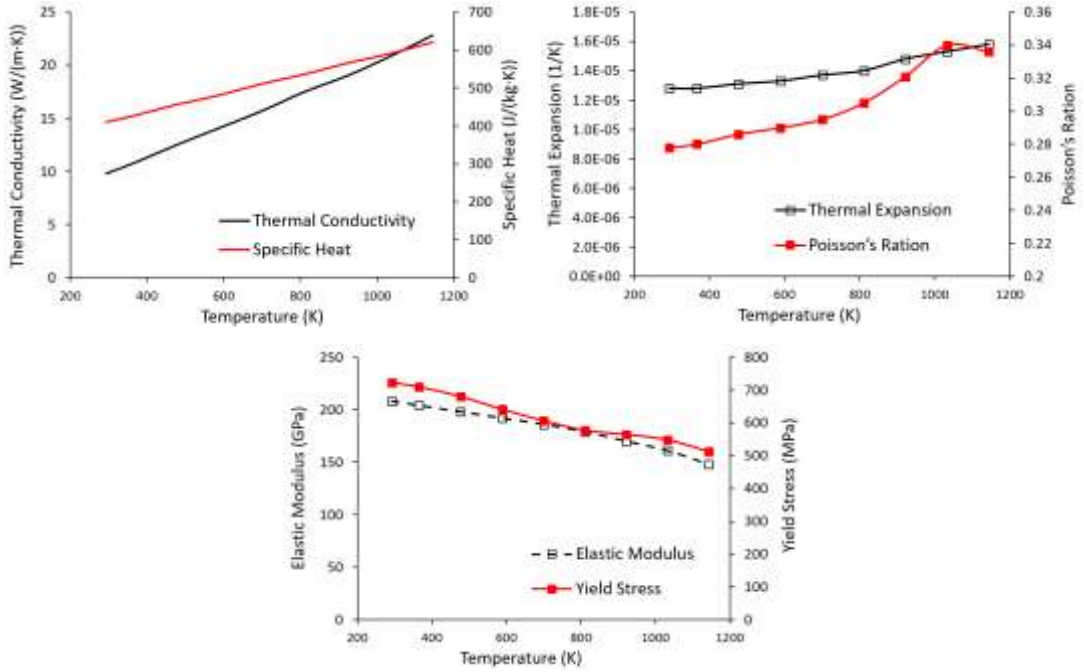

Figure 4.6. Temperature-dependent material properties of Inconel 625 [39, 40].

Table 4.1. Process parameters applied in the PBF modelling.

Symbol	Parameters	Value
η	Absorption coefficient	0.45
P_c	Contour laser power (W)	100
v_c	Contour scanning speed (mm/s)	900
P_i	Infill laser power (W)	195
v_i	Infill scanning speed (mm/s)	800
d_s	Laser spot diameter (μm)	50
L	Layer thickness (μm)	20
H	Hatch spacing (μm)	100

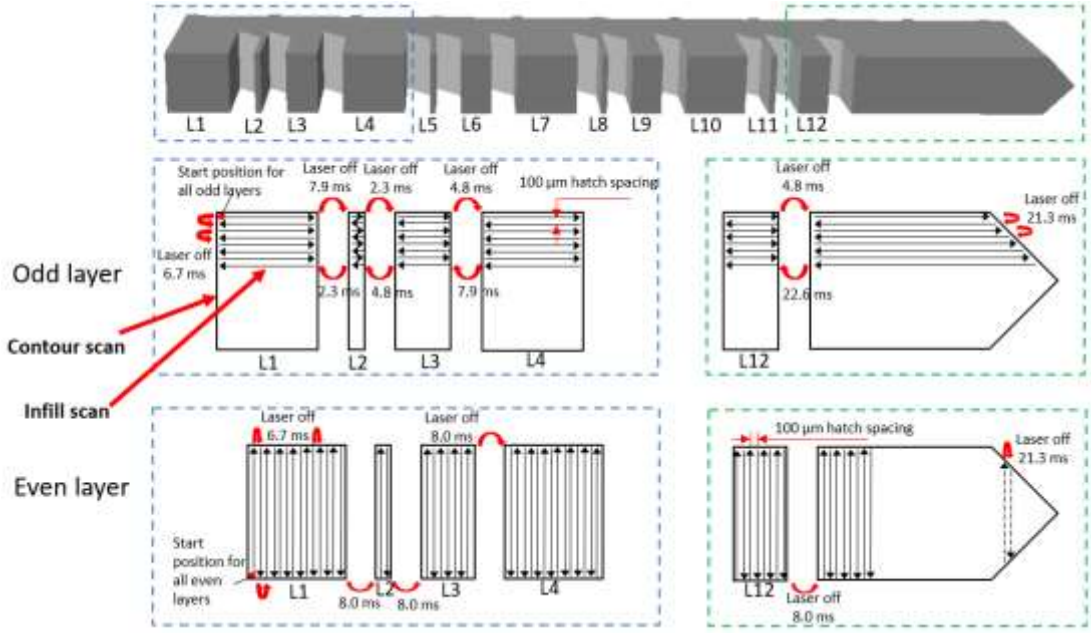

Figure 4.7. Scanning strategy, adapted from NIST AM-Bench website [43].

4.4 Results

4.4.1 Validation of thermo-mechanical FE model

4.4.1.1 Residual strain analysis

To validate the performance of the present FE-based component-level model, prediction of residual strains, residual stresses and distortions in Inconel 625 bridge is compared with the test data of Phan et al. [11]. First, the residual strain in the middle cross section of the manufactured bridge structure is predicted and compared to the experimental measurements (before substrate removal). Figures. 4.8 (a), (c) and (e) shows the predicted distributions of residual strains ε_{xx}, ε_{zz} and ε_{xz}, respectively. The corresponding experimental measurements are shown in Figures. 4.8 (b), (d) and (f). It is clear that all three predicted residual strain distributions are in reasonable agreement with the benchmark measurements from Phan et al. [11], in terms of both magnitude and distribution. Specifically, both FE prediction and XRD measurement of the residual strain ε_{xx} (see Figures. 4.8 (a) and (b)) are mostly tensile across the main body of the bridge structure, while the compressive strains are mainly on the bridge legs. The maximum tensile strains are close to the top and bottom sides of the bridge. The predicted residual

strain ε_{zz} shown in Figure 4.8 (c) is in reasonable agreement with the experimental measured residual strain ε_{zz} (see Figure 4.8 (d)), with mostly compressive strain through the main body and tensile strain on the bridge legs, which is almost a reverse image to that in the X direction. Similar agreement is also obtained for the shear strain ε_{xz} (see Figures. 4.8 (e) and (f)).

In order to make more specific quantitative comparisons, three horizontal paths for comparison between the predicted and XRD measured residual strain ε_{zz} are defined in Figure 4.9 (a). The comparison of the residual strain ε_{zz} at the three different heights are: near the top surface of the bridge structure (Z = 11.25 mm, see Figure 4.9 (b)), near the middle of the top solid section (Z = 9.75 mm, see Figure 4.9 (c)), and through the legs of the bridge structure (Z = 2.25 mm, see Figure 4.9 (d)). Overall, good agreement is obtained between the predictions and experimental measurements. A preliminary study is conducted to optimize the use of multiple cores at each step to minimize the total computational time required for analysis using the component-level approach. For our case, running using processor with 8 cores, the total runtime for this model is about 9.5 hours for thermal analysis and around 43 h for the mechanical analysis.

(a)

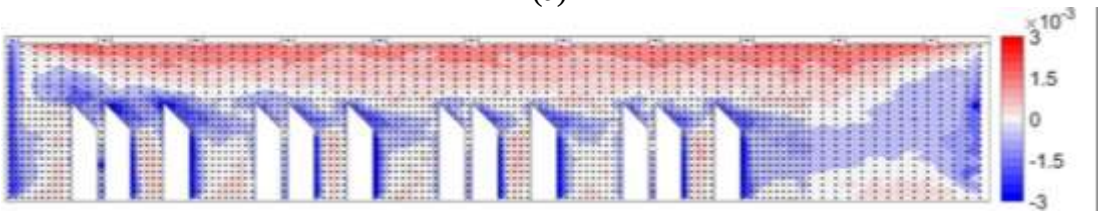

(b)

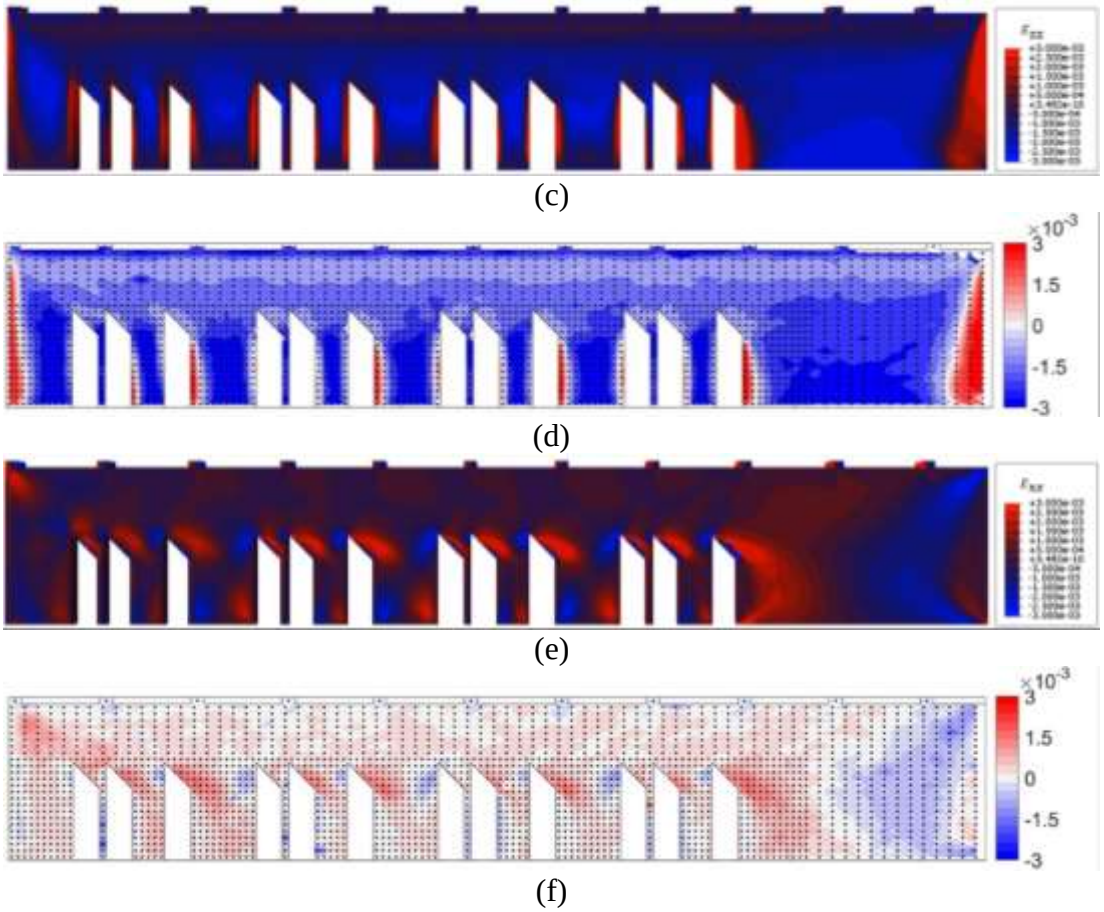

Figure 4.8. The comparison of predicted and XRD measured [11] residual strain in the middle cross section of the bridge structure (before substrate removal): (a) predicted residual strain ε_{xx}, (b) XRD measured residual strain ε_{xx}, (c) predicted residual strain ε_{zz}, (d) XRD measured residual strain ε_{zz}, (e) predicted residual strain ε_{xz}, (f) XRD measured residual strain ε_{xz}.

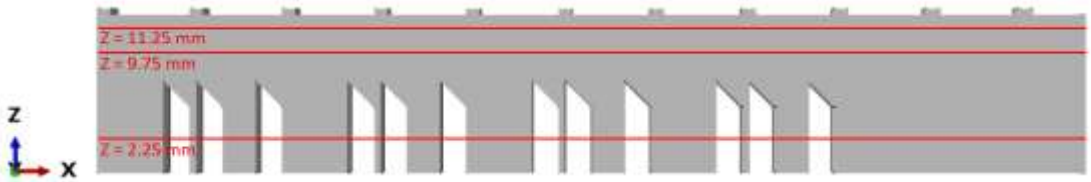

(a)

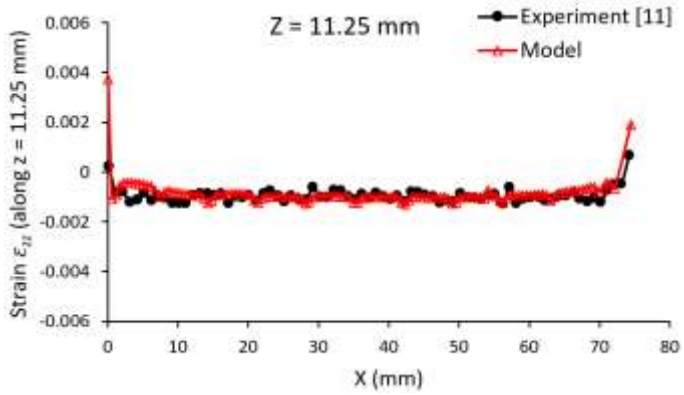

(b)

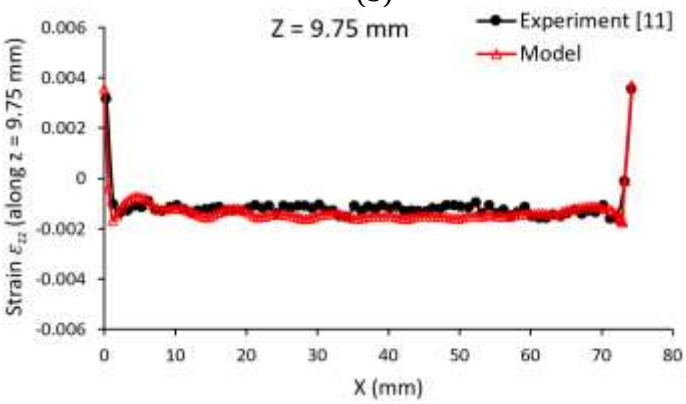

(c)

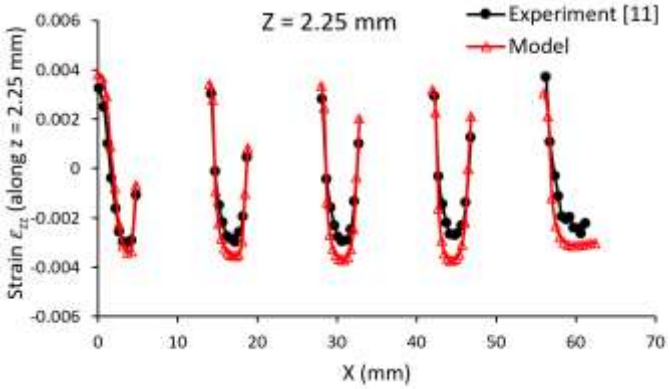

(d)

Figure 4.9. The comparison of predictions and XRD measurements [11] of residual strain ε_{zz} along different paths: (a) locations of the paths, (b) path of Z = 11.25 mm, (c) path of Z = 9.75 mm, (d) path of Z = 2.25 mm.

4.4.1.2 Residual stress analysis

Figure 4.10 shows the comparison of FE predicted and contour method measured residual stress σ_{xx} on the plane at the 7th leg (marked as 'L7', located at X = 31 mm, see Figure 4.10 (a)). The predicted residual stress in the X direction (Figure 4.10 (b)) is in close agreement with the experimental measurement (Figure 4.10 (c)). Figure 4.11 shows the comparison of FE predicted, contour method and neutron diffraction measured residual stress σ_{xx} along the vertical line at the center of the L7 plane. Both the trend and values from the FE prediction and benchmark measurements show reasonable agreement except near the top and bottom of the bridge structure.

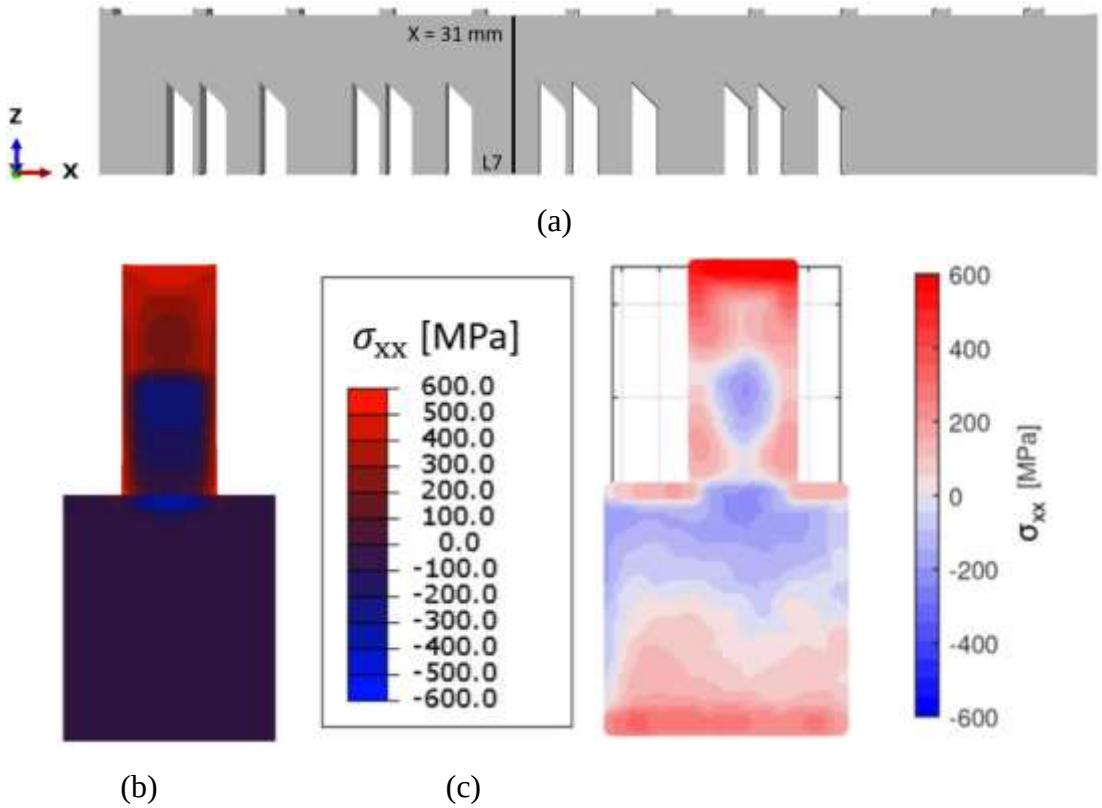

Figure 4.10. The comparison of FE predicted and contour method measured [11] residual stress σ_{xx} on the plane at the 7th leg (marked as 'L7'): (a) location of the 'L7' plane (at X = 31 mm), (b) FE predicted residual stress σ_{xx}, (c) measured residual stress σ_{xx} using the contour method.

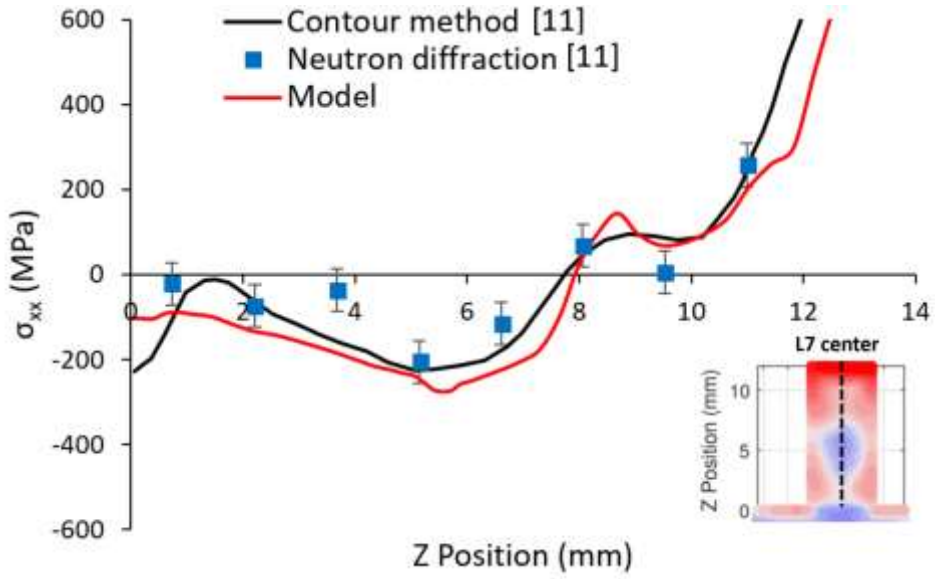

Figure 4.11. Comparison of FE predicted and experimental measured [11] residual stress distributions along the vertical line at the center of the L7 plane.

4.4.1.3 Distortion analysis

Distortion of the bridge after the EDM removal process is simulated to investigate the ability of the present model to predict the direction and magnitude of distortion. Figure 4.12 shows the comparison of the distortion calculated by the FE model with CMM measurements [11]. The measurement points are indicated by the solid black dots on the ridges along the top of the bridge. The Z direction displacement is calculated as the difference between the measurement before and after the twelve legs of the bridge been separated from the substrate. Figure 4.13 shows the corresponding bridge distortion after EDM by Phan et al. [11]. The predicted distortion and the experimental result show the same upward distortion (in the build direction, see Figure 4.5), and the predicted maximum Z displacement is 1.1 mm, which is in close agreement with the experimental measurement of 1.27 mm.

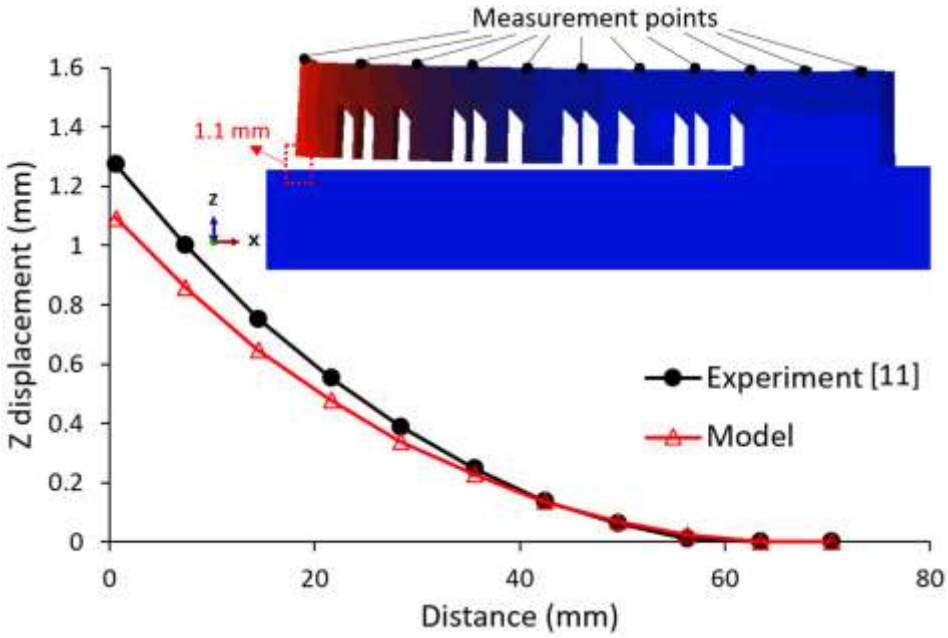

Figure 4.12. Comparison of present FE predicted distortion with experimental measurement [11].

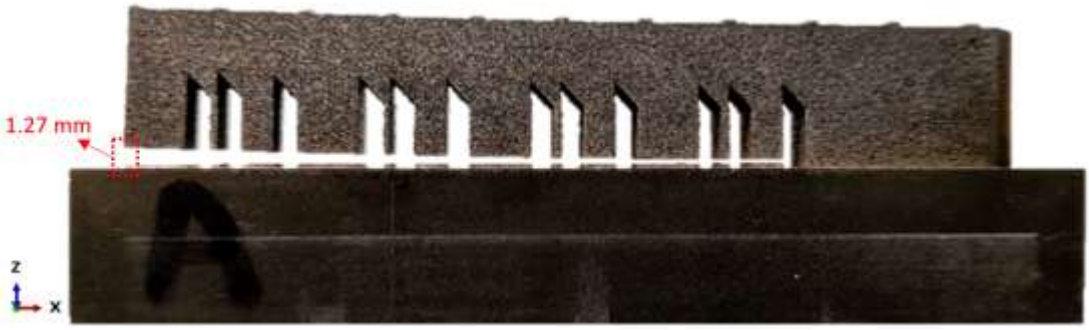

Figure 4.13. Macrograph of bridge distortion after EDM process, adapted from Phan et al. [11].

4.4.2 The effect of substrate removal on the residual stress and distortion

4.4.2.1 Residual stress

Figure 4.14 shows the predicted contours of the maximum principal stress of the bridge before and after removal of the substrate. Before cutting off from the substrate, the maximum principal stress (1385 MPa) is found at the bottom of the bridge (region connected to the substrate, see Figure 4.14 (a)). After cutting off from the substrate, the

maximum principal stress decreases to 1049 MPa, and the location of the stress concentration changes to the side of the bridge legs (see Figure 4.14 (b)). Ahmad et al. [44] evaluated the residual stress in PBF Inconel 718 samples using the contour method, showing that detrimentally-high tensile residual stress occurred at and near the side surfaces of the AM Inconel alloys samples. Figure 4.15 shows the effect of cutting on the residual maximum principal and normal (Cartesian) stress component distributions along two paths, i.e. L1 (along top surface, x-direction) and L2 (through height, z-direction), as shown in Figure 4.14. In general, it can be found that the most significant effect of cutting occurs closest to the plane of cutting, i.e. for low values of Z, as shown in Figures. 4.15 (b), (d), (f) and (h). The σ_{xx} (Mode I type) residual stress along L1 is significantly reduced from tensile (detrimental), about 300 MPa, to compressive (beneficial), about 100 MPa, but the σ_{yy} and σ_{zz} components are negligibly affected along this line. The dominant residual stress before and after cutting is σ_{zz} and it is highest along L1 (top surface) and only negligibly affected there by cutting; through the height (L2), σ_{zz} is significantly reduced from a uniformly high tensile value to a linearly reducing value, reaching almost zero at the bottom surface (cutting plane); in contrast, σ_{xx} and σ_{yy} are negligibly affected except very close to the bottom surface (cutting plane), where the values also reduce to almost zero. Although the residual σ_{zz} stress along the top surface is not typically Mode I, since it is not parallel to the free surface, it is conceivable that these residual tensile stresses could interact with residual porosity and lead to sub-surface cracking in fatigue, or rolling contact fatigue, leading to delamination effects for example [45].

The maximum residual stress values for σ_{xx}, σ_{yy}, σ_{zz} and maximum principal stress, of the bridge before and after cutting off from the substrate, are summarized in Figure 4.16. Removal of the substrate results in decrease in all residual stress components. The maximum decrease is 335.8 MPa, for maximum principal stress, while the minimum decrease in σ_{yy} is only 10.2 MPa.

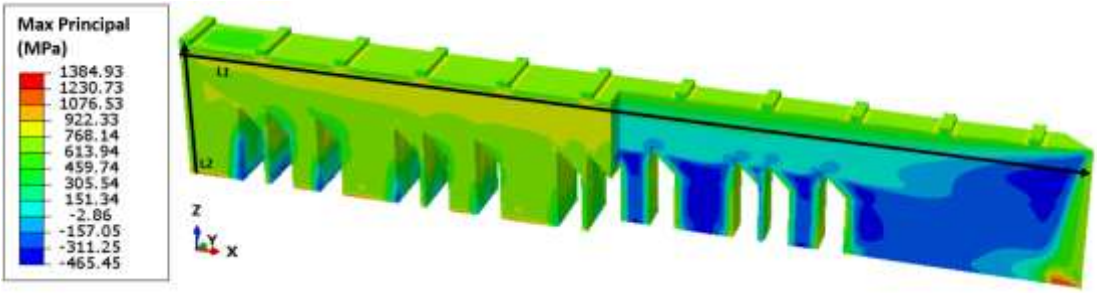

(a)

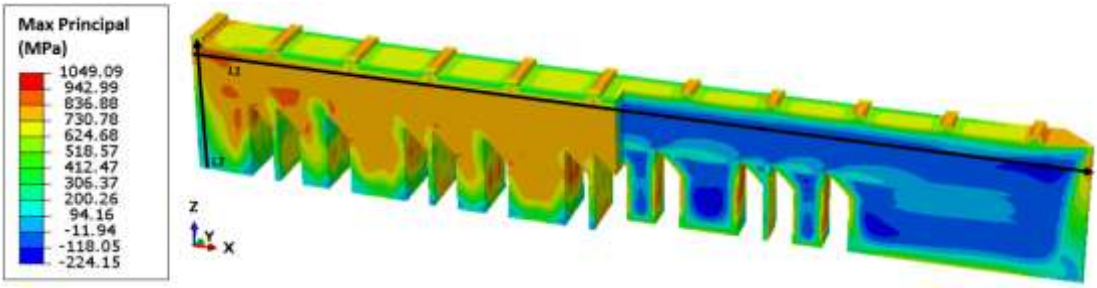

(b)

Figure 4.14. The residual maximum principal stress of the bridge: (a) before cutting off from the substrate, (b) after cutting off from the substrate.

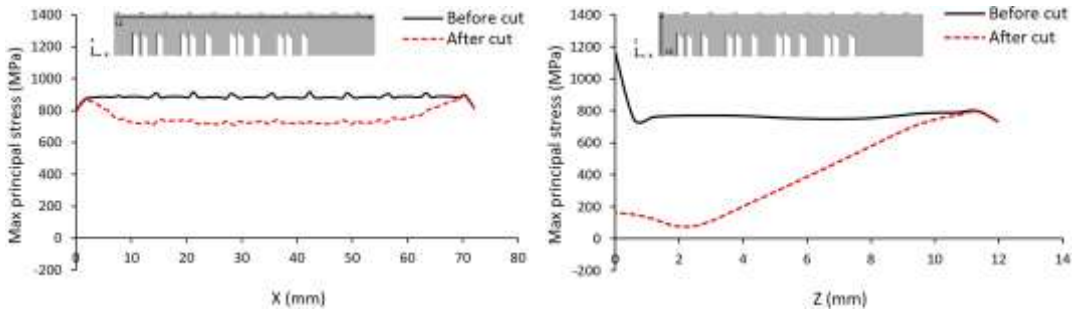

(a) Maximum principal stress along top surface (L1) (b) Maximum principal stress through height (L2)

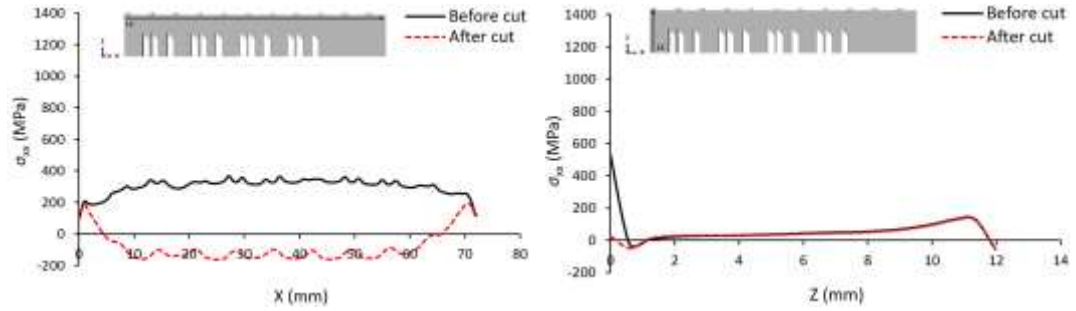

(c) σ_{xx} along top surface (L1) (d) σ_{xx} through height (L2)

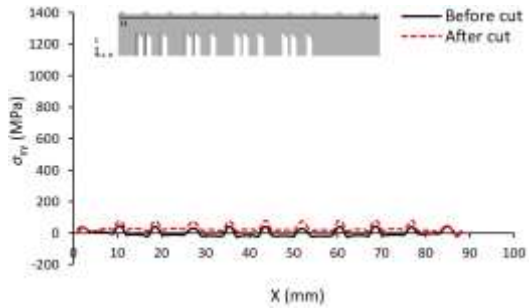

(e) σ_{yy} along top surface (L1)

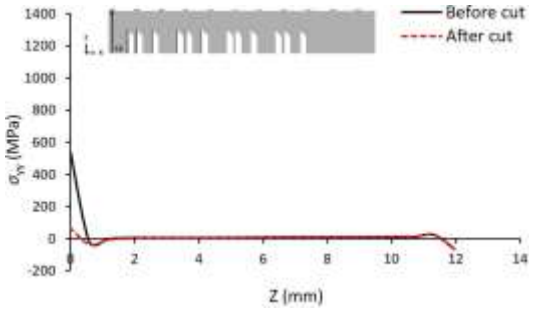

(f) σ_{yy} through height (L2)

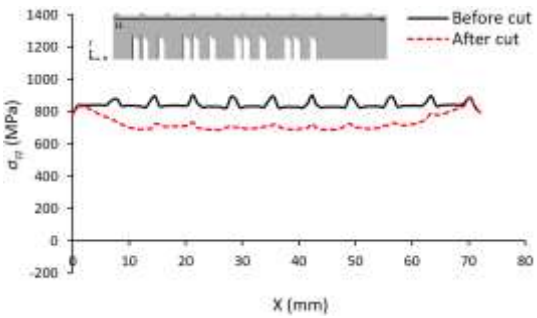

(g) σ_{zz} along top surface (L1)

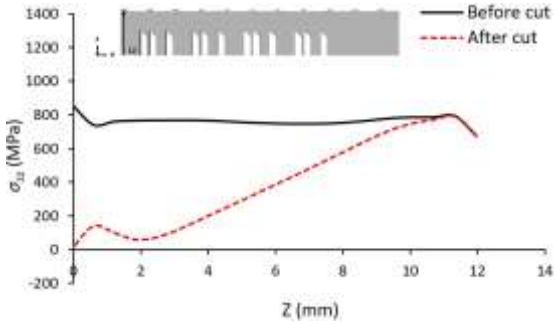

(h) σ_{zz} through height (L2)

Figure 4.15. Effect of cutting on residual stress distributions of bridge for maximum principal stress and normal (Cartesian) stress components along top surface (L1) and through height (L2): (a) maximum principal stress along top surface (L1), (b) maximum principal stress through height (L2), (c) σ_{xx} along top surface (L1), (d) σ_{xx} through height (L2), (e) σ_{yy} along top surface (L1), (f) σ_{yy} through height (L2), (g) σ_{zz} along top surface (L1), (h) σ_{zz} through height (L2).

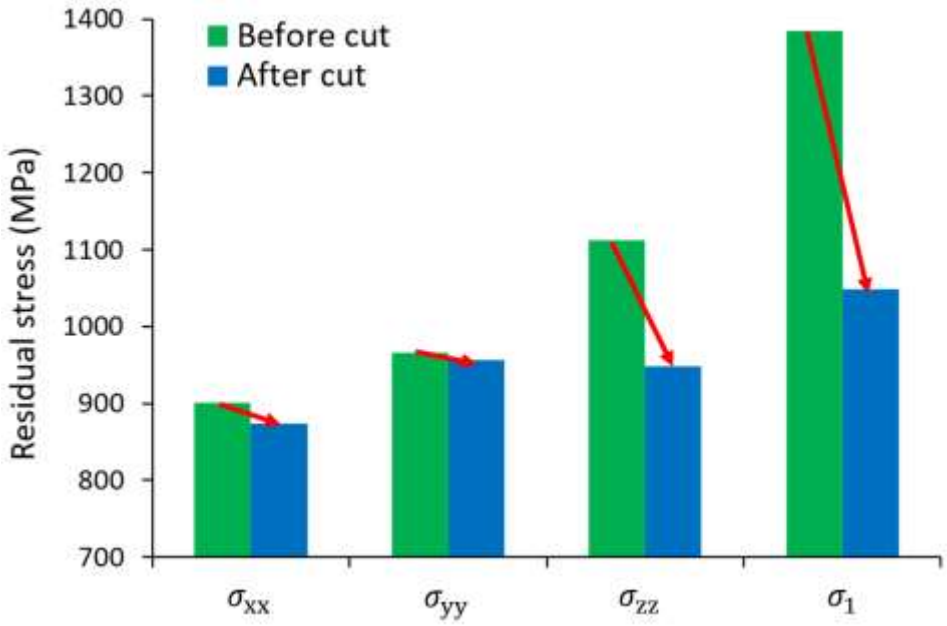

Figure 4.16. Maximum residual stress values for σ_{xx}, σ_{yy}, σ_{zz} and maximum principal stress before and after cutting off from the substrate.

4.4.2.2 Z direction distortion

The distortion of the bridge in the Z (vertical) direction after fully cutting off from the substrate is shown in Figure 4.17, which is different from that of the bridge with twelve legs separated from the substrate (see Figures. 4.12 and 4.13). This is attributes to the lack of constraints from the substrate (after fully cutting off) and thus the bridge has more freedom to deform in both sides.

Figure 4.17. FE-predicted component distortion after fully cutting off from the substrate.

4.4.3 The effect of preheating and cooling rate on the residual stress and distortion

Figure 4.18 shows the comparison of predicted maximum principal stress distributions along path 'L1' under different preheating conditions before and after cutting off from the substrate. The results show that increasing preheating temperature and ambient temperature can effectively mitigate the residual stress. When the preheating temperature is increased to 973 K, with the ambient temperature fixed at 313 K, the maximum principal stress along path 'L1' on the surface of the bridge decreases more than half (from 915.7 MPa to 429.9 MPa) before cutting off from the substrate (see Figure 4.18 (a)). When the ambient temperature is increased to 673 K, the residual maximum principal stress is less than 200 MPa. The same analysis applies after cutting off the substrate, as shown in Figure 4.18 (b).

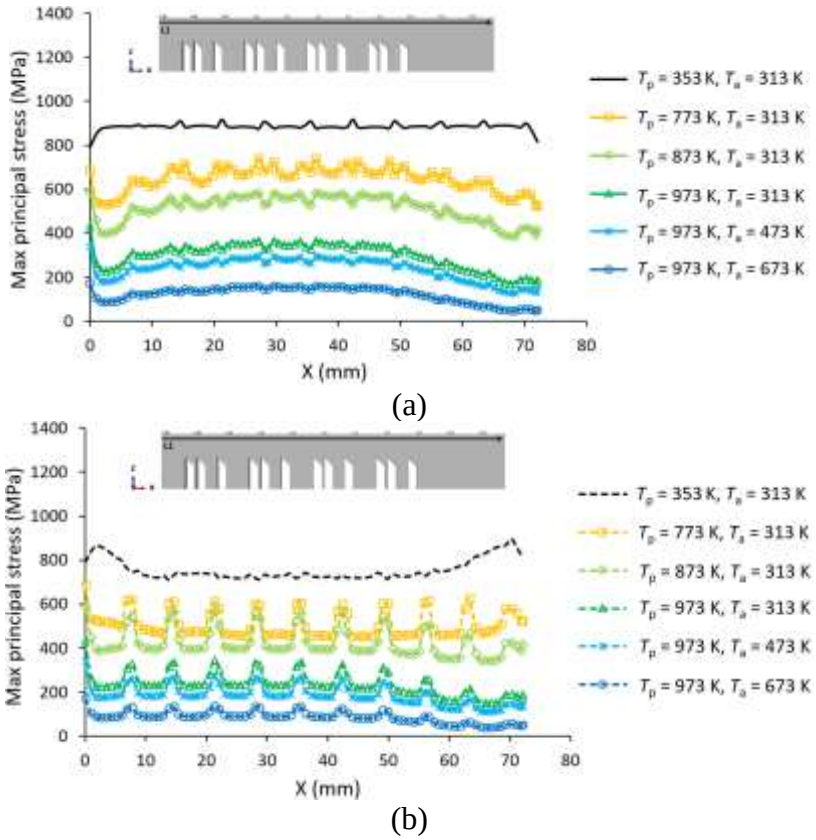

Figure 4.18. The comparison of predicted maximum principal stress distributions along path 'L1' under different preheating conditions: (a) before cutting off from the substrate, (b) after cutting off from the substrate.

Figure 4.19 shows the influence of preheating conditions on the distortion of the bridge after cutting off from the substrate. Increasing the preheating temperature reduces the distortion. In particular, the maximum Z displacement of the bridge does not exceed 0.05 mm when the temperature of the substrate is increased to 973 K (condition 4). When the ambient temperature reaches 673 K, the distortion of the bridge almost vanishes (0.01 mm).

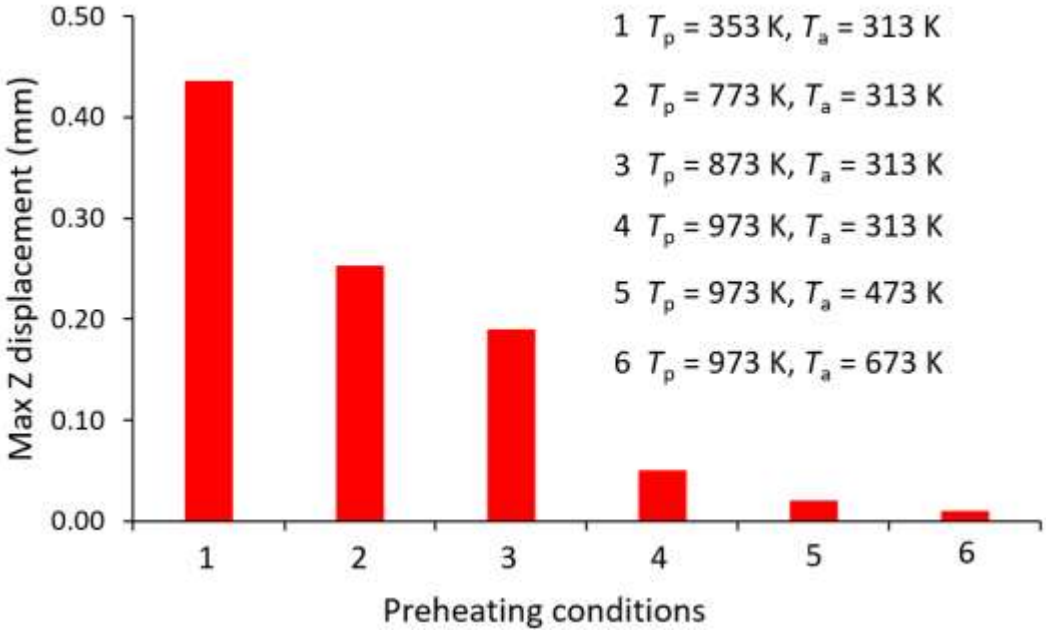

Figure 4.19. The comparison of predicted maximum Z displacement of the bridge after cutting off from the substrate under different preheating conditions.

4.5 Discussion

A key objective of the present study is the prediction of residual stresses and distortions induced by the PBF process. A specific challenge is to study the complex geometries at the component-level while preserving the accuracy and efficiency of the prediction. In this study, the FE-based 'Abaqus AM' method is used for simulating the PBF process of large-scale complex geometry, including investigation on effects of substrate removal and preheating on mitigation of residual stresses and distortions, as most of existing

component-level modelling approaches ignore many of the important influencing factors for reduction of computational time, for example, the effect of scan strategy is not included in the pragmatic part scale model [23]. In the present model, the printing related information, including laser power, velocity, hatch spacing, scanning strategy and laser off time (see Figure 4.7), are directly converted from the actual data (G-code) with no loss of modelling accuracy.

In contrast to the DED process, the layer thickness is relatively small with a larger number of total layers and the process parameters are usually unchanged throughout the PBF process [46, 47]. The model size as well as the number of layers within the model are restricted by the computational expense [48]. Hence, it is important to reduce the computational cost to make the use of FE-based AM modelling method practical for industry applications. Different modelling strategies have been proposed to reduce the computational cost and the output file size, such as layer agglomeration approach (also referred as 'layer lumping approach'), in which many layers are combined into one larger computational layer (viz. use one element to represent multiple layers) [49]. Thus, choice of appropriate element size is essential for a judicious balance between result accuracy and computational time. Therefore, the mesh height of 0.2 mm of the bridge component (of 10 physically printed layers) is chosen in the present study (see Figures. 4.3 and 4.4). In the thermal analysis presented here, the concentrated heat source model is implemented via the built-in point toolpath-mesh intersection module to describe the moving heat flux during the PBF process, due to the relatively large element size compared to the laser beam radius [38]. The moving heat source is calculated based on the actual laser path to capture the spatial and temporal representation of the energy distribution accurately. Song et al. [9] have presented a validation study of the point toolpath-mesh intersection approach for a coarse mesh via comparison against the generally-accepted Goldak-type approach with fine mesh using similar step increment, highlighting the deformations in the PBF process can be captured by the point heating approach with coarse mesh. Nyce et al. [36] have also performed comparison of temperature distributions between the

concentrated point heat source model and the Goldak heat source model. Very similar temperature profiles were obtained for the two heating models.

The mechanical response (residual stresses and distortions) is calculated from the sequentially coupled thermo-mechanical FE analysis in this study. This is valid since the mechanical responses resulting from rapid thermal evolution having very little effect on the associated thermal fields or the phase transformation behaviour, as the laser energy is much larger than the strain energy in the built part [50]. Yang et al. [42] and Huang et al. [51] have compared the sequentially coupled thermal-mechanical analysis to the fully coupled analysis: both cases show negligible difference between the two kinds of analysis. The reasonable agreement between the predicted residual strain and stress contours and experimental measurements (see Figures. 4.8 and 4.10) indicate that a layer scale-up factor of 10 (Figure 4.3) would result in an acceptable prediction accuracy. In other words, it is acceptable to use the layer lumping approach with point heating source. The material expands when the laser beam starts melting the metal powder, which will be limited as the surrounding material is colder. The temperature of the new melted top layer is always higher than the underlying layer during the heating process. During the cooling process, the contraction in the warmer upper layer is greater than the colder underlying layer. However, the contraction is inhibited due to the connection of both layers, causing tensile and compressive residual stress in the upper and underlying layer, respectively [10]. Large tensile residual stress is produced in the upper side (see Figure 4.10) after the printing process, lots of tensile residual stresses are released and the built bridge component stays at a concave shaped distortion after cutting off the twelve legs (see Figures. 4.12 and 4.13) or the whole substrate (see Figure 4.17). It is found that the model predicts the same upward distortion direction as the experiment, but slightly under-predicts the maximum distortion magnitude (viz. 1.1 mm, as compared to 1.27 mm, see Figure 4.12). Similar under-prediction was obtained by Papadakis et al. [52] on an Inconel 718 cantilever using the layer-by-layer modelling method (predicted deformation of 0.6 mm compared to experimental measured deformation of 0.8 mm) and by Li et al. [37] on the AlSi10Mg cantilever using the temperature-thread multiscale FE method (predicted maximum

distortion was 1.5 mm while the measured data was 2.1 mm). One possible reason could be that the EPP material constitutive model is used in the present study instead of considering the complex strain hardening effects and residual stresses induced by phase transformation during the PBF process [53]. Another possible reason could be that the wire EDM process would generate extra residual stress to the bridge since EDM is a thermal process [54], which could make the final distortion larger (see Figure 4.12). These two aspects could be included in future work. Although the present component-level modelling method uses some simplifications (i.e. coarse mesh and large step increment), which affect the predicted thermal history and cooling rate [30], it enables computationally-efficient component-level analysis of the distribution of residual stresses in the printed components without sacrificing accuracy.

A key additional novel contribution of this work is using the validated model to investigate the effects of preheating and cooling rate on the residual stresses and distortions of a complex 3D component. Mirkoohi et al. [55] have proposed a physics-based analytical model to investigate the effect of substrate temperature on residual stress in PBF of Inconel 718, showing that preheating the substrate reduces residual stress in AM parts due to the reduction of temperature gradients, which has been validated against XRD measurements on PBF Inconel 718 samples. The effectiveness of reducing residual stresses by preheating, however, needs to be proven for a complex 3D geometry. Hence, different preheating conditions (preheating temperatures and cooling rates) are examined in this study. The present work successfully reveals and captures the beneficial effect of preheating on the Inconel 625 bridge structure. Significant influences of preheating and cooling rate on residual stress are also predicted by Cao et al. [56] and Lu et al. [57]. Vrancken et al. [58] experimentally measured the residual stress of Ti-6Al-4V parts produced by PBF under different preheating temperatures (100 ^{o}C, 200 ^{o}C, 300 ^{o}C, 400 ^{o}C) using XRD, demonstrating benefits of preheating the substrate, as the residual stress was significantly reduced from 628 MPa with no preheating, to 313 MPa under 400 ^{o}C preheating. Through investigation on the effects of different preheating temperature on PBF Inconel 738 by numerical simulation and experimental analysis, Wang et al. [59]

found that the temperature gradients obviously reduced with increased preheating temperature: the maximum drop in temperature gradients was around 25% when the preheating was increased from 200 ^{o}C to 600 ^{o}C. Lower temperature gradients and cooling rates make the phase change process more stable, which reduces the residual stresses. Based on the results shown in Figures. 4.18 and 4.19, an appropriate preheating condition should be selected for mitigating the residual stress and distortion of AM components, particularly the tensile residual stresses, which are detrimental to fatigue resistance [60]. Hua et al. [61] investigated the influence of residual stress on fatigue performance of Inconel 718, experimentally showing that the fatigue life increased by 83.6% with the mitigation of residual stress by 17.9%. Hence, higher preheating and build chamber temperatures could be integrated into next generation PBF machines for reduced residual stresses [62].

Recently, Yang et al. [20, 63] have presented a process-structure model and a structure-property model, successfully predicting the microstructure attributes (e.g. columnar-equiaxed morphology, phase fractions and lath width) and stress-strain responses (including yield stress, ultimate tensile strength, uniform elongation and flow stress). Zhang et al. [64] introduced an FE-based generic metallurgical phase transformation framework, allowing the user to define and to model phase transformations in an alloy during AM process. Eberechukwu [65] has performed thermodynamic phase transformation simulation of 304L stainless steel using MatCalc and ThermoCalc; the results indicate that for high cooling rates (typically > 10^5 K/s) the proportions of FCC and BCC were comparable while the fractions of FCC increased and that of BCC decreased progressively for lower cooling rates. In future work, it is planned to extend the current model to include the metallurgical phase transformation model (e.g. using ThermoCalc), the process-structure model and the structure-property model to provide a pragmatic model to address the process-structure-property-performance (PSPP) relationships and optimize the AM process for manufacturing real-scale components with improved mechanical performance (e.g. tensile and fatigue) for industrial applications.

4.6 Conclusions

This paper presents an efficient and accurate component-level finite element thermo-mechanical model for predicting residual stress and distortion in the PBF manufactured complex Inconel 625 bridge. The developed model is verified and validated through mesh sensitivity studies and detailed comparisons against NIST benchmark measurements. The validated model is used to investigate the effects of substrate removal and preheating conditions on residual stresses and distortions. The key conclusions are:

- Comparison to detailed measurements from Phan et al. [11] has shown that the component-level finite element process model accurately predicts transient development of residual strains, stresses and distortions.
- It is shown that significant improvement in computational efficiency is achieved with minimal sacrifice in accuracy by simulating multiple printing layers (layer scale-up).
- The model shows that removal of substrate gives a significant beneficial reduction of residual stress of 335.8 MPa (24.2%) and distortion of the Inconel 625 bridge component.
- The model shows that increasing preheating temperature and decreasing cooling rate can significantly mitigate the residual stresses and distortions, by 81% and 98%, respectively.
- The present study offers practical guidelines on selection of optimal PBF protocols and a practical method for integrating finite element based PBF modelling into industry design and manufacturing systems.

4.7 References

[1] W.E. Frazier, Metal additive manufacturing: a review, Journal of Materials Engineering and Performance 23(6) (2014) 1917-1928.
[2] T. Gatsos, K.A. Elsayed, Y. Zhai, D.A. Lados, Review on Computational Modeling of Process–Microstructure–Property Relationships in Metal Additive Manufacturing, JOM 72(1) (2020) 403-419.
[3] E.R. Denlinger, P. Michaleris, Effect of stress relaxation on distortion in additive manufacturing process modeling, Additive Manufacturing 12 (2016) 51-59.
[4] J.L. Bartlett, X. Li, An overview of residual stresses in metal powder bed fusion,

Additive Manufacturing 27 (2019) 131-149.
[5] S.-g. Chen, H.-j. Gao, Q. Wu, Z.-h. Gao, X. Zhou, Review on residual stresses in metal additive manufacturing: formation mechanisms, parameter dependencies, prediction and control approaches, Journal of Materials Research and Technology 17 (2022) 2950-2974.
[6] P. Edwards, M. Ramulu, Fatigue performance evaluation of selective laser melted Ti–6Al–4V, Materials Science and Engineering: A 598 (2014) 327-337.
[7] A. Fatemi, R. Molaei, J. Simsiriwong, N. Sanaei, J. Pegues, B. Torries, N. Phan, N. Shamsaei, Fatigue behaviour of additive manufactured materials: An overview of some recent experimental studies on Ti‐6Al‐4V considering various processing and loading direction effects, Fatigue & Fracture of Engineering Materials & Structures 42(5) (2019) 991-1009.
[8] Z. Xiao, C. Chen, H. Zhu, Z. Hu, B. Nagarajan, L. Guo, X. Zeng, Study of residual stress in selective laser melting of Ti6Al4V, Materials & Design 193 (2020) 108846.
[9] X. Song, S. Feih, W. Zhai, C.-N. Sun, F. Li, R. Maiti, J. Wei, Y. Yang, V. Oancea, L. Romano Brandt, A.M. Korsunsky, Advances in additive manufacturing process simulation: Residual stresses and distortion predictions in complex metallic components, Materials & Design 193 (2020) 108779.
[10] T. Simson, A. Emmel, A. Dwars, J. Böhm, Residual stress measurements on AISI 316L samples manufactured by selective laser melting, Additive Manufacturing 17 (2017) 183-189.
[11] T.Q. Phan, M. Strantza, M.R. Hill, T.H. Gnaupel-Herold, J. Heigel, C.R. D'Elia, A.T. DeWald, B. Clausen, D.C. Pagan, J.Y. Peter Ko, D.W. Brown, L.E. Levine, Elastic Residual Strain and Stress Measurements and Corresponding Part Deflections of 3D Additive Manufacturing Builds of IN625 AM-Bench Artifacts Using Neutron Diffraction, Synchrotron X-Ray Diffraction, and Contour Method, Integrating Materials and Manufacturing Innovation 8(3) (2019) 318-334.
[12] R. Barros, F.J. Silva, R.M. Gouveia, A. Saboori, G. Marchese, S. Biamino, A. Salmi, E. Atzeni, Laser powder bed fusion of Inconel 718: Residual stress analysis before and after heat treatment, Metals 9(12) (2019) 1290.
[13] Ó. Teixeira, F.J. Silva, E. Atzeni, Residual stresses and heat treatments of Inconel 718 parts manufactured via metal laser beam powder bed fusion: an overview, The International Journal of Advanced Manufacturing Technology 113(11) (2021) 3139-3162.
[14] T. Mishurova, S. Cabeza, T. Thiede, N. Nadammal, A. Kromm, M. Klaus, C. Genzel, C. Haberland, G. Bruno, The Influence of the Support Structure on Residual Stress and Distortion in SLM Inconel 718 Parts, Metallurgical and Materials Transactions A 49(7) (2018) 3038-3046.
[15] H. Ali, L. Ma, H. Ghadbeigi, K. Mumtaz, In-situ residual stress reduction, martensitic decomposition and mechanical properties enhancement through high temperature powder bed pre-heating of Selective Laser Melted Ti6Al4V, Materials Science and Engineering: A 695 (2017) 211-220.
[16] M. Narvan, A. Ghasemi, E. Fereiduni, S. Kendrish, M. Elbestawi, Part deflection and residual stresses in laser powder bed fusion of H13 tool steel, Materials & Design 204 (2021) 109659.
[17] M. Chiumenti, E. Neiva, E. Salsi, M. Cervera, S. Badia, J. Moya, Z. Chen, C. Lee, C. Davies, Numerical modelling and experimental validation in Selective Laser Melting,

Additive Manufacturing 18 (2017) 171-185.
[18] A. Hussein, L. Hao, C. Yan, R. Everson, Finite element simulation of the temperature and stress fields in single layers built without-support in selective laser melting, Materials & Design (1980-2015) 52 (2013) 638-647.
[19] N. Hodge, R. Ferencz, J. Solberg, Implementation of a thermomechanical model in diablo for the simulation of selective laser melting, Lawrence Livermore National Laboratory, Livermore, CA (United States), 2013.
[20] X. Yang, R.A. Barrett, M. Tong, N.M. Harrison, S.B. Leen, Towards a process-structure model for Ti-6Al-4V during additive manufacturing, Journal of Manufacturing Processes 61 (2021) 428-439.
[21] P. Promoppatum, V. Uthaisangsuk, Part scale estimation of residual stress development in laser powder bed fusion additive manufacturing of Inconel 718, Finite Elements in Analysis and Design 189 (2021) 103528.
[22] M. Bayat, C.G. Klingaa, S. Mohanty, D. De Baere, J. Thorborg, N.S. Tiedje, J.H. Hattel, Part-scale thermo-mechanical modelling of distortions in Laser Powder Bed Fusion – Analysis of the sequential flash heating method with experimental validation, Additive Manufacturing 36 (2020) 101508.
[23] R.J. Williams, C.M. Davies, P.A. Hooper, A pragmatic part scale model for residual stress and distortion prediction in powder bed fusion, Additive Manufacturing 22 (2018) 416-425.
[24] W.D. Rolph III, K.J. Bathe, An efficient algorithm for analysis of nonlinear heat transfer with phase changes, International Journal for Numerical Methods in Engineering 18(1) (1982) 119-134.
[25] S.-H. Kim, J.-B. Kim, W.-J. Lee, Numerical prediction and neutron diffraction measurement of the residual stresses for a modified 9Cr–1Mo steel weld, Journal of Materials Processing Technology 209(8) (2009) 3905-3913.
[26] K. Karayagiz, A. Elwany, G. Tapia, B. Franco, L. Johnson, J. Ma, I. Karaman, R. Arróyave, Numerical and experimental analysis of heat distribution in the laser powder bed fusion of Ti-6Al-4V, IISE Transactions 51(2) (2018) 136-152.
[27] B. Cheng, S. Shrestha, K. Chou, Stress and deformation evaluations of scanning strategy effect in selective laser melting, Additive Manufacturing 12 (2016) 240-251.
[28] Y. Li, K. Zhou, P. Tan, S.B. Tor, C.K. Chua, K.F. Leong, Modeling temperature and residual stress fields in selective laser melting, International Journal of Mechanical Sciences 136 (2018) 24-35.
[29] Abaqus Analysis User's Guide, Dassault Systemes (2018).
[30] J. Zhou, R.A. Barrett, S.B. Leen, Three-dimensional finite element modelling for additive manufacturing of Ti-6Al-4V components: Effect of scanning strategies on temperature history and residual stress, Journal of Advanced Joining Processes 5 (2022) 100106.
[31] W. Zhang, M. Tong, N.M. Harrison, Scanning strategies effect on temperature, residual stress and deformation by multi-laser beam powder bed fusion manufacturing, Additive Manufacturing 36 (2020) 101507.
[32] L. Lindgren, Computational welding mechanics: Thermomechanical and microstructructural simulations, CRC Press/Woodhead Publishing, Boca Raton, Florida/Cambridge, UK, 2007.

[33] W. Zhang, M. Tong, N.M. Harrison, Multipart Build Effects on Temperature and Residual Stress by Laser Beam Powder Bed Fusion Additive Manufacturing, 3D Printing and Additive Manufacturing (2021).
[34] Y. Yang, M. Allen, T. London, V. Oancea, Residual Strain Predictions for a Powder Bed Fusion Inconel 625 Single Cantilever Part, Integrating Materials and Manufacturing Innovation 8(3) (2019) 294-304.
[35] S.A. Khairallah, A.T. Anderson, A. Rubenchik, W.E. King, Laser powder-bed fusion additive manufacturing: Physics of complex melt flow and formation mechanisms of pores, spatter, and denudation zones, Acta Materialia 108 (2016) 36-45.
[36] A. Nycz, Y. Lee, M. Noakes, D. Ankit, C. Masuo, S. Simunovic, J. Bunn, L. Love, V. Oancea, A. Payzant, C.M. Fancher, Effective residual stress prediction validated with neutron diffraction method for metal large-scale additive manufacturing, Materials & Design 205 (2021) 109751.
[37] C. Li, J.F. Liu, X.Y. Fang, Y.B. Guo, Efficient predictive model of part distortion and residual stress in selective laser melting, Additive Manufacturing 17 (2017) 157-168.
[38] Abaqus Analysis User's Guide, Dassault Systems (2020).
[39] Special Metals, Inconel alloy 625, Special Metals Corporation (2013).
[40] P. Wang, B. Zhang, C.C. Tan, S. Raghavan, Y.-F. Lim, C.-N. Sun, J. Wei, D. Chi, Microstructural characteristics and mechanical properties of carbon nanotube reinforced Inconel 625 parts fabricated by selective laser melting, Materials & Design 112 (2016) 290-299.
[41] A. Anca, V.D. Fachinotti, G. Escobar‐Palafox, A. Cardona, Computational modelling of shaped metal deposition, International Journal for Numerical Methods in Engineering 85(1) (2011) 84-106.
[42] Q. Yang, P. Zhang, L. Cheng, Z. Min, M. Chyu, A.C. To, Finite element modeling and validation of thermomechanical behavior of Ti-6Al-4V in directed energy deposition additive manufacturing, Additive Manufacturing 12 (2016) 169-177.
[43] NIST, 2018 AM-Bench Test Descriptions for AMB2018-01, National Institute of Standards and Technology (2018).
[44] B. Ahmad, S.O. van der Veen, M.E. Fitzpatrick, H. Guo, Residual stress evaluation in selective-laser-melting additively manufactured titanium (Ti-6Al-4V) and inconel 718 using the contour method and numerical simulation, Additive Manufacturing 22 (2018) 571-582.
[45] P. Bidare, A. Jiménez, H. Hassanin, K. Essa, Porosity, cracks, and mechanical properties of additively manufactured tooling alloys: a review, Advances in Manufacturing (2021) 1-30.
[46] D.-G. Ahn, Directed energy deposition (DED) process: state of the art, International Journal of Precision Engineering and Manufacturing-Green Technology 8(2) (2021) 703-742.
[47] B. Soundararajan, D. Sofia, D. Barletta, M. Poletto, Review on modeling techniques for powder bed fusion processes based on physical principles, Additive Manufacturing 47 (2021) 102336.
[48] N. Keller, V. Ploshikhin, New Method for Fast Predictions on Residual Stress and Distortion of AM Parts, 2014 International Solid Freeform Fabrication Symposium, University of Texas at Austin, 2014.

[49] R. Ganeriwala, M. Strantza, W. King, B. Clausen, T.Q. Phan, L.E. Levine, D.W. Brown, N. Hodge, Evaluation of a thermomechanical model for prediction of residual stress during laser powder bed fusion of Ti-6Al-4V, Additive Manufacturing 27 (2019) 489-502.
[50] L. Costa, R. Vilar, T. Reti, A. Deus, Rapid tooling by laser powder deposition: Process simulation using finite element analysis, Acta Materialia 53(14) (2005) 3987-3999.
[51] H. Huang, N. Ma, J. Chen, Z. Feng, H. Murakawa, Toward large-scale simulation of residual stress and distortion in wire and arc additive manufacturing, Additive Manufacturing 34 (2020) 101248.
[52] L. Papadakis, A. Loizou, J. Risse, S. Bremen, J. Schrage, A computational reduction model for appraising structural effects in selective laser melting manufacturing, Virtual and Physical Prototyping 9(1) (2014) 17-25.
[53] X. Jimenez, W. Dong, S. Paul, M.A. Klecka, A.C. To, Residual stress modeling with phase transformation for wire arc additive manufacturing of B91 steel, JOM 72(12) (2020) 4178-4186.
[54] E. Salvati, A. Korsunsky, Micro-scale measurement & FEM modelling of residual stresses in AA6082-T6 Al alloy generated by wire EDM cutting, Journal of Materials Processing Technology 275 (2020) 116373.
[55] E. Mirkoohi, H.-C. Tran, Y.-L. Lo, Y.-C. Chang, H.-Y. Lin, S.Y. Liang, Mechanics Modeling of Residual Stress Considering Effect of Preheating in Laser Powder Bed Fusion, Journal of Manufacturing and Materials Processing 5(2) (2021) 46.
[56] J. Cao, M.A. Gharghouri, P. Nash, Finite-element analysis and experimental validation of thermal residual stress and distortion in electron beam additive manufactured Ti-6Al-4V build plates, Journal of Materials Processing Technology 237 (2016) 409-419.
[57] X. Lu, X. Lin, M. Chiumenti, M. Cervera, Y. Hu, X. Ji, L. Ma, H. Yang, W. Huang, Residual stress and distortion of rectangular and S-shaped Ti-6Al-4V parts by Directed Energy Deposition: Modelling and experimental calibration, Additive Manufacturing 26 (2019) 166-179.
[58] B. Vrancken, S. Buls, J.P. Kruth, J.V. Humbeeck, Preheating of selective laser melted Ti6Al4V: microstructure and mechanical properties, Proceedings of the 13th World Conference on Titanium (2016) 1269-1277.
[59] W. Wang, W. Lin, R. Yang, Y. Wu, J. Li, Z. Zhang, Z. Zhai, Mesoscopic evolution of molten pool during selective laser melting of superalloy Inconel 738 at elevating preheating temperature, Materials & Design 213 (2022) 110355.
[60] J.-R. Poulin, V. Brailovski, P. Terriault, Long fatigue crack propagation behavior of Inconel 625 processed by laser powder bed fusion: Influence of build orientation and post-processing conditions, International Journal of Fatigue 116 (2018) 634-647.
[61] Y. Hua, Z. Liu, Experimental investigation of principal residual stress and fatigue performance for turned nickel-based superalloy Inconel 718, Materials 11(6) (2018) 879.
[62] S. Sillars, C. Sutcliffe, A. Philo, S. Brown, J. Sienz, N. Lavery, The three-prong method: a novel assessment of residual stress in laser powder bed fusion, Virtual and Physical Prototyping 13(1) (2018) 20-25.
[63] X. Yang, R.A. Barrett, N.M. Harrison, S.B. Leen, A physically-based structure-property model for additively manufactured Ti-6Al-4V, Materials & Design 205 (2021) 109709.

[64] Q. Zhang, J. Xie, Z. Gao, T. London, D. Griffiths, V. Oancea, A metallurgical phase transformation framework applied to SLM additive manufacturing processes, Materials & Design 166 (2019) 107618.
[65] E.A. Okoro, Controlling phase fractions of 304L-SS in selective laser melting using cooling rate, Missouri University of Science and Technology, 2018.

5 Effect of Build Orientation and Surface Roughness on Fatigue Behavior of Additively Manufactured 316L Stainless Steel

Jinbiao Zhou[1,2,3], Yefeng Chen[4], Christopher O'Hara[5], David Tormey[5], Richard A. Barrett[1,2,3], Xiaowei Wang[4], Sean B. Leen[1,2,3]

[1]Mechanical Engineering, College of Engineering and Informatics, University of Galway, Galway, Ireland.

[2]Ryan Institute for Environmental, Marine and Energy Research, University of Galway, Galway, Ireland.

[3]I-Form Advanced Manufacturing Research Centre, Ireland.

[4]School of Mechanical and Power Engineering, Nanjing Tech University, Nanjing, China.

[5]Centre for Precision Engineering, Materials and Manufacturing Research, Atlantic Technological University, Sligo, Ireland.

Jinbiao Zhou: Conceptualization, Methodology, Software, Writing - original draft.

Summary

This chapter presents results of mechanical characterization (e.g. density, surface roughness, residual stress measurement) and mechanical (e.g. tensile, fatigue) testing of PBF-LB 316L stainless steel specimens. The fatigue characterization results will be used to guide the life prediction of complex AM components.

5.1 Abstract

Additive manufacturing (AM) has attracted significant attention in many applications due to its capability of fabricating complex and customized metal parts. However, the susceptibility of AM parts to defects, such as voids created by the lack of fusion, prevents more widespread application of AM technique. Formation of such defects depends on the process parameters such as build orientation and post-AM surface treatment. This work examines the effect of build orientation and surface roughness on the fatigue behavior and residual stresses of 316L stainless steel specimens produced by laser beam powder bed fusion (PBF-LB). X-ray diffraction (XRD) and fatigue testing are used to investigate the residual stress and fatigue behavior of AM 316L specimens. Specimens built in different orientations (e.g. horizontal and vertical to the substrate) are considered to account for the anisotropic nature of the AM component. Results show that the fatigue behavior is influenced by the build orientation and surface roughness. These findings will guide the prediction of fatigue life for industrial application with complex geometries, such as for conformally-cooled injection moulding tools.

5.2 Introduction

Additive manufacturing (AM) is the process of manufacturing parts from digital 3D models by connecting materials layer by layer, which enables to fabricate customized parts with high geometric complexity [1-3]. Among the numerous AM technologies, the powder bed fusion (PBF) technique is one of the commonly applied methods for production of AM parts [4, 5]. PBF produced stainless steel (SS) 316L has been frequently applied in aerospace, marine, medical, nuclear and energy industries due to its high

corrosion resistance, strength and bio-functionality [6-8]. Although PBF SS316L offers many advantages, there are inconsistencies in the mechanical properties of PBF SS316L parts due to variations in their thermal history, which result in heterogeneity and anisotropy in their microstructural features [9-11]. In addition, AM parts are commonly vulnerable to microstructural defects, such as lack of fusion (LoF) and gas pores, which has a greater influence on the fatigue strength of a part than on its quasi-static properties [12-14]. Furthermore, it is important to make AM parts have predictable and adaptable fatigue crack initiation (FCI) life to ensure their effective utilization [15].

The build orientation can cause significant variations in the mechanical properties of AM parts [16, 17]. The anisotropic behavior of AM structures and its correlation with the build orientation has been extensively studied in relation to monotonic loading. Liverani et al. [18] investigated the correlation between laser power, hatch spacing and building orientation on the resulting microstructure and mechanical properties of AISI 316L samples produced by PBF and highlighted the fact that PBF SS316L samples fabricated at an angle of 45° showed higher yield strength and ultimate tensile strength and lower elongation compared to the vertically built ones. Hamza et al. [19] presented the fracture toughness property of SS316L made by PBF in different build orientations and revealed that the build orientation has a strong effect on the fracture toughness, for example, the highest fracture toughness value was 176 MPa $m^{1/2}$ in the xz build orientation while the lowest value was 145 MPa $m^{1/2}$ in the z build orientation. Beside the dependency of the mechanical properties on building direction, surface roughness also induced significant differences of mechanical properties of AM materials. Everhart et al. [20] evaluated the difference in the behavior of PBF 17 PH and electron beam melted (EBM) Ti-6Al-4V tensile bars with unimproved surface and those with machined surface, the results indicated that both materials exhibited lower yield strength in unimproved tensile bar, but ultimate tensile strength is only lower on EBM Ti-6Al-4V samples with unimproved surface. Portella et al. [21] performed experimental characterizations (including cross-sectional optical micrographs, X-ray diffraction, phase analyses, surface roughness, micro-tensile testing and microhardness profiles) on the PBF SS316L parts after the surface mechanical attrition treatment (SMAT) post-treatment and highlighted that SMAT

reduced the surface roughness by a factor of 10 and transformed the near-surface tensile residual stress into compressive stress, which enhanced the tensile mechanical properties of PBF 316L specimens. Aboulkhair et al. [22] commented that the focus of numerous studies in the field of AM metals has been on examining the influence of printing process parameters on the monotonic mechanical properties. However, there has been relatively less investigation into the influence of building parameters, such as build orientation and surface roughness, on the fatigue performance and residual stress of AM components.

Consequently, the objective of the present study is investigation of the effect of build orientation and surface roughness on the fatigue behavior and residual stresses of SS316L specimens produced by PBF. Firstly, surface roughness and residual stress analysis are performed in two different material surface conditions: as-built (AB) and machined (M). Secondly, the tensile properties of PBF 316L are investigated by means of tensile tests. In addition, a series of high cycle fatigue (HCF) tests at various stress amplitudes are conducted to examine the effect of stress amplitude on the fatigue behavior.

5.3 Methodology

5.3.1 Sample preparation

All samples were produced using the Concept Laser M1 machine shown in Figure 5.1. An overview of the machine specifications are given in Table 5.1. The samples were produced with optimized building parameters as shown in Table 5.2. The nominal chemical composition of the 316L stainless steel powder were obtained from GE Additive, as listed in Table 5.3.

Figure 5.1**.** Concept Laser M1 machine used for sample fabrication.

Table 5.1. Machine specifications.

Building space	$250 \times 250 \times 250$ mm
Max. scanning speed	7 m/s
Layer thickness	$20 - 80$ µm
Max. laser power	200 W
Focus diameter	$50 - 200$ µm

Table 5.2. PBF process parameters of fabricating 316L SS specimens.

Laser power (W)	**Scanning speed (mm/s)**	**Hatch spacing (µm)**	**Layer thickness (µm)**
180	1200	100	20

Table 5.3. Chemical composition of 316L SS powder provided by GE Additive.

Element	**wt %**

Fe	Balance
Cr	16.5-18.5
Ni	10.0-13.0
Mo	2.0-2.5
Mn	0-2.0
Si	0-1.0
P	0-0.045
C	0-0.03
S	0-0.03

Figure 5.2 shows two different drawings of test specimen [23]. In order to investigate the effect of building orientation, specimens with three building orientations, namely vertical (V), horizontal 1 (H1) and horizontal 2 (H2), were used in tensile and fatigue test experiments. The produced specimens are shown in Figure 5.3.

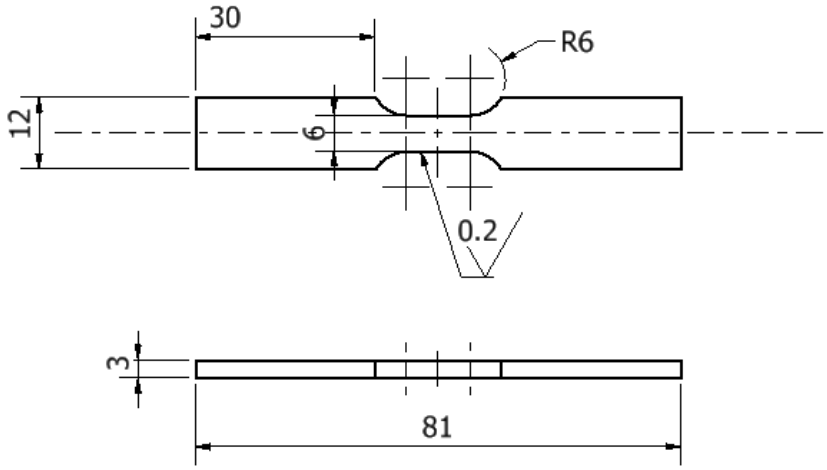

(a)

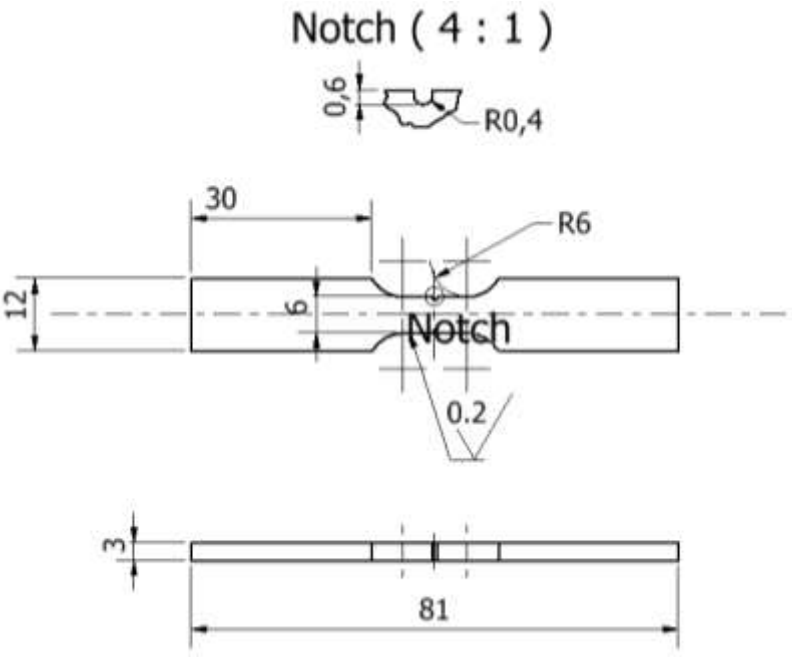

(b)

Figure 5.2**.** Drawing of test specimen: (a) flat specimen, (b) notched specimen.

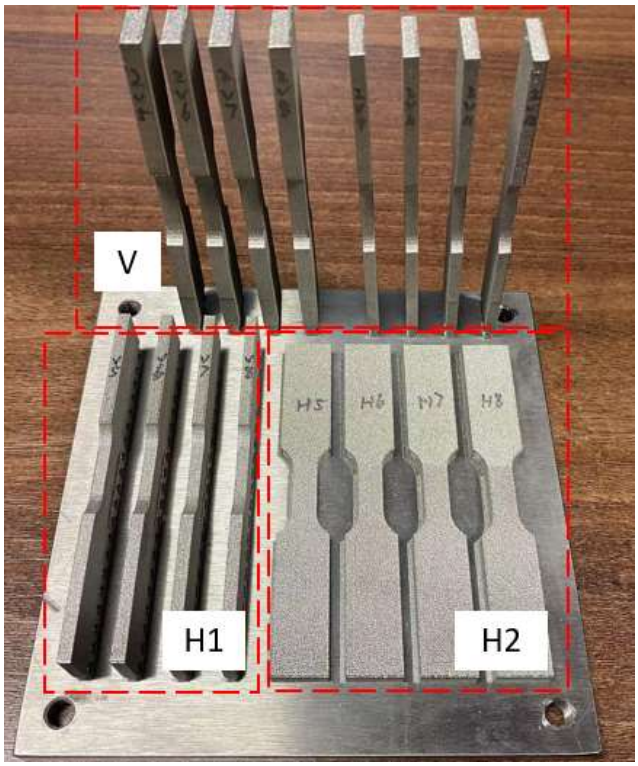

(a)

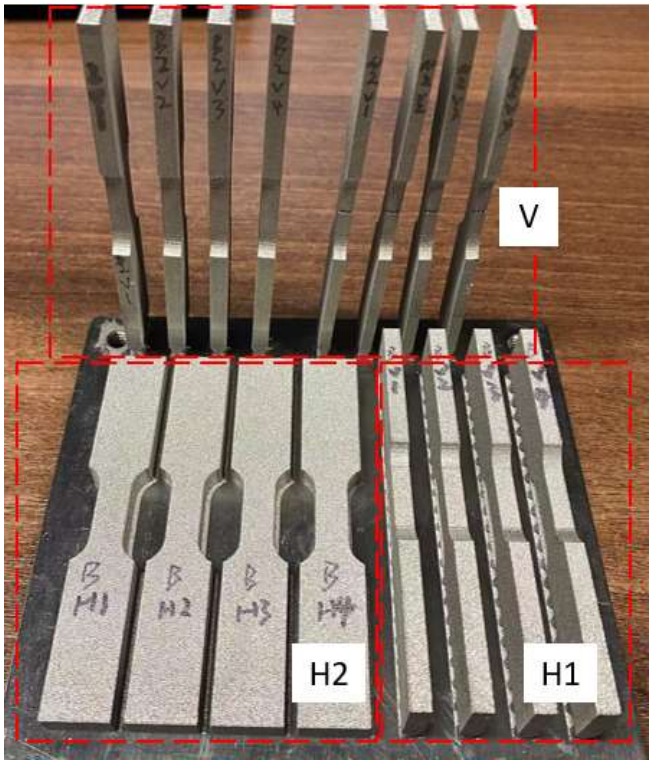

(b)

Figure 5.3**.** Specimens after production.

5.3.2 Experimental testing

5.3.2.1 Density measurement

The Archimedes measurements were performed according to ASTM B311 standard [24], as shown in Figure 5.4.

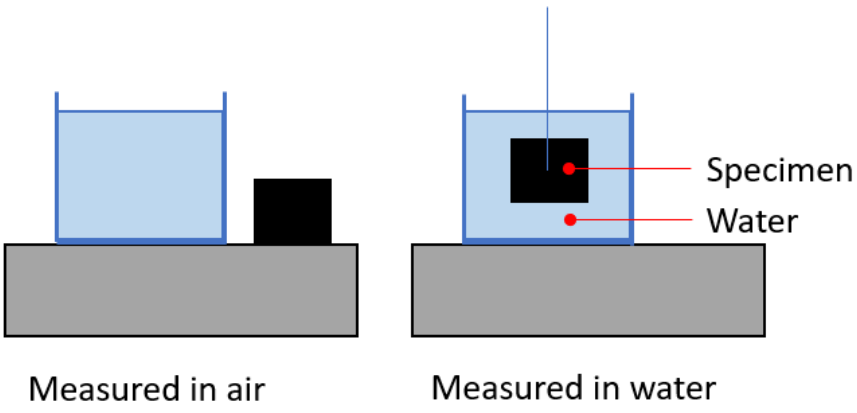

Figure 5.4**.** Density measurement using Archimedes method.

The measurements make it possible to know the mass in the air ($M_{\text{in air}}$) and the mass in the water ($M_{\text{in water}}$) of each sample. And, knowing the density of the water (ρ_{water}), it becomes possible to calculate the density of the specimen (ρ_{specimen}) according to the Eq. (5.1). The comparison of the obtained specimen density with the reference density of the material enables the calculation of the relative density of the specimens, as given by Eq. (5.2).

$$\rho_{\text{specimen}} = \frac{M_{\text{in air}}}{(M_{\text{in air}} - M_{\text{in water}})} \times \rho_{\text{water}} \tag{5.1}$$

$$\rho_{\text{rel}}(\%) = \frac{\rho_{\text{specimen}}}{\rho_{\text{reference}}} \times 100\% \tag{5.2}$$

where ρ_{specimen} is the density of the specimen (g/cm^3), ρ_{water} is the density of distilled water (1 g/cm^3), $M_{\text{in air}}$ is mass of the specimen in air (g), $M_{\text{in water}}$ is mass of the specimen immersed in distilled water (g), ρ_{rel} is relative density, $\rho_{\text{reference}}$ is nominal density of 316L (7.99 g/cm3).

5.3.2.2 Surface roughness measurements

The surface roughness of the specimens was measured using the atomic force microscope (AFM) from Bruker (see Figure 5.5 (a)) in the ScanAsyst mode. A SCANASYST-AIR probe was installed in the AFM holder, as shown in Figure 5.5 (b). AFM images were post-processed with Gwyddion software (version 2.43).

(a) BRUKER Atomic Force Microscopy (AFM)

(b) SCANASYST-AIR probe

Figure 5.5**.** Machine used for surface roughness measurement: (a) BRUKER Atomic Force Microscopy (AFM), (b) SCANASYST-AIR probe.

5.3.2.3 Residual stress measurement

The residual stresses of the specimens were determined by the PROTO-iXRD residual stress analyser, which works by irradiating a material with incident X-rays and then measuring the intensities and scattering angles of the X-rays that leave the material [25], as shown in Figure 5.6. Calibration has been performed according to user's manual of PROTO-iXRD. Table 5.4 lists the parameters set for residual stress measurement.

Figure 5.6**.** Machine used for residual stress measurement.

Table 5.4. Measurement parameters of residual stress.

$\sin^2 \psi$ method	**Value**
X-radiation	Mn K_α
Voltage (kV)	20.0
Beam current (mA)	4.0
Austenite reflection	311
Wave length λ (nm)	0.210314
Elastic constants S_1^{311} (MPa^{-1})	-1.76×10^{-6}
Elastic constants $\frac{1}{2}S_2^{311}$ (MPa^{-1})	7.07×10^{-6}

5.3.2.4 Tensile test

The tensile tests were performed using a Zwick Z050 (Zwick/Roell GmbH, Germany) fitted with Zwick TestXpert software and equipped with an Epsilon clip-on extensometer model 3542 of a 10 mm gauge length, as shown in Figure 5.7. The tensile testing was conducted under a strain rate of 5×10^{-4} s^{-1} at room temperature.

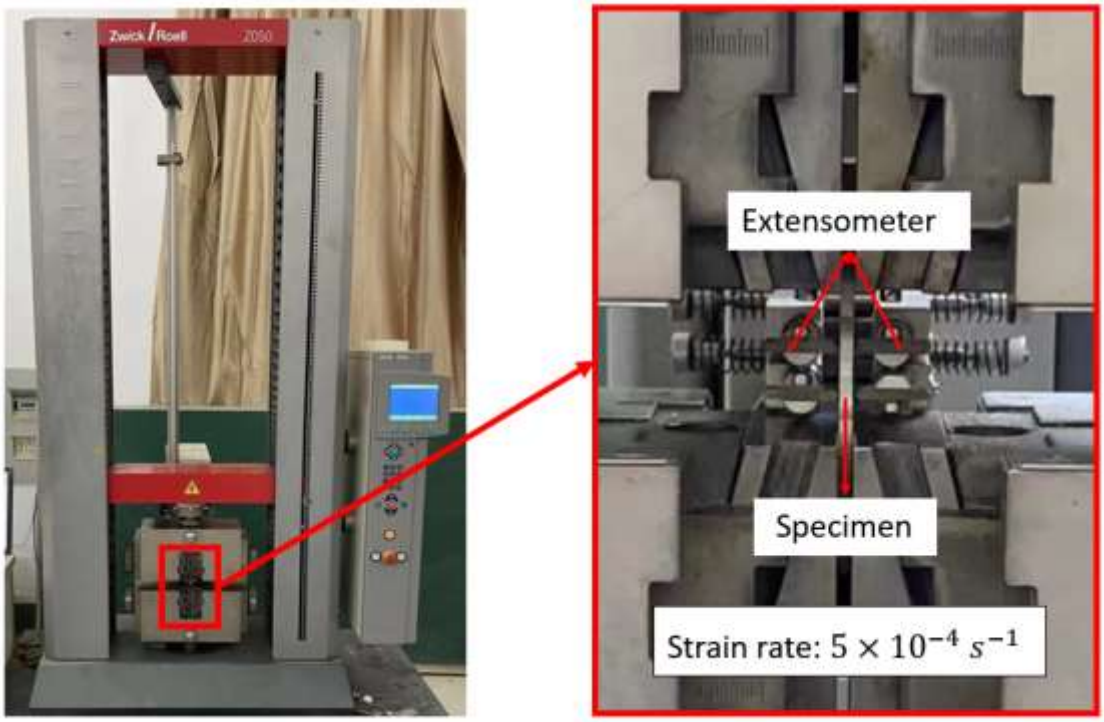

Figure 5.7**.** Tensile testing machine.

5.3.2.5 Fatigue test

The fatigue tests were conducted under load-controlled loading at 12 Hz at room temperature. Figure 5.8 shows the SHIMADZU SERVOPULSER fatigue test system (SHIMADZU, Kyoto, Japan) used in this study.

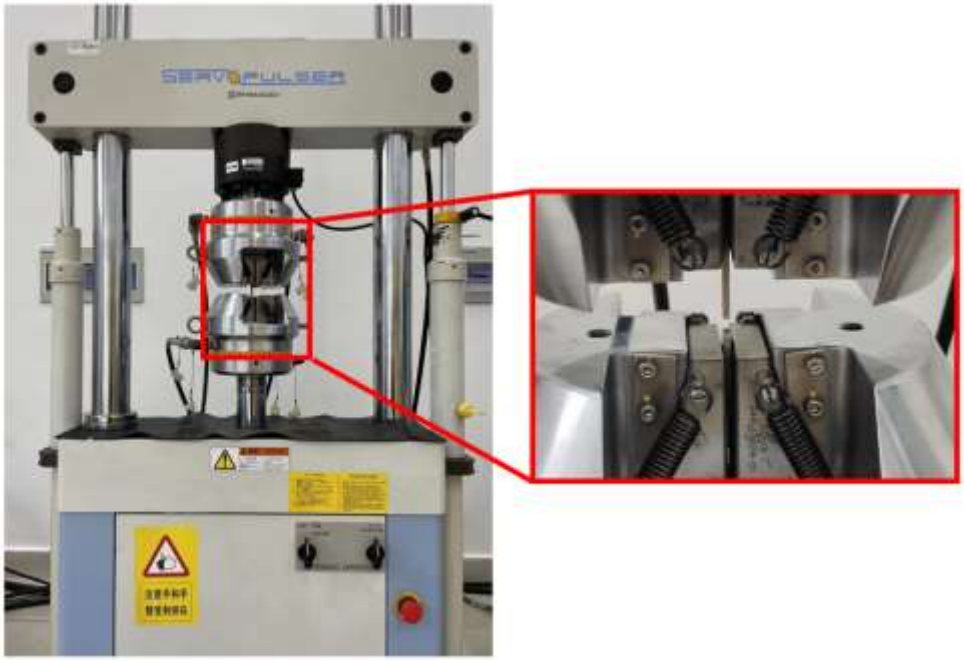

Figure 5.8**.** Fatigue testing machine.

5.4 Results

5.4.1 Density analysis

In order to get insight into the fluctuation range of density measurements, three specimens produced with the same process parameters were measured three times each. The mean density of these specimens and the standard deviation of the density measurements are listed in Table 5.5.

Table 5.5. Density measurement of AM 316L with different orientation.

Specimen group	Relative density (%)	
	Mean	STDEV
V	99.29	0.29
H1	98.62	0.5
H2	96.16	0.83

5.4.2 Surface roughness analysis

Figure 5.9 shows the printed specimens after cutting off from the substrate. The as-built specimens (see Figure 5.9(a)) and specimens after machining (see Figure 5.9(b)) are used to investigate the effect of surface roughness on fatigue behavior. Surface roughness data are an average of minimum three measurements taken in the center of the gauge length of three specimens, as listed in Table 5.6, where R_a is the arithmetic mean roughness and R_z is the average maximum height of the roughness.

(a) as-built (b) Machined

Figure 5.9**.** Specimens after cutting off from the substrate: (a) As-built, (b) Machined.

Table 5.6. Surface roughness analysis on the gauge section of the 316L specimens.

Surface condition	R_a (µm)		R_z (µm)	
	Mean	**STDEV**	**Mean**	**STDEV**
As-built	6.0	N/A	40.0	N/A
Machined	0.2	0.09	0.69	0.29

5.4.3 Residual stress analysis

Figure 5.10 shows the measured residual stress of AM 316L along building direction (Figure 5.10(a)) and scanning direction (Figure 5.10(b)), respectively. The residual stresses of vertical specimens are higher than those of horizontal specimens both along building and scanning directions, which is consistent with the published results [26].

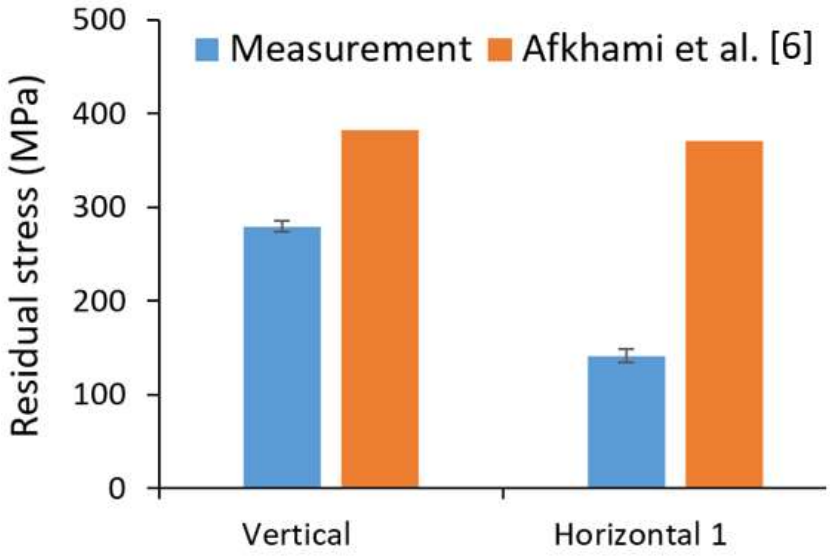

(a) along building direction

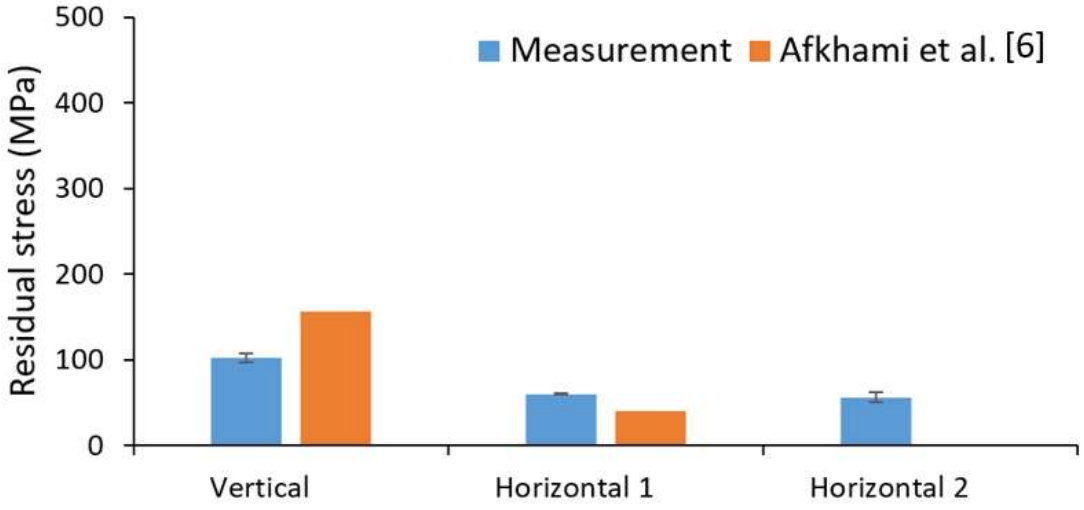

(b) along scanning direction

Figure 5.10**.** Residual stress measurement of AM 316L: (a) along building direction, (b) along scanning direction.

5.4.4 Tensile behaviour

Figure 5.11 presents the engineering stress versus engineering strain for the specimens with different surface conditions and building orientations. For the horizontally built specimen, the loading direction is perpendicular to layer added direction while for vertically built specimen, the loading direction is parallel with layer added direction. It is clear that machining increased the yield strength and ultimate tensile strength, and decreased the elongation compared to the as-built condition. The machined horizontal specimen has higher yield strength and ultimate tensile strength than machined vertical specimen, while lower in terms of elongation.

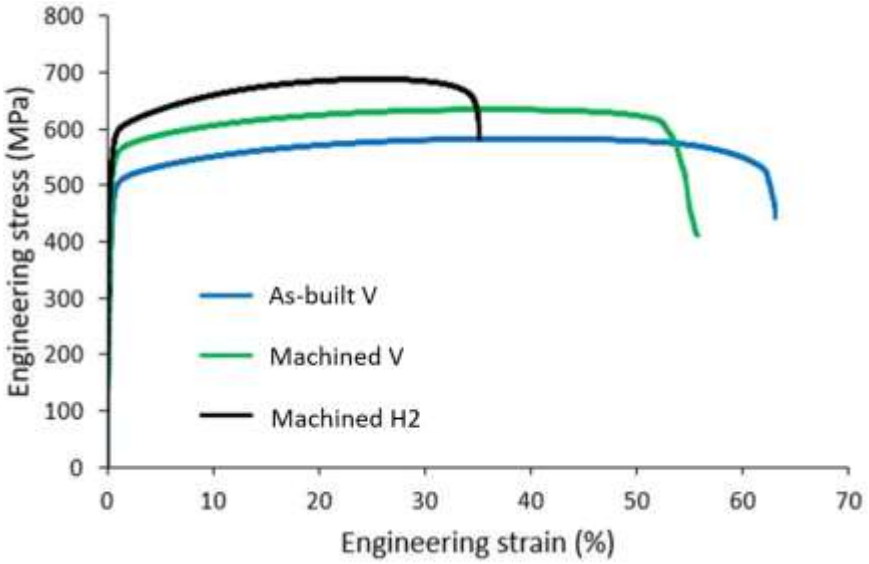

Figure 5.11**.** Results of tensile tests for PBF 316L specimens with different build orientations.

5.4.5 Fatigue behaviour

Figures 7.12, 7.13 and 7.14 show the S-N data for different PBF 316L specimens. As indicated by the S-N data in Figure 5.12, the as-built specimens exhibit the lower fatigue

lives compared to the machined specimens irrespective of build orientation, which is consistent with the published results [27]. As Figure 5.13 shows, the mean stress has a significant effect on the fatigue life (viz. 862872 cycles at R = 0.5 as compared to 382952 cycles at R = -1). Figure 5.14 illustrates that a smoother surface also leads to a significant increase in fatigue lives of notched specimens.

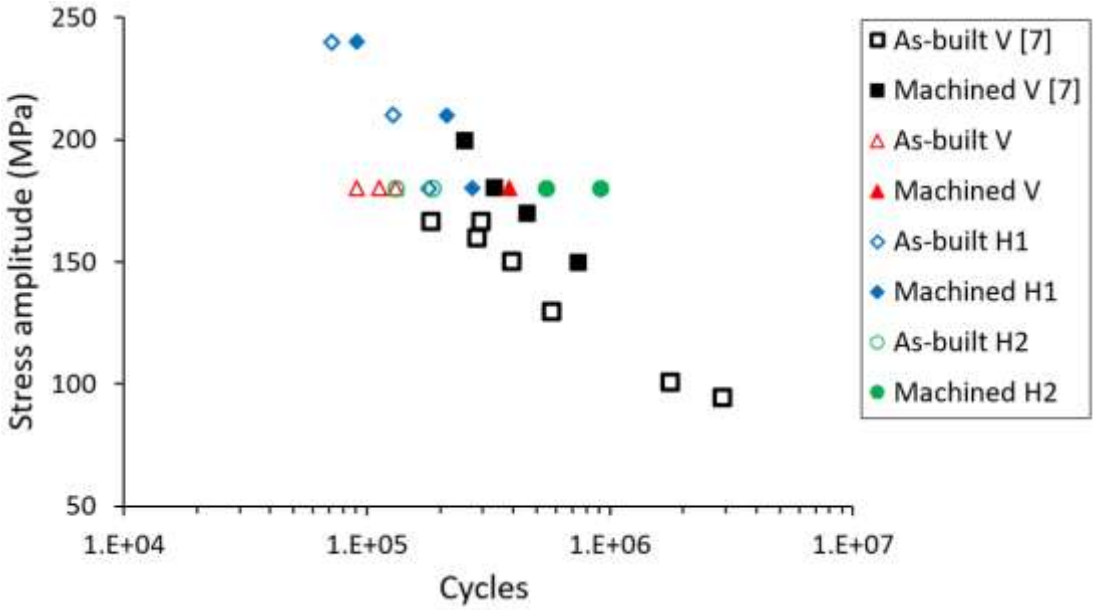

Figure 5.12**.** S-N data for PBF 316L flat specimens (see Figure 5.2(a)) tested at R = -1 (effect of stress amplitude).

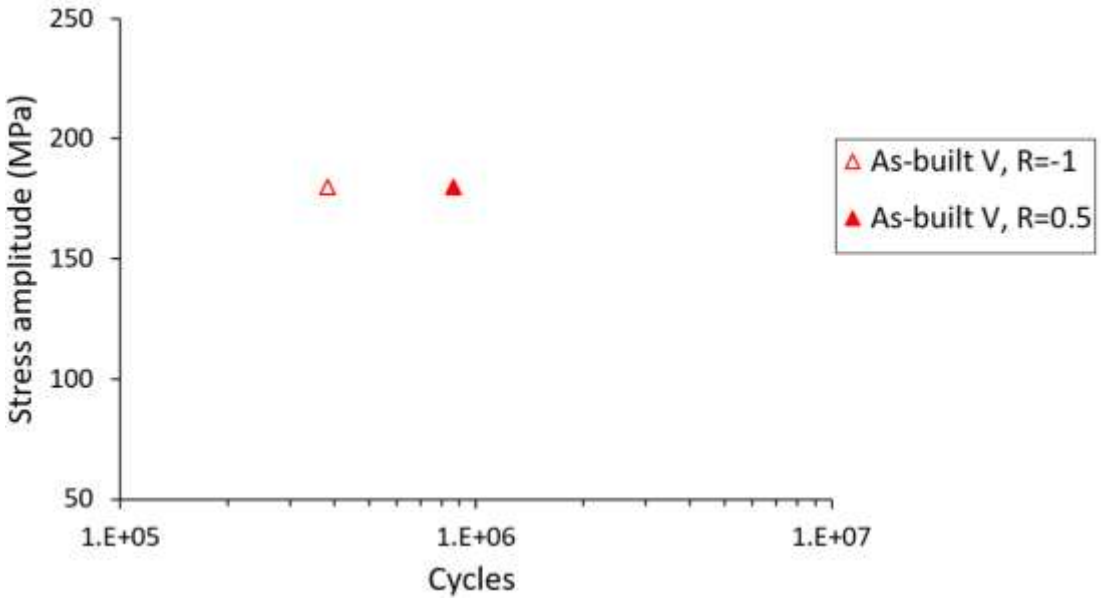

Figure 5.13**.** S-N data for PBF 316L flat specimens (see Figure 5.2(a)) tested at different load ratios (effect of mean stress).

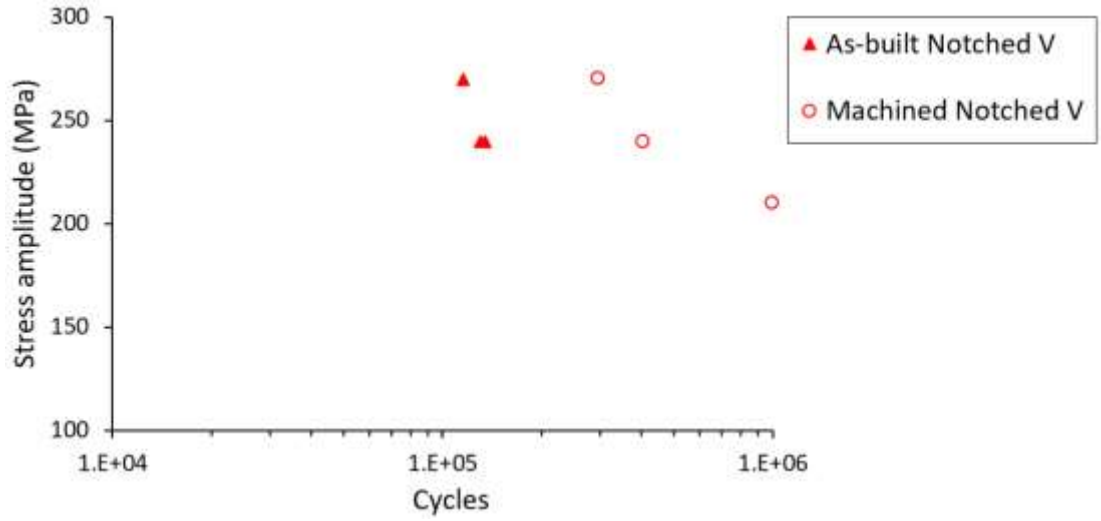

Figure 5.14**.** S-N data for PBF 316L notched specimens (see Figure 5.2(b)) tested at R = -0.1 (effect of stress amplitude).

5.5 Discussion

Researches conducted on PBF SS316L have demonstrated that the high thermal transients and gradients associated occurring in the PBF technique result in a finely textured

microstructure [28-30]. Meanwhile, many studies have been conducted on the microstructure and mechanical properties under quasi-static tensile loading for AM SS316L. The high strength of AM SS316L has been attributed to the smaller grain size, high dislocation density and low-angle grain boundaries, etc. [31-33]. Chen et al. [34] investigated the microstructure and tensile properties of SS316L fabricated by gas metal arc additive manufacturing (GMA-AM) and the results indicated that numerous austenitic dendrites are well-aligned in a vertical orientation in the GMA-AM 316L plate, which result in the formation of sizable columnar grains in the center of the plate. Saboori et al. [35] evaluated the influence of different protective atmosphere (e.g. using simple nitrogen shielding gas or using nitrogen-filled build chamber) on the microstructure of AISI 316L samples produced by Laser-Directed Energy Deposition using X-ray analysis, optical and scanning electron microscopy and on the mechanical performance using tensile testing, their results demonstrated that the protective atmosphere mainly affects the oxides dimensions and the samples produced under nitrogen-filled build chamber show slightly higher tensile strength and elongation compared to samples produced under simple nitrogen shielding gas. Ronneberg et al. [36] revealed the microstructure-property relations in laser powder bed fusion 316L using isothermal heat treatments as an investigative tool and highlighted that the anisotropic yield behaviour was caused by microstructural features alone and not influenced by porosity while the ductility and failure were dominated by lack of fusion porosity. Tanaka and Mura [37] developed a micromechanical fatigue crack initiation (FCI) model with considering the dislocation structure along the persistent slip bands (PSB). Chan [38] further extended the Tanaka–Mura (T-M) model to deal with crack initiation along the slip bands, inclusions and notches, and then further improved to include crack length and depth. Wu [39] revisited the T-M model and obtained a new FCI life expression based on the true strain definition and validated against experimental results on a small number of materials. However, it's worth noting that all of these validations were exclusively conducted on conventionally manufactured materials. In future work, it is planned to adapt the physically based T-M FCI model from conventionally manufactured materials for PBF SS316L. The predictions

using T-M FCI model will be compared with the experimental results to evaluate its capability in terms of predicting the fatigue behavior.

5.6 Conclusions

This chapter presents the results of a test program for (i) mechanical characterization, including measurement of density, surface roughness, residual stress and (ii) mechanical testing, i.e. tensile and fatigue behavior of PBF 316L stainless steel specimens. The key conclusions are:

- The build orientation is found to have impact on the residual stress magnitude. High magnitude residual stresses were consistently found along the building direction, which may be due to the large thermal gradient resulting from the conduction of heat downwards through the substrate.
- PBF 316L SS specimens exhibited higher yield strength, ultimate tensile strength, and elongation to failure when compared to their wrought counterpart irrespective to the build orientation. In general, the horizontally built PBF 316L SS specimens possessed the higher strength, while the least strength was obtained for vertically built specimens.
- It is shown that horizontally built PBF 316L SS specimens possessed higher fatigue life, and notably improvement in fatigue life is achieved by eliminating surface roughness.
- The present study offers practical guidelines on selection of optimal PBF protocols and forms the basis for prediction of fatigue life for industrial application with complex geometries, such as AM conformally-cooled dies.

5.7 References

[1] ISO/ASTM, Additive Manufacturing—General Principles—Terminology, International Organization for Standardization (2015).
[2] D.I. Wimpenny, P.M. Pandey, L.J. Kumar, Advances in 3D printing & additive manufacturing technologies, Springer2017.
[3] I. Gibson, D. Rosen, B. Stucker, M. Khorasani, D. Rosen, B. Stucker, M. Khorasani, Additive manufacturing technologies, Springer2021.

[4] S. Bremen, W. Meiners, A. Diatlov, Selective laser melting: A manufacturing technology for the future?, Laser Technik Journal 9(2) (2012) 33-38.
[5] C.Y. Yap, C.K. Chua, Z.L. Dong, Z.H. Liu, D.Q. Zhang, L.E. Loh, S.L. Sing, Review of selective laser melting: Materials and applications, Applied Physics Reviews 2(4) (2015) 041101.
[6] M. Yakout, M. Elbestawi, S.C. Veldhuis, On the characterization of stainless steel 316L parts produced by selective laser melting, The International Journal of Advanced Manufacturing Technology 95 (2018) 1953-1974.
[7] D. Kong, X. Ni, C. Dong, X. Lei, L. Zhang, C. Man, J. Yao, X. Cheng, X. Li, Bio-functional and anti-corrosive 3D printing 316L stainless steel fabricated by selective laser melting, Materials & Design 152 (2018) 88-101.
[8] J. Sun, Q. Sun, Y. Liu, B. Li, Z. Zhang, B. Xu, S. Xu, Y. Han, Y. Qiao, J. Han, Improving corrosion resistance of selective laser melted 316L stainless steel through ultrasonic severe surface rolling, Journal of Materials Research and Technology 20 (2022) 4378-4391.
[9] J. Suryawanshi, K. Prashanth, U. Ramamurty, Mechanical behavior of selective laser melted 316L stainless steel, Materials Science and Engineering: A 696 (2017) 113-121.
[10] X.-q. Ni, D.-c. Kong, Y. Wen, L. Zhang, W.-h. Wu, B.-b. He, L. Lu, D.-x. Zhu, Anisotropy in mechanical properties and corrosion resistance of 316L stainless steel fabricated by selective laser melting, International Journal of Minerals, Metallurgy, and Materials 26 (2019) 319-328.
[11] J.M. Jeon, J.M. Park, J.-H. Yu, J.G. Kim, Y. Seong, S.H. Park, H.S. Kim, Effects of microstructure and internal defects on mechanical anisotropy and asymmetry of selective laser-melted 316L austenitic stainless steel, Materials Science and Engineering: A 763 (2019) 138152.
[12] A. Sola, A. Nouri, Microstructural porosity in additive manufacturing: The formation and detection of pores in metal parts fabricated by powder bed fusion, Journal of Advanced Manufacturing and Processing 1(3) (2019) 10021.
[13] M. Laleh, A.E. Hughes, S. Yang, J. Wang, J. Li, A.M. Glenn, W. Xu, M.Y. Tan, A critical insight into lack-of-fusion pore structures in additively manufactured stainless steel, Additive Manufacturing 38 (2021) 101762.
[14] F. Stern, J. Tenkamp, F. Walther, Non-destructive characterization of process-induced defects and their effect on the fatigue behavior of austenitic steel 316L made by laser-powder bed fusion, Progress in Additive Manufacturing 5(3) (2020) 287-294.
[15] Z. Jian, G. Qian, D. Paolino, A. Tridello, F. Berto, Y. Hong, Crack initiation behavior and fatigue performance up to very-high-cycle regime of AlSi10Mg fabricated by selective laser melting with two powder sizes, International Journal of Fatigue 143 (2021) 106013.
[16] M. Simonelli, Y.Y. Tse, C. Tuck, Effect of the build orientation on the mechanical properties and fracture modes of SLM Ti–6Al–4V, Materials Science and Engineering: A 616 (2014) 1-11.
[17] N. Hutasoit, R.R. Rashid, S. Palanisamy, A. Duguid, Effect of build orientation and post-build heat treatment on the mechanical properties of cold spray additively manufactured copper parts, The International Journal of Advanced Manufacturing Technology 110 (2020) 2341-2357.

[18] E. Liverani, S. Toschi, L. Ceschini, A. Fortunato, Effect of selective laser melting (SLM) process parameters on microstructure and mechanical properties of 316L austenitic stainless steel, Journal of Materials Processing Technology 249 (2017) 255-263.
[19] H.H. Alsalla, C. Smith, L. Hao, Effect of build orientation on the surface quality, microstructure and mechanical properties of selective laser melting 316L stainless steel, Rapid Prototyping Journal 24(1) (2018) 9-17.
[20] W. Everhart, E. Sawyer, T. Neidt, J. Dinardo, B. Brown, The effect of surface finish on tensile behavior of additively manufactured tensile bars, Journal of Materials Science 51(8) (2016) 3836-3845.
[21] Q. Portella, M. Chemkhi, D. Retraint, Influence of Surface Mechanical Attrition Treatment (SMAT) post-treatment on microstructural, mechanical and tensile behaviour of additive manufactured AISI 316L, Materials Characterization 167 (2020) 110463.
[22] N.T. Aboulkhair, I. Maskery, C. Tuck, I. Ashcroft, N.M. Everitt, Improving the fatigue behaviour of a selectively laser melted aluminium alloy: Influence of heat treatment and surface quality, Materials & Design 104 (2016) 174-182.
[23] ASTM, Standard test method for strain‐controlled fatigue testing, ASTM Standard E606 (2012).
[24] ASTM, B311-93; Test Method for Density Determination for Powder Metallurgy (P/M) Materials Containing Less Than Two Percent Porosity, American Society for Testing and Materials: Philadelphia, PA, USA (2002).
[25] E. Zolotoyabko, Basic concepts of X-ray diffraction, John Wiley & Sons2014.
[26] S. Afkhami, M. Dabiri, H. Piili, T. Björk, Effects of manufacturing parameters and mechanical post-processing on stainless steel 316L processed by laser powder bed fusion, Materials Science and Engineering: A 802 (2021) 140660.
[27] X. Liang, A. Hor, C. Robert, M. Salem, F. Lin, F. Morel, High cycle fatigue behavior of 316L steel fabricated by laser powder bed fusion: Effects of surface defect and loading mode, International Journal of Fatigue 160 (2022) 106843.
[28] M.L. Montero-Sistiaga, M. Godino-Martinez, K. Boschmans, J.-P. Kruth, J. Van Humbeeck, K. Vanmeensel, Microstructure evolution of 316L produced by HP-SLM (high power selective laser melting), Additive Manufacturing 23 (2018) 402-410.
[29] A. Röttger, J. Boes, W. Theisen, M. Thiele, C. Esen, A. Edelmann, R. Hellmann, Microstructure and mechanical properties of 316L austenitic stainless steel processed by different SLM devices, The International Journal of Advanced Manufacturing Technology 108 (2020) 769-783.
[30] B. Zhou, P. Xu, W. Li, Y. Liang, Y. Liang, Microstructure and anisotropy of the mechanical properties of 316l stainless steel fabricated by selective laser melting, Metals 11(5) (2021) 775.
[31] M. Shamsujjoha, S.R. Agnew, J.M. Fitz-Gerald, W.R. Moore, T.A. Newman, High strength and ductility of additively manufactured 316L stainless steel explained, Metallurgical and Materials Transactions A 49 (2018) 3011-3027.
[32] T. Voisin, J.-B. Forien, A. Perron, S. Aubry, N. Bertin, A. Samanta, A. Baker, Y.M. Wang, New insights on cellular structures strengthening mechanisms and thermal stability of an austenitic stainless steel fabricated by laser powder-bed-fusion, Acta Materialia 203 (2021) 116476.
[33] M.-S. Pham, B. Dovgyy, P.A. Hooper, C.M. Gourlay, A. Piglione, The role of side-

branching in microstructure development in laser powder-bed fusion, Nature communications 11(1) (2020) 749.
[34] X. Chen, J. Li, X. Cheng, B. He, H. Wang, Z. Huang, Microstructure and mechanical properties of the austenitic stainless steel 316L fabricated by gas metal arc additive manufacturing, Materials Science and Engineering: A 703 (2017) 567-577.
[35] A. Saboori, A. Aversa, G. Marchese, S. Biamino, M. Lombardi, P. Fino, Microstructure and mechanical properties of AISI 316L produced by directed energy deposition-based additive manufacturing: A review, Applied Sciences 10(9) (2020) 3310.
[36] T. Ronneberg, C.M. Davies, P.A. Hooper, Revealing relationships between porosity, microstructure and mechanical properties of laser powder bed fusion 316L stainless steel through heat treatment, Materials & Design 189 (2020) 108481.
[37] K. Tanaka, T. Mura, A Dislocation Model for Fatigue Crack Initiation, Journal of Applied Mechanics 48(1) (1981) 97-103.
[38] K.S. Chan, A microstructure-based fatigue-crack-initiation model, Metallurgical and Materials Transactions A 34(1) (2003) 43-58.
[39] X. Wu, On Tanaka-Mura's fatigue crack nucleation model and validation, Fatigue & Fracture of Engineering Materials & Structures 41(4) (2018) 894-899.

6 A physically-based method for predicting high temperature fatigue crack initiation in P91 welded steel

Jinbiao Zhou[1,2,3], Richard A. Barrett[1,2,3], Sean B. Leen[1,2,3]

[1]Mechanical Engineering, College of Engineering and Informatics, University of Galway.

[2]Ryan Institute for Environmental, Marine and Energy Research, University of Galway.

[3]I-Form Advanced Manufacturing Research Centre, Ireland.

Jinbiao Zhou: Conceptualization, Methodology, Software, Writing - original draft.

Summary

This chapter presents a methodology for physically-based prediction of high temperature fatigue crack initiation in 9Cr steels, to specifically facilitate explicit incorporation of the effects of microstructure, e.g. grain or sub-grain dimensions, dislocation density, on both cyclic plasticity and fatigue crack initiation behaviour. This is based on (i) the previously presented dislocation mechanics constitutive model of Barrett et al. for yield strength and cyclic plasticity and (ii) a modified form of the energy-based Tanaka-Mura model for fatigue crack initiation. The method is developed, calibrated and validated here for high temperature low cycle fatigue of 9Cr steel welded connections, but is potentially applicable to other manufacturing processes, in particular, additive manufacturing, e.g. DED (Chapter 3) and PBF (Chapters 4 to 5), due to the close similarities to welding. It is envisaged that the method presented here will form the basis of defect-based PSPP assessment for AM within the I-Form Centre for Advanced Manufacturing, e.g. for design and development of AM conformally-cooled dies for improved injection moulding processes for AbbVie using the fatigue characterisation results from Chapter 5.

6.1 Abstract

A methodology is presented for physically-based prediction of high temperature fatigue crack initiation in 9Cr steels, with a focus on material inhomogeneity due to welding-induced metallurgical transformations. A modified form of the Tanaka-Mura model for slip band formation under cyclically-softening conditions is implemented in conjunction with a physically-based unified cyclic viscoplasticity constitutive model. The physically-based constitutive model accounts for the key strengthening mechanisms, including precipitate hardening and hierarchical grain boundary strengthening, successfully predicting cyclic softening in 9Cr steels. A five-material, finite element model of a P91 cross-weld test specimen, calibrated using the physically-based yield strength and constitutive models, successfully predicts the measured detrimental effect of welding on high temperature low-cycle fatigue crack initiation for P91 cross weld tests, via the modified Tanaka-Mura models. A key finding of the current work is the requirement to adopt an energy-based Tanaka-Mura method to account for cyclic softening in 9Cr steels,

with packet size as the critical length-scale for slip band formation. The work demonstrates the significant effect of highly flexible operation on the service life of welded connections.

6.2 Introduction

Since the 1970s, with the outbreak of the energy crisis, while improving the traditional industrial development mode, modern industry began to develop in the direction of economy, security and sustainability. At the same time, in recent years, with the continuous warming of global temperature, the "greenhouse effect" is becoming more and more serious and the petrochemical and energy power industries are developing towards higher temperature and higher pressure. This will inevitably pose many new challenges to the safe design and life analysis of high temperature key components, requiring materials and structures, such as welded connections, which are resistant to thermal fatigue, creep-fatigue and thermo-mechanical fatigue. A key obstacle to safe design of such plant, to protect personnel, assets and the environment, is the need for appropriate structural integrity assessment methods. In the face of frequent start-up, shut-down and large-scale load variations, increased occurrence of repeated thermal and mechanical stresses will lead to increased low cycle fatigue damage [1]. P91 steel is a 9Cr1Mo nano-strengthened, tempered martensitic alloy for high-temperature applications, specially developed for the power generation industry due to its high thermal conductivity and low thermal diffusion coefficient [2]. The microstructure of P91 is hierarchical in nature, with numerous different associated salient length-scales (e.g. high and low-angle grain boundaries). In this context of increased thermo-mechanical fatigue, the heat-affected zone (HAZ) of welded connections is particularly susceptible to fatigue crack initiation (FCI) [3, 4].

This work focuses on predicting high temperature FCI in P91 steels, which is a key stage of metal fatigue. Traditional models for high temperature fatigue [5-7] do not explicitly incorporate the effects of microstructure, such as grain size, grain boundaries, etc. Existing studies on the nucleation of microcracks have shown that for many materials, microcracks initiate in the slip bands of grains [8, 9]. Although some models, such as Tanaka-Mura

[10], have been developed for the effects of microstructure on FCI, these have not generally been applied to materials such as P91 with hierarchical microstructures, due to the complexities of cyclic deformation and associated uncertainty regarding dominant fatigue-critical length-scale. The location of crack initiation depends on microstructure and type of applied stress, among other factors. For high temperature low cycle fatigue (HTLCF) of hierarchical microstructures, the problem is particularly complex due to concomitant temperature-induced microstructure evolution and fatigue damage accumulation.

Tanaka and Mura [10] created an energy balance of the dislocation structure along the persistent slip bands (PSB) to predict crack initiation. For the number of cycles to fatigue crack initiation in a PSB, a closed-form solution was derived, which was expressed in a Coffin-Manson form and shows a Hall-Petch-type dependency on grain size. Chan [11] extended the Tanaka–Mura model to deal with crack initiation along the slip bands, inclusions and notches, and then extended this further to include crack size and related microstructural parameters. Wu [12] revisited the Tanaka–Mura model and, based on the true strain definition, a new fatigue crack nucleation life expression was obtained and validated against (limited) experimental data on a small number of materials.

Li et al. [13] adopted a dislocation model to study the effects of alloy chemistry, thermal–mechanical treatment and temperature on the tensile deformation process in P91 and P92. Barrett et al. proposed a dislocation mechanics cyclic viscoplasticity model, which combines the key physical and microscopic mechanisms of strengthening and softening at high temperature, which can be applied to predict the cyclic behavior of P91 steel in order to study the effect of microstructure on fatigue crack initiation [14]. More recently, the latter proposed a physically-based high temperature yield strength model for P91 steels which includes the interdependent effects of dislocations, solutes, precipitates and grain boundaries [15]. The fatigue behavior and microstructure evolution of other 9-12% Cr steels have also been studied in detail [16-20].

Hence, a mechanistic-based computational method for predicting high-temperature FCI in P91 steels is developed in the present paper. The method is based on a modified Tanaka-Mura (T-M) [10] model for cyclically-softening behavior, implemented within a physically-based (PB) constitutive framework consisting of high temperature yield strength (YS) and PB cyclic viscoplasticity (VP) models, Chaboche-type viscoplasticity model [21-24]. This will facilitate PB FCI prediction of welded joints for high flexibility, high efficiency power generation. A PB FCI model is presented, which captures material property inhomogeneity in P91 cross-weld (CW) specimen. The model incorporates measured microstructural parameters across HAZ obtained from various published and in-house sources for to estimate YS of P91 parent material (PM), inter-critical heat affected zone (ICHAZ), fine grain heat affected zone (FGHAZ) and coarse grain heat affected zone (CGHAZ). Very little work has been done in modelling the mechanical properties of P91 HAZs, particularly with application to fatigue life prediction. A three-material model was developed by Li [25] to simulate the mismatch of cyclic plasticity in the three different welded regions (PM, HAZ and weld material (WM)) based on the work of Farragher et al [26]. However, the HAZ was treated as a homogeneous material in their work, which omitted key aspects such as HAZ sub-regions and their heterogeneous material properties. During welding, the temperature is high enough to cause transformation to the part to a different microstructure [27]. It is confirmed that significant variation in yield strengths [28] and hardness [29, 30] can be found among various microstructural zones, which is critical for predicting fatigue life of HAZ. Therefore, incorporation of each sub-region of P91 welded joints is necessary for the development of more accurate computational models. Some experimental methods for study the heterogeneity of material properties of P91 welded joints have been proposed. For example, through the creep tests of Hyde et al. [31], the material data for the HAZs can be obtained, and by the digital image correlation (DIC) tests of Touboul et al. [32], the mechanical response of each zone of P91 welded joint are determined, and the validated constitutive parameters also show that the heterogeneity of the welded joint need to be considered. However, additional experimental work is required for different temperatures and test strain-ranges. In contrast, the approach of the present paper represents, via

calibration and validation against HTLCF test data for parent metal and cross-weld tests, of a more accurate FCI prediction model by application of the PB YS and VP models to calibration of five-material cross-weld HTLCF model with the modified T-M model to account for cyclic softening. The method is shown to successfully capture the detrimental effect of welding on HTLCF life and failure of such complex steels.

In the present paper, a physically-based computational methodology for prediction of high temperature fatigue crack initiation in 9Cr steels is developed. Section 2 presents the physically-based yield strength model, physically-based cyclic viscoplasticity model, modified Tanaka-Mura model and five-material finite element model for P91 cross weld specimen. Section 3 presents material parameter identification, investigation of the yield strength heterogeneity and inhomogeneity of the cyclic response across the heat affected zone regions, as well as fatigue crack initiation prediction. The objective is to predict the effect of welding on fatigue crack initiation of P91 welded joint under HTLCF conditions, with a view to gain insight into potential failure locations. Some comparison are made between the predicted behavior and experimental data in Section 4, the Discussion section.

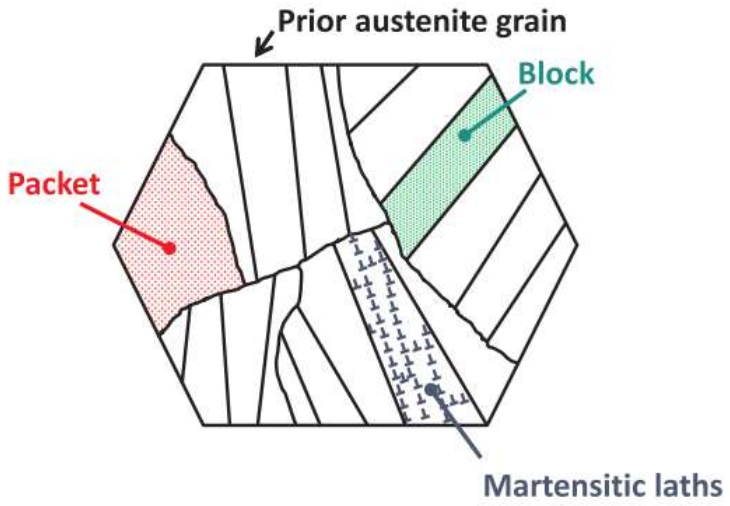

Figure 6.1. Hierarchical microstructure of P91 steel [15].

Table 6.1. Chemical composition of P91 steel in wt. %. The balance is Fe [33, 34].

C	Mn	P	S	Si	Cr
0.08-0.12	0.30-0.60	0.02 max	0.01 max	0.20-0.50	8.00-9.50
Mo	**Ni**	**V**	**Nb**	**N**	**Al**
0.85-1.05	0.4 max	0.18-0.25	0.03-0.10	0.03-0.07	0.04 max

6.3 Methodology

6.3.1 Material

In this work, attention is focused on P91 steel weldments. The chemical composition for P91 is presented in Table 6.1, and the balance is made up of Fe. P91 is a high strength martensitic-ferritic steel, with a complex hierarchical microstructure in nature, consisting of prior austenite grains, packets, blocks and martensitic lath [14], as illustrated in Figure 6.1. P91 requires heat treatment (normalizing and tempering) to achieve the desired microstructure and mechanical properties, specifically the required martensitic structure [33, 34], which confers high temperature creep resistance. Also, $M_{23}C_6$ (M = Cr, Fe, Mo, W) carbides are dispersed along grain and lath boundaries and MX (M = Nb, V; X = C, N) carbonitrides within the martensitic lath interiors, which prevent dislocation motion, and further improve creep strength.

In order to identify, calibrate and validate the constitutive and failure models across the heat-affected sub-zones and in the WM and PM, tests results from Farragher et al. [26] are employed, including HTLCF testing of PM, WM and CW specimens obtained from a P91 pipe weldment. The HTLCF tests were conducted at different temperatures, strain-ranges, under isothermal conditions of controlled strain-rate. The results of Farragher's HTLCF tests [26] were analyzed to determine the material parameters of different welding zones.

6.3.2 Material model

6.3.2.1 Physically-based yield strength model

Barrett et al. [15] recently presented a temperature-independent, physically-based yield strength model for P91. In the present work, this model is adopted to represent the welding-induced heterogeneity of YS in the different HAZ sub-regions, viz. IC-, FG-, CG-HAZ. This heterogeneity is considered key to capturing the effects of thermal transformations due to welding on fatigue crack nucleation. The model assumes that the yield strength is composed of contributions from dislocations, τ_{A}, and obstacles, τ_{B}, following the model of Kocks et al. [35], as follows:

$$\sigma_{\mathrm{y}} = M(\tau_{\mathrm{A}}^2 + \tau_{\mathrm{B}}^2)^{1/2} \tag{6.1}$$

where M is the Taylor factor. τ_{A} is defined by the Taylor hardening expression:

$$\tau_{\mathrm{A}} = \alpha_1 \mu b \sqrt{\rho_{\mathrm{i}}} \tag{6.2}$$

where α_1 is a material constant between 0.2 and 0.5, μ is temperature dependent shear modulus, b is magnitude of Burgers vector and ρ_{i} is initial dislocation density, whist τ_{B} is defined as the sum of various obstacle contributions:

$$\tau_{\mathrm{B}} = \tau_{\mathrm{PN}} + \tau_{\mathrm{bd}} + \tau_{\mathrm{SS}} + \tau_{\mathrm{in}} + \tau_{\mathrm{ph}} \tag{6.3}$$

where τ_{PN} is Peierls-Nabarro [36] stress, τ_{bd} is contribution of GBs, τ_{SS} is solute atoms term, τ_{in} is interstitial atoms term and τ_{ph} is precipitates term.

6.3.2.2 Physically-based cyclic viscoplasticity model

It is well known that the high-temperature 9Cr martensitic-ferritic steels undergo softening during high temperature cyclic deformation [37], due to significant thermo-mechanically induced microstructural evolution. This is attributable to thermomechanical deformation induced microstructure evolution, including specifically reduced dislocation density due to dislocation annihilation and martensitic lath widening [15]. The PB cyclic viscoplasticity model of Barrett et al. [14] based on a dislocation-mechanics framework was specifically developed to represent this complex nano-, micro-scale behavior for macro-scale simulations. This model is adopted here to facilitate interrogation of the

effects of differences in cyclically-induced microstructure evolution across the HAZ sub-regions of P91 weldments on HTLCF. The inelastic strain-rate is defined as a function of the key microstructural variables:

$$\dot{\varepsilon}_{\mathrm{in}} = f(d_{\mathrm{b}}, w, \lambda, c, \rho) \tag{6.4}$$

where d_{b} is martensitic block width, w is lath width, λ is precipitate spacing, c is concentration of solutes and ρ is dislocation density. More specifically:

$$\dot{\varepsilon}_{\mathrm{in}} = A\exp\left(\frac{-\Delta F}{k_{\mathrm{B}}T}\right)\sinh\left(\frac{\sigma_{\mathrm{v}}\Delta V}{Mk_{\mathrm{B}}T}\right)\mathrm{sgn}\,(\sigma - \sigma_{\mathrm{b}}) \tag{6.5}$$

where A is the pre-exponential viscous constant, ΔF is the Helmholtz free energy, k_{B} is Boltzmann's constant, T is the absolute temperature, ΔV is the activation volume, σ_{v} is viscous stress, σ is stress, σ_{b} is the kinematic back-stress. The viscous (thermal) stress under uniaxial loading is defined as:

$$\sigma_{\mathrm{v}} = |\sigma - \sigma_{\mathrm{b}}| - \sigma_{\mathrm{y}}^{\mathrm{cyc}} \tag{6.6}$$

where $\sigma_{\mathrm{y}}^{\mathrm{cyc}}$ is cyclic yield stress and kinematic back-stress is:

$$\sigma_{\mathrm{b}} = \sigma_{\mathrm{p}} + \sigma_{\mathrm{g}} + \sigma_{\mathrm{w}} \tag{6.7}$$

where σ_{p}, σ_{g} and σ_{w} are the back-stress contributions due to particles, dislocation pileups at HAGBs, and dislocation substructure, respectively.

Further details of the original implementation of this model are given in Barrett et al. [14]. A key novelty of the present work is the application of this model, in conjunction with the PB YS model of Section 2.2.1, to the different sub-regions of the HAZ in P91, using physically-measured microstructure parameters from the HAZ sub-regions.

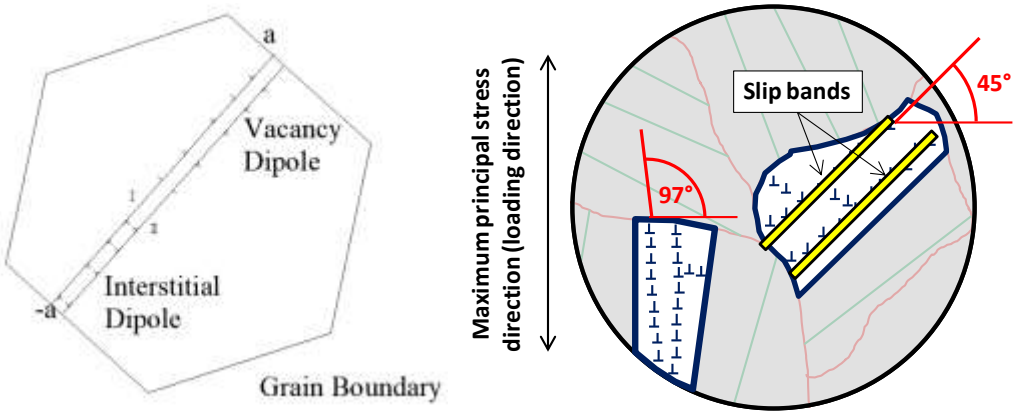

(a) (b)

Figure 6.2**.** (a) Dislocation motion in a grain, adapted from Tanaka and Mura [10], (b) illustration of fatigue persistent slip bands assumed to correspond to packet size in hierarchical microstructure of P91 steels.

6.3.2.3 Modified Tanaka-Mura model

Tanaka and Mura [10] presented a micromechanical fatigue nucleation model in which dislocations accumulate irreversibly on the slip band of grains, leading to an energy-based crack initiation criterion. The key challenge here is to adapt the Tanaka-Mura model to study the cyclic softening behaviour of 9Cr steels [37]. The energy-based formulation of Tanaka-Mura is specifically appropriate and suitable for such cyclically-induced microstructure and dislocation evolution, as compared to more commonly-used stress-based approaches. Figure 6.2(a) shows the dislocation motion in a favourably oriented grain, of size 2*a*. Figure 6.2(b) shows the assumed mechanistic basis for fatigue persistent slip bands corresponding to packet size in the P91 microstructure.

The Tanaka-Mura model assumes that if the stored strain energy due to dislocation accumulation becomes equal to a critical value of surface energy after *N* cycles, the layers of dislocation dipoles transform into a free surface, i.e. a micro-crack. The life to crack initiation N_i is thereby defined as the number of cycles when the following energy condition is satisfied.

$$\begin{cases} \Delta\tau = \dfrac{\Delta\sigma}{M} \\ \Delta\gamma = \dfrac{\Delta\varepsilon^{\mathrm{pl}}}{M} \\ \Delta U = \dfrac{\Delta\gamma(\Delta\tau - 2k_{\mathrm{f}})}{2} \\ U \geq 2d_{\mathrm{p}}w_{\mathrm{s}} \end{cases} \tag{6.8}$$

where $\Delta\tau$ is the shear stress range, $\Delta\sigma$ is the stress range ($\Delta\sigma = \sigma_{\max} - \sigma_{\min}$), $\Delta\gamma$ is the shear plastic strain range, $\Delta\varepsilon^{\mathrm{pl}}$ is the plastic strain range ($\Delta\varepsilon^{\mathrm{pl}} = \varepsilon^{\mathrm{pl}}_{\max} - \varepsilon^{\mathrm{pl}}_{\min}$), M is the Taylor factor (taken here as 2.9, based on bcc ferritic-martenstic P91 material), U is the stored strain energy, d_{p} is the packet size, k_{f} is frictional shear stress and w_{s} is the specific fracture energy per unit area. The key adaptation to the Tanaka-Mura equations here is the use of a combined shear stress-strain ΔU expression within a cumulative computation of U to capture the cyclically-evolving response, due to microstructure evolution effects (e.g. lath coarsening, dislocation annihilation).

6.3.3 Finite element model of P91 cross-weld

Figure 6.3 shows the P91 cross-weld HTLCF specimen of Farragher et al. [26] and the corresponding axisymmetric five-material finite element model developed here, showing the key dimensions identified for HAZ sub-regions. The overall height of the model is 12.5 mm corresponding to the gage length of the extensometer used by Farragher et al. [26]. The width of the HAZ is estimated to be 2.7 mm, as identified from optical microscopy and hardness measurements [26, 38]. Accurate demarcation of the HAZ sub-regions is challenging. Other authors have similarly attempted detailed SEM measurement of HAZ sub-regions [26, 38], identifying respective widths of 0.7 mm, 0.7 mm and 0.3 mm for IC-, FG- and CG-HAZ respectively. Based on interrogation of the microscopy and hardness data from Farragher et al., in comparison also with the latter (more detailed) measurements, widths of 1.1 mm, 1.1 mm and 0.5 mm are identified here for the IC-, FG- and CG-HAZ regions, respectively.

The yield surface is defined by:

$$f = J(\boldsymbol{\sigma}' - \boldsymbol{\chi}') - R - k \tag{6.9}$$

where f is the multiaxial flow-rule, $\boldsymbol{\sigma}'$ is the deviatoric stress tensor, $\boldsymbol{\chi}'$ is the deviatoric back-stress tensor, R is isotropic stress, k is the cyclic yield stress. Within the Ziegler non-linear kinematic hardening model [39], two kinematic back-stress terms are defined to describe the initial and later strain hardening regions, as following:

$$\dot{\boldsymbol{\chi}}_{\mathrm{i}} = \frac{C_{\mathrm{i}}}{(k+R)}(\boldsymbol{\sigma} - \boldsymbol{\chi})\dot{p} - \gamma_{\mathrm{i}}\boldsymbol{\chi}_{\mathrm{i}}\dot{p} \tag{6.10}$$

$$\dot{\boldsymbol{\chi}} = \dot{\boldsymbol{\chi}}_1 + \dot{\boldsymbol{\chi}}_2 \tag{6.11}$$

The Chaboche isotropic hardening model [23, 24] is used to simulate the measured cyclic softening response of P91, as follows:

$$\dot{R}(p) = b(Q - R)\dot{p} \tag{6.12}$$

where Q is the saturation value and b controls rate of decay. Cyclic softening is achieved using a negative Q-value [40]. The creep strain is obtained from the multiaxial version of the following Norton power law [41]:

$$\dot{\varepsilon}_{\mathrm{c}} = A\sigma^{\mathrm{n}} \tag{6.13}$$

where A and n are temperature-dependent material constants, $\dot{\varepsilon}_{\mathrm{c}}$ is creep strain rate. For the five-material cross-weld simulations in Abaqus, the combined NLKIH Chaboche and Norton secondary creep models are used within the two-layer viscoplasticity material model. A two-layer parameter F needs to be defined for each material zone.

The HTLCF cyclic PM and WM behavior was experimentally measured using PM and WM HTLCF specimens machined from the welded connection by Farragher et al. [26]. As discussed in the next section, the NLKIH parameters for IC-, FG- and CG-HAZ regions are identified using the physically-based YS and VP models described above. It is not generally possible to measure this response for these HAZ sub-regions, due to the very small size scale, relative to typical LCF specimen dimensions. A detailed mesh convergence study was conducted for the five-material model to establish a suitable mesh,

with particular focus on the interfaces between the five different weld-affected zones, where material discontinuities occur. The final mesh (shown in Figure 6.3) uses an element size (axial direction) of 98 μm, converged to within 5% with respect to maximum principal stress, using eight-node biquadratic axisymmetric quadrilateral elements with reduced integration.

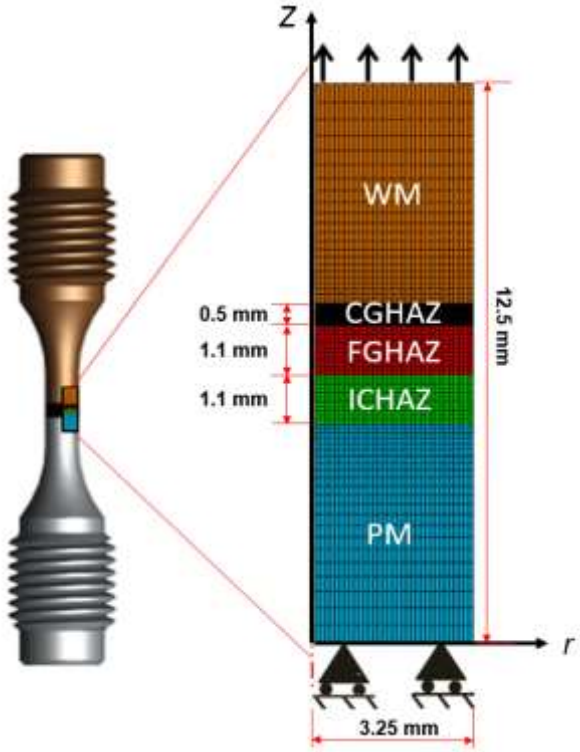

Figure 6.3**.** Schematic of P91 cross-weld HTLCF specimen of Farragher et al. [26] and corresponding axisymmetric five-material finite element model developed here, showing key dimensions for HAZ sub-regions.

6.4 Results

6.4.1 Parameter identification

Representative values for the microstructural parameters required for the proposed physically-based models described above are identified based on previously measured data as summarized in Table 6.2**,** corresponding to P91 welded joints from published sources [28, 42-44]. In materials with hierarchical microstructure, dislocation density has

a strong correlation with lath width. Therefore, the following empirical relationship is used to estimate dislocation density from lath width, based on published data [43, 45-48], as shown in Figure 6.4:

$$w^{-1} = 0.161\rho^{1/2} + 11 \quad (6.14)$$

where w is lath width, ρ is the dislocation density.

Table 6.2. Identified microstructural parameters for PM, IC-, FG- and CG-HAZ at 500°C.

Parameter		**PM**	**ICHAZ**	**FGHAZ**	**CGHAZ**
PAG size (μm)		14	18	5	50
d_p (packet size) (μm)		7.6	9.2	4	22
block width (μm)		4	5.3	3	9.1
w (lath width) (nm)		700	600	900	350
ρ_i (mm^{-2})		0.78×10^8	1.06×10^8	0.47×10^8	3.13×10^8
Volume fraction (-)	$M_{23}C_6$	2%			
	MX	0.1%			
radii of precipitates (nm)	$M_{23}C_6$	74	64	100	50
	MX	25	32.5	50	25

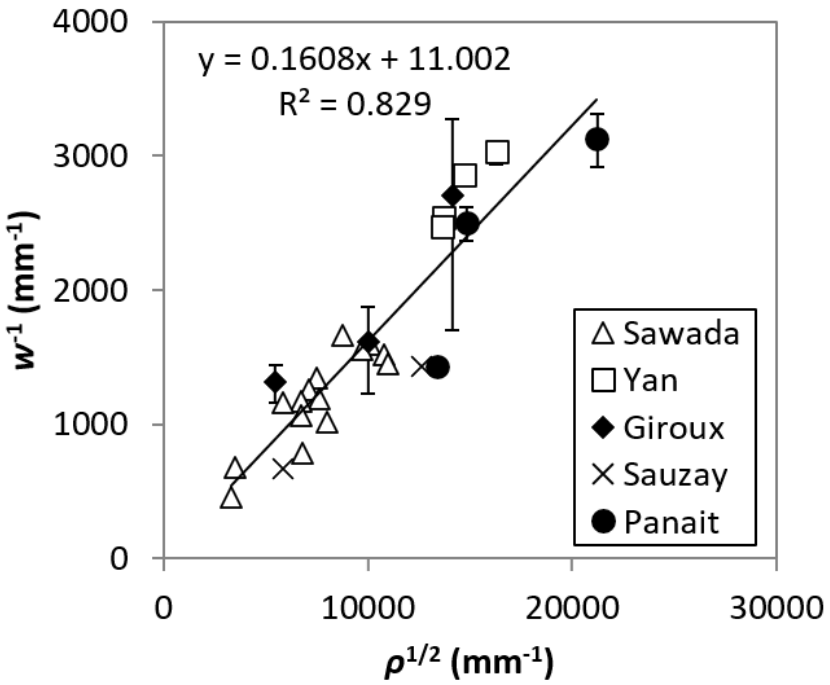

Figure 6.4**.** Relationship between lath width and dislocation density for 9Cr steels based on previously measured data.

Figure 6.5 shows the full complex interaction and calibration-identification processes required to combine the different physically-based (PB-YS and PB-VP) and Chaboche NLKIH model with the modified T-M FCI model and the five-material cross-weld HTLCF FE model. The material parameter identification process (e.g. Barrett et al. [49]) for cyclic NLKIH parameters is applied here to IC-, FG-, CG-HAZ sub-zones, based on the predictions from the physically-based viscoplasticity model for ICHAZ, FGHAZ and CGHAZ. Previously-published material parameters for the PM and WM are adopted here [25]. As shown in Figure 6.5(a), Young's modulus, *E*, and Poisson's ratio, *v*, are identified first. The isotropic softening constants (Q, b) and kinematic hardening constants (C_i, γ_i) are then identified using a step-by step approach.

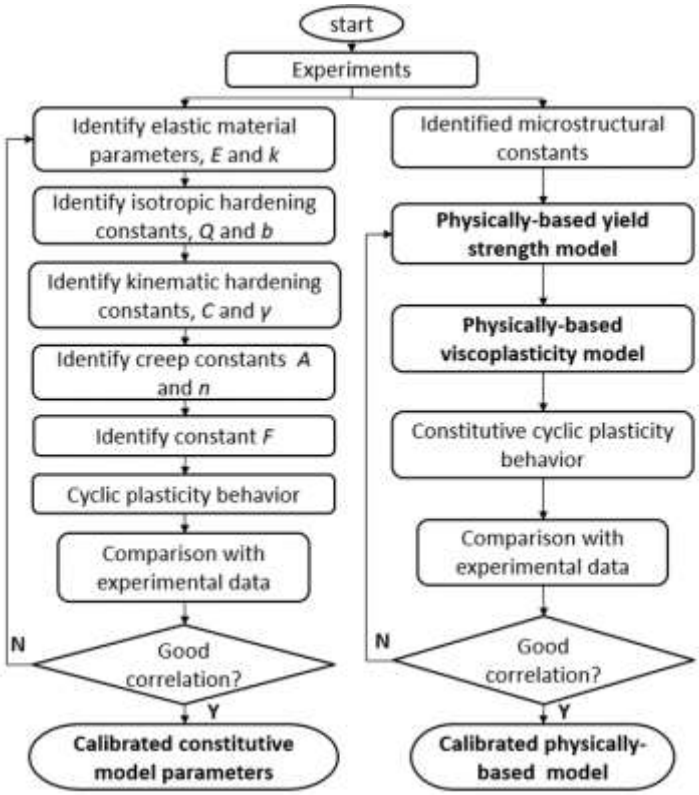

(a) Step 1

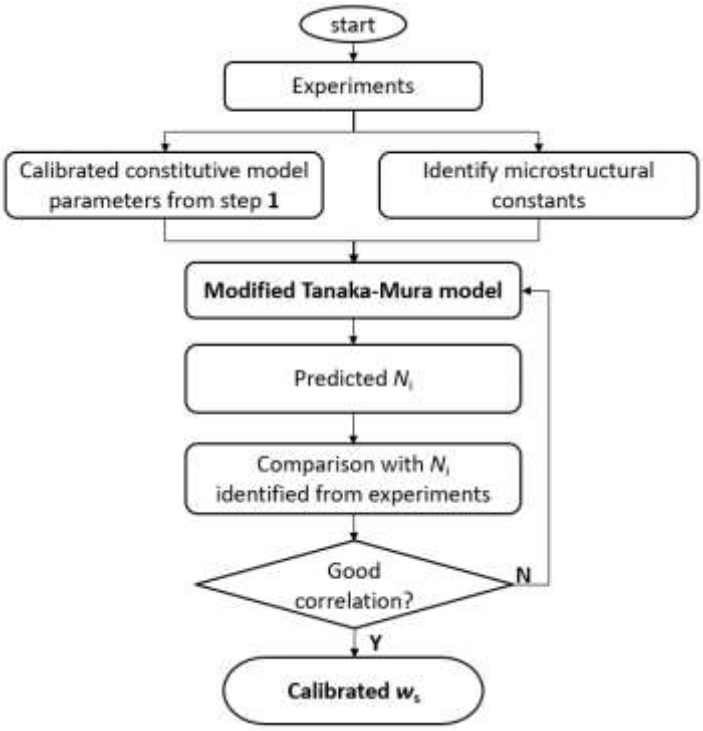

(b) Step 2

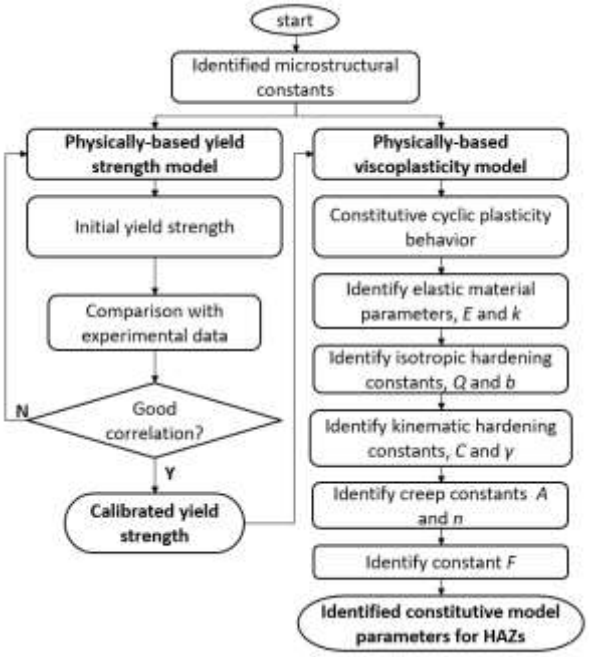

(c) Step 3

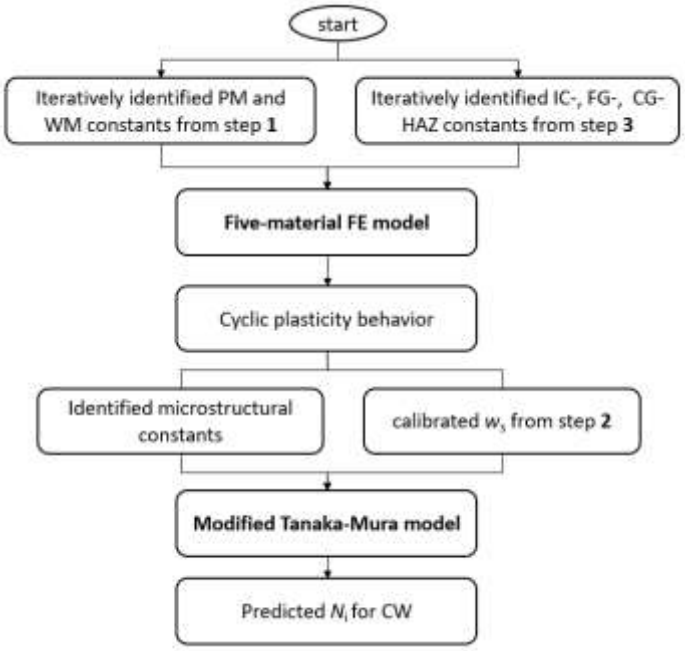

(d) Step 4

Figure 6.5**.** Flowchart of main processes for predicting FCI in P91 steels: (a) Step 1: Chaboche NLKIH parameter identification for PM and WM, and calibration of PB model, (b) Step 2: Modified T-M calibration for PM, (c) Step 3: Calibration of Chaboche NLKIH and Norton creep models using PB-YS and PB-VP models for IC-, FG-, CG-HAZ and (d) Step 4: five-material FE model with modified T-M prediction.

The isotropic hardening constants, Q and b, are identified from cyclic softening data derived from the curves of cyclic softening stress and accumulated effective plastic strain. It is assumed in the identification of isotropic hardening parameters that time-dependent microstructure-coarsening effects do not affect isotropic hardening [18]. Under uniaxial loading conditions, the stress is defined as:

$$\sigma = \chi + (R + k + \sigma_{\mathrm{v}})\mathrm{sgn}(\sigma - \chi) \tag{6.15}$$

The cyclic softening stress R is the difference between the maximum stress of each cycle and that of the first cycle. The accumulated effective plastic strain is estimated for each cycle using the maximum and minimum stresses. The relationship between the accumulated effective plastic strain and a given cycle for LCF is given as below:

$$p = 2\sum_{n=1}^{N}(\Delta\varepsilon - \frac{\Delta\sigma_{\mathrm{n}}}{E}) \tag{6.16}$$

where N is the total number of cycles where p is obtained, $\Delta\varepsilon$ is the total applied strain range (in a strain-controlled test or simulation), and $\Delta\sigma_{\mathrm{n}}$ is the stress range for a given cycle, n. The isotropic softening saturation stress may be estimated when the isotropic softening stress and accumulated effective plastic strain have been obtained. The least squares method is used to fit the *b* value describing the *R* decay rate with the experimental data. The *b* value can be obtained by using the least square method fitting the softening curve with equation (6.18), as shown for CGHAZ, as an example, in Figure 6.6:

$$R = Q(1 - e^{-\mathrm{bp}}) \tag{6.17}$$

The least squares optimization function to be minimized is:

$$f(b_{\mathrm{k}}) = \sum_{j=1}^{m}(R^{\mathrm{thr}}(b_{\mathrm{k}}) - R^{\mathrm{exp}})^2 \tag{6.18}$$

where b_{k} represents the material parameters to be optimised and the superscripts ‘thr’ and ‘exp’ denote theoretical and experimental values of the cyclic softening stress respectively.

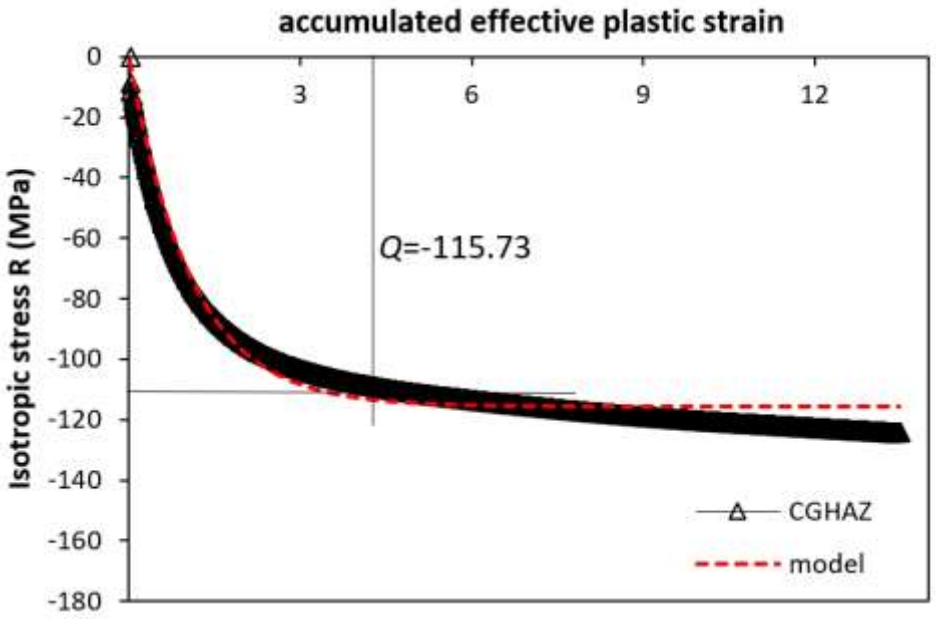

Figure 6.6. Softening curve of CGHAZ for 1.0 % strain-range at 500°C.

The non-linear kinematic hardening model is given as:

$$\chi_1 = \frac{C_1}{\gamma_1}(1 - e^{-\gamma_1 \varepsilon_p}) \tag{6.19}$$

$$\chi_2 = \frac{C_2}{\gamma_2}(1 - e^{-\gamma_2 \varepsilon_p}) \tag{6.20}$$

It can be assumed that the initial stages of strain hardening (χ_1) have a constant (maximum) value of $\frac{C_1}{\gamma_1}$ when the later stages of hardening are considered. Thus the equation (6.15) can be simplified to:

$$\sigma = \frac{C_1}{\gamma_1} + \frac{C_2}{\gamma_2}(1 - e^{-\gamma_2 \varepsilon_p}) + R + k + \sigma_v \tag{6.21}$$

Differentiating equation (6.21) with respect to ε_p and taking the natural logarithm of both sides to obtain the following equation (assuming yield stress, k, and viscous stress, σ_v, to be constants):

$$\mathrm{In}\left(\frac{\partial\sigma}{\partial\varepsilon_{\mathrm{p}}} - Qbe^{-\mathrm{bp}}\right) = \mathrm{In}(C_2) - \gamma_2\varepsilon_{\mathrm{p}} \tag{6.22}$$

Following the approach of Hyde [50], the term $\frac{\partial\sigma}{\partial\varepsilon_{\mathrm{p}}}$ can be determined using the chain rule as

$$\frac{\partial\sigma}{\partial\varepsilon_p} \approx \frac{d\sigma}{d\varepsilon_p} = \frac{d\sigma}{d\varepsilon}\cdot\frac{1}{\dot{\varepsilon}_p}\cdot\dot{\varepsilon} \tag{6.23}$$

The plastic strain-rate can be defined as:

$$\dot{\varepsilon}_p = \dot{\varepsilon}\left(1 - \frac{1}{E}\cdot\frac{d\sigma}{d\varepsilon}\right) \tag{6.24}$$

The term $\frac{d\sigma}{d\varepsilon}$ can be determined using the Ramberg-Osgood equation:

$$\frac{\varepsilon}{\varepsilon_0} = \frac{\sigma}{\sigma_0} + \left(\frac{\sigma}{\sigma_0}\right)^{n_0} \tag{6.25}$$

This can be re-expressed, using $E = \sigma_0/\varepsilon_0$, as follows:

$$\log(E\varepsilon - \sigma) = n_0\log(\sigma) + (1 - n_0)\log(\sigma_0) \tag{6.26}$$

The constants n_0 and σ_0 can then be determined as the slope and intercept of a plot of $\log(E\varepsilon - \sigma)$ versus $\log(\sigma)$. Figure 6.7 shows the identification of the Ramberg-Osgood parameters for IC-, FG-, CG-HAZ at 500 ^{o}C. Table 6.3 shows the identified Ramberg-Osgood constants for IC-, FG-, CG-HAZ at 500 ^{o}C.

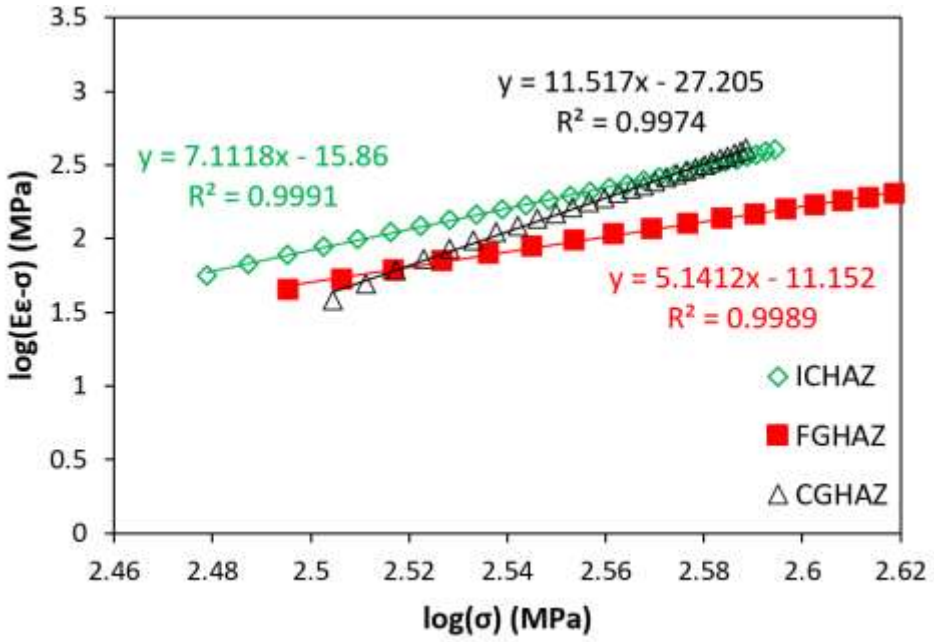

Figure 6.7. Identification of Ramberg-Osgood constants for IC-, FG-, CG-HAZ at 500°C.

Table 6.3. Identified Ramberg-Osgood constants for IC-, FG-, CG-HAZ at 500°C.

Material	σ_0 (MPa)	n_0 (-)
ICHAZ	394.23	7.11
FGHAZ	493.99	5.14
CGHAZ	386.16	11.52

By plotting $\mathrm{In}\left(\frac{\partial\sigma}{\partial\varepsilon_\mathrm{p}} - Qbe^{-\mathrm{bp}}\right)$ versus ε_p , the kinematic back-stress constants C_2 and γ_2 can be determined as intercept and slope, as presented in Figure 6.8(a) for CGHAZ, for example. The initial kinematic back-stress term C_1 and γ_1 can then be identified by plotting $\mathrm{In}\left(\frac{\partial\sigma}{\partial\varepsilon_\mathrm{p}} - \frac{\partial\chi}{\partial\varepsilon_\mathrm{p}} - Qbe^{-\mathrm{bp}}\right)$ versus ε_p from equation (5.1), as presented in Figure 6.8(b).

$$\mathrm{In}\left(\frac{\partial\sigma}{\partial\varepsilon_\mathrm{p}} - \frac{\partial\chi}{\partial\varepsilon_\mathrm{p}} - Qbe^{-\mathrm{bp}}\right) = \mathrm{In}(C_1) - \gamma_1\varepsilon_\mathrm{p} \tag{6.27}$$

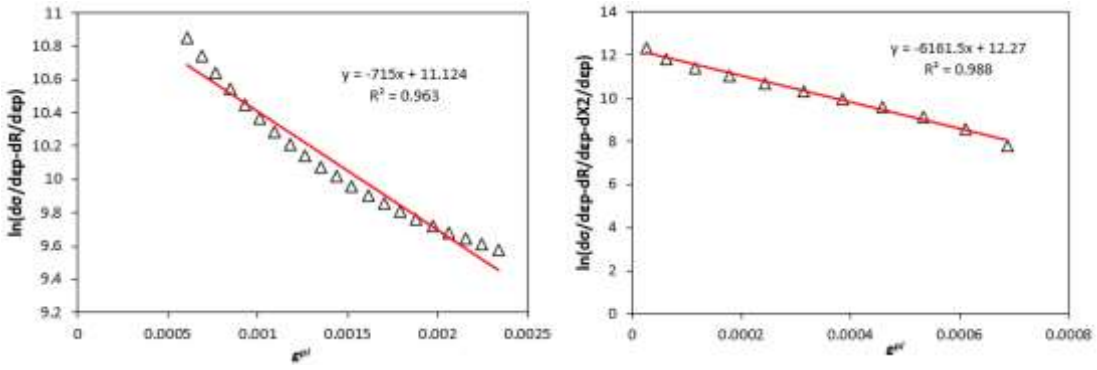

(a) C_2 and γ_2 (b) C_1 and γ_1

Figure 6.8**.** Identification of non-linear kinematic hardening parameters for CGHAZ (a) C_2 and γ_2 and (b) C_1 and γ_1 at temperatures of 500℃.

The same identification process was adopted for ICHAZ and FGHAZ. The final set of identified material parameters for the P91 welded joint are presented in Table 6.4.

Table 6.4. Identified cyclic material parameters for PM, IC-, FG-, CG-HAZ, WM at 500℃.

Material	PM	ICHAZ	FGHAZ	CGHAZ	WM
E **(MPa)**	168220	161957	161957	161957	181000
k **(MPa)**	130	125.42	127.24	143.18	325
Q **(MPa)**	-96.5	-57.65	-27.81	-115.73	-150
b	0.25	0.71	0.67	0.92	0.6
C_1 **(MPa)**	728687	257301	362217	213203	797311
γ_1 **(-)**	12534	5459	6358	6162	8035
C_2 **(MPa)**	258073	94278	170416	67778	79567
γ_2 **(-)**	1100	626	727	715	719
A **($MPa^{-n}s^{-1}$)**	4.28×10^{-40}	2.75×10^{-58}	2.84×10^{-63}	6.76×10^{-57}	1.77×10^{-59}
n	13.55	20.84	22.17	20.37	20.2
F	0.1	0.96	0.96	0.96	0.05

The Norton creep constants *A* and *n* were identified for each of the IC-, FG- and CG-HAZ regions by calibrating the stress relaxation data as $\log(\dot{\sigma})$ versus $\log(\sigma)$, in comparison with the PB-VP stress-relaxation responses for these sub-zones, with the microstructural data of Table 6.2. The identified values for each sub-zone are given in Table 6.4 and comparison of stress relaxation responses predicted by PB-VP model for IC-, FG- and CG-HAZ to the calibrated Norton model responses at 500°C are shown in Figure 6.9(a). Finally, the combined NLKIH-Norton IC-, FG- and CG-HAZ responses, using the two-layer viscoplasticity model in Abaqus, are compared to the stress relaxation responses to identify suitable values of the additional *F* parameter; the final cyclic viscoplasticity values for all weld-affected sub-regions are given in Table 6.4. Figure 6.9(b) shows a validation comparison of the CW relaxation response from the five-material CW FE model of Figure 6.3, using the latter identified parameters for the HAZ sub-regions, with the measured test data at 500°C.

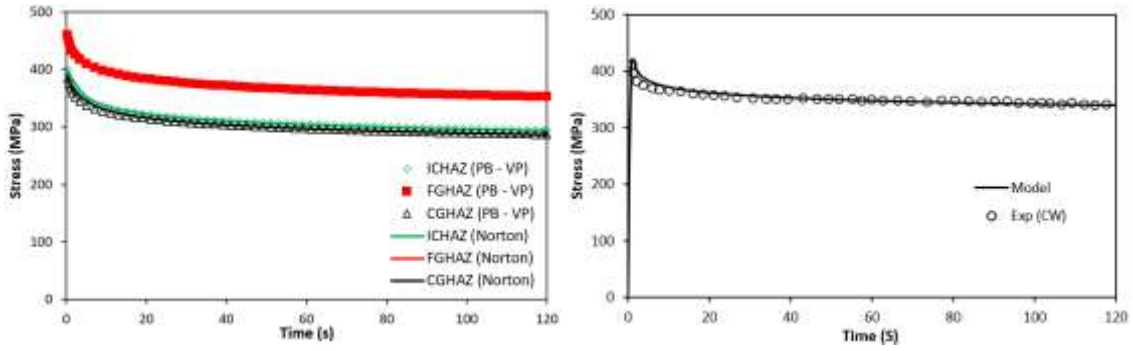

(a) (b)

Figure 6.9. (a) Comparison of stress relaxation responses predicted by PB-VP model for IC-, FG- and CG-HAZ to the calibrated Norton model responses at 500°C (held at 0.5 % tensile strain for 120 s), (b) comparison of FE-predicted (five-material) CW stress response, using calibrated Norton creep constants for HAZ sub-zones, against measured test data for strain-controlled stress relaxation at 500°C.

6.4.2 Validation of NLKIH cyclic viscoplasticity model

The predicted constitutive responses of P91 PM, WM and CW are compared with the experimental responses. Details of the experimental methods and results were presented previously [26]. Figure 6.10(a) shows the comparison of the predicted and measured responses for PM at 500°C for strain-range 1.0% and strain-rate 0.033%/s. It is clear that the initial cyclic softening behaviour is captured over the half-life. Figure 6.10(b) shows the corresponding softening curves for three different strain-ranges. The effects of fatigue damage on stress response are not included in this work; thus, the final damage-dominated softening, as shown more clearly in Figure 6.10(b), is not explicitly modelled here. Comparisons for the WM are shown in Figure 6.11, showing similar level of agreement up to half-life. Figure 6.12 shows the predicted response using the five-material FE model of the cross-weld HTLCF tests including comparisons for three strain-ranges. In this case, only 500 cycles are simulated, up to stabilisation of the secondary softening response. The comparisons capture the key trends of the experimental data up to about 500 cycles; similar agreement was obtained for the other strain-ranges, 0.6% and 0.8%.

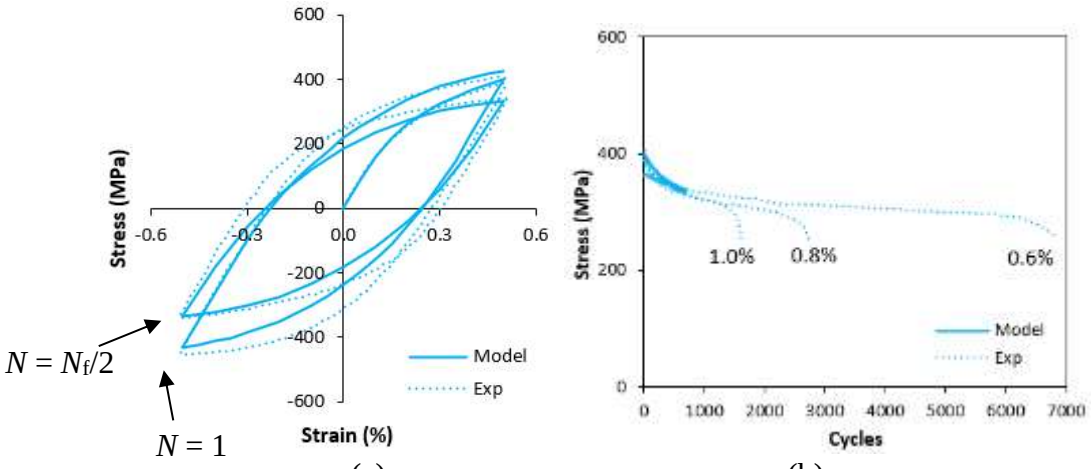

(a) (b)

Figure 6.10. Comparison of predicted and test observed (a) stress-strain response for 1.0% strain-range at 0.033%/s and (b) cyclic softening in PM at 500°C.

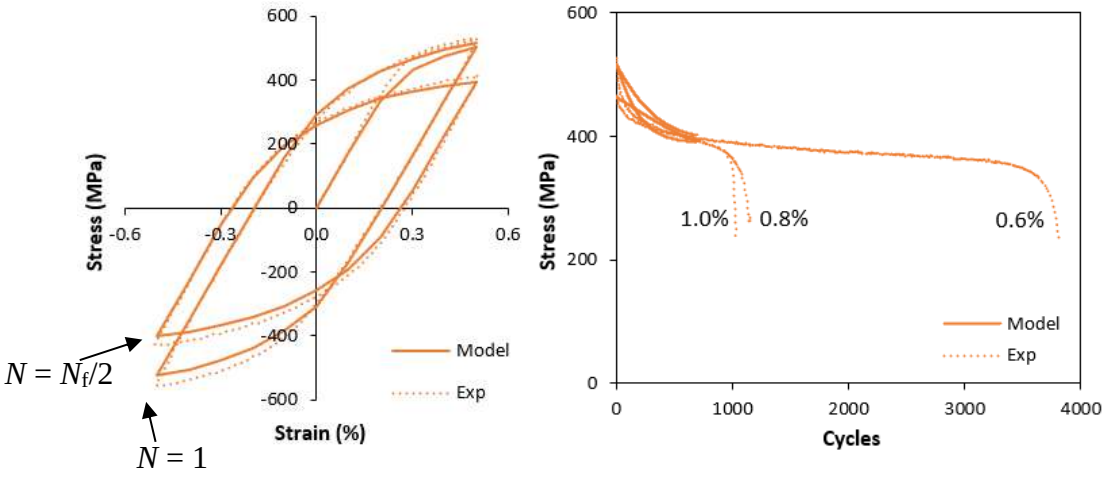

(a) (b)

Figure 6.11. Comparison of predicted and test observed (a) stress-strain response for 1.0% strain-range at 0.033%/s and (b) cyclic softening in WM at 500°C.

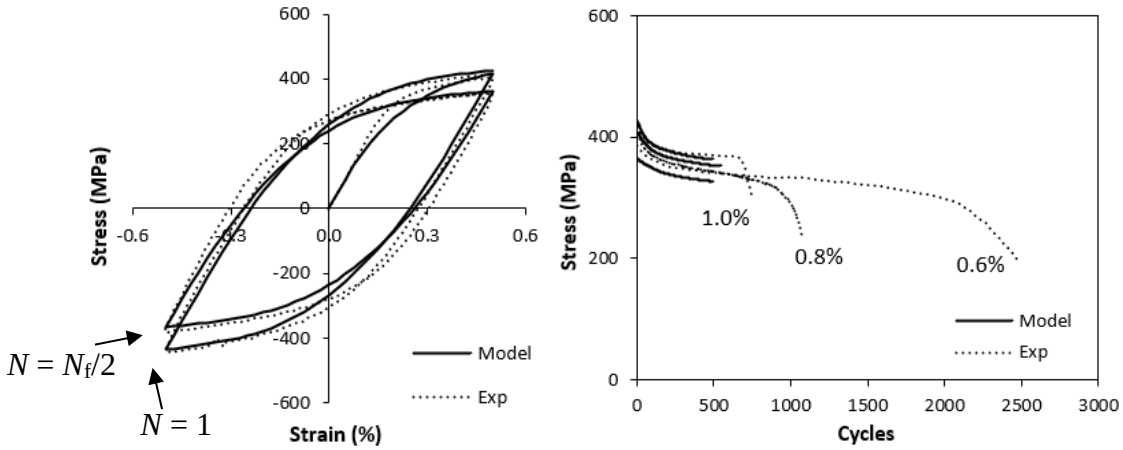

(a) (b)

Figure 6.12. Comparison of predicted and test observed (a) stress-strain response for 1.0% strain-range at 0.033%/s and (b) cyclic softening in CW at 500°C.

6.4.3 Grain boundary strengthening

As can be seen from Table 6.2, the grain diameter of CGHAZ is around 10 times that of FGHAZ, and lath width of FGHAZ is highest among these materials, which is approximately 2.5 times that of CGHAZ. Because of the hierarchical microstructure of P91, predicted grain diameter that contributes to grain boundary strengthening is based on the minimum HAGB dimension (mean block width). The calculated grain boundary

strengthening contributions are presented in Table 6.5. The contribution of LAB is significantly larger than that of HAGB, except perhaps for FGHAZ, illustrating the key role of LAB strengthening at high temperature. It is calculated that the total contribution of grain boundaries in FGHAZ is the largest, primarily due to the significant HAGB contribution.

Table 6.5. Predicted grain boundary YS contributions (MPa).

Boundary	PM	ICHAZ	FGHAZ	CGHAZ
HAGB	17.94	16.84	22.43	12.86
LAB	24.23	24.37	26.39	29.37
Total	42.17	41.21	48.82	42.23

6.4.4 Yield strength heterogeneity

Figure 6.13 shows the comparison of the contributions from different strengthening mechanisms for P91 welded joints. In all cases, the most significant YS contributor is the Taylor hardening (dislocation), each accounting for 15% and 30% of the total yield stresses; other main strengthening mechanisms include the Peierls-Nabarro stress, solid solution strengthening HAGB and LAB strengthening and precipitate strengthening. The higher dislocation density of the CGHAZ leads to a significantly higher dislocation strengthening contribution for this sub-zone. Figure 6.14 shows (a) the hardness profile of the actual P91 weld joint at 550℃ and (b) a comparison of the calculated yield stresses for P91 welded joint at 500℃. The results of the PB-YS model show the following order of yield strengths of each zone: CGHAZ > PM > FGHAZ > ICHAZ, which is consistent with observed hardness measurements [28, 29, 51]. Compared with FGHAZ, the YS of ICHAZ is lower, mainly due to increased packet size.

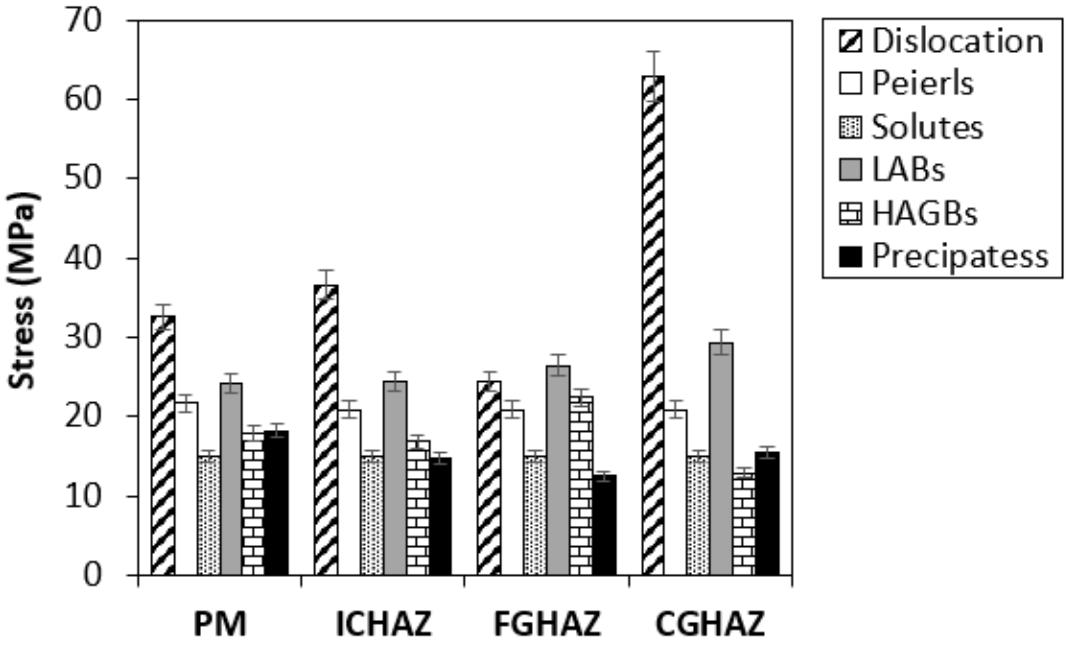

Figure 6.13**.** YS contributions of major strengthening mechanisms for P91 welded joint at 500℃.

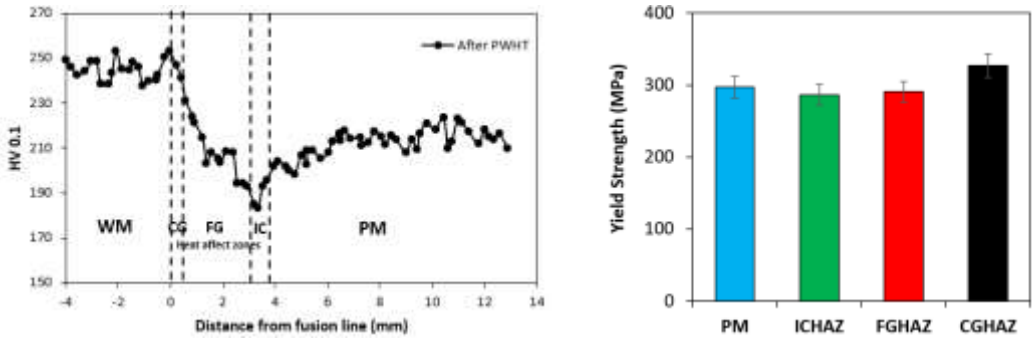

(a) (b)

Figure 6.14**.** (a) Hardness values of P91 weld joint at 550℃ , adapted from [28] and (b) comparison of results of PB YS model at 500℃.

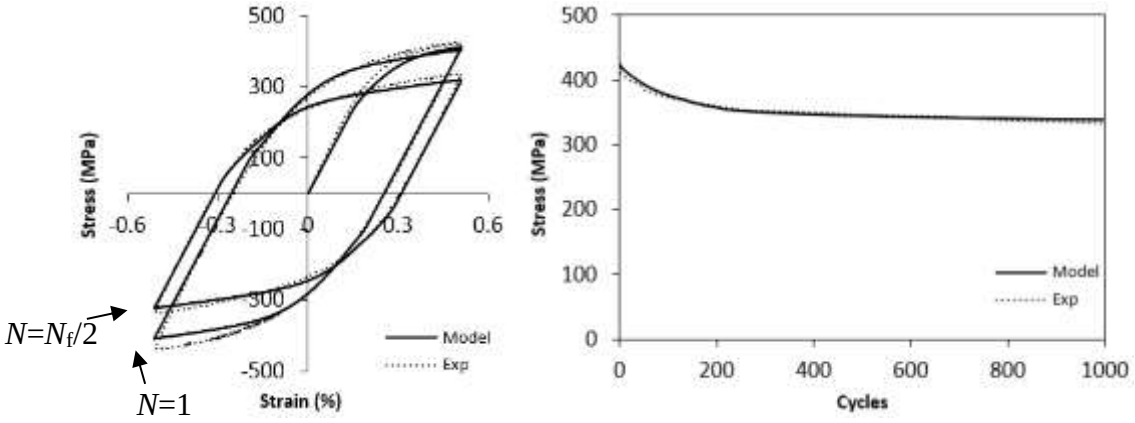

(a) (b)

Figure 6.15. Comparison of PB-VP model and test data for (a) stress–strain response for 1.0% strain-range and (b) cyclic softening in PM at 500°C.

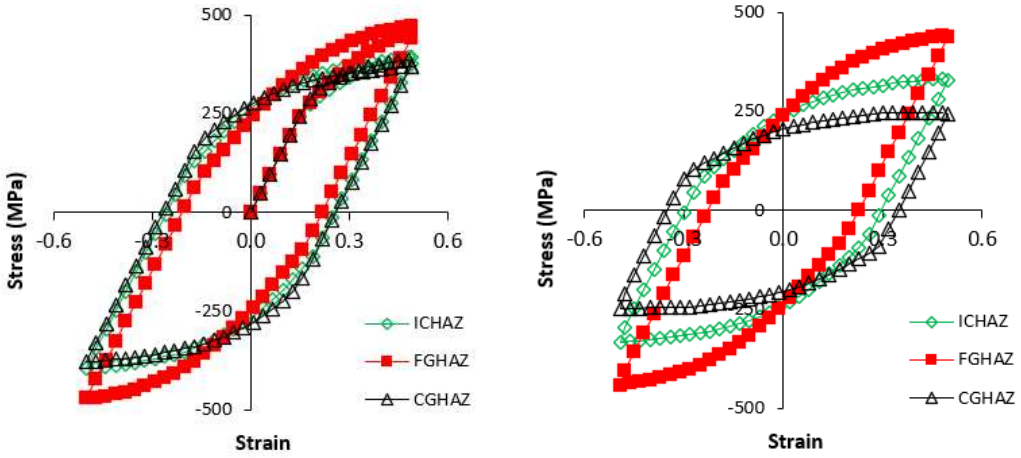

(a) (b)

Figure 6.16. The predicted stress-strain response for P91 IC-, FG-, CG-HAZ at 500°C with (a) N=1, (b) N=1000 for 1.0% strain-range.

Figure 6.15(a) shows the comparison of PB-VP predicted response against the test data for PM at 500 °C. The comparison of softening behaviour is shown in Figure 6.15(b). Figure 6.16 presents the stress-strain responses predicted by the PB-VP model for IC-, FG-, CG-HAZ at the 1st and 1000st cycle for 1.0% strain-range. The model predicts significant differences across HAZ, due to different martensitic block width and lath width for three sub-zones. Compared with ICHAZ and FGHAZ, CGHAZ exhibits the softest response because the block width increases and the lath width decreases significantly.

FGHAZ showed the hardest response through the cycles, which is due to the reduced block width and prevalence of lath microstructure, compared with ICHAZ. The comparison of predicted and experimentally measured evolution of cyclic softening in P91 welded joint is shown in Figure 6.17. It can be clearly seen that the FGHAZ is significantly harder than the other HAZ sub-zones through all the cycles, and the model predicts that CGHAZ is the cyclically softest region in the HAZ due to the coarse microstructure. The evolution of strain distributions for the cross-weld five-material model after different numbers of HTLCF cycles are presented in Figure 6.18. These results indicate that (i) the inhomogeneity of all five regions (PM, IG-, FG, CG-HAZ and WM) is significant, and (ii) the inhomogeneous distribution of strain in the loading direction evolves from the first cycle due to the heterogeneous material behaviour of HAZ sub-zones. As the number of cycles increases, strain re-distribution occurs throughout the HAZ sub-zones, in particular, leading to significant strain localisation within the CGHAZ near the outer surface.

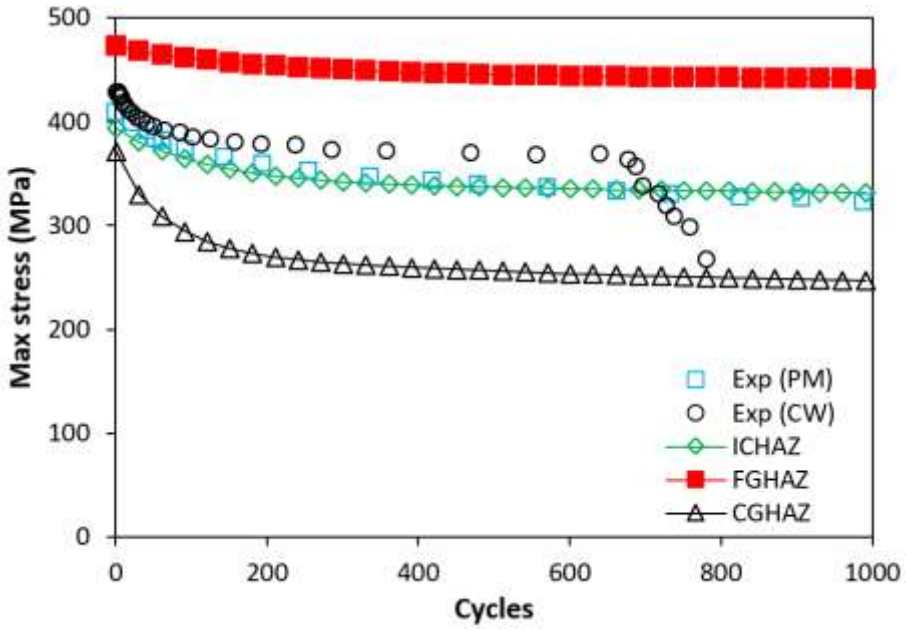

Figure 6.17. Comparison of predicted and measured cyclic softening in P91 welded joint for 1.0% strain-range at 500℃.

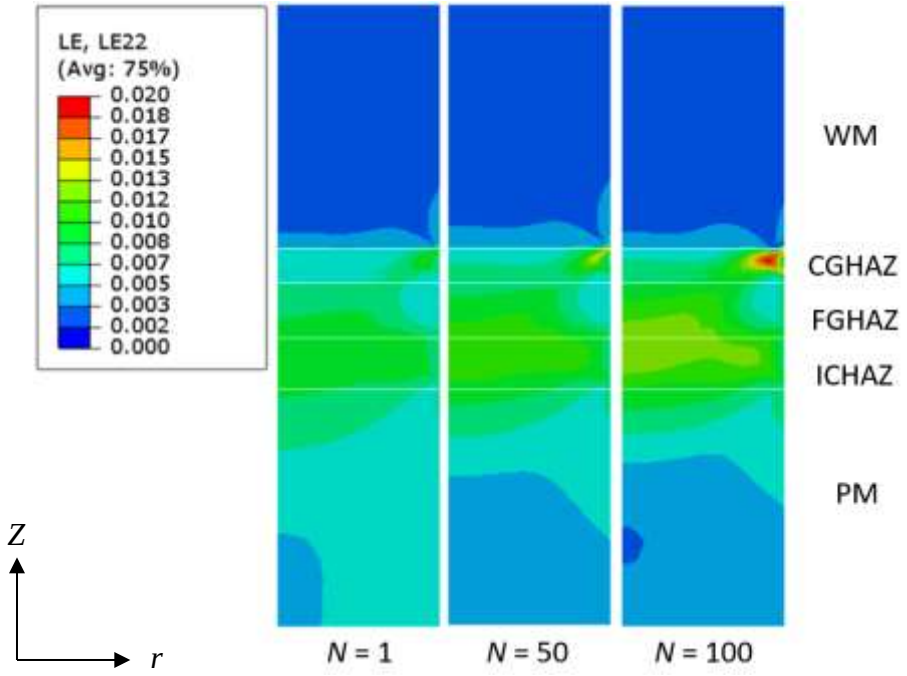

Figure 6.18**.** Cyclic evolution of (axial) strain distribution in the FE model of P91 CW HTLCF cylindrical test specimen for 1.0% strain-range at 500℃.

6.4.5 Identification of Tanaka-Mura parameters for parent material

A key novelty of the present work is the calibration of the modified Tanaka-Mura model for the cyclically-softening HTLCF behaviour of P91. Figure 6.19(a) shows the typical cyclic softening maximum stress evolution with number of cycles for HTLCF testing of PM at 500℃ for $\Delta\varepsilon$ =1.0%. Figure 6.19(b) shows the procedure adopted here for identification of FCI for PM tests at 500℃ [26, 52], based on the assumption of initiation being identified with end of the estimated recovery-induced softening phase. Using this approach for the corresponding HTLCF test data at 400℃, 500℃, and 600℃, the Tanaka-Mura critical surface energy w_s values have been identified, as shown in Table 6.6. Figure 6.20 shows the comparison of resulting T-M predictions against the experimental data. In general, the model slightly under-predicts for the lower strain ranges at 400℃ and 500℃, whereas at 600℃ it slightly under-predicts for the higher strain ranges. The FCI predictions, in general, show close agreement with the experimental measurements, with the largest difference being less than 20% (conservative). The data in Table 6.6 shows a significant effect of temperature on critical surface energy.

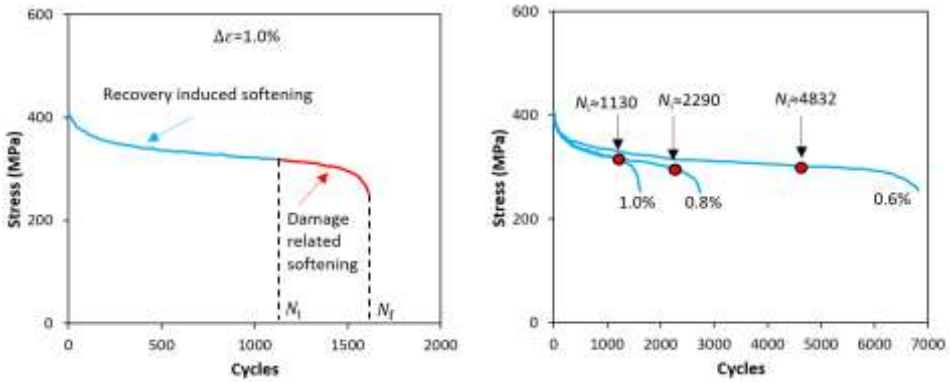

(a) (b)

Figure 6.19**.** (a) Cyclic softening of PM 1.0% strain range at 500 °C, (b) the identification of FCI for PM tests at 500°C.

Table 6.6. Identified w_s for PM at 400, 500 and 600°C.

***T* (°C)**	w_s **(J/m^2)**
400	22
500	15
600	7.5

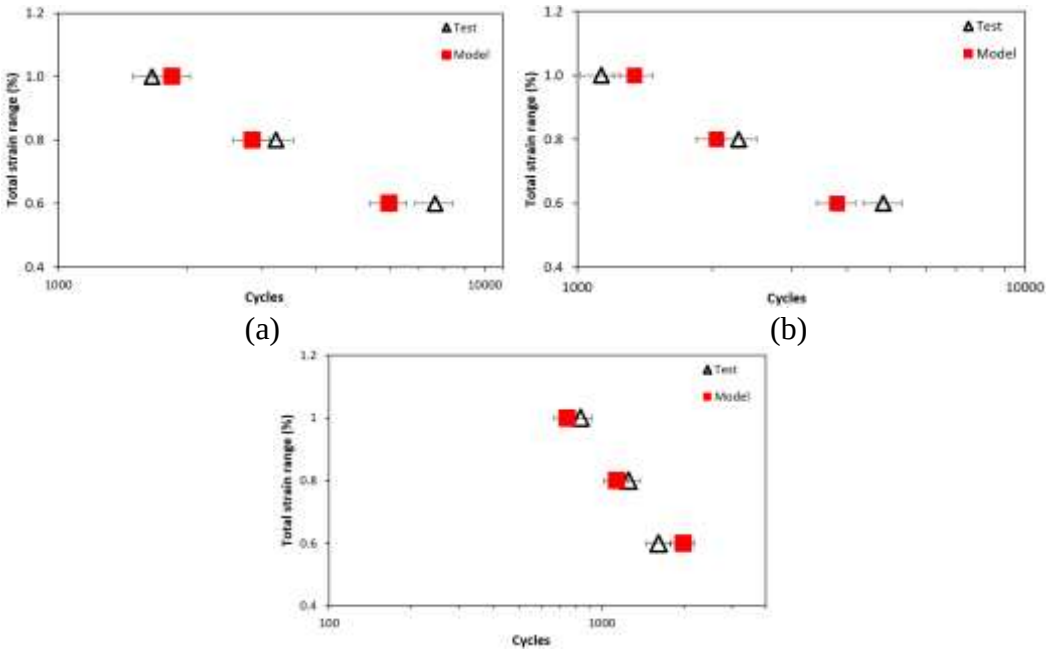

(a) (b)

(c)

Figure 6.20**.** The comparison of FCI prediction to experimental results for PM (a) 400°C, (b) 500°C, (c) 600°C.

6.4.6 Fatigue crack initiation prediction using modified Tanaka-Mura model for five-material model

The overall end objective of the present work is to facilitate prediction of the effect of welding on fatigue crack initiation. Consequently, the cross-weld (five-material) model, with the NLKIH model calibrated via the physically-based YS and VP models, and combined with the modified T-M model, as shown in Figure 6.5, has been applied here for FCI prediction, with comparison against measured HTLCF test data at 500°C. Figure 6.21 shows the comparison of FCI predictions for PM and CW under different strain ranges at 500°C, thus conveying the weld strength reduction factor due to welding on HTLCF. The scatter bar is obtained from the standard deviation of packet size, which is the critical length-scale for slip band formation in the modified Tanaka-Mura model. The model slightly under-predicts the effect at the higher and lower strain-ranges. Overall, it is clear that the model successfully captures the significant reduction (knockdown) in FCI life due for the cross-weld P91 HTLCF tests. Figure 6.22 shows the predicted FCI of the modified T-M model for the different HAZ sub-zones. The minimum life is predicted in FG-HAZ as 299 cycles and IC-HAZ as 613 cycles, which are significantly lower than for PM (1340 cycles) and CG-HAZ (2051 cycles). Figure 6.23 shows the evolution of normalized stored strain energy (energy divided by failure energy of that local region) distributions for the cross-weld five-material model after different numbers of HTLCF cycles. The contour plot shows predicted FCI in the FGHAZ, towards the interface with ICHAZ.

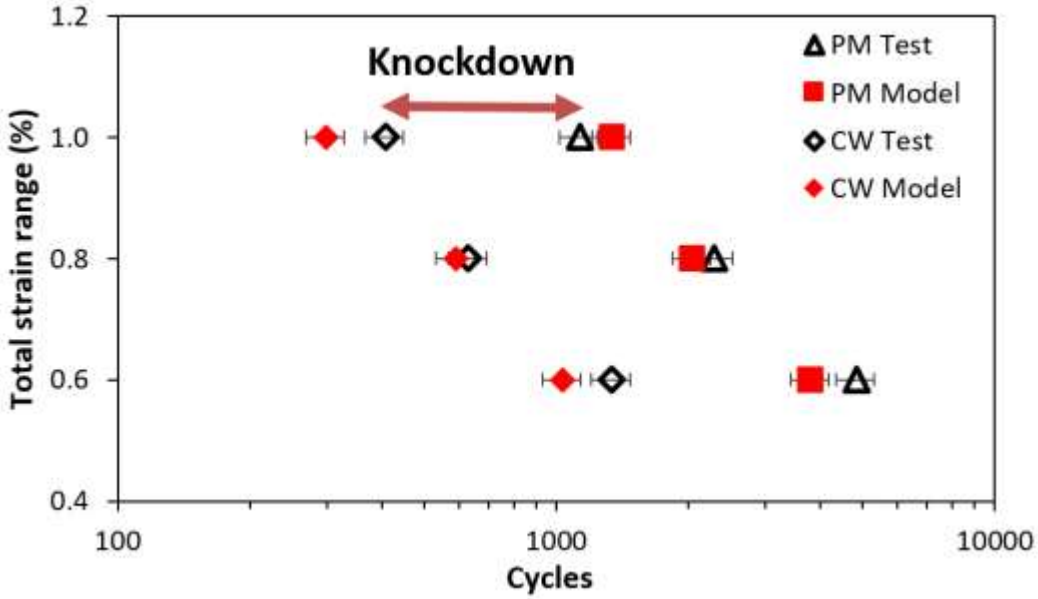

Figure 6.21. Comparison of FCI prediction for PM and CW for HTLCF tests at 500°C.

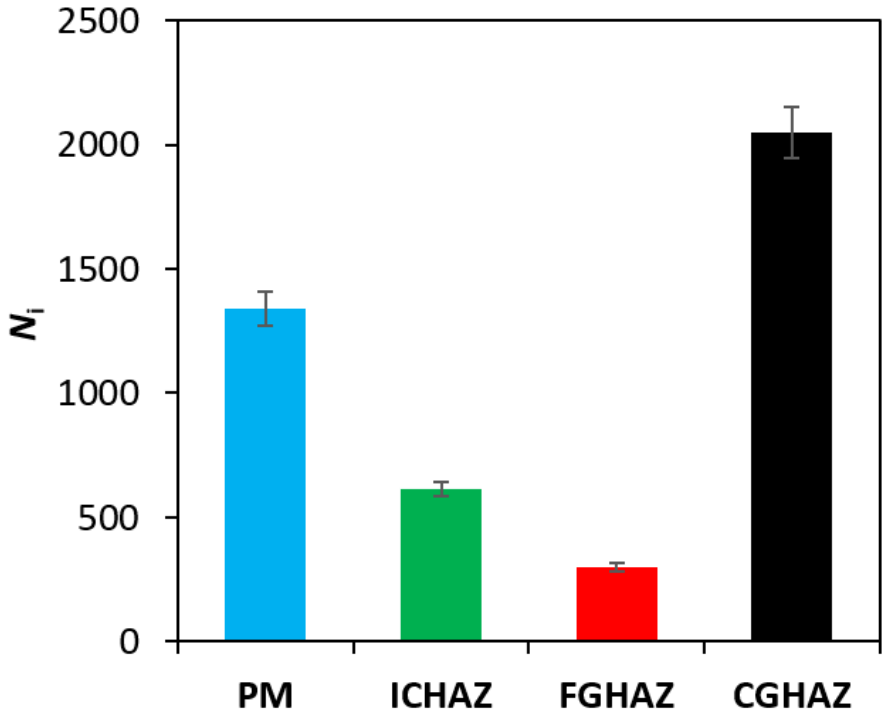

Figure 6.22. Comparison of predicted cycles to FCI in different sub-zones of the HAZ using the modified T-M equation and the five-material FE cross-weld model for 1.0% strain range at 500°C.

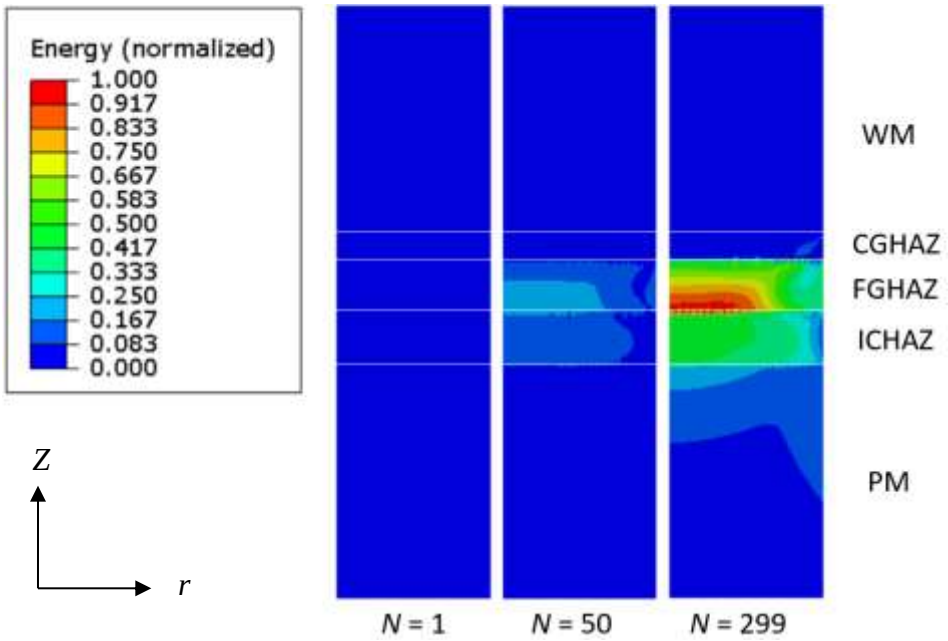

Figure 6.23. Cyclic evolution of normalized stored strain energy distribution in the FE model of P91 CW HTLCF cylindrical test specimen for 1.0% strain-range at 500°C.

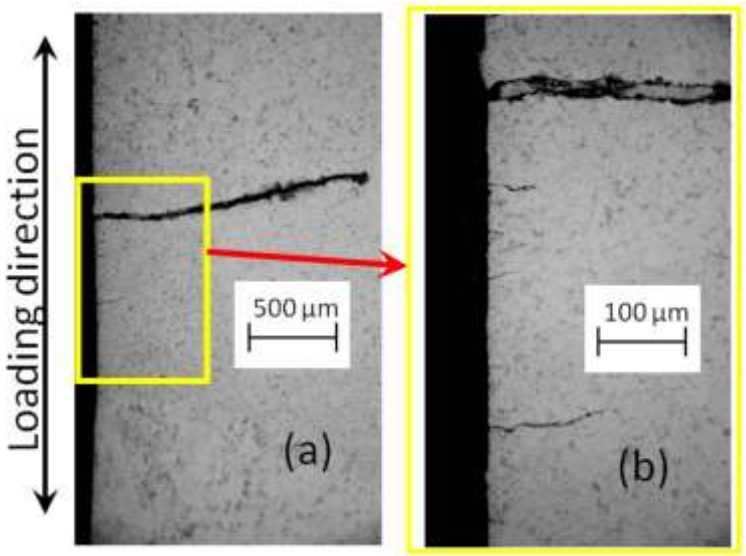

Figure 6.24**.** Optical micrograph of (a) primary crack (occurring in the HAZ) and (b) magnified view of primary and secondary (surface) crack of the CW specimen for 1.0% strain range at 500°C [26].

6.5 Discussion

The proposed mechanisms-based computational model shows that IC-, FG-HAZ regions are key hotspots for HTLCF crack initiation in welded P91. The five-material model, calibrated via physically-based YS and viscoplasticity models, with modified Tanaka-Mura, predicts the inhomogeneity in cyclic response between across the HAZ region and detrimental effect of welding on fatigue crack initiation.

The physically-based YS model presented here for weld-affected P91 captures the measured YS inhomogeneity across the P91 welded joint [28, 32]. Specifically, the model captures the increased YS (and thus hardness) value for CGHAZ, about 10% increase for the model compared to about 15% measured, and the decrease for ICHAZ material, about 5% predicted compared to about 10% measured. Mariappan et al. [28] have suggested that the substantial decrease of yield strength from CGHAZ to FGHAZ and ICHAZ is due to the lower soaking temperature during PWHT leads to a decrease in the solubility of MX-type precipitates and hence in solid solution strengthening contribution. Despite the significantly higher HAGB strengthening in FGHAZ, compared with that of CGHAZ, due to grain (mean block width) refinement, the significantly reduced lath width and increased dislocation density lead to pre-dominant dislocation strengthening contribution (Taylor hardening) in the CGHAZ. It can thus be concluded that with measurable microstructural parameters in the different weld-affected material regions, the physically-based YS model can predict welding-induced YS inhomogeneity, both qualitatively and quantitatively, with reasonable accuracy.

The influence of the microstructure and the strain-range on the first and stabilized stress-strain response of P91 welded joint is accurately captured by the physically-based cyclic viscoplasticity model, through the difference between the width of the martensite block and the width of the lath. The results show that the model based on the rule of mixtures formulation is in agreement with the experimental data. Specifically, for example, the maximum stresses have been calculated quite well compared to the measured data [26], and the general shape of the loop is captured. The inhomogeneity of cyclic softening

response within the PM and across the different HAZ sub-regions is also captured by the model, consistent with the DIC-measured observations of Touboul et al. [32] for tensile response of P91 welded joints at 625^{o}C. The physical cause of the increased softening rate in CGHAZ, e.g. see Figure 6.16, is the presence of freshly formed martensite combined with new, uncoarsened laths with high dislocation density [53]. The present physically-based model captures cyclic softening via evolution of the low angle boundary microstructure in P91 steels, including precipitate hardening and hierarchical grain boundary strengthening.

A five-material FE model was developed to study the HTLCF behaviour of P91 cross weld test specimens. It is known that long-term and short-term responses of materials like P91 at high temperature differ significantly, e.g. see [54], so that the Norton constants for short-term creep are generally different to those for long-term creep. The two-layer viscoplasticity model has been employed previously for P91 under HTLCF conditions [22]. Only the short term creep response is directly relevant to this work, since we are looking at HTLCF prediction, not involving long term (stress controlled) creep. Figure 6.9(b) shows a validation comparison of FE-predicted (five-material model) CW stress relaxation response of the two-layer viscoplasticity model used here for 0.5% applied strain, which correlates reasonably closely with the experimental data. The five-material FE model used here thus captures reasonably well the short-term stress relaxation effect in P91 steels under HTLCF conditions, although more extensive calibration and validation may be required to confirm applicability across a broader range of strain-rate and stress. Focusing on the strain distribution of the entire welded joint, the results show that as the number of cycles increases, complex cyclic evolution of multi-material stress and strain re-distribution is observed due to changes of constitutive behaviour of each material. CGHAZ predicted to have the highest strain concentration after significant cyclic loading. One might expect cyclic strain localization to concentrate within the ICHAZ, due it being the softest weld-affected sub-zone in P91 welded joints. However, the present modelling results demonstrate a more complex trend, viz. since the CGHAZ is determined to display a more rapid and extensive cyclic softening, strain localization appears there, mainly near

the edges of the welded joint. However, this is not pre-dominant in terms of failure location (see Figure 6.22). The normalised stored strain energy in Figure 6.23 is the ratio of local (integration point) energy to critical Tanaka-Mura energy for crack initiation in that material zone. Hence, a value of 1 for normalised energy indicates Tanaka-Mura fatigue crack initiation (FCI) at that material point. Significantly lower cycles to FCI are predicted for IC- and FG-HAZ than for CG-HAZ, despite the cyclic strain localisation in the latter. This is consistent with the observed cracking of P91 cross-weld HTLCF specimens in Figure 6.24, indicating cracking within the FG- and IC-HAZ regions [26].

Table 6.7. Comparison of measured and predicted weld life reduction factors (WLRF) for HTLCF of CW specimen at 500^{o}C.

Strain-range (%)	**Test**	**Modified Tanaka-Mura model**
0.6	3.6	3.7
0.8	3.6	3.5
1.0	2.8	4.5

A key novel contribution of this work is the modification of an energy-based Tanaka-Mura (T-M) method to account for cyclic softening in 9Cr steels, with packet size as the critical length scale for slip band formation [18], which is characteristic length in a hierarchical microstructure. The predictions of this mechanisms-based computational model are shown to agree consistently with initiation lives inferred from published test data for the effect of welding on HTLCF life in CW test specimens [26]. The modified T-M model has been adapted to predict cycles to FCI for the P91 welded joint. The results are in qualitative agreement with the findings from Shankar's work at 550^{o}C and 600^{o}C [4], which also showed failure within the ICHAZ (also consistent with the present work) and a detrimental effect of welding for HTLCF of P91 CW tests. The phenomenon of continuous cyclic softening here is a complicating factor, in terms of utilizing a conventional load-drop approach [55-57], for example. In this work, based on the rationale of Li et al. [52], the number of cycles to crack initiation has been estimated from the cyclic

softening curves for each strain-range and temperature (e.g. see Figure 6.19(b)), based on the assumption that the initial cyclic softening (gradual load drop with decreasing rate) is high temperature recovery-induced in terms of dislocation annihilation and microstructure coarsening, leading to diffuse micro-cracking, not due to the presence of a localized macroscale crack (e.g. as might occur after coalescence of multiple micro-cracks), giving a final, more sudden load drop towards zero, with increasing rate. Hence, in this work we distinguish between cycles to initiated micro-cracking N_{i} (identified as the end of recovery-induced softening in Figure 6.19(a)) and macro-scale cracking N_{f}, corresponding to final, more sudden load drop towards zero, with increasing rate. Nonetheless, it is true that slip band crack initiation will be conservative relative, even, to the recovery-induced N_{i}. Table 6.7 shows a comparison of predicted and measured weld life reduction factors, where $WLRF = N_i^{\mathrm{PM}}/N_i^{\mathrm{CW}}$, is the ratio of numbers of cycles to FCI in PM to that in CW. Clearly, the model and test data both show significant reduction in FCI life due to welding, and very close correlation for lower strain-ranges; the model is conservative relative to the test data at the highest (1%) strain range. Significant WLRF is also predicted by Mac Ardghail for HTLCF [58], with damage initiating in the ICHAZ during welding. Devaney [59] showed that the impact of welding on the room temperature fatigue life performance of X100 bainitic steel is very significant, resulting in a life reduction of up to two orders of magnitude. Long [60] provided a mechanistic explanation for the detrimental effect of welding on fatigue of X100 using FE modelling combined with physically-based modelling. A key next step for welded connections and the present model, is the extension to include fatigue crack propagation. Recently, Kramberger et al. [61] have presented a multi-scale numerical approach for evaluation of fatigue crack initiation and propagation in thermally cut martensitic steels, where the micro-crack initiation in the sub-model is based on the Tanaka-Mura model, similar to the present work, and fatigue crack propagation in the macro model is predicted using linear elastic fracture mechanics (LEFM), showing reasonably good correlation with experimental test results.

6.6 Conclusions

This paper presents a mechanisms-based fatigue crack initiation model for the effect of welding on the high temperature low cycle fatigue of P91 steel. The method is based on the combined use of (i) a modified Tanaka-Mura equation for cyclic softening martensitic steel, due to microstructure evolution effects, including lath coarsening and dislocation annihilation, (ii) application of previously-published physically-based yield strength and cyclic viscoplasticity models to the different material zones in a cross-weld specimen and (iii) implementation within phenomenological finite element modelling of the cross-weld high temperature low cycle fatigue tests. The key conclusions are:

- The physically-based yield strength model enables prediction of yield strength heterogeneity as a result of welding-induced metallurgical transformations on the P91 welded joints. The measured microstructural parameters of the heat affect zone obtained from published sources provide insights into the changes in the key strengthening mechanisms that lead to yield strength inhomogeneity in P91 steel.
- Variations in block width and lath width are shown to have a significant effect on yield strength heterogeneity. Compared with the coarse grain heat affected zone, the reduced block width in fine grain heat affected zone resulting in an 74% increase in high angle grain boundarie strengthening. The reduction in the lath width causes coarse grain heat affected zone to have the highest low-angle boundary strengthening and the highest Taylor hardening contribution, leading to highest yield strength in the coarse grain heat affected zone.
- The dislocation-mechanics cyclic viscoplasticity model successfully predicts the inhomogeneity in cyclic response across the heat affected zone region by directly representing the microstructural parameters of these different regions, which is also a key step to predict the inhomogeneous constitutive and fatigue life of P91 welded joints. coarse grain heat affected zone is determined to have the highest degree of cyclic softening, and consequently rapidly becomes the cyclically softest heat affected zone sub-zone.
- The constitutive behaviours of different regions of P91 welded joints including parent material, inter-critical heat affected zone, fine grain heat affected zone,

coarse grain heat affected zone and weld material have been successfully modelled using a Chaboche-type viscoplasticity model, which have also been used in the five-material FE model. With an increasing cycle number during high temperature low cycle fatigue loading, complex cyclic evolution of multi-material stress and strain re-distribution are observed across the cross weld fatigue model; coarse grain heat affected zone is predicted to have highest cyclic strain localisation.

- A modified form of the energy-based Tanaka-Mura equation has been developed for cyclically-softening metal and applied to successfully predict effect of strain-range on high temperature low cycle fatigue crack initiation in cyclic softening 9Cr steel at different temperatures.
- The modified Tanaka-Mura model has been applied to the different weld-affected sub-zones, including inter-critical , fine grain and coarse grain heat affected zone , as well as parent material and weld material, on the basis of packet size the key microstructural length scale for crack initiation, to successfully predict (i) the detrimental effect of welding and (ii) the quantitative effect in terms of weld life reduction factor. The inter-critical and fine grain heat affected zone regions are predicted as key hotspots for fatigue crack initiation in high temperature low cycle fatigue, consistent with previously published experimental work.
- Dislocations, precipitates, solutes, and high and low angle grain boundaries strengthen the complex hierarchical microstructure of 9Cr steels. It is necessary to establish a physical-based yield strength model, combined with physically-based strengthening and softening mechanisms and life prediction method, to accurately explain the microstructure evolution caused by the interaction of creep, fatigue and oxidation.

6.7 References

[1] T.P. Farragher, S. Scully, N. O'Dowd, S. Leen, Thermomechanical analysis of a pressurized pipe under plant conditions, Journal of Pressure Vessel Technology 135(1) (2013) 011204.
[2] R. Viswanathan, J. Henry, J. Tanzosh, G. Stanko, J. Shingledecker, B. Vitalis, R. Purgert, US program on materials technology for ultra-supercritical coal power plants,

Journal of Materials Engineering and Performance 14(3) (2005) 281-292.
[3] F. Abe, M. Tabuchi, M. Kondo, S. Tsukamoto, Suppression of Type IV fracture and improvement of creep strength of 9Cr steel welded joints by boron addition, International Journal of Pressure Vessels and Piping 84(1-2) (2007) 44-52.
[4] V. Shankar, K. Mariappan, R. Sandhya, M. Mathew, Evaluation of low cycle fatigue damage in grade 91 steel weld joints for high temperature applications, Procedia Engineering 55 (2013) 128-135.
[5] O. Basquin, The exponential law of endurance tests, American Society for Testing and Materials Proceedings 10 (1910) 625-630.
[6] L. Coffin, Fatigue at high temperature, Fatigue at elevated temperatures, ASTM International1973.
[7] K. Smith, A stress-strain function for the fatigue of metals, Journal of Materials 5 (1970) 767-778.
[8] K. Tokaji, T. Ogawa, Y. Harada, Z. Ando, Limitations of linear elastic fracture mechanics in respect of small fatigue cracks and microstructure, Fatigue & Fracture of Engineering Materials & Structures 9(1) (1986) 1-14.
[9] S. Glodež, B. Aberšek, J. Flašker, Z. Ren, Evaluation of the service life of gears in regard to surface pitting, Engineering Fracture Mechanics 71(4-6) (2004) 429-438.
[10] K. Tanaka, T. Mura, A Dislocation Model for Fatigue Crack Initiation, Journal of Applied Mechanics 48(1) (1981) 97-103.
[11] K.S. Chan, A microstructure-based fatigue-crack-initiation model, Metallurgical and Materials Transactions A 34(1) (2003) 43-58.
[12] X. Wu, On Tanaka-Mura's fatigue crack nucleation model and validation, Fatigue & Fracture of Engineering Materials & Structures 41(4) (2018) 894-899.
[13] M. Li, L. Wang, J.D. Almer, Dislocation evolution during tensile deformation in ferritic–martensitic steels revealed by high-energy X-rays, Acta materialia 76 (2014) 381-393.
[14] R.A. Barrett, P.E. O'Donoghue, S.B. Leen, A physically-based constitutive model for high temperature microstructural degradation under cyclic deformation, International Journal of Fatigue 100 (2017) 388-406.
[15] R.A. Barrett, P.E. O'Donoghue, S.B. Leen, A physically-based high temperature yield strength model for 9Cr steels, Materials Science and Engineering: A 730 (2018) 410-424.
[16] J. Earthman, G. Eggeler, B. Ilschner, Deformation and damage processes in a 12% Cr · Mo · V steel under high temperature low cycle fatigue conditions in air and vacuum, Materials Science and Engineering: A 110 (1989) 103-114.
[17] F. Masuyama, N. Komai, Evaluation of long-term creep rupture strength of tungsten-strengthened advanced 9-12% Cr steels, Key Engineering Materials 171 (2000) 179-188.
[18] M.N. Batista, M.C. Marinelli, S. Hereñú, I. Alvarez-Armas, The role of microstructure in fatigue crack initiation of 9–12%Cr reduced activation ferritic–martensitic steel, International Journal of Fatigue 72 (2015) 75-79.
[19] W. Zhang, X. Wang, H. Chen, T. Zhang, J. Gong, Evaluation of the effect of various prior creep-fatigue interaction damages on subsequent tensile and creep properties of 9% Cr steel, International Journal of Fatigue 125 (2019) 440-453.
[20] X. Wang, T. Zhang, W. Zhang, M.A. Wahab, J. Gong, An improved unified viscoplastic model for modelling low cycle fatigue and creep fatigue interaction loadings

of 9–12% Cr steel, European Journal of Mechanics-A/Solids 85 (2021) 104123.
[21] Abaqus Theory Guide, Dassault Systemes (2014).
[22] T.P. Farragher, S. Scully, N. O'Dowd, S. Leen, Development of life assessment procedures for power plant headers operated under flexible loading scenarios, International Journal of Fatigue 49 (2013) 50-61.
[23] J. Chaboche, G. Rousselier, On the plastic and viscoplastic constitutive equations—Part I: Rules developed with internal variable concept, Journal of Pressure Vessel Technology 105 (1983) 153–158.
[24] J.-L. Chaboche, G. Rousselier, On the plastic and viscoplastic constitutive equations—Part II: application of internal variable concepts to the 316 stainless steel, Journal of Pressure Vessel Technology 105 (1983) 159-164.
[25] M. Li, R.A. Barrett, S. Scully, N.M. Harrison, S.B. Leen, P.E. O'Donoghue, Cyclic plasticity of welded P91 material for simple and complex power plant connections, International Journal of Fatigue 87 (2016) 391-404.
[26] T.P. Farragher, S. Scully, N. O'Dowd, C.J. Hyde, S. Leen, High temperature, low cycle fatigue characterization of P91 weld and heat affected zone material, Journal of Pressure Vessel Technology 136(2) (2014) 021403.
[27] H. Bhadeshia, Models for the elementary mechanical properties of steel welds, Institute of materials, London 650 (1997) 229-284.
[28] M. K, V. Shankar, B. A. K, Comparative evaluation of tensile properties of simulated heat affected zones of P91 steel weld joint, Materials at High Temperatures 37(2) (2020) 114-128.
[29] C. Pandey, The Characterization of Soft Fine‐Grained Heat‐Affected Zones in P91 Weldments under Creep Exposure Conditions, Steel Research International 91(1) (2019) 1900342.
[30] C. Pandey, M.M. Mahapatra, P. Kumar, N. Saini, A. Srivastava, Microstructure and mechanical property relationship for different heat treatment and hydrogen level in multi-pass welded P91 steel joint, Journal of Manufacturing Processes 28 (2017) 220-234.
[31] T.H. Hyde, W. Sun, Determining high temperature properties of weld materials, JSME International Journal Series A Solid Mechanics and Material Engineering 43(4) (2000) 408-414.
[32] M. Touboul, J. Crepin, G. Rousselier, F. Latourte, S. Leclercq, Identification of Local Viscoplastic Properties in P91 Welds from Full Field Measurements at Room Temperature and 625 °C, Experimental Mechanics 53(3) (2012) 455-468.
[33] R. Swindeman, M. Santella, P. Maziasz, B. Roberts, K. Coleman, Issues in replacing Cr–Mo steels and stainless steels with 9Cr–1Mo–V steel, International Journal of Pressure Vessels and Piping 81(6) (2004) 507-512.
[34] F. Abe, Analysis of creep rates of tempered martensitic 9% Cr steel based on microstructure evolution, Materials Science and Engineering: A 510 (2009) 64-69.
[35] U.F. Kocks, A.S. Argon, M.F. Ashby, Thermodynamics and kinetics of slip, Pergamon Press1975.
[36] F. Nabarro, Dislocations in a simple cubic lattice, Proceedings of the Physical Society 59(2) (1947) 256.
[37] P.-F. Giroux, Experimental study and simulation of cyclic softening of tempered martensite ferritic steels, École Nationale Supérieure des Mines de Paris, 2011.

[38] Y. Wang, R. Kannan, L. Zhang, L. Li, Microstructural analysis of the as-welded heat-affected zone of a grade 91 steel heavy section weldment, Welding Journal 96(6) (2017) 203-219.
[39] A.S. Khan, S. Huang, Continuum theory of plasticity, John Wiley & Sons1995.
[40] A. Saad, C.J. Hyde, W. Sun, T. Hyde, Thermal-mechanical fatigue simulation of a P91 steel in a temperature range of 400–600 C, Materials at High Temperatures 28(3) (2011) 212-218.
[41] F.H. Norton, The creep of steel at high temperatures, McGraw-Hill Book Company1929.
[42] K. Mariappan, V. Shankar, A.K. Bhaduri, Effect of change in microstructures due to simulation temperatures on the low cycle fatigue behavior of P91 steel, International Journal of Fatigue 140 (2020) 105847.
[43] M. Sauzay, B. Fournier, M. Mottot, A. Pineau, I. Monnet, Cyclic softening of martensitic steels at high temperature—Experiments and physically based modelling, Materials Science and Engineering: A 483 (2008) 410-414.
[44] V.T. Paul, S. Saroja, P. Hariharan, A. Rajadurai, M. Vijayalakshmi, Identification of microstructural zones and thermal cycles in a weldment of modified 9Cr-1Mo steel, Journal of Materials Science 42(14) (2007) 5700-5713.
[45] C.G. Panait, A. Zielińska-Lipiec, T. Koziel, A. Czyrska-Filemonowicz, A.-F. Gourgues-Lorenzon, W. Bendick, Evolution of dislocation density, size of subgrains and MX-type precipitates in a P91 steel during creep and during thermal ageing at 600 C for more than 100,000 h, Materials Science and Engineering: A 527(16-17) (2010) 4062-4069.
[46] P.-F. Giroux, F. Dalle, M. Sauzay, J. Malaplate, B. Fournier, A.-F. Gourgues-Lorenzon, Mechanical and microstructural stability of P92 steel under uniaxial tension at high temperature, Materials Science and Engineering: A 527(16-17) (2010) 3984-3993.
[47] P. Yan, Z. Liu, H. Bao, Y. Weng, W. Liu, Effect of microstructural evolution on high-temperature strength of 9Cr–3W–3Co martensitic heat resistant steel under different aging conditions, Materials Science and Engineering: A 588 (2013) 22-28.
[48] K. Sawada, M. Takeda, K. Maruyama, R. Ishii, M. Yamada, Y. Nagae, R. Komine, Effect of W on recovery of lath structure during creep of high chromium martensitic steels, Materials Science and Engineering: A 267(1) (1999) 19-25.
[49] R. Barrett, T. Farragher, C.J. Hyde, N. O'Dowd, P. O'Donoghue, S.B. Leen, A unified viscoplastic model for high temperature low cycle fatigue of service-aged P91 steel, Journal of Pressure Vessel Technology 136(2) (2014).
[50] C.J. Hyde, W. Sun, S.B. Leen, Cyclic thermo-mechanical material modelling and testing of 316 stainless steel, International Journal of Pressure Vessels and Piping 87(6) (2010) 365-372.
[51] K. Chandravathi, K. Laha, K. Bhanu Sankara Rao, S. Mannan, Microstructure and tensile properties of modified 9Cr–1Mo steel (grade 91), Materials Science and Technology 17(5) (2001) 559-565.
[52] D.-F. Li, R.A. Barrett, P.E. O'Donoghue, N.P. O'Dowd, S.B. Leen, A multi-scale crystal plasticity model for cyclic plasticity and low-cycle fatigue in a precipitate-strengthened steel at elevated temperature, Journal of the Mechanics and Physics of Solids 101 (2017) 44-62.

[53] V. Shankar, B. AK, Comparative evaluation of tensile properties of simulated heat affected zones of P91 steel weld joint, Materials at High Temperatures 37(2) (2020) 114-128.
[54] R.A. Barrett, P. O'Donoghue, S.B. Leen, An improved unified viscoplastic constitutive model for strain-rate sensitivity in high temperature fatigue, International Journal of Fatigue 48 (2013) 192-204.
[55] K.B.S. Rao, M. Valsan, R. Sandhya, S. Ray, S. Mannan, P. Rodriguez, On the failure condition in strain-controlled low cycle fatigue, International Journal of Fatigue 7(3) (1985) 141-147.
[56] ASTM, Standard test method for strain‐controlled fatigue testing, ASTM Standard E606 (2012).
[57] R. Brommesson, M. Ekh, M. Hörnqvist, Correlation between crack length and load drop for low-cycle fatigue crack growth in Ti-6242, International Journal of Fatigue 81 (2015) 1-9.
[58] P. Mac Ardghail, N. Harrison, S. Leen, A process-structure-property model for welding of 9Cr power plant components: The influence of welding process temperatures on in-service cyclic plasticity response, International Journal of Pressure Vessels and Piping 173 (2019) 26-44.
[59] R.J. Devaney, P.E. O'Donoghue, S.B. Leen, Effect of welding on microstructure and mechanical response of X100Q bainitic steel through nanoindentation, tensile, cyclic plasticity and fatigue characterisation, Materials Science and Engineering: A 804 (2021) 140728.
[60] D. Long, R. Devaney, P. O'Donoghue, H. Song, R. Barrett, S. Leen, Characterisation of LCF Performance of X100 Weld-Joints: Mechanistic Yield Strength Modelling, Finite Element Analyses and DIC Testing, Journal of Advanced Joining Processes (2021) 100057.
[61] J. Kramberger, N. Jezernik, P. Göncz, S. Glodež, Extension of the Tanaka–Mura model for fatigue crack initiation in thermally cut martensitic steels, Engineering Fracture Mechanics 77(11) (2010) 2040-2050.

7 Conclusion and future work

7.1 Conclusion

The primary outcomes of this thesis are (i) the development of high efficiency, high accuracy FE models (using the Abaqus built-in AM module) for three-dimensional thermo-mechanical simulation of full-scale additive manufacturing processes (at component level) to facilitate process-structure-property-performance (PSPP) model for mitigation of residual stresses and deformations and (ii) development of a novel physically-based methodology for high temperature fatigue in welded connections. An efficient and accurate FE simulation method with detailed validation has been developed and applied to realistic DED Ti-6Al-4V and PBF Inconel 625 components. A physically based FE method has been developed for prediction of FCI in P91 welded joints under HTLCF conditions. These provide key building blocks towards physically-based process-structure-property-performance modelling of the effects of manufacturing process on fatigue.

The FE models of the AM process developed here using the Abaqus AM module shows the efficiency and accuracy of this approach for simulating the full AM process and predicting residual stress distributions and distortions of realistic DED and PBF components. Comparison with the more simplified, but commonly-used layer-by-layer method has demonstrated that the Abaqus-based AM tool is significantly more accurate for capturing peak temperatures and specific temporal variation (e.g. cooling rate, a key parameter for predicting phase transformations), and therefore the ‘Abaqus AM’ method has been adopted in our work.

Through the investigation of effect of scanning strategy, substrate removal and preheating condition on residual stresses and distortions using the validated model, it has been shown that: (i) it is possible to mitigate detrimental tensile residual stress effects via design of scanning strategy, (ii) removal of the substrate gives a significant beneficial reduction of residual stress and distortion and (iii) increasing preheating temperature and decreasing cooling rate can also significantly mitigate the residual stresses and distortions.

The development of a mechanisms-based FCI model will facilitate physically based FCI prediction in P91 welded joints for high flexibility, high efficiency power generation. The yield strength heterogeneity as a result of welding-induced metallurgical transformations and inhomogeneity in cyclic response across the HAZ region in P91 welded joints have been captured. The developed physically based computational model successfully predicts (i) the detrimental effect of welding on HTLCF life and (ii) the quantitative effect in terms of weld life reduction factor.

In summary, the developed FE models (using the Abaqus built-in AM module) for simulating AM process (DED and PBF) are accurate without significant computational cost, the residual stress and distortion can be predicted based on the actual process parameters means the model can be used as guideline for the selection of optimal manufacturing protocols for the industry. The developed physically-based methodology for modelling the effects of welding process on HTLCF of P91welded connections for CCGT thermal power plants, which is an important step towards future work, where physically-based FCI criterion based on the modified Tanaka-Mura model will be implemented to predict FCI in AM components. It is envisaged that the physically-based FCI prediction model will be combined with the high-efficiency AM process modelling method presented here (Chapters 3 and 4) to achieve development of a holistic physically-based process-structure-property-performance predictive methodology (see Figure 7.1) for application to metal AM. The intention is to directly address some identified key shortcomings of AM processes, viz. residual stresses-deformations and complexity of predicting post-build mechanical behaviour (e.g. fatigue) and thus contribute to more widespread adoption of AM in Irish, EU and international engineering industry. This will be achieved within the broader framework of the SFI I-Form Centre for Advanced Manufacturing in Ireland, which part-funded the present work. I-Form aims to provide the Irish manufacturing industry with capability for enhanced understanding of the effects of manufacturing processes on fatigue of AM. The work will also directly contribute to the development of digital twins for life assessment of strategically-important welded structures, including offshore wind turbine support structures and structural steelwork for

pumped storage, for example, to tackle ongoing and new challenges for the Irish energy industry, to allow increased uptake of renewable energy and improved grid stability and thus lead to cost savings for industry and contribute to the reduction of greenhouse gases and global warming. The welded fatigue aspect of this project has been conducted in collaboration with ESB, within the MECHANNICS SFI project.

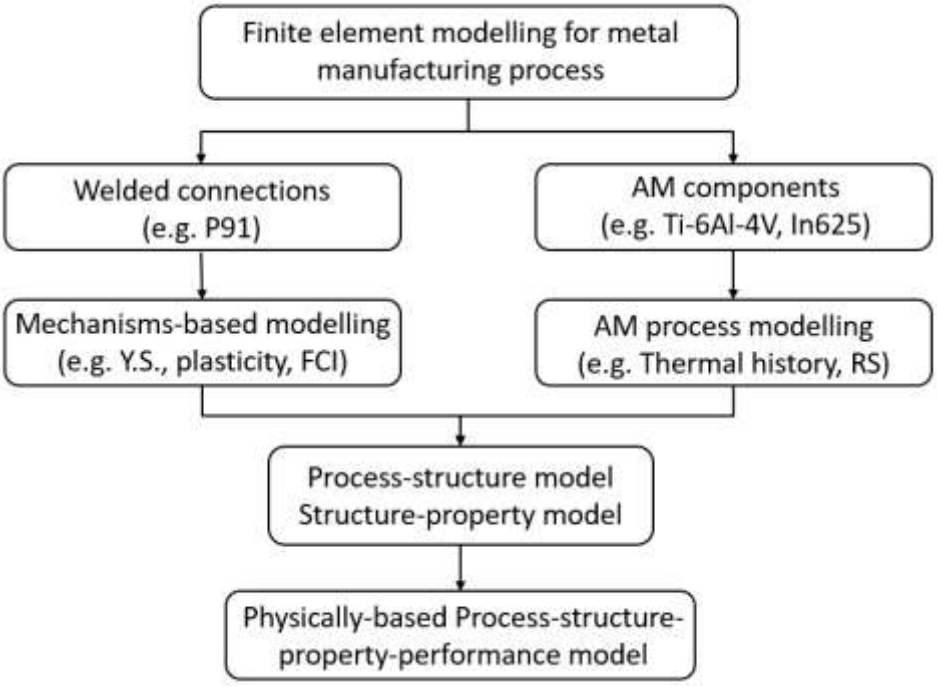

Figure 7.1. A flowchart summarizing the development of physically-based process-structure-property-performance model.

7.2 Future work

7.2.1 Future AM process modelling

Productivity is an especially important factor in the deployment of metal AM across industry [1, 2]. Systems with multi-laser beams have been developed to address the perceived low productivity of single-laser beam PBF systems [3, 4]. It is necessary to investigate the effect of scanning strategy and process parameters on residual stress and distortion by multi-laser beam PBF manufacturing via computational modelling at the component-level, which can offer guidelines to future equipment development strategies.

The high geometric design complexity offered by AM is often limited when printing complex geometries due to an inability to support the stresses inherent in the manufacturing process [5, 6]. Therefore, additional support structures are often needed. By following the results of the present work, support structures can be examined for better design for heat transfer, and mitigation of residual stress and distortion in AM processes.

In the AM process, metal powder particles are melted to form parts. Hence, a comprehensive understanding of particle behaviour is a key prerequisite for developing optimization process parameters to improve the production quality and efficiency [7, 8]. The discrete element method (DEM), which can be used to model discrete matter, such as powder particles, by tracking the motion and temperature of individual particles, has gained popularity in AM modelling studies [9, 10]. Future work should consider combining a mixed representation involving both DEM and FEM to develop a multi-physics modelling approach.

7.2.2 Full-field metallurgical phase transformation modelling for AM process

The high energy heat source in the AM process always generates a large thermal gradient within the printed part which can produce unique microstructures compared with other conventional manufacturing processes [11]. Furthermore, the quality of AM components is extremely sensitive to the selection of process parameters, including power of laser heat source, laser scanning velocity, hatch spacing and layer thickness [12, 13]. Hence, it is critical to characterize the correlation between processing parameters and the resulting microstructure and defects of the AM components. Zhang et al. [14] have presented an FE-based framework for predicting volume fractions of metallurgical phase transformation applied to AM processes, successful validation was performed via comparison against temperature measurements and volume fractions, with metallographic assessments using EBSD/XRD of printed and heat-treated PBF Ti-6Al-4V samples. It is planned to combine the computational model developed in Chapter 3 and 4 with metallurgical phase transformation model in the future, to directly link AM process conditions to microstructural features at the component-level.

7.2.3 Implement with the PSPP model for application at component-level

The development of a PSPP model could make a significant contribution to the AM process optimization, such as saving time and cost compared to existing trial-and-error methods. Recently, Yang et al. [15] have presented a physically-based structure-property model for assessing the mechanical properties (yield stress, ultimate tensile strength, uniform elongation and flow stress) of PBF manufactured Ti-6Al-4V, including the effects of solutes, grain size, phase volume fraction and dislocation density; the predicted tensile stress-strain responses were validated against measured tensile test data from 25 ˚C to 1000 ˚C. The effects of temperature-dependence on tensile stress-strain response are captured more accurately by including solid-state phase transformation (SSPT) effects; while stress is significantly over-predicted for temperatures above 400 ˚C by including the SSPT effects. In future work, it is planned to combine the current model with the process-structure model [16] for microstructure prediction based on the FE predicted thermal histories at the component-level, and with the structure-property model [15] for resultant mechanical properties prediction of realistic, large-scale AM components, to capture the effects of key AM manufacturing parameters for AM process optimization. Fatigue life prediction is particularly important for AM processed metals. It is also intended to integrate the achieved PSPP tool with the developed physically-based FCI model in Chapter 5 to predict the effects of AM-induced microstructure inhomogeneity on the fatigue response and investigate the effect of microstructure features on mechanical performance of complex AM geometries, such as conformally cooled injection moulding dies.

7.2.4 Experimental measurements

Within the I-Form Centre for Advanced Manufacturing in Ireland, we are working with Atlantic Technological University, industrial partners (e.g. AbbVie Ireland Unlimited Company) and international collaborations (e.g. Nanjing Tech University) to develop PSPP methods for prediction of fatigue of complex geometrical components, e.g. AM conformally-cooled injection moulding dies and inserts. This is an very important practical motivation behind the present work on the computational investigation of

residual stress in macro-scale complex PBF component. Experimental measurements of residual stress and distortion in conformally-cooled injection moulding dies might be considered in future work. Heat treatment after the printing process are normally performed to reduce residual stress and internal defects of AM components [17, 18]. Experimental investigation of preheating and heat treatment effects on residual stress of PBF conformally cooled injection moulding dies might also be considered in future work. Furthermore, Zhang et al. [19] have performed tribological and profilometry tests on the AM and forged Ti-6Al-4V, their results show that the hardness and wear resistance of the AM Ti-6Al-4V are superior to those of the forged Ti-6Al-4V. Hence, it appears reasonable to experimentally investigate the wear and erosion behaviour of AM material in order to provide a wider characterization of their properties in order to evaluate new applications, such as bringing the potential benefits of AM material for improved tribological performance (wear and friction), particularly for medical device applications.

The effect of build orientation and surface roughness on the fatigue behavior and residual stress will be examined in future work. Specimens built in different orientations (e.g. horizontal and vertical to the substrate) will be considered to account for anisotropy effects in fatigue of AM components. The physically-based T-M model will be adapted and verified for prediction of FCI in AM 316L stainless steel. Future work involves another paper in preparation based on the work being done at Nanjing Tech University including (i) surface roughness measurement, (ii) residual stress measurement, (iii) tensile and fatigue testing and (iv) microstructure analysis of 316L stainless steel specimens produced by PBF. The current test results are shown in Appendix.

7.3 References

[1] Y. Zhai, D.A. Lados, J.L. LaGoy, Additive manufacturing: making imagination the major limitation, JOM 66(5) (2014) 808-816.
[2] V.V. Popov, A. Fleisher, Hybrid additive manufacturing of steels and alloys, Manufacturing Review 7 (2020) 6.
[3] M. Masoomi, S.M. Thompson, N. Shamsaei, Quality part production via multi-laser additive manufacturing, Manufacturing Letters 13 (2017) 15-20.
[4] K. Wei, F. Li, G. Huang, M. Liu, J. Deng, C. He, X. Zeng, Multi-laser powder bed fusion of Ti–6Al–4V alloy: defect, microstructure, and mechanical property of overlap

region, Materials Science Engineering: A 802 (2021) 140644.
[5] J. Jiang, X. Xu, J. Stringer, Support structures for additive manufacturing: a review, Journal of Manufacturing Materials Processing 2(4) (2018) 64.
[6] S.C. Subedi, A. Shahba, M. Thevamaran, D.J. Thoma, K. Suresh, Towards the optimal design of support structures for laser powder bed fusion-based metal additive manufacturing via thermal equivalent static loads, Additive Manufacturing 57 (2022) 102956.
[7] E.J. Parteli, T. Pöschel, Particle-based simulation of powder application in additive manufacturing, Powder Technology 288 (2016) 96-102.
[8] C. Meier, R. Weissbach, J. Weinberg, W.A. Wall, A.J. Hart, Critical influences of particle size and adhesion on the powder layer uniformity in metal additive manufacturing, Journal of Materials Processing Technology 266 (2019) 484-501.
[9] T.I. Zohdi, Additive particle deposition and selective laser processing-a computational manufacturing framework, Computational Mechanics 54(1) (2014) 171-191.
[10] K. Marchais, J. Girardot, C. Metton, I. Iordanoff, A 3D DEM simulation to study the influence of material and process parameters on spreading of metallic powder in additive manufacturing, Computational Particle Mechanics 8(4) (2021) 943-953.
[11] Y. Lian, Z. Gan, C. Yu, D. Kats, W.K. Liu, G.J. Wagner, A cellular automaton finite volume method for microstructure evolution during additive manufacturing, Materials & Design 169 (2019) 107672.
[12] J. Delgado, J. Ciurana, C.A. Rodríguez, Influence of process parameters on part quality and mechanical properties for DMLS and SLM with iron-based materials, The International Journal of Advanced Manufacturing Technology 60(5) (2012) 601-610.
[13] B. Onuike, A. Bandyopadhyay, Additive manufacturing in repair: Influence of processing parameters on properties of Inconel 718, Materials Letters 252 (2019) 256-259.
[14] Q. Zhang, J. Xie, Z. Gao, T. London, D. Griffiths, V. Oancea, A metallurgical phase transformation framework applied to SLM additive manufacturing processes, Materials & Design 166 (2019) 107618.
[15] X. Yang, R.A. Barrett, N.M. Harrison, S.B. Leen, A physically-based structure-property model for additively manufactured Ti-6Al-4V, Materials & Design 205 (2021) 109709.
[16] X. Yang, R.A. Barrett, M. Tong, N.M. Harrison, S.B. Leen, Towards a process-structure model for Ti-6Al-4V during additive manufacturing, Journal of Manufacturing Processes 61 (2021) 428-439.
[17] R. Barros, F.J. Silva, R.M. Gouveia, A. Saboori, G. Marchese, S. Biamino, A. Salmi, E. Atzeni, Laser powder bed fusion of Inconel 718: Residual stress analysis before and after heat treatment, Metals 9(12) (2019) 1290.
[18] Ó. Teixeira, F.J. Silva, E. Atzeni, Residual stresses and heat treatments of Inconel 718 parts manufactured via metal laser beam powder bed fusion: an overview, The International Journal of Advanced Manufacturing Technology 113(11) (2021) 3139-3162.
[19] T. Zhang, N. Harrison, P. McDonnell, P. McHugh, S. Leen, A finite element methodology for wear–fatigue analysis for modular hip implants, Tribology International 65 (2013) 113-127.